NOTE TO USERS

This reproduction is the best copy available.

UMI®

UNIVERSITY OF CALIFORNIA

Los Angeles

Multiscale Modeling and Control of Thermal Spray Processing of Nanostructured Coatings

A dissertation submitted in partial satisfaction of the requirements for the degree Doctor of Philosophy in Chemical Engineering

by

Mingheng Li

2004

UMI Number: 3164412

INFORMATION TO USERS

The quality of this reproduction is dependent upon the quality of the copy submitted. Broken or indistinct print, colored or poor quality illustrations and photographs, print bleed-through, substandard margins, and improper alignment can adversely affect reproduction.

In the unlikely event that the author did not send a complete manuscript and there are missing pages, these will be noted. Also, if unauthorized copyright material had to be removed, a note will indicate the deletion.

UMI®

UMI Microform 3164412

Copyright 2005 by ProQuest Information and Learning Company.

All rights reserved. This microform edition is protected against unauthorized copying under Title 17, United States Code.

ProQuest Information and Learning Company
300 North Zeeb Road
P.O. Box 1346
Ann Arbor, MI 48106-1346

The dissertation of Mingheng Li is approved.

Sheldon K. Friedlander

Robert M'Closkey

Gerassimos Orkoulas

Panagiotis D. Christofides, Committee Chair

University of California, Los Angeles

2004

Contents

1 Introduction **1**

1.1 Nanostructured coatings 1

1.2 Thermal spray process 2

1.3 Motivation for process control 7

1.4 Research objective and thesis structure 11

2 Generic Modeling and Control Issues in HVOF Thermal Spray Process **18**

2.1 Principle of HVOF thermal spray process 19

2.2 Generic modeling issues in HVOF thermal spray process 20

2.2.1 Modeling assumptions and modeling procedure 20

2.2.2 Modeling of compressible nozzle flow 23

2.2.3 Modeling of particle motion and temperature 27

2.2.4 Process simulation results and analysis 29

2.3 Modeling of powder size distribution 34

2.4 Generic control issues in HVOF thermal spray process 39

2.4.1 Control problem formulation and controller design 39

2.4.2 Simulation results of HVOF process under feedback control . . 42

2.5 Summary 50

3 Diamond Jet Hybrid HVOF Thermal Spray Process: Control-relevant Modeling of Gas-phase and Particle Behavior 53

3.1 Modeling of gas thermal and flow fields in the Diamond Jet hybrid HVOF thermal spray process 54

3.1.1 Process characteristics and modeling procedure 54

3.1.2 Modeling of gas thermal and flow fields in the entire flow field 56

3.2 Modeling of particle velocity, temperature and melting degree in the Diamond Jet hybrid HVOF thermal spray process 64

3.3 Analysis of gas and particle behavior in the Diamond Jet hybrid HVOF thermal spray process 68

3.3.1 Analysis of the gas dynamics without air 68

3.3.2 Analysis of gas dynamics including the air stream 75

3.3.3 Analysis of particle velocity, temperature and melting ratio . . 79

3.4 Summary 82

4 Diamond Jet Hybrid HVOF Thermal Spray Process: Rule-based Modeling and Analysis of Coating Microstructure 86

4.1 Introduction 87

4.2 Characteristics of deposition and coating growth 89

4.2.1 Deformation 90

4.2.2 Pore formation 91

4.2.3 Surface roughness 94

4.3 Computer simulation of coating formation 95
4.3.1 Simulation procedure 95
4.3.2 Coating growth rules 98
4.3.3 Simulation settings 101
4.4 Simulation results and discussions 103
4.4.1 Microstructure of coatings made of particles of different molten states 103
4.4.2 Influence of operating conditions on coating properties 108
4.4.3 Comparison of stochastic simulation results and experimental studies 118
4.5 Summary 119

5 Diamond Jet Hybrid HVOF Thermal Spray Process: Model-based Estimation and Control of Particle Velocity and Melting 121

5.1 Feedback control of HVOF thermal spray process 122
5.1.1 Control problem formulation and controller design for the Diamond Jet hybrid HVOF thermal spray process 122
5.1.2 Simulation results of HVOF process model under feedback control 125
5.2 Model-based estimation and control of particle velocity and melting ratio in HVOF thermal spray 136
5.2.1 Real-time estimation of volume-averaged particle velocity and melting ratio 136
5.2.2 Model-based control of particle velocity and melting degree . . 141
5.3 Summary 149

6 Control of HVOF Thermal Spray Process: Application to the Processing of WC-Co Coatings **150**

6.1 Gas and Particle behavior 150

6.2 Closed-loop simulations 159

6.3 Summary 167

7 CFD Modeling and Analysis of HVOF Thermal Spray Process **170**

7.1 Introduction 171

7.2 Fluid dynamics 176

7.2.1 Torch geometry 176

7.2.2 Governing equations 177

7.2.3 Eddy dissipation Model 180

7.3 Particle dynamics 182

7.4 Results and discussion 185

7.4.1 Analysis of gas dynamics 185

7.4.2 Analysis of particle inflight behavior 195

7.4.3 Analysis of coating microstructure formation 206

7.5 Summary 209

8 Conclusions **211**

8.1 Conclusions 211

8.2 Future work 215

Bibliography **219**

List of Figures

1.1 TEM dark images of (a) plasma sprayed nanocrystalline CoCr and (b) HVOF sprayed nanocrystalline Ni coatings [78, 1]. 3

1.2 (a) HVOF thermal spray processing and (b) plasma thermal spray processing. 4

1.3 A schematic of the Diamond Jet hybrid HVOF thermal spray process. 6

1.4 SEM images of Cu-10 wt.% Al powders milled for 10 hours in (a) methanol, and (b) liquid nitrogen [76]. 6

1.5 Bright field TEM images of Cu-10 wt.% Al powders for 20 hours in (a) methanol, and (b) liquid nitrogen [76]. 7

1.6 Cross-sectional morphology of four HVOF sprayed hydroxyapatite (HA) particles with different melting degrees and a TEM image of the as-sprayed HA coating showing the interface between melted and unmelted parts of HA splat [70]. 9

1.7 Multiscale character of the HVOF thermal spray process [87]. 12

2.1 (a) Schematic and (b) computational domain of the HVOF torch. . . 20

2.2 (a) Axial velocity and (b) temperature profiles of gas and particle along the flow field for different particle sizes d_p = 5, 10, 20, 30, and 50 μm under operating conditions P = 9 bar and φ = 1.0 and three different injection velocities v_0 = 0, 40 and 80 m/s. 31

2.3 (a) Axial velocity and (b) temperature as a function of flight time for different particle sizes d_p = 5, 10, 20, 30, and 50 μm under operating conditions P = 9 bar and φ = 1.0 and three different injection velocities v_0 = 0, 40 and 80 m/s. 32

2.4 Particle velocity and temperature as a function of combustion chamber pressure and equivalence ratio - (a) P = 4, 7 and 11 bar, φ = 1.0. (b) φ = 0.8, 1.0 and 1.2, P = 9 bar. 33

2.5 Gas properties in the combustion chamber (dash-dot line: gas temperature) and at the exit of the nozzle (dashed line: gas temperature, solid line: gas velocity) - (a) P = 9 bar, φ = 0.8 - 1.2. (b) φ = 1.0, P = 9 - 15 bar. 34

2.6 Gas density at the exit of the nozzle - φ = 1.0 and P = 9 - 15 bar. . 35

2.7 (a) Axial particle velocity and (b) temperature at the point of impact on substrate as a function of particle size and particle injection velocity. Operating conditions: P = 9 bar, φ = 1.0. 36

2.8 Schematic of the HVOF control system. 41

2.9 Profiles of (a) volume-based average particle velocity and (b) particle temperature with respect to time - Control problem formulation accounting for powder size distribution. 44

2.10 Profiles of (a) chamber pressure and (b) equivalence ratio with respect to time - Control problem formulation accounting for powder size distribution. 44

2.11 Profiles of (a) volume-based average particle velocity and (b) particle temperature with respect to time - Control problem formulation without accounting for powder size distribution. 46

2.12 Profiles of (a) chamber pressure and (b) equivalence ratio with respect to time - Control problem formulation without accounting for powder size distribution. 46

2.13 Profiles of (a) volume-based average particle velocity and (b) particle temperature with respect to time in the presence of a 30% disturbance on spray distance. Open-loop system (solid curve) and closed-loop system (dashed curve). 47

2.14 Profiles of (a) chamber pressure and (b) equivalence ratio with respect to time in the presence of a 30% disturbance on spray distance. Open-loop system (solid curve) and closed-loop system (dashed curve). . . . 48

2.15 Profiles of (a) volume-based average particle velocity and (b) particle temperature with respect to time in the presence of 80 m/s variation in initial particle velocity. Open-loop system (solid curve) and closed-loop system (dashed curve). 48

2.16 Profiles of (a) chamber pressure and (b) equivalence ratio with respect to time in the presence of 80 m/s variation in initial particle velocity. Open-loop system (solid curve) and closed-loop system (dashed curve). 49

2.17 Profiles of (a) volume-based average particle velocity and (b) particle temperature with respect to time in the presence variation in powder size distribution. Open-loop system (solid curve) and closed-loop system (dashed curve). 50

2.18 Profiles of (a) chamber pressure and (b) equivalence ratio with respect to time in the presence of variation in powder size distribution. Open-loop system (solid curve) and closed-loop system (dashed curve). . . . 51

3.1 Profiles of (a) equilibrium temperature and (b) total mass flow rate with respect to P and φ. Operating conditions: $P = 5$ - 15 *bar* and φ = 0.5 - 1.6. 70

3.2 Profiles of (a) gas density and (b) velocity at the throat with respect to P and φ. Operating conditions: $P = 5$ - 15 *bar* and $\varphi = 0.5$ - 1.6. 70

3.3 Profiles of (a) temperature and (b) momentum flux at the throat with respect to P and φ. Operating conditions: $P = 5$ - 15 *bar* and $\varphi =$ 0.5 - 1.6. 71

3.4 Normalized average molecular weight, temperature, and sonic velocity at the throat of the nozzle under operating conditions: (a) $P = 5$ - 15 *bar*, $\varphi = 1.0$, and (b) $P = 9$ *bar*, $\varphi = 0.5$ - 1.6. Normalization is done with respect to the corresponding gas properties under operating conditions: $P = 9$ *bar* and $\varphi = 1.0$ (Table 3.3). 73

3.5 Normalized gas temperature, velocity, momentum flux, and mass flow rate in the internal field under operating conditions: (a) P = 5 - 15 bar, φ = 1.0 and (b) P = 9 bar, φ = 0.5 - 1.6. Normalization is done with respect to the corresponding gas properties under operating conditions: P = 9 bar and φ = 1.0 (Table 3.3). 74

3.6 Profiles of (a) pressure and (b) equilibrium temperature with respect to φ and m/m_{bl}. Operating conditions: x the same as the one in the baseline condition (Propylene: 176 $scfh$ (standard cubic feet per hour), Oxygen: 578 $scfh$, Air: 857 $scfh$, Nitrogen: 28.5 $scfh$), total mass flow rate varying from 0.8 to 1.2 times the one of the baseline value (18.1 g/s), and φ = 0.5 - 2.0. 76

3.7 Profiles of (a) equilibrium temperature and (b) pressure with respect to φ and x. Operating conditions: total mass flow rate the same as the one in the baseline condition, φ = 0.5 - 2.0, and x = 0 - 16.7. . . 77

3.8 Profile of optimal equivalence ratio corresponding to the peak temperature of the gas with respect to x. Operating conditions: total mass flow rate the same as the one in the baseline condition, x = 0 - 16.7. . 77

3.9 Profiles of particle velocity, temperature, and melting ratio along the flow field (x = 0 corresponds to the nozzle exit). 81

3.10 Velocity, temperature and melting ratio at the 0.254 m standoff (point of impact on substrate) as a function of particle size. 83

3.11 Effect of disturbances on operating conditions (particle injection velocity and spray distance) on particle velocity, temperature and flight time. 84

4.1 Deformation of (a) fully melted particle and (b) partially melted particle upon impact on the substrate. 92

4.2 Schematic of the five types of pores. 94

4.3 Modeling procedure for coating microstructure. 96

4.4 Sketch of the splat position used in the model. 98

4.5 Splat formation rules (shaded area corresponds to added splat and dotted area corresponds to pore formation) - (a) coating surface before impact of partially melted particle, (b) coating structure after impact of partially melted particle, (c) splat breaking up, (d) pore formation at the corner of a step, (e) pore formation in a gap and (f) splat pileup on a step. 99

4.6 Simulated coating section using fully-melted particles and partially-melted particles. 105

4.7 Comparison of simulation results for fully melted and partially melted particles under baseline operating conditions. 107

4.8 The melting ratio of particles with different size under baseline operating conditions. 107

4.9 The effect of oxygen flow rate on (a) particle melting behavior, (b) coating porosity, (c) surface roughness and (d) deposition efficiency. . 110

4.10 The effect of fuel flow rate on (a) particle melting behavior, (b) coating porosity, (c) surface roughness and (d) deposition efficiency. 112

4.11 The effect of air flow rate on (a) particle melting behavior, (b) coating porosity, (c) surface roughness and (d) deposition efficiency. 114

5.1 Schematic of the proposed feedback control system. 125

5.2 Profiles of (a) controlled outputs (average particle velocity and melting ratio), (b) manipulated inputs (flow rate of propylene, oxygen and air), and (c) total mass flow rate and equivalence ratio, under the request of 5% increase in average particle velocity and 5% decrease in the melting ratio - Control problem formulation accounts for the effect of powder size distribution. 128

5.3 Profiles of (a) controlled outputs (average particle velocity and melting ratio), (b) manipulated inputs (flow rate of propylene, oxygen and air), and (c) total mass flow rate and equivalence ratio, under the request of 5% increase in average particle velocity and 5% decrease in the melting ratio - Control problem formulation does not account for the effect of powder size distribution. 130

5.4 Profiles of (a) controlled outputs (average particle velocity and melting ratio), (b) manipulated inputs (flow rate of propylene, oxygen and air), and (c) total mass flow rate and equivalence ratio, in the presence of disturbance (20% increase) in the spray distance. 132

5.5 Profiles of (a) controlled outputs (average particle velocity and melting ratio), (b) manipulated inputs (flow rate of propylene, oxygen and air), and (c) total mass flow rate and equivalence ratio, in the presence of disturbance (20% decrease) in the spray distance. 133

5.6 Profiles of (a) controlled outputs (average particle velocity and melting ratio), (b) manipulated inputs (flow rate of propylene, oxygen and air), and (c) total mass flow rate and equivalence ratio, in the presence of disturbance (10% increase) in particle injection velocity. 134

5.7 Profiles of (a) controlled outputs (average particle velocity and melting ratio), (b) manipulated inputs (flow rate of propylene, oxygen and air), and (c) total mass flow rate and equivalence ratio, in the presence of disturbance (20% decrease) in particle injection velocity. 135

5.8 Profiles of (a) controlled outputs (average particle velocity and melting ratio), (b) manipulated inputs (flow rate of propylene, oxygen and air), and (c) total mass flow rate and equivalence ratio, in the presence of disturbance (10% increase) in particle injection velocity. 137

5.9 Profiles of (a) controlled outputs (average particle velocity and melting ratio), (b) manipulated inputs (flow rate of propylene, oxygen and air), and (c) total mass flow rate and equivalence ratio, under the request of 5% increase in average particle velocity and 5% decrease in the melting ratio - Closed-loop simulation in the presence of measurement error. . 138

5.10 Diagram of the gas phase measurement system. 140

5.11 (a) Average particle velocity and (b) particle melting ratio at the point of impact on the substrate under noise in the measurements of gas phase - simulation with and without adaptive filter. 142

5.12 Diagram of the closed-loop system under the proposed estimator/controller structure. 143

5.13 Profiles of (a) average particle velocity, (b) average particle melting ratio, (c) gas flow rates of propylene, (d) gas flow rates of oxygen, (e) combustion pressure and (f) equivalence ratio under the request of set-point change in the average particle velocity and average particle melting ratio. 145

5.14 Profiles of (a) average particle velocity, (b) average particle melting ratio, (c) gas flow rates of propylene, (d) gas flow rates of oxygen, (e) combustion pressure and (f) equivalence ratio, in the presence of a 30% decrease in the spray distance. 147

5.15 Profiles of (a) average particle velocity, (b) average particle melting ratio, (c) gas flow rates of propylene, (d) gas flow rates of oxygen, (e) combustion pressure and (f) equivalence ratio, in the presence of 3% increase in the powder size. 148

6.1 Modeling procedure of the gas and particle field. 151

6.2 Correlation of (a) gas velocity, (b) temperature and (c) density in the supersonic free jet. data 1 - mach number=1.8, ρ_e/ρ_{air} = 3.7 [62, 63], data 2 - mach number = 2.0, data 3 - mach number = 2.0 [73], ρ_e/ρ_{air} = 7-8 [125, 126]. 155

6.3 Profiles of (a) gas velocity, (b) temperature and (c) density along the centerline. 156

6.4 Profiles of (a) particle velocity, (b) temperature and (c) degree of melting along the centerline. 158

6.5 (a) Particle velocity, (b) temperature and (c) degree of melting at the 8 *inch* (0.203 *m*) standoff (point of impact on substrate) as a function of particle size. 160

6.6 Profiles of (a) controlled outputs (average particle velocity and melting ratio), (b) manipulated inputs (flow rate of propylene, oxygen and air), and (c) pressure and equivalence ratio under the request of 5% increase in particle velocity and 5% increase in melting ratio. 162

6.7 Profiles of (a) controlled outputs (average particle velocity and melting ratio), (b) manipulated inputs (flow rate of propylene, oxygen and air), and (c) pressure and equivalence ratio in the presence of 10% decrease in spray distance. 164

6.8 Profiles of (a) controlled outputs (average particle velocity and melting ratio), (b) manipulated inputs (flow rate of propylene, oxygen and air), and (c) pressure and equivalence ratio in the presence of 10% increase in spray distance. 165

6.9 Profiles of (a) controlled outputs (average particle velocity and melting ratio), (b) manipulated inputs (flow rate of propylene, oxygen and air), and (c) pressure and equivalence ratio in the presence of variation in powder size distribution. 166

6.10 Profiles of (a) controlled outputs (average particle velocity and melting ratio), (b) manipulated inputs (flow rate of propylene, oxygen and air), and (c) pressure and equivalence ratio under the request of 5% increase in particle velocity and 5% increase in melting ratio - Closed-loop simulation in the presence of measurement error. 168

7.1 Schematic diagram of the Diamond Jet Hybrid Thermal Spray Gun. . 176

7.2 Computational domain and boundary conditions. 186

7.3 Contours of flooded gas properties (upper plot) and centerline profiles of gas properties (lower plot) - (a) static pressure (b) density (c) axial velocity (d) static temperature and (e) mach number. 188

7.4 Schematic of wave structure in the overexpanded jet. 189

7.5 Contour of static temperature outside of the torch. 190

7.6 Contour of static temperature in the combustion chamber. 190

7.7 Mole fraction of each gas component along the centerline. 191

7.8 Influence of gas flow rates on gas properties - (a) static pressure, (b) density, (c) axial velocity, (d) static temperature, and (e) mach number in the centerline. 194

7.9 Comparison of (a) axial velocity, (b) temperature, and (c) density of gas phase in the centerline using a simplified one dimensional model [87, 88] and the CFD model [85]. 196

7.10 Influence of substrate on (a) axial velocity and (b) static temperature in the centerline. 197

7.11 Profiles of (a) particle velocity, (b) temperature and (c) melting ratio along the centerline. 199

7.12 (a) velocity and (b) temperature of particles of different sizes under 20 m/s injection velocity and different spray distances. 201

7.13 (a) velocity and (b) temperature of particles of different sizes under 0.2 m spray distance and different injection velocities. 201

7.14 (a) gas momentum flux and (b) gas temperature along the centerline under different gas flow rates. Normalization is done with respective to the corresponding properties under baseline gas flow rates. 206

7.15 (a) velocity and (b) temperature of particles of different sizes at 0.2 m standoff under different gas flow rates. 207

7.16 (a) Simulated coating microstructure and (b) pore distribution in the coatings made of fully melted particles (ideal case). 209

7.17 (a) Simulated coating microstructure and (b) pore distribution in the coatings made of particles of nonuniform molten states, which are deposited under the baseline conditions. 210

7.18 (a) Simulated coating microstructure and (b) pore distribution in the coatings made of particles of nonuniform molten states, which are deposited under the conditions in case 4. 210

List of Tables

1.1 Typical operating conditions and main characteristics of the Diamond Jet Hybrid HVOF thermal spray process. 6

2.1 Process parameters used in the open-loop simulation. 30

2.2 Process parameters used in the closed-loop simulation 42

3.1 Dimension of the air cap. 55

3.2 Comparison of computational and experimental results for a Diamond Jet process [111]. 63

3.3 Gas properties under operating conditions: $P = 9\ bar$ and φ =1.0. . 74

3.4 Nine different gas flow rates. 78

3.5 Calculated gas properties for different operating conditions. 79

3.6 Thermophysical properties of powder particles. 80

4.1 Operating conditions for the Diamond Jet hybrid thermal spray process in the simulation. 102

4.2 Thermophysical properties of powder particles. 102

4.3 Experimental systems for parametric analysis. 118

5.1 Process and controller parameters used in the closed-loop simulation. 126

5.2 Estimator and controller parameters used in the closed-loop simulation. 144

5.3 Operating conditions. 146

6.1 Baseline operating conditions. 152

6.2 Calculated gas equilibrium composition under baseline conditions. . . 153

6.3 Calculated gas properties in the internal flow field. 153

6.4 Calculated gas thermodynamic and transport properties in the internal and external flow fields under the baseline operating conditions. . . . 154

6.5 Parameters used in the closed-loop simulation. 161

7.1 Summary of previous CFD modeling work. 174

7.2 Specified gas flow rate for parametric analysis of Diamond Jet Hybrid HVOF gun. 187

7.3 Reaction formula obtained from equilibrium chemistry. 193

7.4 Thermophysical properties of WC-12%Co particles [122]. 198

ACKNOWLEDGEMENTS

I am grateful to my advisor, Prof. Panagiotis D. Christofides, who has helped and encouraged me in various ways. His dedication to academic excellence, both in research and teaching, has been a constant source of inspiration for me.

I am grateful to Prof. Sheldon K. Friedlander, Prof. Robert M'Closkey, and Prof. Gerassimos Orkoulas for agreeing to participate in my examining committee.

I would like to thank the members of the Process Control group, especially Dan, for having created a pleasant and stimulating working atmosphere. Finally, I am indebted to my wife, Lina, for her constant support, encouragement, and dedication.

VITA

November 2, 1975	Born, Tianmen City, Hubei Province, China
1997	B. E., Chemical Engineering Beijing University of Chemical Technology Beijing, China
2000	M. E., Chemical Engineering Tsinghua University Beijing, China
2000-04	Graduate Student Department of Chemical Engineering University of California, Los Angeles, CA

PUBLICATIONS

Hu, S.; Li, M.; Li Y.; Shen, J.; Liu, Z. "Reaction Path Synthesis Methodology for Waste Minimization ," *Science in China Series B: Chemistry*, **47**, 206-213, 2004.

Li, M.; Christofides, P. D. "Modeling and Analysis of HVOF Thermal Spray Process Accounting for Powder Size Distribution," *Chemical Engineering Science*, **58**, 849-857, 2003.

Li, M.; Christofides, P. D. "Feedback Control of HVOF Thermal Spray Process Accounting for Powder Size Distribution," *Journal of Thermal Spray Technology*, **13**, 108-120, 2004.

Li, M.; Hu, S.; Li Y.; Shen, J. "A Hierarchical Optimization Method for Reaction Path Synthesis," *Industrial and Engineering Chemistry Research*, **39**, 4315-4319, 2000.

Li, M.; Hu, S.; Li Y.; Shen, J. "Reaction Path Synthesis for a Mass Closed-cycle System," *Computers and Chemical Engineering*, **24**, 1215-1221, 2000.

Li, M.; Shi, D.; Christofides, P. D. "Modeling and Control of HVOF Thermal Spray Processing of WC-Co Coatings," *Powder Technology*, 2004. (in press)

Li, M.; Shi, D.; Christofides, P. D. "Model-based Estimation and Control of Particle Velocity and Melting in HVOF Thermal Spray," *Chemical Engineering Science*, 2004. (in press)

Li, M.; Shi, D.; Christofides, P. D. "Diamond Jet Hybrid HVOF Thermal Spray: Gas-phase and Particle Behavior Modeling and Feedback Control Design," *Industrial and Engineering Chemistry Research*, **43**, 3632-3652, 2004.

Shi, D.; Li, M.; Christofides, P. D. "Diamond Jet Hybrid HVOF Thermal Spray: Rule-based Modeling of Coating Microstructure," *Industrial and Engineering Chemistry Research*, **43**, 3653-3665, 2004.

ABSTRACT OF THE DISSERTATION

Multiscale Modeling and Control of Thermal Spray Processing of Nanostructured Coatings

by

Mingheng Li

Doctor of Philosophy in Chemical Engineering

University of California, Los Angeles, 2004

Professor Panagiotis D. Christofides, Chair

This thesis presents our work on the multiscale modeling and control of the HVOF thermal spray processing of nanostructured coatings, which is motivated by the superior qualities of nanostructured coatings and high sensitivity of the coated material to arbitrary variation in the operating environment. The central idea of the controller design is to use the models that describe the dynamic behavior of the various components of the HVOF thermal spray process to synthesize feedback controllers that can be readily implemented in practice.

We developed a comprehensive multiscale model, which includes continuum type differential equations that describe the evolution of gas and particle temperature and velocity, and a rule-based stochastic simulator that predicts the evolution of coating microstructure. Based on the process model, a detailed comprehensive parametric analysis is carried out to study the relationship between the key process parameters and the particle inflight behavior as well as the resulting coating properties. This

analysis shows that the particle velocity and melting ratio play a very important role in the formation of coating microstructure, which in turn, can be almost independently adjusted by manipulating the combustion pressure and the fuel/oxygen ratio. To develop a feedback controller that can be readily implemented in practice, the control problem is formulated as the one of regulating volume-based averages of the melting ratio and velocity of the particles at the point of impact on the substrate by directly manipulating the flow rate of fuel, oxygen and air at the entrance of the HVOF gun. A multivariate control system is developed and applied to a fundamental process model. Closed-loop simulations demonstrate that the proposed control system is effective in driving the particle velocity and melting ratio at impact into set-point values and is also robust with respect to various disturbances in the operating environment.

Chapter 1

Introduction

1.1 Nanostructured coatings

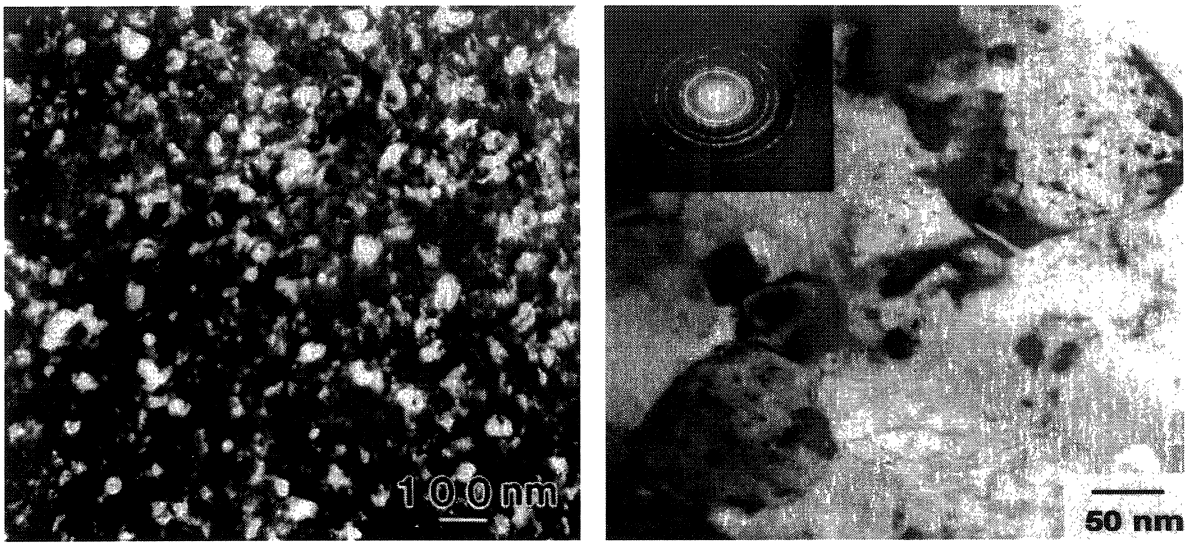
Nanostructured (also called nanoscale, nanophase or nanocrystalline) materials are materials with grain sizes less than about 100 nm, and are generally obtained by processing of nanosize powders. Currently, there is a great interest in the understanding and processing of nanostructured materials which stems from the cost-effective production of high-quality nanosize powders as well as the discovery that such materials have properties superior to those of conventional bulk materials, including strength, hardness, ductility, sinterability, size-dependent light absorption, reactivity, etc. (see, for example, [41, 51, 59, 78, 136, 113, 3, 135, 68, 69, 77, 67, 117].) The superior properties of nanostructured materials motivate their use in a wide variety of applications such as protective coatings for heat engines and gas turbines, hard materials for machine tools, ductile ceramics, catalysts, new electronic and optical devises, etc.

With prompt advances in the production of high quality unagglomerated nanoscale powders, including atomization, colloidal precipitation, mechanical milling, and vapor phase nucleation and growth (see, for example, [104, 105, 134, 138]), the focus

of nanostructured materials research is now shifting from synthesis to processing, for example, the fabrication of nanostructured coatings using the so-called thermal spray technology [78, 53, 1]. Figure 1.1 shows two typical dark field Transmission Electron Microscopy (TEM) images of the nanocrystalline CoCr coating prepared by plasma thermal spraying [78] and the nanocrystalline Ni coating prepared by HVOF thermal spraying [1], illustrating an average grain size smaller than 100 nm. Compared to the traditional counterparts, the nanostructured coatings exhibit superior qualities in several aspects including increased hardness and strength, improved ductility, and enhanced diffusivity and sinterability [129, 61, 74, 75]. Nowadays, the nanostructured coatings are widely used in many industries as thermal-barrier, wear-resistant and corrosion-protective surface layers to extend product life, increase performance and reduce production and maintenance costs. Other primary uses of nanostructured coatings include dimensional restoration, maintaining precise clearances, and modifying thermal and electrical properties.

1.2 Thermal spray process

In the simplest terms possible, the thermal spray processes represent a group of particulate deposition processes in which a material, in powder or wire form, are propelled and heated in a gas/plasma stream and deposited on a given substrate in a molten or semi-molten state, and the coating microstructure results from the solidification and sintering of the particles [109]. Thermal spray processes provide a low-cost and energy-efficient route for the processing of nanostructured coatings because they require significantly fewer manufacturing steps than conventional welding processes. They are also characterized by zero dilution of the substrate as a result of mechanical bonding, the ability to apply thin coatings, and a high rate of area



(a) (b)

Figure 1.1: TEM dark images of (a) plasma sprayed nanocrystalline CoCr and (b) HVOF sprayed nanocrystalline Ni coatings [78, 1].

coverage, compared to arc welding processes. Thermal spray processes of most commercial interest include high velocity oxygen fuel (HVOF) and atmospheric plasma arc spraying (PAS). (see Figure 1.2 for a schematic of these two processes.) In the HVOF thermal spray process, the fuel is burnt with oxygen at a high pressure and generate a sonic or supersonic exhaust jet, which heats up the powders and propels them to the substrate. Currently, there is an increasing interest in the HVOF thermal spray processing of nanostructured coatings, which owes to its unique process characteristics - very high gas/particle velocity and relatively low gas/particle temperature, as compared to those in plasma spray process. On the one hand, the extremely high particle velocity helps to densify the coating and to increase the deposition rate. On the other hand, the very short residence time in the relatively low temperature gas flame makes the powder particles highly plastic and superheating or vaporization is prevented [17, 19].

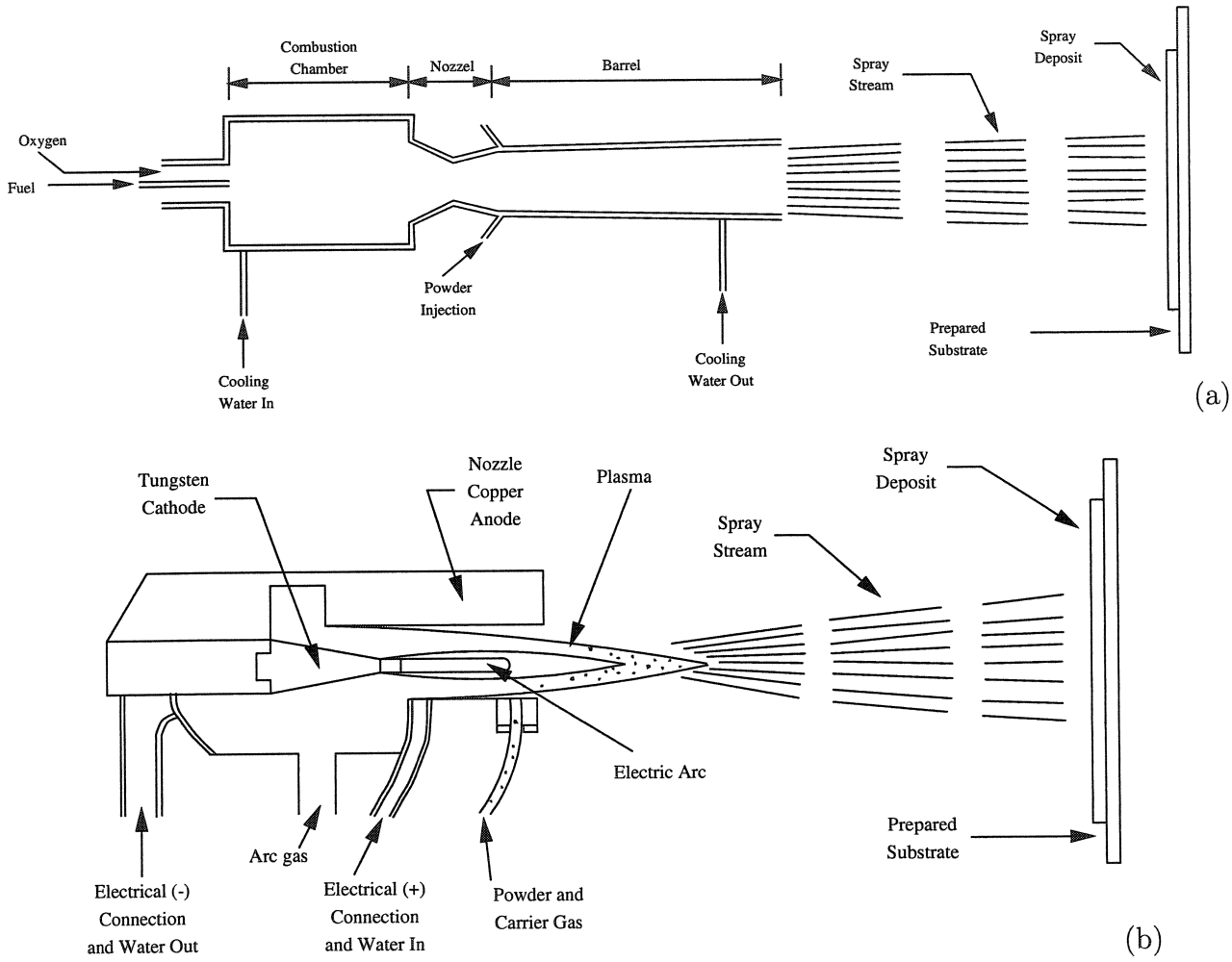


Figure 1.2: (a) HVOF thermal spray processing and (b) plasma thermal spray processing.

Figure 1.3 shows a schematic diagram of the Diamond Jet hybrid HVOF thermal spray gun (Sulzer Metco, Westbury, NY), which is currently used in industry. In this process, the premixed fuel (typically propylene or hydrogen) and oxygen are fed from the annular gap to the air cap (also referred to as convergent-divergent nozzle), where they react to produce high temperature combustion gases. The exhaust gases, together with the air injected from the annular inlet orifice, expand through the nozzle to reach supersonic velocity. The air cap is water-cooled to prevent from being melted. The powder particles are injected from the central inlet hole using nitrogen as the carrier gas. Consequently, rapid momentum and heat transfer between the gas and the powder particles leads to acceleration and heating of the powder particles. The molten or semi-molten particles exit the air cap and move towards the substrate. The particles hit the substrate, cool and solidify, forming a thin layer of dense and hard coating. The typical operating conditions and main characteristics of the Diamond Jet Hybrid HVOF thermal spray process are given in Table 1.1. It should be noted that although the gain size of nanostructured coatings is about 100 nm, the powders used for coating processing are actually nanostructured agglomerates whose sizes are typically on the magnitude of 10 μm (see Figures 1.4 and 1.5 for SEM images of the flake-shaped Cu-10 wt.% Al agglomerates produced by methanol- and cryo-milling and TEM images of the corresponding TEM images illustrating nanosize grains). This is because, in the thermal spray processing, very small particles usually follow the gas stream and do not stick on the substrate, which will be illustrated in Chapter 7.

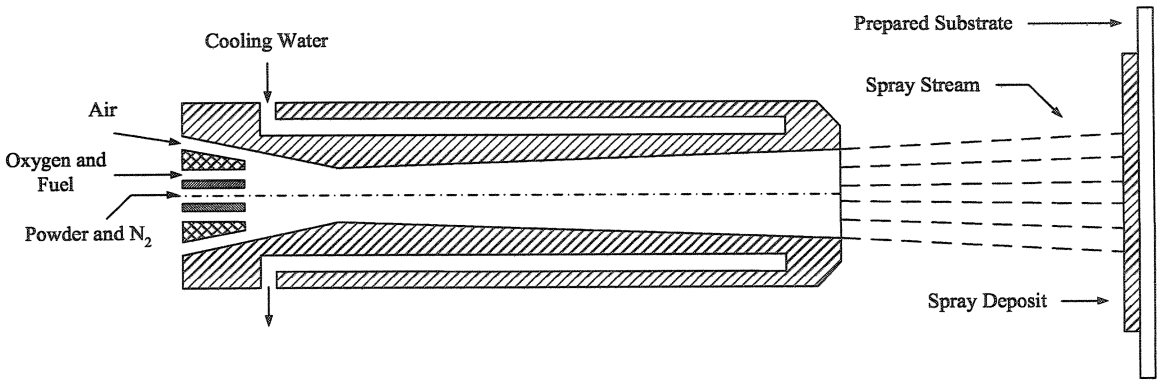
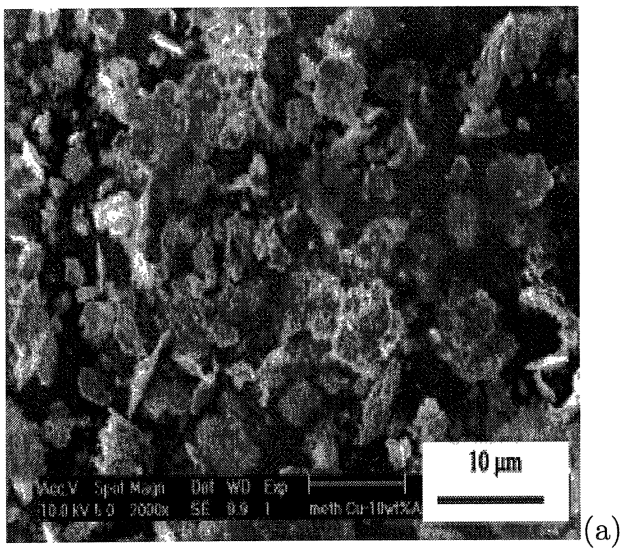
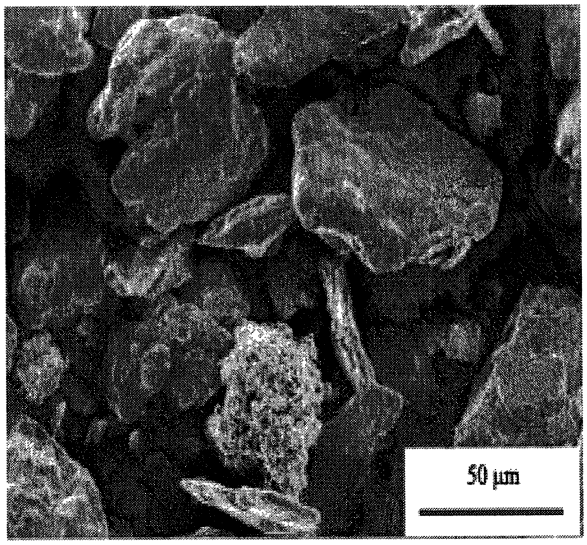


Figure 1.3: A schematic of the Diamond Jet hybrid HVOF thermal spray process.



(a)



(b)

Figure 1.4: SEM images of Cu-10 wt.% Al powders milled for 10 hours in (a) methanol, and (b) liquid nitrogen [76].

Table 1.1: Typical operating conditions and main characteristics of the Diamond Jet Hybrid HVOF thermal spray process.

Typical operating conditions		Main process characteristics	
Gas flow rate	18 g/s (12 l/s)	Flame temperature	2800 ^{0}C
Powder feed rate	20 - 80 g/min	Exit Mach number	2
Powder size	5 - 45 μm	Exit gas velocity	2000 m/s
Coating thickness	100 - 300 μm	Deposition efficiency	70 %
Spray distance	150 - 300 mm	Coating porosity	1 - 2 %

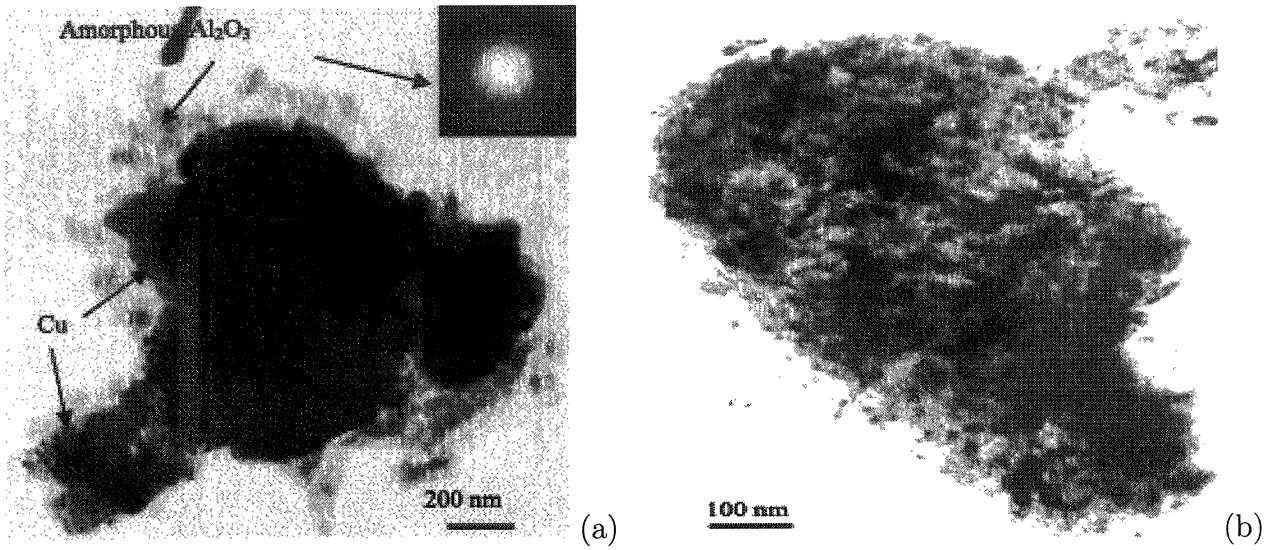


Figure 1.5: Bright field TEM images of Cu-10 wt.% Al powders for 20 hours in (a) methanol, and (b) liquid nitrogen [76].

1.3 Motivation for process control

Although the past three decades have witnessed the wide application of thermal spray process as a means of materials processing in many industries, it is only recently that there has been a great interest in the processing of nanostructured materials [17]. In order for these practical applications to be realized in a broad industrial scale, the basic engineering problem of controlled processing of the nanopowders into useful nanostructured materials has to be addressed. Whereas thermal spray processing provides a natural way for the processing of nanopowders to useful nanostructured materials with desired properties, for the most part, they have been developed through costly trial and error procedures. In many cases, a general knowledge of the overall behavior has been attained, but fundamental understanding and critical parameters that affect the final product are not clearly defined. Consequently, the final product yield and precise regulation of final product properties has been low due to the lack

of tight monitoring and control of the critical parameters. For example, the work of Khor et al. [70] shows that the particle melting ratio plays a very important role in the formation of coating microstructure and resulting coating properties (see Figure 1.6). Therefore, this parameter should be precisely controlled during the deposition process to achieve coating uniformity.

Over the last decade, the need to optimally design and operate thermal spray processes has motivated significant research on the development of fundamental mathematical models for thermal spray processes that explicitly account for various physicochemical phenomena and the dynamic behavior of various process components. Specifically, fundamental models have been developed targeting the complex gas/particle flow behavior involved in the internal and external flow field of the HVOF gun (see review papers [121, 17]); molten droplet formation, motion, impact and deposition [94, 93, 8, 137]; droplet solidification, microstructure development, surface roughness and coating porosity [128, 61, 10, 82, 133]; phase transformations of nanocrystalline powders [23]; and the relationship between the nanostructure and the mechanical properties of the end-product [44, 11, 10, 31]. In addition, research has been carried out in the integration of the detailed models of the aforementioned components to develop general simulators that describe the behavior of entire thermal spray processes [140, 85].

These modeling efforts have been complemented with significant research on the development of intelligent measurement sensors for thermal spray process monitoring including laser light scattering techniques for ensemble and single particle sizing [7, 115, 4, 5, 55, 7, 60, 79, 12, 57, 58, 118, 81, 13]; optical methods for particle velocity [132, 38] and particle temperature [108, 36] and measurement of melt flowrate [45, 57, 58, 81]. Comprehensive reviews of results in this area can be found in [60, 55, 79, 9].

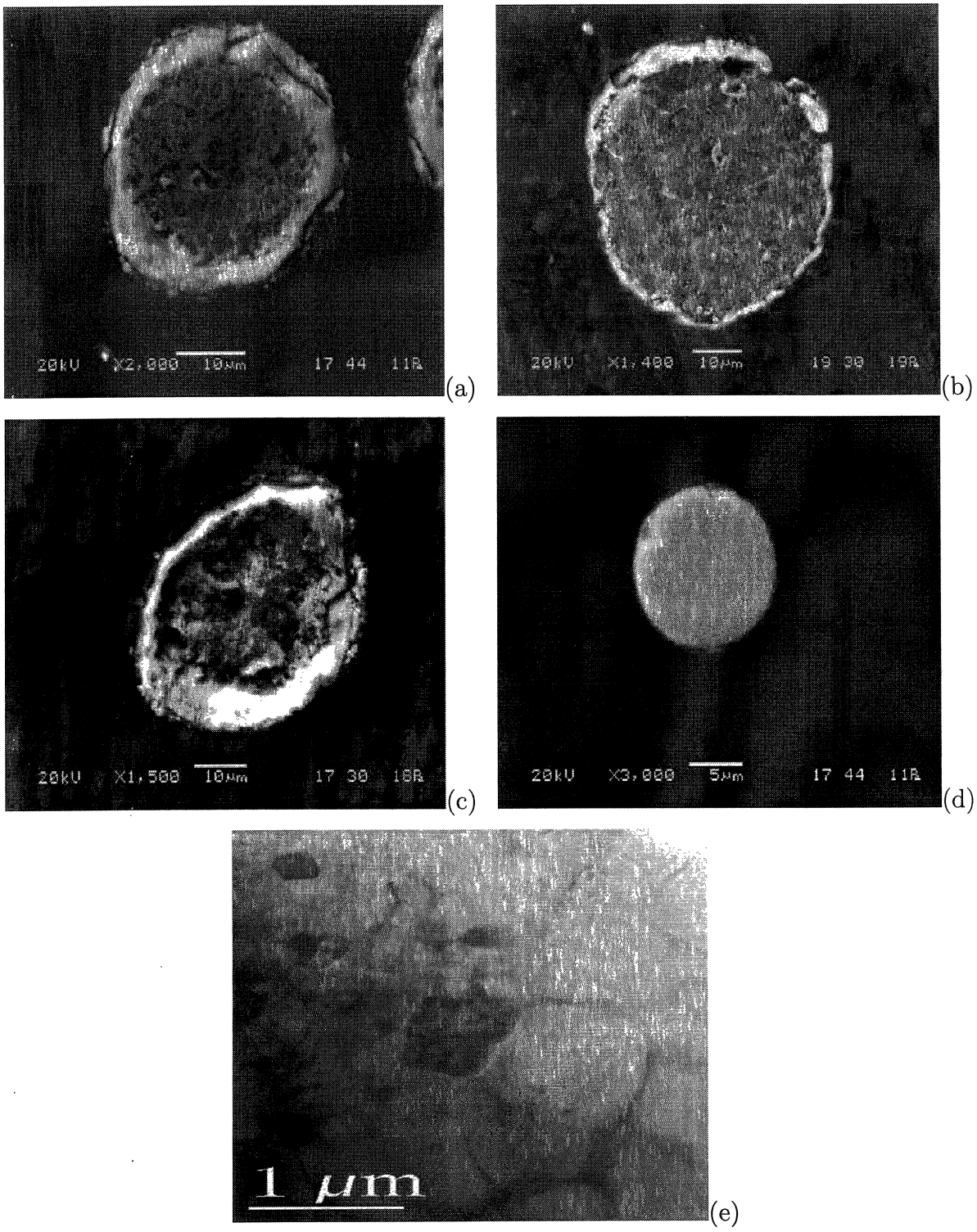


Figure 1.6: Cross-sectional morphology of four HVOF sprayed hydroxyapatite (HA) particles with different melting degrees and a TEM image of the as-sprayed HA coating showing the interface between melted and unmelted parts of HA splat [70].

An effort to integrate real-time diagnostic techniques with simple control schemes has been done in the context of expert systems (e.g., [123]). However, expert systems provide simple supervisory control and cannot deal with the critical issue of precise control of the size distribution of the droplets impinging on the substrate which affects the structure and end-properties of the nanostructured coatings.

In order for HVOF thermal spray process to be widely used in industry for the processing of nanostructured coatings, it is important to achieve excellent real-time diagnosis and control of the processing stage which will allow to obtain coatings with nanostructures that yield the desired thermal and mechanical properties. Despite the recent progress on modeling of the various phenomena that affect droplet motion, deposition, solidification and microstructure development in HVOF thermal spray process, at this stage, there exists no systematic framework for integrated on-line diagnosis and control of the HVOF thermal spray processing which will be capable of achieving precise regulation of the microstructure and ultimate mechanical properties of the sprayed materials and coatings. Since the incorporation of the advanced feedback control on thermal spray processes has been reported to lead to significant improvements in their operation and performance [2, 98], it is of great significance to close this gap by integrating fundamental models that accurately describe the inherent relationships between the coating micro- and nano-structure and the processing parameters (such as substrate surface condition, gas flow rate, and fuel/oxygen ratio etc.) with on-line state-of-the-art diagnostic techniques and advanced nonlinear control algorithms, to develop high-performance real-time computer control systems for thermal spray processes which on-line manipulate process variables flow rate, gas pressure, spray motion and angle, substrate motion, to regulate the microstructure and end-properties of the deposits. In addition, incorporation of advanced real-time

diagnosis and control schemes into thermal spray processes is expected to reduce operational cost and environmental impact, and improve end-product properties and yield. Recent efforts in this direction have mainly focused on diagnostics and control of plasma thermal spray (see [37]); the reader may also refer to [102] for a discussion of various process optimization and control issues.

1.4 Research objective and thesis structure

The objective of the present research is to develop a computational methodology to precisely control the coating micro- or nano-structure, which determines the coating mechanical and physical properties, by manipulating macro-scale operating conditions such as the gas flow rate and spray distance, etc. The major challenge on this problem lies in the development of multiscale models linking the macroscopic scale process behavior (i.e., gas dynamics and particle inflight behavior) and the microscopic scale process characteristics (evolution of coating microstructure), and the integration of models, measurements, and control theory to develop measurement/model-based control strategies [24]. The underlying multiscale behavior of the HVOF process is shown in Figure 1.7 [87]. On the one hand, the microstructure of thermally sprayed coatings results from the deformation, solidification and sintering of the deposited particles, which are dependent on the substrate properties (e.g., substrate temperature) as well as the physical and chemical state (e.g., temperature, velocity, melting ratio, and oxidant content etc.) of the particles at the point of impact on the substrate. On the other hand, the particle inflight behavior, however, is coupled with the gas dynamics, which can be manipulated by adjusting operating conditions such as the total gas flow rate and the fuel/oxygen ratio. While the macroscopic thermal/flow field can be readily described by continuum type differential equations governing the compress-

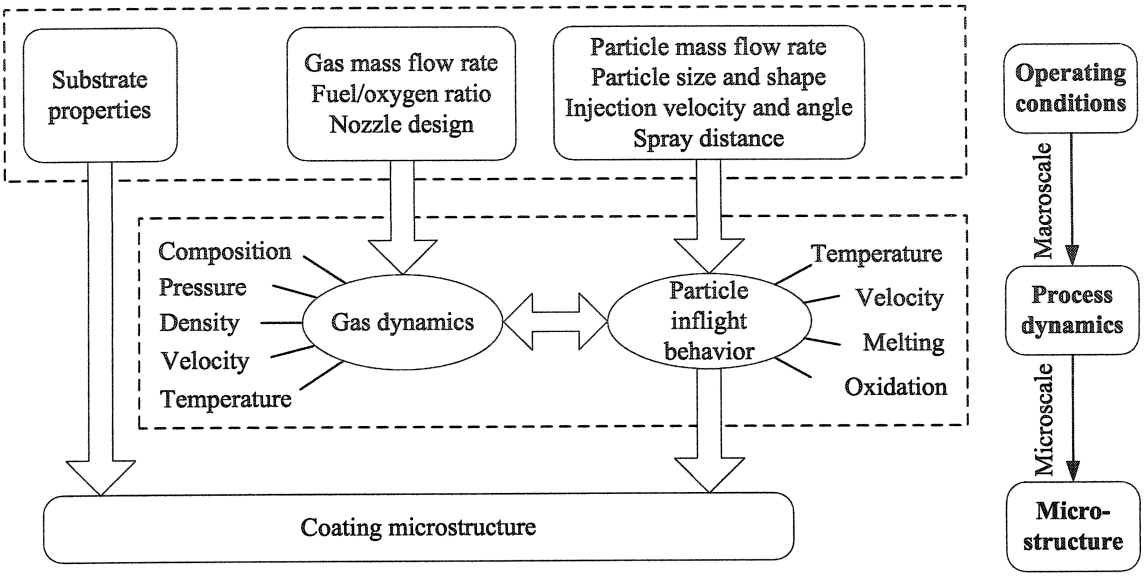


Figure 1.7: Multiscale character of the HVOF thermal spray process [87].

ible two-phase flow, the process of particle deposition is stochastic and discrete in nature, and thus, it can be best described by stochastic simulation methods [72]. By manipulating macroscopic operating conditions, such as gas flow rate, fuel/oxygen ratio, spray distance etc., one can adjust gas and particle dynamics, and eventually, control coating microstructure.

To address this problem, we conducted research in the following areas:

- **Generic Modeling and Control Issues in HVOF Thermal Spray [83, 84]**

This work presents the principle of the HVOF thermal spray process and generic modeling and control issues. Commonly used equations and formulas as well as widely acknowledged assumptions in the process modeling are discussed. Based on the proposed fundamental mathematical model, control relevant parametric analysis is made to show the influence of operating conditions and particle size on the velocity and temperature of particles at the point of impact on the substrate, which are two main control objectives in the HVOF thermal spray process. Based on the model

predictions and available experimental data, the control problem is formulated as the one of regulating volume-based averages of velocity and temperature of particles at the point of impact on the substrate by manipulating two process parameters - chamber pressure and fuel/oxygen ratio. A feedback control system is developed and applied to a detailed mathematical model of the process, and the dynamic behavior of the HVOF thermal spray process under feedback control is tested through computer simulations. The proposed modeling and control strategy provides preliminaries for the development of a practical control system of an industrial HVOF thermal spray process.

- **Diamond Jet Hybrid HVOF Thermal Spray Process: Control-relevant Modeling and Analysis of Gas-phase and Particle Behavior [87]**

This work focuses on the extensive control relevant parametric analysis of the industrial HVOF thermal spray process. At this point, it is important to note that a comprehensive computational fluid dynamic (CFD) model is not practical for the development of control system to be implemented in practice. (However, for offline optimization and analysis, a comprehensive CFD based modeling work will be presented at the end of this thesis.) To address this issue, a one-dimensional model for the industrial Diamond Jet Hybrid HVOF thermal spray process is initially developed. The model describes the evolution of the gas thermal and velocity fields, the motion and temperature of agglomerate particles of different sizes, and explicitly accounts for the effect of powder size distribution. A contribution of this work is to take into account the particle melting behavior during flight. In addition to providing useful insight into the in-flight behavior of different-size particles, the model is used to make a comprehensive parametric analysis of the HVOF process. This analysis allows us to systematically characterize the influence of controllable process variables such as

combustion pressure, oxygen/fuel ratio, as well as the effect of powder size distribution, on the values of particle velocity and temperature (or melting ratio) at the point of impact on substrate. Specifically, the study shows that the gas momentum flux (ρu^2) and the gas temperature, which provide driving forces for particle motion and particle heating, can be almost independently adjusted by manipulating the chamber pressure and the fuel oxygen ratio. These findings are consistent with existing experimental studies and set the basis for the formulation of the control problem for the HVOF thermal spray process.

- **Diamond Jet Hybrid HVOF Thermal Spray Process: Rule-based Modeling and Analysis of Coating Microstructure [119]**

This work focuses on the computational modeling and simulation of microstructure of coatings prepared by the industrial Diamond Jet Hybrid HVOF thermal spray process. Based on the understanding of coating structure and mechanisms of pore formation inside of the coating obtained from experimental studies, a stochastic simulation procedure is used to explore the evolution of the microstructure of the coatings. In the coating growth model, the velocity, temperature and degree of melting of particles hitting on the substrate are determined by a previously developed mathematical model [87] describing gas and particle behavior, and the complex characteristics of the thermally sprayed coatings are captured by applying certain basic rules that encapsulate the main physical features of the deposition process. In addition to providing useful insight into the pore formation and coating growth, the model is used to make a comprehensive parametric analysis, which allows us to systematically characterize the influence of operating conditions, such as the gas flow rate, spray distance, as well as the effect of particle size, on the particle melting behavior, coating porosity, surface roughness and deposition efficiency. Comparison of simulation results

and experimental studies shows that the proposed model can reasonably predict the relationship between macroscopic processing conditions and coating microstructure.

- **Diamond Jet Hybrid HVOF Thermal Spray Process: Model-based Estimation and Control of Particle Velocity and Melting [87, 86]**

This work focuses on the feedback control of the Diamond Jet hybrid HVOF thermal spray process. Based on the modeling of gas and particle behavior and coating microstructure evolution and available experimental studies, the control problem is formulated as the one of regulating volume-based averages of the velocity, temperature and degree of melting at the point of impact on the substrate (these are the variables that directly influence coating microstructure and porosity, which, in turn, determine coating strength and hardness) by directly manipulating the flow rate of fuel, oxygen and air at the entrance of the HVOF thermal spray gun, through which the chamber pressure and the fuel/oxygen ratio can be adjusted. A feedback control system is developed and applied to a detailed mathematical model of the process. Closed-loop simulations demonstrate that the proposed controller is effective in driving the controlled outputs (the particle velocity and melting ratio at the point of impact on the substrate) to desired set-point values and is also robust with robust with respect to disturbances in spray distance and particle injection velocity, and variations in powder size distribution.

We note that in practice, it is difficult to directly measure the degree of melting of individual particles and consequently, the average degree of melting of the entire particle size distribution. To overcome this limitation, we propose an estimation scheme to obtain real-time estimates of particle velocity, temperature and degree of melting. The proposed estimation scheme is based on the modeling equations which describe the evolution of particle temperature, velocity and degree of melting

coupled with the available gas phase measurements. Then, a feedback control system, which directly uses the estimation scheme, is designed to regulate the volume-based average of the particle velocity and degree of melting by manipulating the inlet gas flow rates to the process. The proposed estimation/control structure is applied to a fundamental model of the industrial HVOF thermal spray process and its performance and robustness properties are tested through simulations.

- **Control of HVOF Thermal Spray Process: Application to WC-Co Coating Processing** [88]

The previously developed modeling and control framework is applied to the processing of WC-Co coatings. The behavior of the open-loop system and the closed-loop system are tested through simulations.

- **Computational Fluid Dynamic (CFD) Modeling and Analysis of the Diamond Jet Hybrid HVOF Thermal Spray Process** [85]

This work focuses on the multiscale modeling and analysis of the HVOF thermal spray process, using state-of-the-art CFD technique. It aims to provide a comprehensive understanding of the physicochemical behavior involved in the HVOF thermal spray process. A hybrid (deterministic/stochastic) fundamental model is proposed in this work. The model includes continuum type differential equations that describe the evolution of gas and particle temperature and velocity, and a rule-based stochastic simulator that predicts the evolution of coating microstructure. On the macroscopic gas/particle dynamics side, the Reynolds and Favre-averaged Navier-Stokes equations and energy balance equations are solved with the renormalization group (RNG) k-ϵ turbulence model, and the particle trajectories, temperature histories and melting degrees are determined using the 4th order Runge-Kutta method. On the microscopic

particle deposition process, the formation of coating microstructure is captured by certain rules that encapsulate the main physical features of particle deformation, solidification and coating growth [119]. Based on the proposed model, a detailed comprehensive parametric analysis is carried out to study the relationship between the key process parameters and the particle inflight behavior as well as the resulting coating properties.

Chapter 2

Generic Modeling and Control Issues in HVOF Thermal Spray Process

This chapter[1] presents the principle of the HVOF thermal spray process and generic modeling and control issues. Commonly used equations and formulas as well as widely acknowledged assumptions in the process modeling are discussed. Based on the proposed fundamental mathematical model, control relevant parametric analysis is made to show the influence of operating conditions and particle size on the velocity and temperature of particles at the point of impact on the substrate, which are two main control objectives in the HVOF thermal spray process. Based on the model predictions and available experimental data, the control problem is formulated as the one of regulating volume-based averages of velocity and temperature of particles at the point of impact on the substrate by manipulating two process parameters - chamber pressure and fuel/oxygen ratio. A feedback control system is developed and

[1] Chapter 2 is based on [83] and [84].

applied to a detailed mathematical model of the process, and the dynamic behavior of the HVOF thermal spray process under feedback control is tested through computer simulations. The proposed modeling and control strategy provides preliminaries for the development of a practical control system of an industrial HVOF thermal spray process, which will be elaborated in chapter 3.

2.1 Principle of HVOF thermal spray process

The HVOF thermal spray process is a continuous combustion flow process. A typical schematic diagram of the HVOF thermal spray system is shown in Figure 2.1a. It consists of a combustion chamber, a convergent-divergent nozzle (or referred to as the Laval nozzle) and a barrel. The fuel (typically propylene, propane or hydrogen) and oxygen are continuously fed to the combustion chamber, where they react to produce high temperature combustion gases. As long as a enough nozzle pressure ratio (NPR) is maintained in the chamber, the combustion gases can be accelerated to supersonic velocity through the convergent-divergent nozzle. This is because a unique characteristic of *compressible flow* in the supersonic region is that an increase in the cross-sectional area of the channel results in an increase in the gas velocity [114]. In the convergent part, the gases are accelerated from subsonic velocity to sonic velocity at the throat of the nozzle, where the cross sectional area reaches minimum. In the divergent part, the gases are further accelerated to supersonic velocity. To maintain energy balance, the gas temperature typically decreases along the axial direction in the nozzle. If the gas pressure at the exit of the gun barrel does not match the ambient pressure, the supersonic free jet will adjust to the ambient pressure by a series of compression and expansion waves, and visible shock diamonds will be formed downstream of the barrel exit due to the associated temperature variations

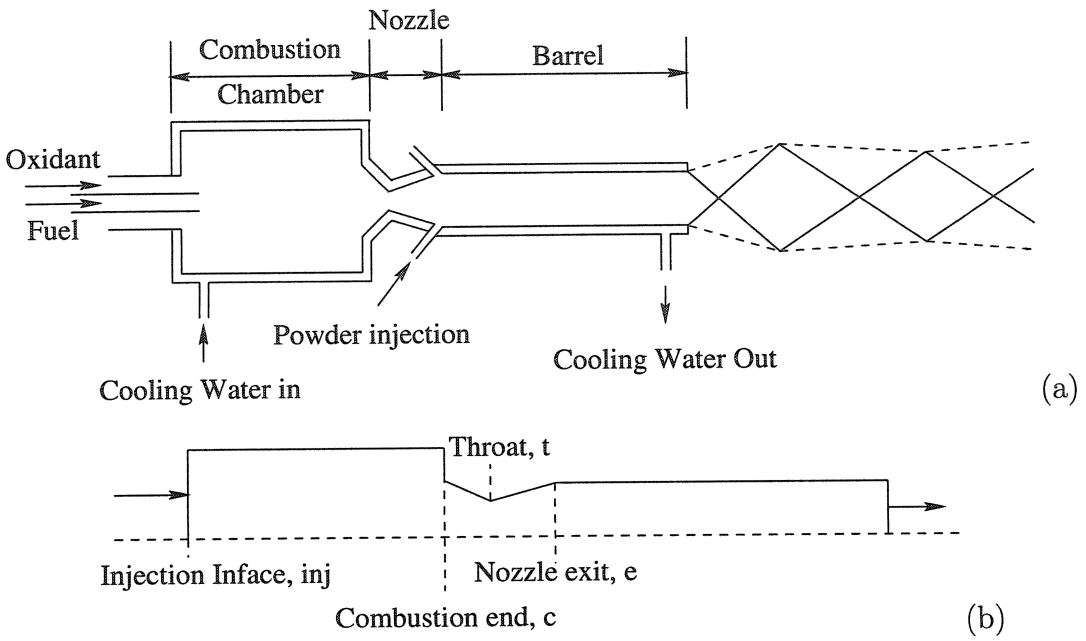


Figure 2.1: (a) Schematic and (b) computational domain of the HVOF torch.

in the flame. The solid particles of metal or cermet powders are injected axially into the gas stream at the exit of the nozzle, where the pressure is not so high as that in the combustion chamber, so that powders can easily enter the gas stream. The powder particles are accelerated and heated in the barrel and in the free jet, and then impinge on the substrate with high velocity to deposit coatings.

2.2 Generic modeling issues in HVOF thermal spray process

2.2.1 Modeling assumptions and modeling procedure

From a modeling point of view, the HVOF is a complex process which involves reaction, two phase compressible flow, heat transfer and subsonic/supersonic flow transitions. To be able to develop a fundamental model for this process that is computationally tractable and capable of capturing the main features of the process, it

is usually assumed that the presence of particles has a negligible effect on the gas velocity and temperature field. This assumption is standard and reasonably valid because the particle loading, which is defined as the ratio of mass flow rate of particles to that of gases, is typically less than 4% [139]. As a consequence, the two-phase problem can be decoupled so that the gas field can be solved first, followed by the simulation of particle infight behavior using the resulting gas thermal and velocity fields. To further simplify the analysis, the following standard assumptions are also made: (1) the flame gas obeys the ideal gas law; (2) species reach equilibrium in the combustion chamber and the composition of the combustion products is frozen at the combustion condition during passage through the nozzle and barrel due to the very short residence time of combustion gases in the nozzle and barrel; (3) the combustion gases behave like a perfect gas during isentropic compression and expansion, and the ratio of specific heat at constant pressure to that at constant volume (c_p/c_v) is nearly a constant; and (4) the friction and cooling water effects along the nozzle and barrel are negligible so that laws of isentropic flow of compressible fluids apply.

The assumption of frozen flow was validated by the work of Swank et al. [125], which revealed that the combustion products at the exit of the gun barrel are far from chemical equilibrium, because the values of gas enthalpy, temperature and velocity at the gun exit predicted by numerical simulations with the instantaneous equilibrium model were significantly higher than the experimentally measured values. Based on the fact that the internal flow is close to frozen rather than in equilibrium, it was suggested in the aforementioned paper that a one dimensional model with chemical equilibrium in the combustion chamber and frozen composition flow during passage through the nozzle and barrel should give a more accurate prediction than the one with instantaneous equilibrium flow. Frozen flow means that the composition of the

combustion gases during passage through the nozzle and the barrel is the same as the one in the combustion chamber because the gas residence time is much shorter than the time scale associated with the chemical kinetics. The assumption of negligible heat exchange with surroundings can be validated by the fact of the very short residence time of gases in the thermal spray gun so that the cooling water has a minimal effect on the gas thermal and velocity fields. In fact, as mentioned before, the cooling water is used mainly to protect the gun instead of manipulating the gas flow and thermal fields.

Referring to Figure 2.1b, the computational domain includes the combustion chamber, the Laval nozzle and the barrel in the internal field and the supersonic free jet in the external field. There are four important cross sections involved in the internal field: the injection interface (inj) and the combustion end (c), both in the combustion chamber, the nozzle throat (t) and the nozzle exit (e), which will be discussed in subsection 2.2.2. To solve the gas field, the composition and temperature at the injection interface of the combustion chamber are calculated first using the instantaneous chemical equilibrium model with the given information of chamber pressure and fuel/oxygen ratio, following which the gas properties during passage through the nozzle, the barrel and the free jet are solved in sequence. The profiles of particle velocity and temperature in the barrel and in the free jet are solved using the momentum transfer equation and the heat transfer equation together with the resulting gas velocity and thermal fields. Average particle velocity and temperature at the point of impact on substrate are calculated including the influence of the powder size distribution.

2.2.2 Modeling of compressible nozzle flow

In order to calculate the equilibrium composition in the combustion chamber, the fuel/oxygen ratio needs to be specified first. In practice, this term is usually expressed by the equivalence ratio:

$$\varphi = \frac{Fuel/Oxygen}{(Fuel/Oxygen)_{st}} \tag{2.1}$$

which is the actual fuel/oxygen ratio divided by its stoichiometric (denoted by the subscript st) value. The reactive system is fuel rich if $\varphi > 1$ or fuel lean if $\varphi < 1$. Based on this definition, the reaction of a hydrocarbon fuel and air can be represented by a general equation of the form:

$$\varphi C_n H_m + (n + \frac{m}{4}) \left[O_2 + \frac{78}{21} N_2 + \frac{1}{21} Ar \right] \Rightarrow \sum_{i \in pr} \xi_i (PR)_i \tag{2.2}$$

where ξ_i is the molar fraction of component i in the combustion products (pr), which include CO_2, H_2O and inerts (N_2 and Ar), and possibly CO, O_2 etc., depending on the value of the equivalence ratio. However, under normal conditions, $C_n H_m$ does not show up at the right hand side of the above reaction formula.

The equilibrium composition and temperature at the injection interface of the chamber can be calculated by minimizing of the Gibbs free energy of the whole reactive system, which shows the advantage than the equilibrium constant method because, the specification of a set of reactions a priori, is not necessary [46]. With the assumptions of adiabatic reaction and ideal gas behavior, the calculation of equilibrium composition in the combustion chamber can be formulated as an optimization

problem below.

$$\begin{aligned}
\min G &= \sum_{i\in pr} \mu_i \xi_i \\
\sum_{i\in pr} a_{ij}\xi_i &= b_j \ (\forall j \in l) \\
\sum_{i\in re} \xi_i H_i^{\emptyset}(T_a) &= \sum_{j\in pr} \xi_j H_j^{\emptyset}(T_{inj}) \\
\mu_i &= \mu_i^{\emptyset}(T_{inj}) + RT_{inj} \ln \frac{P_{inj}\xi_i}{P^{\emptyset}\sum_{i\in pr}\xi_i} \ (\forall i \in pr \ \ with \ \ \xi_i \neq 0) \\
\xi_i &\geq 0 \ (\forall i \in pr)
\end{aligned} \tag{2.3}$$

where G is the Gibbs energy of the reactive system; H_i and μ_i are the enthalpy and chemical potential of species i, respectively; T_a and T_{inj} represent the ambient temperature and chamber temperature, respectively; superscript $^{\emptyset}$ represents the standard condition; a_{ij} is the number of element j in species i, b_j the sum of the number of element j in each molecule of reactants and l is the total number of chemical elements involved in the system; R is the gas constant and P is the pressure. The first equation listed in the constraints is the mass balance of each element involved in the reactive system, the second one is the energy balance, and the third one is the definition of chemical potential for ideal gases. Usually, the heat capacity of each species can be correlated as a polynomial of temperature and the enthalpy is derived as the integral of heat capacity with respect to temperature. If the oxidant used in the HVOF process is pure oxygen instead of air, a similar procedure can be followed (see Chapter 3 for detailed information).

For the compressible frozen flow in the internal flow field, the governing equations include continuity, momentum balance and energy balance. For example, the momentum balance between the injection interface and the combustion end can be listed as

$$(P + \rho u^2)_{inj} = (P + \rho u^2)_c \tag{2.4}$$

and the energy balance equation is

$$\sum_{i\in pr}\xi_i H_i^{\emptyset}(T_{inj}) + \frac{1}{2}(\bar{M}_{pr}\sum_{i\in pr}\xi_i)u_{inj}^2 \;=\; \sum_{i\in pr}\xi_i H_i^{\emptyset}(T_c) + \frac{1}{2}(\bar{M}_{pr}\sum_{i\in pr}\xi_i)u_c^2 \qquad (2.5)$$

where u is the gas velocity and $\bar{M}_{pr}$ is the average molecular weight of the product. In supersonic flow, gas velocity can be expressed by:

$$u \;=\; \mathbf{M}a \;=\; \mathbf{M}\sqrt{\gamma P/\rho} \qquad (2.6)$$

where ρ is the gas density, $\mathbf{M}$ is the mach number which is defined as the ratio of the gas velocity to the local sonic velocity ($a = \sqrt{\gamma P/\rho}$) and γ is the adiabatic constant calculated by $\gamma = \bar{c}_p/(\bar{c}_p - R)$.

During the subsonic/supersonic transition, gases obtain sonic velocity at the throat of the Laval nozzle, or the mach number ($\mathbf{M}_t$) is one. For isentropic flow along the Laval nozzle, the relationship between area ratio and mach number at two cross sections is determined by

$$\frac{A_2}{A_1} \;=\; \frac{\mathbf{M}_1}{\mathbf{M}_2}\left\{\frac{1+[(\gamma-1)/2]\mathbf{M}_2^2}{1+[(\gamma-1)/2]\mathbf{M}_1^2}\right\}^{(\gamma+1)/2(\gamma-1)} \qquad (2.7)$$

where A is the area of the cross section that is perpendicular to the flow direction. For a nozzle with specific configuration, the mach number at the combustion end and the one at the nozzle exit can be solved based on area ratios A_c/A_t and A_e/A_t (see Figure 2.1). Note that the same area ratio corresponds to two mach numbers, with one larger than and the other less than 1, and therefore, an appropriate initial guess should be chosen to get the right solution when Newton-Raphson iteration is used.

Combing Eqs.2.4-2.7 with the ideal gas law, and ignoring u_{inj}, one can solve for the gas properties such as velocity, temperature, pressure, and mach number at the combustion end. Then, the following relationships for isentropic compressible flow, together with Eq. 2.7, can be applied to compute the gas properties at other cross

sections along the nozzle:

$$\frac{T_2}{T_1} = \frac{1+[(\gamma-1)/2]\mathrm{M}_1^2}{1+[(\gamma-1)/2]\mathrm{M}_2^2} \tag{2.8}$$

$$\frac{P_2}{P_1} = \left\{\frac{1+[(\gamma-1)/2]\mathrm{M}_1^2}{1+[(\gamma-1)/2]\mathrm{M}_2^2}\right\}^{\gamma/(\gamma-1)} \tag{2.9}$$

$$\frac{\rho_2}{\rho_1} = \left\{\frac{1+[(\gamma-1)/2]\mathrm{M}_1^2}{1+[(\gamma-1)/2]\mathrm{M}_2^2}\right\}^{1/(\gamma-1)} \tag{2.10}$$

The above equations are derived from the governing equations for isentropic compressible flow and the reader may refer to the book [114] for a detailed derivation. The mass flow rate through a Laval nozzle, denoted by $\dot{m}_g$, can be grossly calculated by

$$\dot{m}_g = \frac{P_{inj}}{\sqrt{T_{inj}}} A_t \sqrt{\frac{\bar{M}_{pr}}{R}\gamma\left(\frac{2}{\gamma+1}\right)^{(\gamma+1)/(\gamma-1)}} \tag{2.11}$$

which is dependent on the temperature and pressure in the chamber.

Under the assumptions of negligible friction and cooling water effect, the gas properties are kept constant during passage through the barrel. However, the exhaust gases cannot maintain the high velocity and temperature in the free jet [63, 20]. From the exit of the gun to a position whose distance is not larger than the potential core length (L_{pc}), the gas velocity and temperature keep almost constant. Further downstream, gas velocity and temperature decay rapidly because of the entrainment of the surrounding air, roughly following the empirical formulas below [127]:

$$\frac{u}{u_e} = 1 - \exp\left(\frac{0.85}{1-x/L_{pc}}\right) \tag{2.12}$$

and

$$\frac{T-T_a}{T_e-T_a} = 1 - \exp\left(\frac{1.25}{1-x/L_{pc}}\right) \tag{2.13}$$

where x is the axial distance from the exit of the gun barrel ($x > L_{pc}$) and L_{pc} can be correlated to a function of the mach number at the exit of gun barrel (M_e) and

barrel diameter (D)

$$L_{pc}/D = 3.5 + 1.0\mathrm{M}_e^2 \tag{2.14}$$

The above formulaes are valid for $1.5 \leq \mathrm{M}_e \leq 2.5$, $1500K \leq T_e \leq 3000K$.

2.2.3 Modeling of particle motion and temperature

The particle trajectories and temperature histories in the gas field are computed by the momentum and heat transfer equations. Since the acceleration and deceleration of particles in the moving gas in the HVOF thermal spray system are dominated by the drag force [109], the particle motion can be adequately described by the following two first-order ordinary differential equations:

$$\begin{aligned} m_p \frac{dv_p}{dt} &= \frac{1}{2} C_D \rho_g A_p (v_g - v_p)|v_g - v_p|, \;\; v_p(0) = v_{p0} \\ \frac{dx_p}{dt} &= v_p, \;\; x_p(0) = 0 \end{aligned} \tag{2.15}$$

where m_p is the particle mass, v_p is the particle axial velocity, A_p is the projected area of the particle on the plane perpendicular to the flow direction, ρ_g is the gas density, C_D is the drag coefficient, and x_p is the particle position, calculated from the exit of the nozzle. Note that one difference between particle motion in a stagnant fluid and particle motion in a moving fluid is that there is an absolute sign in the relative velocity between particle and gas (term $|v_g - v_p|$ in the right-hand side of the momentum equation) in the latter case, which guarantees that a particle is accelerated if its velocity is less than that of the gas and decelerated otherwise. In order to take into consideration the fact that many powders used in the HVOF process are not spherical, a formula for the drag coefficient C_D, which accounts for the particle shape using the concept of sphericity ϕ (defined as the ratio of the surface area of a sphere with equivalent volume to the actual surface area of the particle) is used in this work,

which has the following form [18, 39]:

$$\frac{C_D}{K_2} = \frac{24}{ReK_1K_2}\left[1+0.1118(ReK_1K_2)^{0.6567}\right] + \frac{0.4305}{1+3305/ReK_1K_2} \tag{2.16}$$

where K_1 and K_2 are two sphericity-related factors. The local Reynolds number (Re) for this two phase flow problem is defined based on the relative velocity $Re = d_p \mid v_g - v_p \mid \rho_g/\eta_g$, where d_p is either the particle diameter if the particle is spherical or the equivalent diameter if not, and η_g is the gas viscosity.

In the HVOF process, the Biot number of the particles ($Bi = hx/\lambda_p$, h is the heat transfer coefficient, x is a characteristic dimension defined by the ratio of particle volume to its surface area, and λ_p is the thermal conductivity of the particle) is typically less than 0.1 [18]; this means that the particles are heated with negligible internal resistance and temperature gradients inside them can be ignored [40]. Consequently, the equation describing the heat transfer between a single particle and the gas reduces to a first-order ordinary differential equation of the form:

$$m_p c_{p_p} \frac{dT_p}{dt} = hA'_p(T_g - T_p), \; T_p(0) = T_0 \tag{2.17}$$

where T_p is the particle temperature, A' is the surface area of a particle, and h is the heat transfer coefficient computed by the Ranz-Marshall empirical equation [6]:

$$\frac{hd_p}{\lambda_g} = Nu = 2 + 0.6Re^{\frac{1}{2}}Pr^{\frac{1}{3}} \tag{2.18}$$

where the Prandtl number (Pr) is calculated by $Pr = c_{p_g}\eta_g/\lambda_g$. We note that Eq. 2.17 does not account for the effect of particle melting; such an effect will be taken into account in Chapter 3.

The equations for particle motion and temperature are solved by numerical integration. Specifically, Eqs. 2.15 and 2.17 are integrated with a small enough time step (10^{-7} sec) such that the gas velocity and temperature, the local Reynolds number

can be considered constant over the time interval (Δt) of each time step. After one time step, the gas velocity and gas temperature are updated according to the new position of the particle and then the same strategy is repeated for the next step. This methodology was proposed in [29] and was shown to be computationally economical and accurate. Specifically, the iterative formulaes for particle velocity, position and temperature are shown as the following:

$$\begin{aligned} v_p^{i+1} &= v_g^i - (v_g^i - v_p^i)\exp\left(-\Delta t/\tau_p\right) \\ x_p^{i+1} &= v_p^i \Delta t \\ T_p^{i+1} &= T_g^i - (T_g^i - T_p^i)\exp\left(-\Delta t/\omega_p\right) \end{aligned} \tag{2.19}$$

where $\tau_p = \dfrac{4\rho_p d_p^2}{3\eta_g C_D Re}$ and $\omega_p = \dfrac{\rho_p c_p d_p^2}{6Nu\lambda_g}$.

2.2.4 Process simulation results and analysis

Several simulation runs of the process model were performed to evaluate the effect of controllable process variables on particle velocity and temperature and to investigate the dependence of the particle velocity and temperature on particle size. The parameters used in these open-loop system (i.e., process model without feedback control) simulations are given in Table 2.1.

Figure 2.2 displays the axial velocity and temperature of gas and particles with different sizes along the flow field. To show the effect of particle injection velocity on the velocity and temperature profiles, the simulation was ran under three different injection velocities (0, 40, and 80 m/s). Under each specific injection velocity, particles with different sizes are all accelerated in the barrel and in some region of the supersonic free jet (where their velocities are less than that of the combustion gases), and are decelerated after they reach the same velocity as that of the gases. Furthermore, fine particles change velocities more easily than coarser ones because of their small momentum inertias. For example, a particle with a diameter 5 μm attains

Table 2.1: Process parameters used in the open-loop simulation.

Fuel	=	Propane	
Oxidant	=	Oxygen	
Powder	=	Inconel 718	
Barrel Diameter	=	1.0	cm
Barrel Length	=	0.2	m
Spray Distance	=	0.3	m
A_e/A_t	=	2.0	
η_g	=	5×10^{-5}	$kg/m \cdot s$
λ_g	=	0.08	$W/m \cdot K$
ρ_p	=	9000	kg/m^3
c_{p_p}	=	462	$J/kg \cdot K$
ϕ	=	1.0	

velocity as high as about 1300 m/s during flight. However, its velocity decreases rapidly. Particles with even smaller size fully track the motion of the exhaust gases and may not stick to the substrate. In Chapter 7, where the effect of substrate on the gas flow field is taken into account, this behavior of small particles in the gas field will be very apparent. Similar behavior is also observed for the particle temperature. Note that in the processing of nanostructured coatings, it is of great significance to keep a relatively high particle temperature at the point of impact on the substrate while at the same time to prevent particles from being superheated during flight in order to reserve the nanocrystalline structure of particles. The behavior of particles with very small sizes in the gas stream explains why they are not suitable for thermal spraying.

From the simulation runs of particle velocity and temperature along the gas field under three different particle injection velocities, we can conclude the following. First, the particle injection velocity has a minimal effect on particle velocity profile (except for the initial part), especially for particles with small sizes. This phenomena can

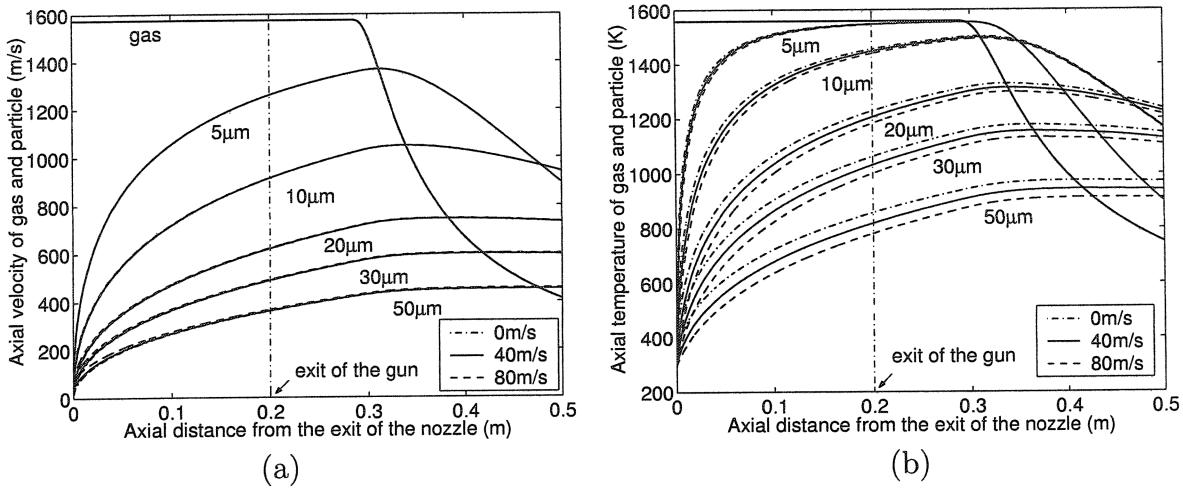


Figure 2.2: (a) Axial velocity and (b) temperature profiles of gas and particle along the flow field for different particle sizes d_p = 5, 10, 20, 30, and 50 μm under operating conditions P = 9 bar and φ = 1.0 and three different injection velocities v_0 = 0, 40 and 80 m/s.

be explained by Figure 2.3a, from which it can be seen that particles with larger injection velocity have a shorter acceleration stage and reach the critical point (where the gas and particle velocities are equal) sooner. Near the critical point, the drag force is very small. Second, larger particle injection velocity shortens the residence time of particles in the gas flame (refer to Figure 2.3b), and as a consequence, particle temperature drops. Third, the disturbances on particle injection velocity have a more significant effect on particle temperature profile for coarse particles than finer ones. Note that the change of particle injection velocity has an effect on the process somewhat similar to changes in the injection position; the changes in the particle velocity and temperature at the point of impact on substrate are consistent with the experimental observations in [49].

Figure 2.4 shows the influence of combustion chamber pressure and equivalence ratio on the velocity and temperature profiles of an individual particle of size d_p = 40 μm. In Figure 2.4a, the equivalence ratio is fixed at 1.0 and the pressure in the

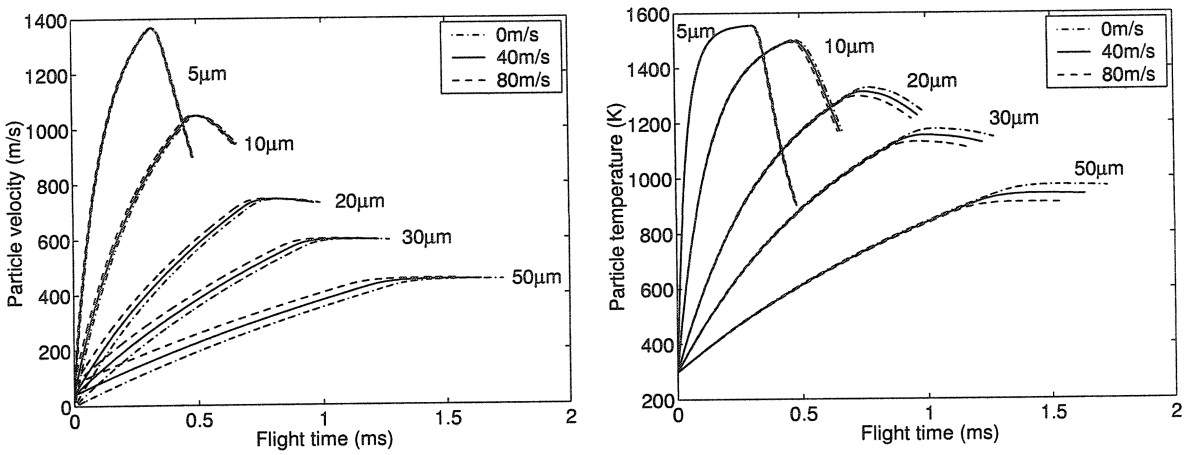


Figure 2.3: (a) Axial velocity and (b) temperature as a function of flight time for different particle sizes d_p = 5, 10, 20, 30, and 50 μm under operating conditions P = 9 bar and φ = 1.0 and three different injection velocities v_0 = 0, 40 and 80 m/s.

combustion chamber varies from 4 to 11 bar. It can be seen that the particle velocity changes much more than the particle temperature. Furthermore, chamber pressure does not significantly influence gas velocity, while it affects particle velocity because the drag force on particle depends strongly on gas density, which, in turn, depends on chamber pressure (see also [125] for similar conclusions). In Figure 2.4b, the combustion chamber pressure is fixed at 9 bar and the equivalence ratio varies from 0.8 to 1.2. It is found that while the particle temperature changes significantly, the particle velocity remains almost constant. Particle temperatures are higher at $\varphi = 1.0$ than those at $\varphi = 1.2$ and $\varphi = 0.8$, which implies that when the reaction occurs close to stoichiometric condition it tends to achieve higher particle temperature. From these two figures, it can be concluded that the particle velocity is primarily influenced by the combustion chamber pressure and the particle temperature depends mainly on the equivalence ratio; a conclusion which is in good agreement with available experimental observations [49, 126].

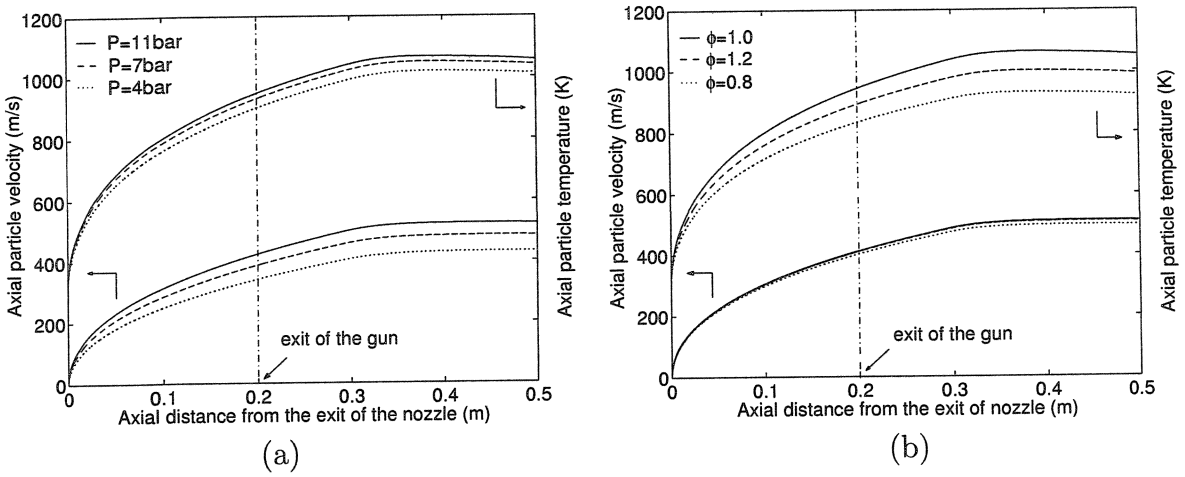


Figure 2.4: Particle velocity and temperature as a function of combustion chamber pressure and equivalence ratio - (a) $P = 4$, 7 and 11 *bar*, $\varphi = 1.0$. (b) $\varphi = 0.8$, 1.0 and 1.2, $P = 9$ *bar*.

To explain the above phenomena, Figure 2.5 and shows the gas temperature in the combustion chamber as well as the gas velocity and temperature at the exit of the nozzle under different operating conditions. In Figure 2.5a, chamber pressure is fixed to be 9 *bar* and the equivalence ratio varies from 0.8 to 1.2. It is found that in the equivalence ratio range of interest, gas velocity at the exit of the nozzle changes much less than the gas temperature. As the equivalence ratio increases from 0.8 to 1.2, gas temperature at the exit of the nozzle increases initially, reaching its maximum value 1478 K at an equivalence ratio slightly above 1.0, and then decreases. A similar phenomenon is also observed for the gas temperature in the combustion chamber. From these it can be concluded that reaction under near-stoichiometric condition achieves higher gas temperature than others. In Figure 2.5b, the equivalence ratio is kept constant at 1.0 and the chamber pressure is changed from 9 *bar* to 15 *bar*. It can be seen that gas temperature in the combustion chamber as well as gas velocity and gas temperature at the exit of the nozzle change little in the chamber pressure range of interest.

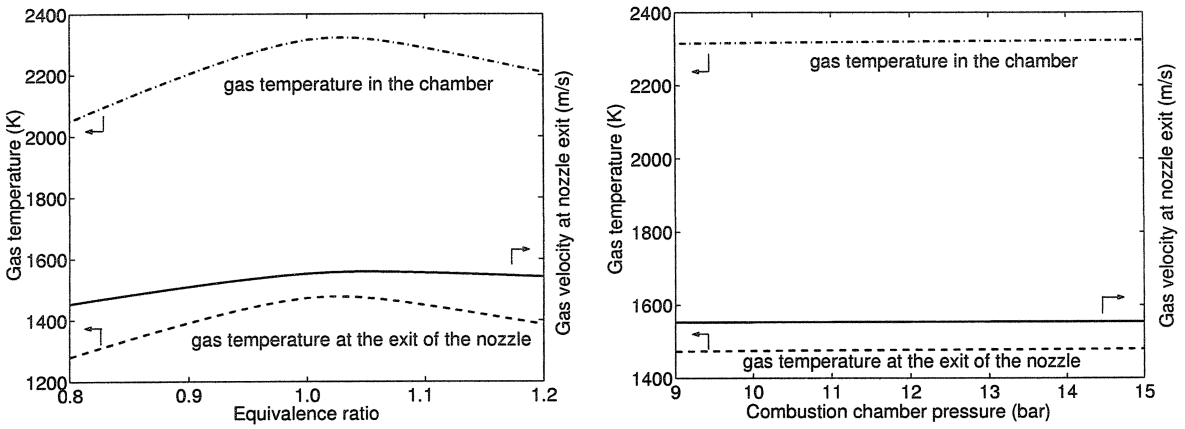


Figure 2.5: Gas properties in the combustion chamber (dash-dot line: gas temperature) and at the exit of the nozzle (dashed line: gas temperature, solid line: gas velocity) - (a) P = 9 bar, φ = 0.8 - 1.2. (b) φ = 1.0, P = 9 - 15 bar.

While it is concluded from Figure 2.5b that chamber pressure does not affect gas velocity, the strong effect of chamber pressure on particle velocity is not unexpected. This is because chamber pressure influences gas density, and thus, particle velocity. Figure 2.6 shows gas density at the exit of the nozzle as a function of the chamber pressure. The gas density is nearly proportional to the chamber pressure.

2.3 Modeling of powder size distribution

Figure 2.7 shows the particle velocity and temperature at the 0.3 m standoff under operating conditions P = 9 bar, φ =1.0 in the particle size range 1 - 100 μm. As particle diameter increases, both particle velocity and particle temperature increase first, and then decrease. The maximum values of both particle velocity and temperature corresponding to moderate particle sizes can be explained by the interplay of gas dynamics and particle mass/thermal inertia. It is well known that the particles are typically accelerated in the barrel and in some region of the free jet, and then they

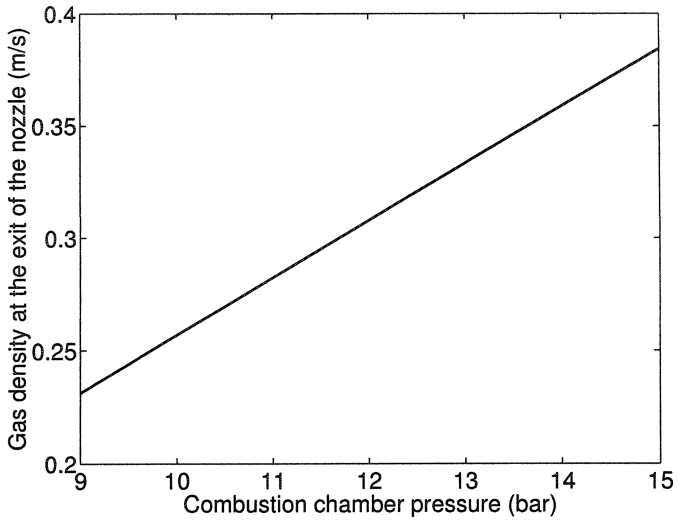


Figure 2.6: Gas density at the exit of the nozzle - $\varphi = 1.0$ and $P = 9$ - 15 bar.

are decelerated. Particles of very small size have small mass inertias and are easily accelerated when the gas velocity is larger than the particle velocity. However, small particles are also easily decelerated when the particle velocity is larger than the gas velocity. On the other hand, large size particles are difficult to be accelerated as well as decelerated. As a result, particles of moderate sizes tend to have higher velocities at the point of impact on substrate than both bigger and smaller particles. A similar explanation can be given for the dependence of particle temperature at the point of impact on substrate on particle size.

The fact that particle temperature and velocity at the point of impact on substrate depend strongly on particle size implies that particle size of the feedstock is one of the key parameters deciding coating quality. This property, together with the significant polydispersity of most powders used in the thermal spray process, motivates accounting for the effect of powder size distribution in the process model, the control problem formulation and the controller design. Previous experimental work [90, 80]) has shown that lognormal functions can adequately describe the size distribution of

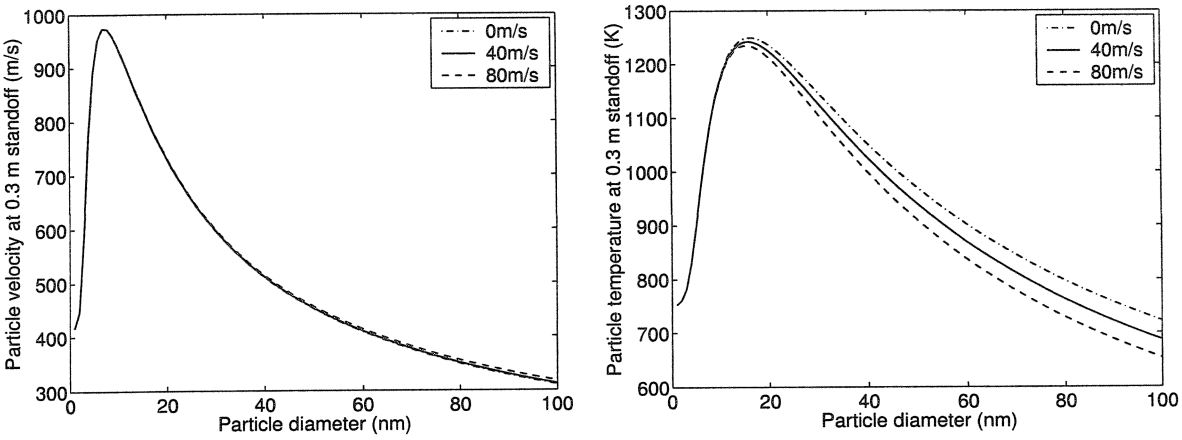


Figure 2.7: (a) Axial particle velocity and (b) temperature at the point of impact on substrate as a function of particle size and particle injection velocity. Operating conditions: $P = 9\ bar$, $\varphi = 1.0$.

many powders used in the HVOF process. To this end, a lognormal function is used in this work to describe the powder size distribution with the following form [27]:

$$f(d_p) = \frac{1}{\sqrt{2\pi}\sigma d_p} \exp\left[-\frac{(\ln d_p - \mu)^2}{2\sigma^2}\right] \tag{2.20}$$

where $f(d_p)$ is the size distribution function, μ and σ^2 are two dimensionless parameters corresponding to the mean and the variance of $\ln d_p$, which obeys the normal distribution:

$$F = \frac{\int_0^{d_p} \frac{1}{6}\pi\rho x^3 f(x)dx}{\int_0^{\infty} \frac{1}{6}\pi\rho x^3 f(x)dx} \tag{2.21}$$

The numerator

$$\begin{aligned}
\int_0^{d_p} \frac{1}{6}\pi\rho x^3 f(x)dx &= \frac{1}{6}\pi\rho\int_0^{d_p} x^3 \frac{1}{\sqrt{2\pi}\sigma x}\exp\left[-\frac{(\ln x-\mu)^2}{2\sigma^2}\right]dx \\
&= \frac{1}{6}\pi\rho\int_{-\infty}^{\ln d_p} \frac{1}{\sqrt{2\pi}\sigma}\exp\left[3y-\frac{(y-\mu)^2}{2\sigma^2}\right]dy \ \ (let\ \ y=\ln x) \\
&= \frac{1}{6}\pi\rho e^{3\mu+\frac{9}{2}\sigma^2}\int_{-\infty}^{\ln d_p} \frac{1}{\sqrt{2\pi}\sigma}e^{-\frac{[y-(\mu+3\sigma^2)]^2}{2\sigma^2}}dy \\
&= \frac{1}{6}\pi\rho e^{3\mu+\frac{9}{2}\sigma^2}\int_{-\infty}^{\ln d_p-(\mu+3\sigma^2)} \frac{1}{\sqrt{2\pi}\sigma}e^{-\frac{t^2}{2\sigma^2}}dt \ \ (let\ \ t=y-(\mu+3\sigma^2)) \\
&= \frac{1}{6}\pi\rho e^{3\mu+\frac{9}{2}\sigma^2}\int_{-\infty}^{\frac{\ln d_p-(\mu+3\sigma^2)}{\sigma}} \frac{1}{\sqrt{2\pi}}e^{-\frac{u^2}{2}}du \ \ (let\ \ u=t/\sigma)
\end{aligned} \tag{2.22}$$

Therefore,

$$F = \int_{-\infty}^{\frac{\ln d_p-(\mu+3\sigma^2)}{\sigma}} \frac{1}{\sqrt{2\pi}}e^{-\frac{x^2}{2}}dx \tag{2.23}$$

The upper bound of the integral in the above equation can be determined based on the value of the cumulative function F

$$\begin{cases}
\dfrac{\ln d_{10}-(\mu+3\sigma^2)}{\sigma} &= -1.28 \\
\dfrac{\ln d_{50}-(\mu+3\sigma^2)}{\sigma} &= 0 \\
\dfrac{\ln d_{90}-(\mu+3\sigma^2)}{\sigma} &= 1.28
\end{cases} \tag{2.24}$$

From the above equations it can be seen that if powders obey lognormal distribution, d_{50} should be the square root of the product of d_{10} and d_{90}. When there are three sets of data available, parameter estimation should be made to minimize the square sum of difference between experimental data and theoretical prediction.

$$\begin{aligned}
\min g = \ & [\ln d_{10}-(\mu+3\sigma^2)+1.28\sigma]^2+[\ln d_{50}-(\mu+3\sigma^2)]^2 \\
& +[\ln d_{90}-(\mu+3\sigma^2)-1.28\sigma]^2
\end{aligned} \tag{2.25}$$

which is equivalent to

$$\begin{cases}
\dfrac{\partial g}{\partial \mu} &= 0 \\
\dfrac{\partial g}{\partial \sigma} &= 0
\end{cases} \tag{2.26}$$

and the solution is

$$\begin{cases} \mu + 3\sigma^2 &= \ln \sqrt[3]{d_{10}d_{50}d_{90}} \\ 1.28\sigma &= \ln \sqrt{\dfrac{d_{90}}{d_{10}}} \end{cases} \tag{2.27}$$

Therefore, for particles that are lognormally distributed, μ and σ can be determined using the following formulas:

$$\begin{cases} \mu &= \ln \sqrt[3]{d_{10}d_{50}d_{90}} - 1.831 \left(\ln \sqrt{\dfrac{d_{90}}{d_{10}}} \right)^2 \\ \sigma &= 0.781 \ln \sqrt{\dfrac{d_{90}}{d_{10}}} \end{cases} \tag{2.28}$$

where d_{10}, d_{50} and d_{90} are three characteristic diameters which can be obtained experimentally [77].

It is known that the integration of a standard Gaussian distribution from -3 to 3 is very near to 1 (0.9973). To capture almost all the particle weight in the simulation, we can ignore the particles which is out of the size range $\{d_{lb}, d_{ub}\}$ such that

$$\begin{cases} \dfrac{\ln d_{lb} - (\mu + 3\sigma^2)}{\sigma} &= -3 \\ \dfrac{\ln d_{ub} - (\mu + 3\sigma^2)}{\sigma} &= 3 \end{cases} \tag{2.29}$$

or

$$\begin{cases} d_{lb} &= -3\sigma + (\mu + 3\sigma^2) \\ d_{ub} &= 3\sigma + (\mu + 3\sigma^2) \end{cases} \tag{2.30}$$

Particle coagulation in the HVOF thermal spray process has not been reported in the literature, which may be explained by the following argument. The average distance between individual particles in the HVOF thermal spray process can be estimated based on the analysis of Crowe et al. [28]. Specifically,

$$\frac{L_d}{d_p} = \left[\frac{\pi}{6} \frac{1+\kappa}{\kappa} \right]^{1/3} \tag{2.31}$$

where L_d is the distance between two particles and κ is the ratio of particle loading to particle/gas density ratio. Usually the particle loading is about 4%, the density

ratio is about 10^{3-4}, therefore L_d/d_p is about 20-50, which implies that the individual powder particles can be considered isolated from each other. Therefore, in this work, we assume that particle coagulation is negligible and the powder size distribution does not change during flight.

There are many ways to define average powder properties. For example, they can be averaged with respect to particle number or particle volume. In this work, the average powder properties ($\overline{PP}$) are calculated based on particle volume because larger particles have a stronger influence on coating properties than smaller ones. Volume-based average powder properties can be computed as follows:

$$\overline{PP} = \frac{\int_0^\infty \frac{1}{6}\pi d_p^3 PP(d_p) f(d_p) d(d_p)}{\int_0^\infty \frac{1}{6}\pi d_p^3 f(d_p) d(d_p)} \tag{2.32}$$

2.4 Generic control issues in HVOF thermal spray process

2.4.1 Control problem formulation and controller design

Based on the model predictions, and the available experimental results, the control problem for the HVOF system is formulated as the one of regulating the volume-based averages of temperature and velocity of particles at impact on the substrate (these are the variables that directly influence coating microstructure and porosity) by manipulating the combustion chamber pressure and the oxygen/fuel ratio. From the simulation results of subsection 2.2.4, it follows that ρ_g, which strongly affects T_p, can be almost independently adjusted by manipulating the combustion chamber pressure, $u_1(t)$, which is related to total gas flow rate, and the equivalence ratio, $u_2(t)$, respectively. At this point, it is important to note that control of an average particle property, such as volume-averaged particle temperature and velocity, is all that can be achieved using two lumped manipulated variables. Control of velocity

and temperature of individual particles or of particles with different sizes cannot be achieved with just two manipulated variables. The usefulness of the proposed approach based on volume-averaged particle velocity and temperature will be shown in the next subsection.

The proposed formulation of the control problem can be readily used in the context of experimental HVOF systems because, both the chamber pressure and the equivalence ratio can be manipulated in real-time, by adjusting the total flow rate of fuel and oxidant (Eq. 2.11) and their ratio, respectively. A schematic of the feedback control system for the HVOF process is shown in Figure 2.8. The manipulated input variables are the flow rates of oxygen and fuel; these are the variables that can be adjusted by the control system to change the behavior of the process. The controlled output variables, which are the variables that the controller tries to set at desired values, are the average particle velocity and temperature before impact on the substrate, which can be measured experimentally using non-intrusive optical techniques, for example, Laser Doppler Velocimetry [38], Particle Imaging Velocimetry [71, 130], and Two Color Pyrometry [124, 49, 36], etc. The controller obtains information from the measurement system, and makes decisions, which are sent to the controlled valves (total flow of gases to the process and oxygen/fuel ratio), to adjust the manipulated input variables until the deviation of the controlled outputs from their corresponding set-point values falls within a tolerable region. One of the great advantages of feedback control is that it can compensate for the effect of disturbances in the process operating conditions.

Owing to the almost decoupled nature of the manipulated input/controlled output pairs, two proportional integral (PI) controllers are used to regulate the process.

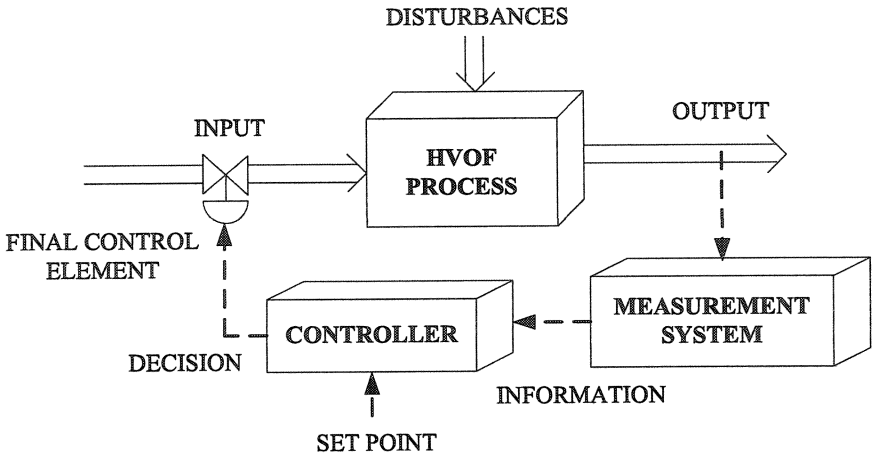


Figure 2.8: Schematic of the HVOF control system.

Specially, the controllers have the following form:

$$\begin{aligned} \dot{\zeta}_i &= y_{sp_i} - y_i, \ \zeta_i(0) = 0, \ i = 1, 2 \\ u_i &= K_{c_i}(y_{sp_i} - y_i) + \frac{1}{\tau_{c_i}}\zeta_i + u_{0_i}, \ i = 1, 2 \end{aligned} \tag{2.33}$$

where y_{sp_i} is the desired set-point value and y_i is the value of the output obtained from the measurement system (y_1 is average particle velocity and y_2 is average particle temperature). u_i is the manipulated input (u_1 is the chamber pressure and u_2 is the equivalence ratio). K_{c_i} is the proportional gain and τ_{c_i} is the integral time constant. The values of the controller parameters K_{c_i} and τ_{c_i} were chosen to achieve smooth controlled output transient responses in the closed-loop system (i.e., process model under feedback control) without using unrealistically large control action (see simulation results in the next subsection). From Eq. 2.33 it is easy to see that the controller includes integral action, which means that u_i will continuously change with time until the deviation of the measured output from its set point value is zero. Finally, note that while the shape of the powder size distribution is accounted for in the formulation of the control problem (i.e., selection of controlled outputs y_1 and y_2), the feedback control system of Eq. 2.33 does not make direct use of the process

Table 2.2: Process parameters used in the closed-loop simulation

K_{c_1}	=	1000	
K_{c_2}	=	0.001	
τ_1	=	0.2	
τ_2	=	0.2	
d_{10}	=	27	μm
d_{50}	=	80	μm
d_{90}	=	144	μm
ϕ	=	1.0	

model. The design of a model-based feedback control system, employing nonlinear control techniques for particulate processes (see [21, 64] and the book [25] for details), as well as applications of the control system to more detailed HVOF process model (i.e., two-dimensional in space models for gas and particle motion and temperature) and an experimental system, will be the subject of future work.

2.4.2 Simulation results of HVOF process under feedback control

In this subsection, simulation runs of the closed-loop system are presented. In several cases, the outputs of the closed-loop system are compared to the outputs of the open-loop system (i.e., process model with P and φ set at fixed values). The outputs $y_1(t)$ and $y_2(t)$ are computed by averaging the individual particle velocity and temperature data obtained from the process model using Eq. 2.32. To account for the powder size distribution, up to 100 particles of different size are traced simultaneously to obtain the average velocity and temperature. This requires solving simultaneously 300 ordinary differential equations. The parameters used in the closed-loop system simulations are shown in Table 2.2.

Several simulation runs of the process model under the feedback controller were performed to evaluate the ability of the controller to: a) drive the particle temperature

and velocity at the point of impact on substrate to desired set-point values, and b) to attenuate the effect of disturbances on process operating conditions. In addition, the proposed formulation and solution to the control problem is compared with an approach which assumes monodisperse powder size distribution. The first simulation studies the behavior of the closed-loop system in the presence of changes in the set-point. Initially, the process is assumed to operate at $P = 6\ bar$ and $\varphi = 1.0$ (which corresponds to $\bar{v}_p = 367.8\ m/s$ and $\bar{T}_p = 851.1\ K$), and at time t $= 0\ sec$, the average particle velocity set-point value increases by 10% and the average particle temperature set-point value decreases by 10%. Figures. 2.9 and 2.10 show how the controlled outputs ($\bar{v}_p$ and $\bar{T}_p$) and manipulated inputs (P and φ) move in the case of requesting such changes in the set-point values. The feedback controller drives the controlled outputs to the new set points ($\bar{v}_p = 404.6\ m/s$ and $\bar{T}_p = 766.7\ K$) in about 20 *sec* (note that 20 *sec* is the time needed for the controlled outputs to reach the new set-point values, not the time for the particles to hit the substrate, which is on the order of 10^{-3} *sec*). Further investigation of Figure 2.9 shows that the time needed to achieve 90% of the desired set-point values is about 5 *sec* for particle velocity and 10 *sec* for particle temperature, which means that the controller is quite effective and validates the feasibility of implementation of feedback control on the HVOF process. We also note that faster closed-loop output response can be achieved at the expense of using larger control action (i.e., larger values for φ and P); in practice, the speed of the closed-loop response (and thus, the optimal values of K_{c_i} and τ_{c_i}) depends on the specific HVOF thermal spray system and should be determined using several experiments.

To show that the proposed formulation of the control problem (which explicitly accounts for the effect of powder size distribution) leads to a solution of the control

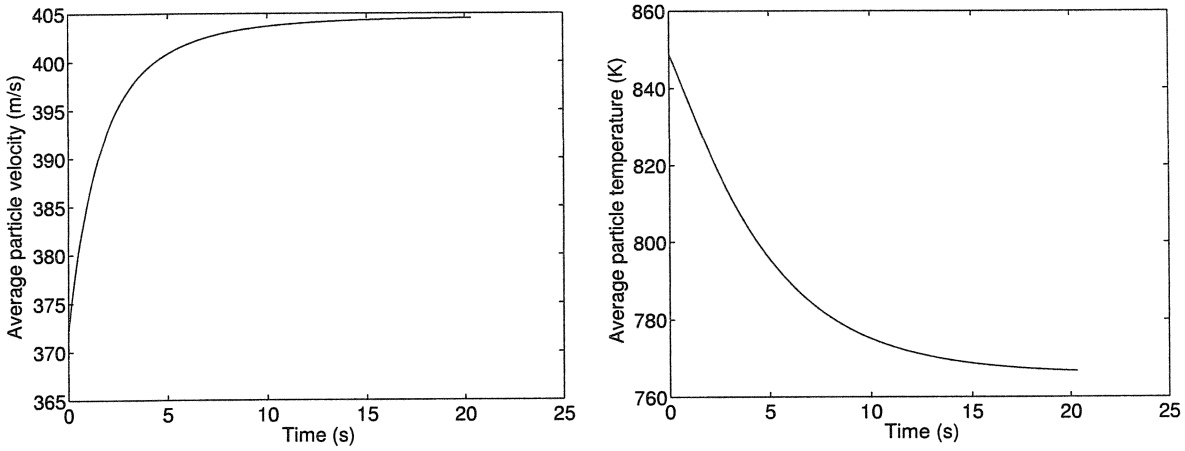


Figure 2.9: Profiles of (a) volume-based average particle velocity and (b) particle temperature with respect to time - Control problem formulation accounting for powder size distribution.

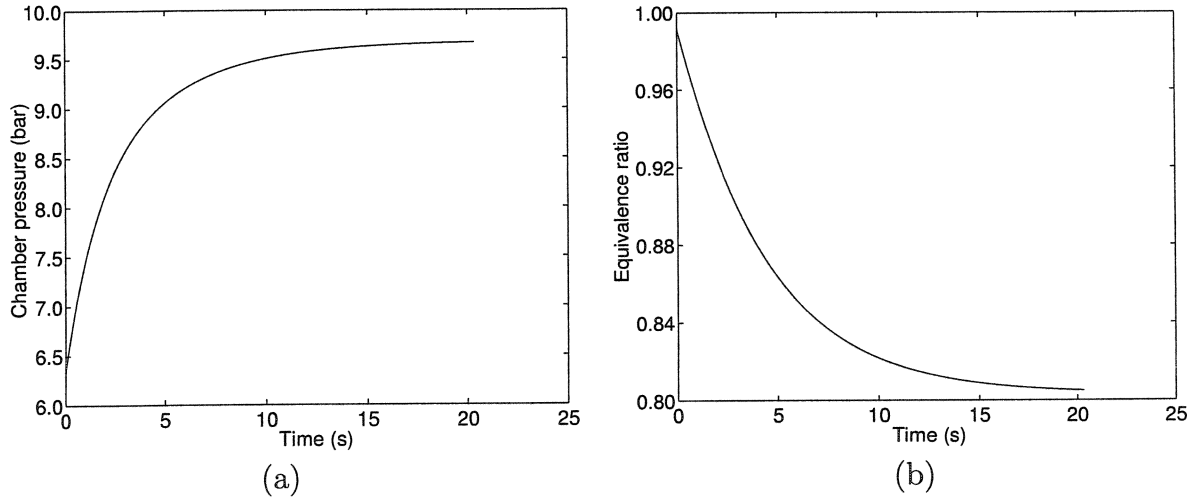


Figure 2.10: Profiles of (a) chamber pressure and (b) equivalence ratio with respect to time - Control problem formulation accounting for powder size distribution.

problem that is superior (with respect to the control action needed to achieve the desired control objectives) to a solution that assumes a monodisperse powder size distribution, the two PI controllers are also implemented on the process model using the same controlled outputs but assuming that the velocity and temperature measurements are based on a single particle whose size is taken to be $d_p = 20\ \mu m$. The corresponding controlled and manipulated variables are given in Figures 2.11 and 2.12, respectively. The results show that the average particle velocity increases by 22.9% (final $\bar{v}_p = 451.8\ m/s$) and the average particle temperature decreases by 7.0% (final $\bar{T}_p = 791.9\ K$). Therefore, the desired objectives of 10% change in the set-point values are not achieved (compare the controlled output profiles of Figure 2.11 and Figure 2.9, where the desired set-point change is achieved); this occurs because, as it has been previously shown, the behavior of an individual particle is insufficient to represent that of the entire powder size distribution. This makes clear the need to account for the effect of powder size distribution in the control problem formulation and solution.

To test the robustness of the proposed control problem formulation and of the feedback controller, the problem of controlling the HVOF process in the presence of disturbances was studied. Figures 2.13 and 2.14 show the controlled output and manipulated input profiles in the presence of 30% disturbance in the spray distance (i.e. the spray distance increases from 0.3 m to 0.39 m and then stays at this value) which occurs at t = 10 *sec.* Without control, the process jumps to a new steady state in a very short time (owing to the very short time of particle fight), and both the particle velocity (solid curve in Figure 2.13a) and temperature (solid curve in Figure 2.13b) drop instantaneously due to further particle cooling and deceleration. With feedback control, the process outputs (dashed curves in Figure 2.13a, b) move

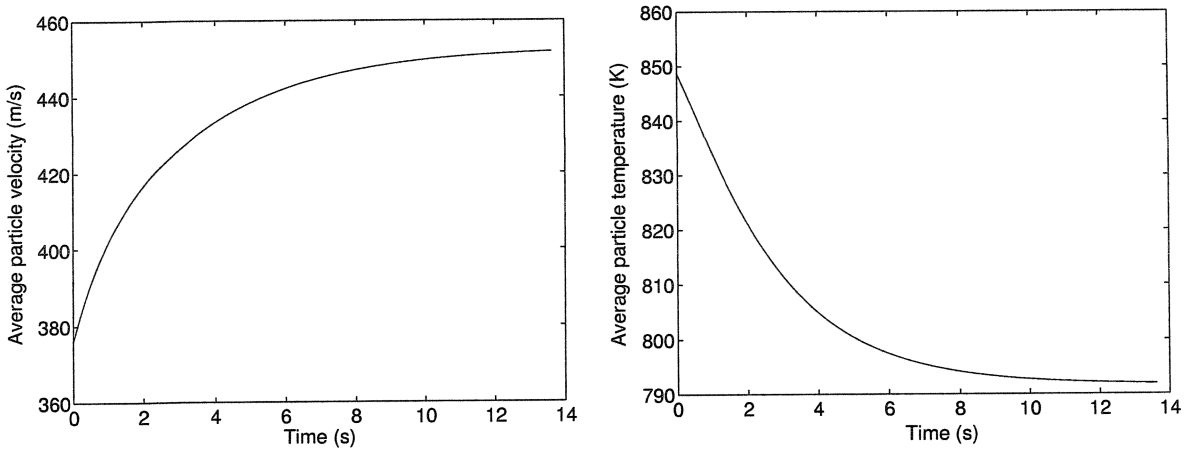


Figure 2.11: Profiles of (a) volume-based average particle velocity and (b) particle temperature with respect to time - Control problem formulation without accounting for powder size distribution.

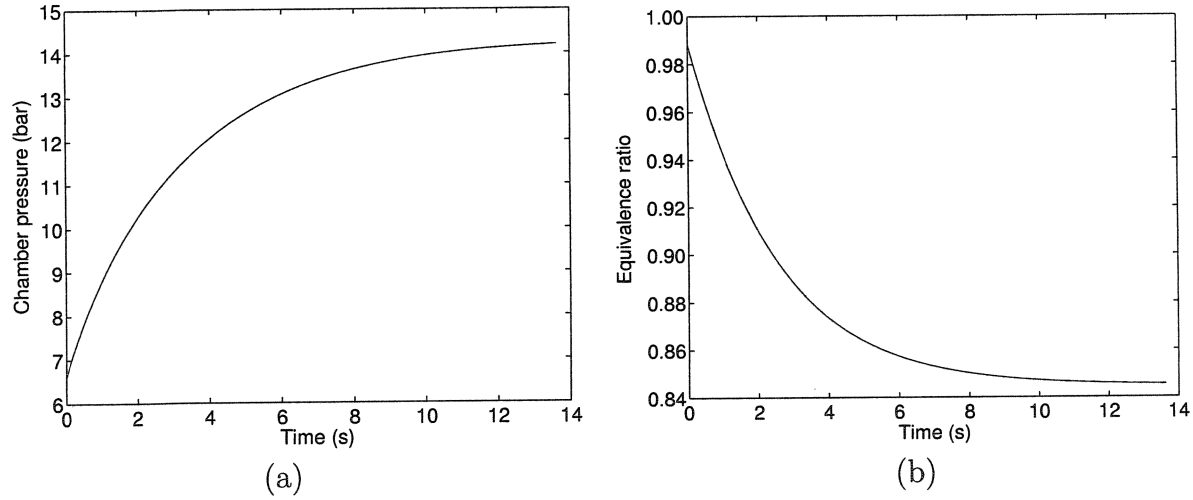


Figure 2.12: Profiles of (a) chamber pressure and (b) equivalence ratio with respect to time - Control problem formulation without accounting for powder size distribution.

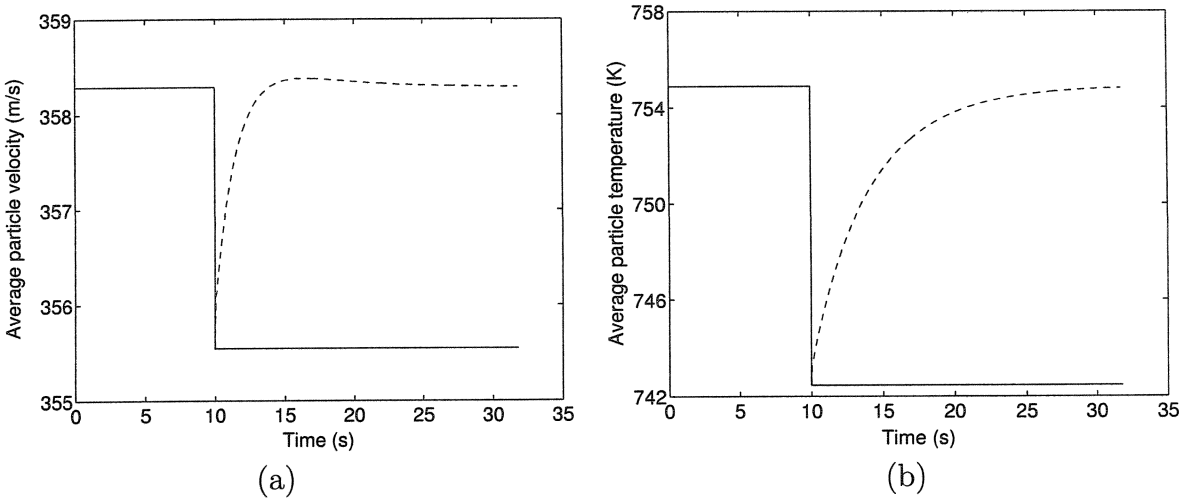


Figure 2.13: Profiles of (a) volume-based average particle velocity and (b) particle temperature with respect to time in the presence of a 30% disturbance on spray distance. Open-loop system (solid curve) and closed-loop system (dashed curve).

gradually and finally achieve their desired set-point values in about 30 *sec.*

Figures 2.15 and 2.16 show the controlled output and manipulated input profiles in the presence of 80 m/s change in initial particle velocity at t = 10 *sec.* Without control, the system jumps to a new steady state in a very short time. The impact particle velocity increases by about 6 m/s while the impact particle temperature decreases by about 48 K. The drop of particle temperature is explained by the shortened residence time of particles in the flame gas, which is caused by an increase of the particle velocity along the flight, although the particle velocity at the point of impact remains nearly the same. Such a temperature change can have a significant effect on the molten state of the particle and the resulting coating microstructure. Under feedback control, the manipulated inputs drive the process outputs to their original steady state values in about 30 *sec*, attenuating the effect of disturbance on particle injection velocity.

Another source of disturbance, especially in an industrial environment, is the

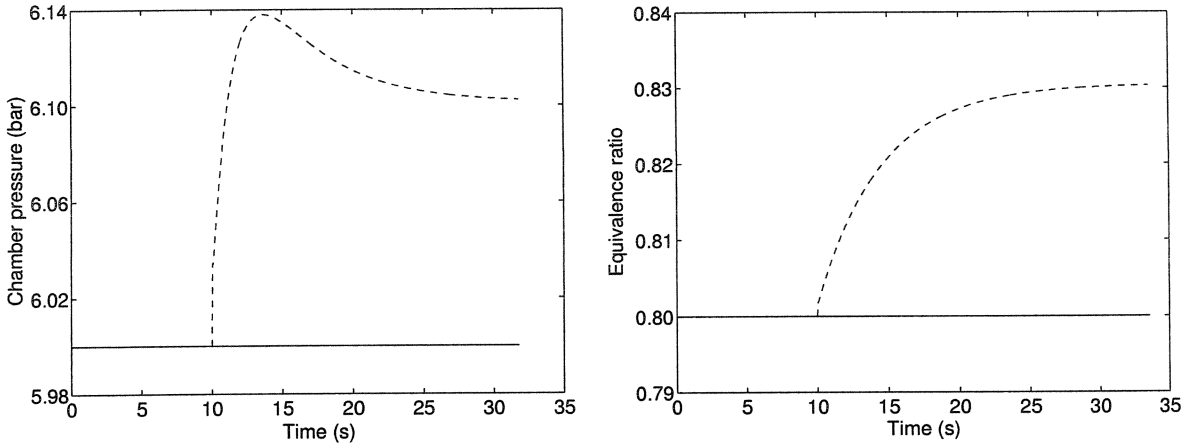


Figure 2.14: Profiles of (a) chamber pressure and (b) equivalence ratio with respect to time in the presence of a 30% disturbance on spray distance. Open-loop system (solid curve) and closed-loop system (dashed curve).

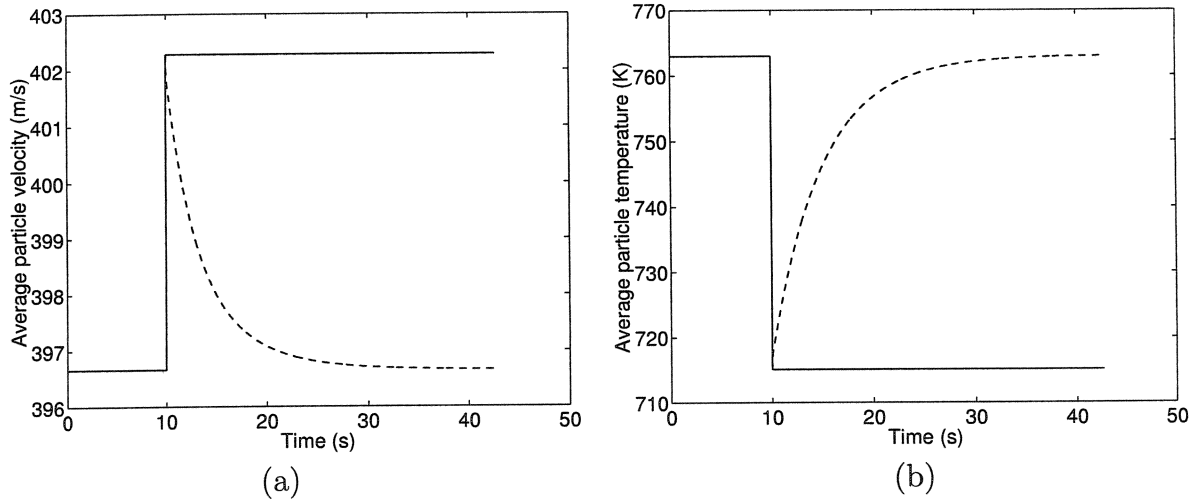


Figure 2.15: Profiles of (a) volume-based average particle velocity and (b) particle temperature with respect to time in the presence of 80 m/s variation in initial particle velocity. Open-loop system (solid curve) and closed-loop system (dashed curve).

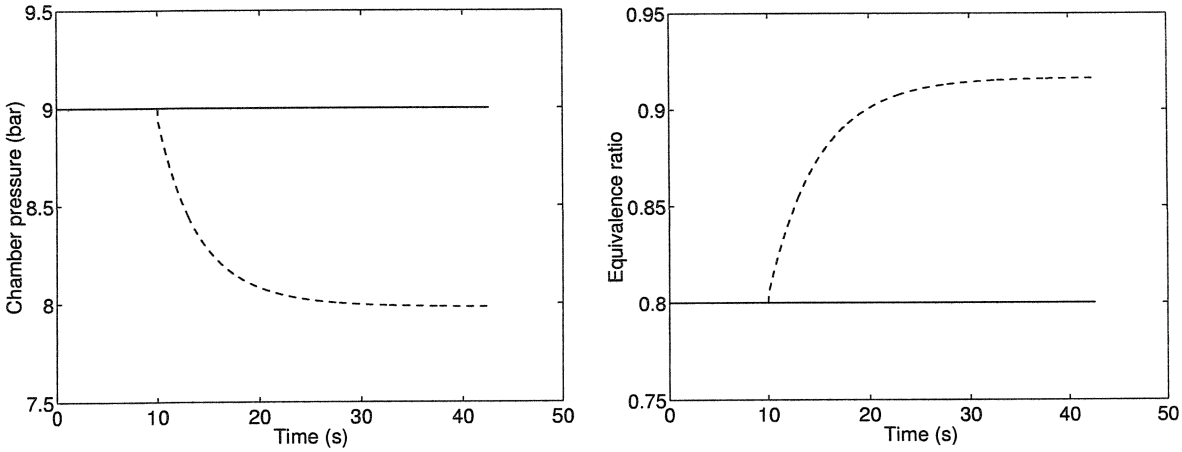


Figure 2.16: Profiles of (a) chamber pressure and (b) equivalence ratio with respect to time in the presence of 80 m/s variation in initial particle velocity. Open-loop system (solid curve) and closed-loop system (dashed curve).

variation of the size distribution of the powder during the operation of the HVOF process. This may have a significant influence on the particle velocity and particle temperature at the point of impact on the substrate based on the analysis of the previous sections. In the following simulation, it is assumed that the process is at steady state in the first 100 *sec* and then the powder size distribution changes gradually (specifically, in the following calculation, μ increases according to the expression $\mu = \mu_0 * [1 + 0.05(1 - e^{-t/100})]$ and σ^2 is kept constant). In order to reduce the computational cost of this closed-loop simulation, the integral time step for the particle motion and temperature equation is taken to be 5×10^{-6} *sec* instead of 1×10^{-7} *sec* and the total number of particles with different sizes which are simultaneously traced is taken to be 40 instead of 100. Figures 2.17 and 2.18 (dashed curves) show the controlled outputs and the manipulated inputs in the presence of such variation in the powder size distribution. Both particle velocity (Figure 2.17a) and temperature (Figure 2.17b) fluctuate in a very narrow range and eventually reach the desired set-

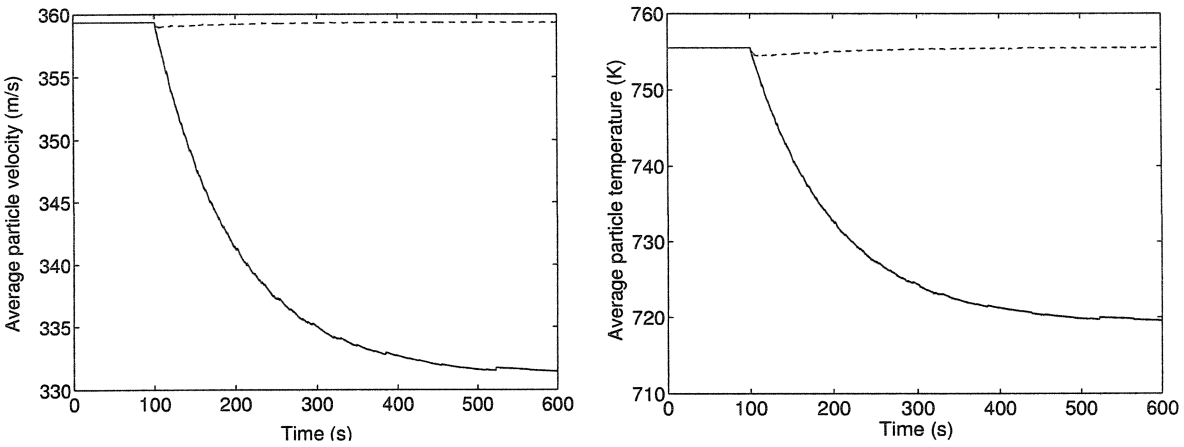


Figure 2.17: Profiles of (a) volume-based average particle velocity and (b) particle temperature with respect to time in the presence variation in powder size distribution. Open-loop system (solid curve) and closed-loop system (dashed curve).

point values. When no control is used (Figures 2.17 and 2.18 solid curves), in which case the chamber pressure and the equivalence ratio are kept constant, both particle velocity and particle temperature decrease with time, which may have an undesirable effect on the resulting coating properties. In summary, the closed-loop system simulations in the presence of disturbances show that the controller attenuates the effect of disturbances and drives the controlled outputs to the desired set-point values within about 20 *sec.* Faster disturbance rejection could be achieved at the expense of using larger control action; for an experimental HVOF system, the optimal speed of disturbance rejection should be determined on the basis of the system response to the disturbances.

2.5 Summary

This work presents generic modeling and control issues in the HVOF thermal spray process. The principle of the HVOF thermal spray process is presented, and a funda-

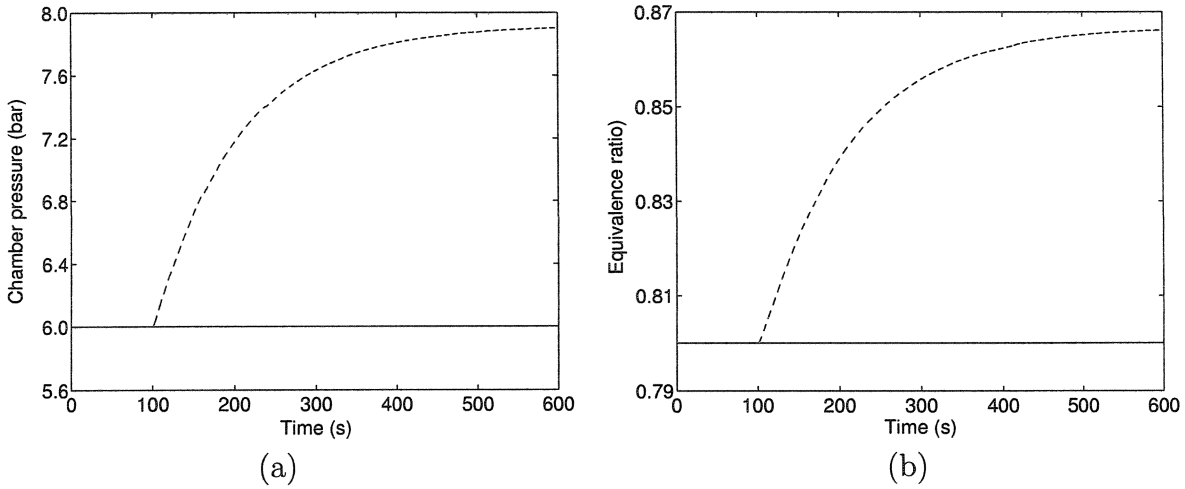


Figure 2.18: Profiles of (a) chamber pressure and (b) equivalence ratio with respect to time in the presence of variation in powder size distribution. Open-loop system (solid curve) and closed-loop system (dashed curve).

mental process model as well as generally accepted assumptions are discussed. The modeling and control framework is applied to a process that uses propane as fuel, air as oxidant, and Inconel as powder. It is shown that the higher the combustion pressure, the higher the gas momentum flux, and thus, the higher the particle velocity at impact. Moreover, the closer the equivalence ratio to 1.05 (for propane/air system), the higher the gas temperature, and thus, the higher the particle temperature at impact. Furthermore, both velocity and temperature of particles at impact are size dependent. Based on model predictions, the control problem is formulated as the one of regulating volume-based averages of the velocity and temperature of particles at the point of impact on the substrate by directly manipulating the chamber pressure (proportional to the gas momentum flux) and the equivalence ratio. A feedback control system is developed and applied to a detailed mathematical model of the process. Closed-loop simulations show that the average particle velocity and temperature at the point of impact on substrate reach the desired values in a short time. It is also

shown that the proposed formulation of the control problem (which accounts for the effect of powder size distribution) leads to a solution of the control problem that is superior (with respect to the achievement of the desired control objectives) to a solution that assumes a monodisperse powder size distribution. Finally, the proposed control problem formulation and the feedback control system are shown to be robust with respect to disturbances in spray distance and particle injection velocity, and variations in powder size distribution.

Chapter 3

Diamond Jet Hybrid HVOF Thermal Spray Process: Control-relevant Modeling of Gas-phase and Particle Behavior

This chapter[1] focuses on control-relevant modeling of gas-phase and particle behavior in an industrial high velocity oxygen-fuel (HVOF) thermal spray process (Diamond Jet hybrid gun, Sulzer Metco, Westbury, NY). We initially develop a fundamental model for the process which describes the evolution of the gas thermal and velocity fields, the motion and temperature of particles of different sizes, and explicitly accounts for the effect of powder size distribution. Based on the proposed model, a comprehensive parametric analysis is made to systematically characterize the influence of controllable process variables such as combustion pressure, oxygen/fuel ratio, as well as the effect of powder size distribution, on the values of particle velocity, temperature and degree of melting at the point of impact on substrate (these

[1]Chapter 3 is based on [87].

are the variables that directly influence coating microstructure and porosity, which, in turn, determine coating strength and hardness, see Chapter 4 for details). The control-relevant modeling provides basis for the development of a control system for the industrial HVOF thermal spray process, which will be discussed in Chapter 5.

3.1 Modeling of gas thermal and flow fields in the Diamond Jet hybrid HVOF thermal spray process

3.1.1 Process characteristics and modeling procedure

The schematic diagram of the Diamond Jet hybrid HVOF thermal spray gun is shown in Figure 1.3 and its dimension is given in Table 3.1. As we stated before, there are three major physicochemical processes involved in the HVOF thermal spray process: transformation of chemical energy into thermal energy by the combustion of the fuel, conversion of thermal energy into kinetic energy of the burning gases by passing through the nozzle, and transfer of momentum and heat from the gases to the powder particles. These processes occur simultaneously and make the fundamental modeling of the HVOF process a very difficult task. For example, detailed fundamental modeling of the gas flow and thermal fields requires state-of-the-art Computational Fluid Dynamics (CFD) methodologies and leads to complex two- or three-dimensional time-dependent partial differential equations [85, 32, 50, 111]. For the purposes of control system design and implementation, a compromise between the model complexity, computational cost and model ability to capture the dominant (from a control point of view) phenomena occurring in the process is essential. To simplify the analysis, the process model used in this work is based on the one-way coupling assumption, i.e., the existence of particles has a minimal influence on the gas dynamics while the particle inflight behavior is dependent on the gas thermal/flow field. This assumption

Table 3.1: Dimension of the air cap.

Inlet Diameter	=	14	*mm*
Nozzle Diameter	=	7.16	*mm*
Outlet Diameter	=	11	*mm*
Inlet half angle	=	12	*degree*
Outlet half angle	=	2	*degree*
Length of convergent part	=	16	*mm*
Length of divergent part	=	54	*mm*

is reasonably accurate because the particle loading in the HVOF process, which is defined as the ratio of mass flow rate of particles to that of gases, is typically less than 4% [139]. In addition, the assumptions of instantaneous equilibrium at the entrance of the HVOF gun and frozen isentropic flow during passage through the nozzle are made. These assumptions were initially proposed and justified by Swank et al [125]. based on the comparison of numerical simulations and experimental results, and later also recommended by Cheng et al [16]. Comparisons of simulation results and experimental data which will be shown later further substantiate the validity of these assumptions (see discussion in subsections 3.3.1 and 3.3.2).

Regarding the role of the air stream, it is really hard to predict what portion of the air takes part in the reaction. Whereas the air was treated as coolant solely to isolate the wall from the high temperature flame gases in some references [19, 106], it was assumed in others [32, 47, 111] that all the oxygen coming from the air participates in the reaction. The latter assumption is employed here, since it is pointed out clearly by Gourlaouen et al. [47] that the airflow mixing with the oxygen/propylene mixture should be more effective in the currently used Diamond Jet hybrid gun (which is the process under consideration in this work) than the previous Diamond Jet gun, as implied by the "water-cooled" (not "air-cooled") nozzle. Other assumptions in the

modeling include: (1) all the gases obey ideal gas law; (2) the combustion gases behave like a perfect gas during isentropic compression and expansion, and the specific heat ratio is nearly constant; and (3) the friction and cooling water effects along the nozzle and barrel are negligible so that laws of isentropic flow of compressible fluids apply.

Because the flow is chocked at the throat of the nozzle, the convergent part of the air cap and the divergent one can be solved separately [111]. The modeling procedure that is followed in the simulation is based on the sequential modular method. Specifically, given the mass flow rates of each stream (fuel, oxygen, air, and carrier gas) and a postulated combustion pressure, the temperature and gas composition at the entrance of the nozzle is calculated using an instantaneous equilibrium model, and then the nozzle flow using standard isentropic compressible flow relationships is solved. The total mass flow rate at the throat of the nozzle is then calculated and compared with the one at the entrance. The combustion pressure is then adjusted using the shooting method [112], until the discrepancy between the calculated and specified values of the total mass flow rate falls below the specified tolerance. After the gas properties at the nozzle throat are determined, the divergent part is solved using isentropic flow relationships. The external thermal/flow field in the free jet is described by empirical formulas.

3.1.2 Modeling of gas thermal and flow fields in the entire flow field

To calculate the equilibrium composition and temperature of the combustion gases, the method of minimization of the Gibbs free energy under adiabatic conditions is employed. This approach is advantageous compared to the equilibrium constant method because it can track a large number of species simultaneously without specifying a set of reactions a priori [46]. In this section, the detailed procedure of chemical equilib-

rium calculation will be presented. Specifically, Based on the assumption of adiabatic combustion under constant pressure, the calculation of equilibrium temperature and composition can be formulated as an optimization problem of the following form:

$$\begin{aligned} \min G &= \sum_{j\in pr} \mu_i \xi_i \\ \text{s.t.} & \\ 0 &= \sum_{j\in pr} a_{ij}\xi_j - b_i^0, \quad (i = 1, ..., l) \quad \text{(Mass Balance)} \\ 0 &= \sum_{j\in pr} \xi_j H_j^{\emptyset}(T_{eq}) + \frac{1}{2}v_{eq}^2 - h_0 - E_0 \quad \text{(Energy Balance)} \end{aligned} \tag{3.1}$$

where G is the Gibbs free energy of the product mixture (including inert gases and excess reactants), pr stands for products, ξ_i, H_i and μ_i correspond to the stoichiometric coefficient, enthalpy and chemical potential of species i, respectively, T_{eq} is the equilibrium temperature (subscript eq represents equilibrium), a_{ij} is the number of element i in species j, l is the total number of chemical elements involved in the system, and the superscript $^{\emptyset}$ stands for the standard condition. $b_i^0 = \sum_{k\in re} a_{ik}\xi_k$ is the number of moles of elements i per kilogram reactants (subscript re represents reactants), $h_0 = \sum_{k\in re} \xi_k H_k^{\emptyset}(T_{in})$ is the enthalpy per kilogram of reactants (subscript in represents inlet), and $E_0 = \sum_{k\in re} \frac{1}{2}\xi_k M_k v_k^2$ is the kinetic energy per kilogram of reactants (M_k is the molecular weight and v_k is the velocity of species k). For a gas obeying the ideal gas law, the chemical potential can be determined by the following expression:

$$\mu_i(T) = \mu_i^{\emptyset}(T) + RT \ln \frac{P}{P^{\emptyset}} + RT \ln \frac{\xi_i}{\sum_{i\in pr} \xi_i} \tag{3.2}$$

where R is the gas constant and P is the pressure. Due to continuity, the gas velocity after the combustion reaction is given by the following expression:

$$v_{eq} = \frac{\dot{m}_g}{\rho A_{in}} = \frac{\dot{m}_g RT_{eq}}{PA_{in}\bar{M}_{pr}} = \frac{\dot{m}_g \xi_T RT_{eq}}{PA_{in}} \tag{3.3}$$

where $\dot{m}_g$ is the total mass flow rate of the gas, A_{in} is the cross sectional area at the inlet of the air cap, $\bar{M}_{pr}$ is the average molecular weight of the product mixture, and $\xi_T = \sum_{j \in pr} \xi_j$. From Eq. 3.3, it follows that:

$$\frac{1}{2} v_{eq}^2 = \frac{\dot{m}_g^2 \xi_T^2 R^2 T_{eq}^2}{2P^2 A_{in}^2} \tag{3.4}$$

Defining $f = G + \sum_{i=1}^{l} \lambda_i \left[\sum_{j \in pr} a_{ij} \xi_j - b_i^0 \right]$, where λ_i are the so-called Lagrangian multipliers, the optimal solution of the optimization problem of Eq. 3.1 can be determined by solving the following nonlinear algebraic equations:

$$\begin{aligned}
0 &= \mu_j^{\emptyset} + RT_{eq} \ln(P/P^{\emptyset}) + RT_{eq} \ln(\xi_j/\xi_T) + \sum_{i \in l} \lambda_i a_{ij} \quad (j = 1, ..., s) \\
0 &= \sum_{j \in pr} a_{ij} \xi_j - b_i^0 \quad (i = 1, ..., l) \\
0 &= \sum_{j \in pr} \xi_j - \xi_T \\
0 &= \sum_{j \in pr} \xi_j H_j^{\emptyset}(T_{eq}) + \frac{\dot{m}_g^2 \xi_T^2 R^2 T_{eq}^2}{2P^2 A_{in}^2} - h_0 - E_0
\end{aligned} \tag{3.5}$$

The variables to be determined are equilibrium compositions ξ_j $(j = 1, ..., s)$, Lagrangian multipliers λ_i $(i = 1, ..., l)$, total number of moles ξ_T, and equilibrium temperature T_{eq}. The set of $s+l+2$ nonlinear algebraic equations of Eq. 3.5 are solved using the decent Newton-Raphson method. The central idea of Newton-Raphon method is to apply multivariable Taylor series expansion to a nonlinear vector function and truncate all terms that contain derivatives of second order and higher, and then use the resulting expression to build an iterative formula which can be used to compute the solution given an initial guess that is close to the solution; the reader may refer to the book [112] for details.

To solve the nonlinear Eq. 3.5, we followed the method developed by Gordon and McBride [46]. Define $\Delta \ln \xi_j$ $(j = 1, ..., s)$, $\pi_i = -\lambda_i / RT$ $(i = 1, ..., l)$, $\Delta \ln \xi_T$, and

$\Delta \ln T$ as the correction variables, it follows that the first equation in Eq. 3.5 can be converted to

$$\frac{\mu_j}{RT} - \sum_{i \in l} \pi_i a_{ij} = 0 \quad (j = 1, ..., s) \tag{3.6}$$

its Newton-Raphson iterative formula should be

$$\frac{\mu_j}{RT} - \sum_{i \in l} \pi_i a_{ij} + \frac{\partial \left[\frac{\mu_j}{RT}\right]}{\partial T} \Delta T + \frac{\partial \left[\frac{\mu_j}{RT}\right]}{\partial \xi_T} \Delta \xi_T + \frac{\partial \left[\frac{\mu_j}{RT}\right]}{\partial \xi_j} \Delta \xi_j = 0 \quad (j = 1, ..., s) \tag{3.7}$$

Note $\frac{\partial \left[\frac{\mu_j}{RT}\right]}{\partial T} = \frac{-\mu_j^{\emptyset} - ST}{RT^2} = \frac{-H_j^{\emptyset}}{RT^2}$, $\frac{\Delta \xi}{\xi} = \Delta \ln \xi$, and $\frac{\Delta T}{T} = \Delta \ln T$, the above equation yields

$$\frac{\mu_j}{RT} - \sum_{i \in l} \pi_i a_{ij} - \frac{H_j^{\emptyset}}{RT} \Delta \ln T - \Delta \ln \xi_T + \Delta \ln \xi_j = 0 \quad (j = 1, ..., s) \tag{3.8}$$

Similarly, the Newton-Raphson iterative formulas for the other three equations can be determined as follows,

$$\sum_{j \in pr} a_{ij} \xi_j - \sum_{k \in re} a_{ik} \xi_k + \sum_{j \in pr} a_{ij} \xi_j \Delta \ln \xi_j = 0 \quad (i = 1, ..., l) \tag{3.9}$$

,

$$\sum_{j \in pr} \xi_j - \xi_T + \sum_{j \in pr} \xi_j \Delta \ln \xi_j - \xi_T \Delta \ln \xi_T = 0 \tag{3.10}$$

and

$$\sum_{j \in pr} \frac{\xi_j H_j^{\emptyset}}{RT} \Delta \ln \xi_j + \left[\sum_{j \in pr} \frac{\xi_j c_{p_j}^{\emptyset}}{R} + \frac{\dot{m}_g^2 \xi_T^2 RT}{P^2 A_{in}^2}\right] \Delta \ln T + \left[\frac{\dot{m}_g^2 \xi_T^2 RT}{P^2 A_{in}^2}\right] \Delta \ln \xi_T$$
$$= \frac{T_{in}}{T} \sum_{k \in re} \frac{H_k(T_{in})^{\emptyset}}{RT_{in}} \xi_k - \sum_{j \in pr} \frac{H_j^{\emptyset}}{RT} \xi_j - \frac{\dot{m}_g^2 \xi_T^2 RT}{2P^2 A_{in}^2} + \frac{E_0}{RT} \tag{3.11}$$

In order to simplify the calculation, especially under the situation of a large of species, Gordon and McBride put forward the reduced Gibbs iteration equations. The

central idea is to cancel $\Delta\xi_j$ in Eqs. 3.9-3.11 using the relationship expressed by Eq. 3.8. The resulting equations are

$$\begin{aligned}
&\sum_{i\in l}\left[\sum_{j\in pr} a_{kj}a_{ij}\xi_j\right]\pi_i + \left[\sum_{j\in pr} a_{kj}\xi_j\right]\Delta\ln\xi_T + \left[\sum_{j\in pr}\frac{a_{kj}\xi_j H_j^{\emptyset}}{RT}\right]\Delta\ln T \\
&= \left[\sum_{m\in re} a_{km}\xi_m - \sum_{j\in pr} a_{kj}\xi_j + \sum_{j\in pr}\frac{a_{kj}\xi_j\mu_j}{RT}\right] \quad (k=1,...,l)
\end{aligned} \tag{3.12}$$

$$\begin{aligned}
&\sum_{i\in l}\left[\sum_{j\in pr} a_{ij}\xi_j\right]\pi_i + \left[\sum_{j\in pr}\xi_j - \xi_T\right]\Delta\ln\xi_T + \left[\sum_{j\in pr}\frac{\xi_j H_j^{\emptyset}}{RT}\right]\Delta\ln T \\
&= \left[\xi_T - \sum_{j\in pr}\xi_j + \sum_{j\in pr}\frac{\xi_j\mu_j}{RT}\right]
\end{aligned} \tag{3.13}$$

$$\begin{aligned}
&\sum_{i\in l}\left[\sum_{j\in pr}\frac{a_{ij}\xi_j H_j^{\emptyset}}{RT}\right]\pi_i + \left[\sum_{j\in pr}\frac{\xi_j H_j^{\emptyset}}{RT} + \frac{\dot{m}_g^2\xi_T^2 RT}{P^2A_{in}^2}\right]\Delta\ln\xi_T \\
&+ \left[\sum_{j\in pr}\frac{\xi_j c_{p_j}^{\emptyset}}{R} + \sum_{j\in pr}\frac{\xi_j H_j^{\emptyset 2}}{R^2T^2} + \frac{\dot{m}_g^2\xi_T^2 RT}{P^2A_{in}^2}\right]\Delta\ln T \\
&= \left[-\sum_{j\in pr}\frac{\xi_j H_j^{\emptyset}}{RT} + \frac{T_{in}}{T}\sum_{j\in re}\frac{\xi_j H_j(T_{in})^{\emptyset}}{RT_{in}} + \sum_{j\in pr}\frac{\xi_j H_j^{\emptyset}\mu_j}{R^2T^2} + \frac{E_0}{RT} - \frac{\dot{m}_g^2\xi_T^2 RT}{2P^2A_{in}^2}\right]
\end{aligned} \tag{3.14}$$

The procedure is to solve π_j $(j = 1,...,l)$, $\Delta\ln\xi_T$, and $\Delta\ln T$ using the above $l+2$ linear equations, and then to calculate $\ln\xi_j$ $(j = 1,...,s)$ using Eq. 3.8. The the following formulas are applied to update the involved variables.

$$\begin{cases}
(\ln\xi_j)^{(m+1)} &= \ln{\xi_j}^{(m)} + \alpha^{(m)}\Delta(\ln\xi_j)^{(m)} \quad (j=1,...,s) \\
(\ln\xi_T)^{(m+1)} &= \ln{\xi_T}^{(m)} + \alpha^{(m)}\Delta(\ln\xi_T)^{(m)} \\
(\ln T)^{(m+1)} &= \ln T^{(m)} + \alpha^{(m)}\Delta(\ln T)^{(m)}
\end{cases} \tag{3.15}$$

When the composition and/or temperature is far from equilibrium, a positive α that is small than one should be chosen to avoid divergence. When the state is close to equilibrium, α is set to be 1.

Because ξ_j, ξ_T and T should be positive numbers, in order to avoid taking the logarithm of negative numbers in the iteration procedure, we have chosen $\Delta \ln \xi_j$ $(j = 1, ..., s)$, $\Delta \ln \xi_T$, $\Delta \ln T$ and $-\lambda_i/RT$ $(i = 1, ..., l)$ as the solution variables at each iteration step. In the above equations, the thermodynamic data, such as the heat capacity, enthalpy, entropy and chemical potential of each species are calculated by the following equations [46]:

$$\begin{cases} \dfrac{c_p^{\emptyset}(T)}{R} &= \dfrac{a_1}{T^2} + \dfrac{a_2}{T} + a_3 + a_4 T + a_5 T^2 + a_6 T^3 + a_7 T^4 \\ \dfrac{H^{\emptyset}(T)}{RT} &= -\dfrac{a_1}{T^2} + \dfrac{a_2}{T} \ln T + a_3 + \dfrac{a_4}{2} T + \dfrac{a_5}{3} T^2 + \dfrac{a_6}{4} T^3 + \dfrac{a_7}{5} T^4 + \dfrac{a_8}{T} \\ \dfrac{S^{\emptyset}(T)}{R} &= -\dfrac{a_1}{2T^2} - \dfrac{a_2}{T} + a_3 \ln T + a_4 T + \dfrac{a_5}{2} T^2 + \dfrac{a_6}{3} T^3 + \dfrac{a_7}{4} T^4 + a_9 \\ \dfrac{\mu_j^{\emptyset}}{RT} &= \dfrac{H^{\emptyset}(T)}{RT} - \dfrac{S^{\emptyset}(T)}{R} \end{cases} \tag{3.16}$$

where $a_1, \ldots, a_9$ are constants for a given species. It usually takes about 10 iterations to get a convergent solution.

Under the assumption of isentropic frozen flow, the properties of gas phase during passage through the nozzle (both the convergent part and the divergent part) can be solved using the following equations (which are derived by solving conservation equations governing compressible flow) [114]:

$$\frac{A_2}{A_1} = \frac{\mathbf{M}_1}{\mathbf{M}_2} \left\{ \frac{1 + [(\gamma - 1)/2]\mathbf{M}_2^2}{1 + [(\gamma - 1)/2]\mathbf{M}_1^2} \right\}^{(\gamma+1)/2(\gamma-1)} \tag{3.17}$$

$$\frac{T_2}{T_1} = \frac{1 + [(\gamma - 1)/2]\mathbf{M}_1^2}{1 + [(\gamma - 1)/2]\mathbf{M}_2^2} \tag{3.18}$$

$$\frac{P_2}{P_1} = \left\{ \frac{1 + [(\gamma - 1)/2]\mathbf{M}_1^2}{1 + [(\gamma - 1)/2]\mathbf{M}_2^2} \right\}^{\gamma/(\gamma-1)} \tag{3.19}$$

$$\frac{\rho_2}{\rho_1} = \left\{ \frac{1 + [(\gamma - 1)/2]\mathbf{M}_1^2}{1 + [(\gamma - 1)/2]\mathbf{M}_2^2} \right\}^{1/(\gamma-1)} \tag{3.20}$$

where A is the cross-sectional area perpendicular to the flow direction, ρ is the gas density, γ is the specific heat ratio calculated by the expression $\gamma = \bar{c}_p/(\bar{c}_p - R)$ where $\bar{c}_p = \sum_i \xi_i c_p^i / \sum_i \xi_i$, and $\mathbf{M}$ is the mach number defined by the ratio of gas velocity to the local sonic velocity ($a = \sqrt{\gamma P/\rho}$). At the throat of the nozzle, where the mach number is 1 [114], the mass flow rate can be calculated using the formula:

$$\dot{m}_g = \rho_t v_t A_t = \sqrt{\gamma P_t \rho_t} A_t \tag{3.21}$$

where the subscript g stands for gas and the subscript t stands for throat. With a postulated combustion pressure, the calculated mass flow rate at the throat is usually different from the one at the entrance of the gun. The shooting method is then applied to adjust the combustion pressure until these two flow rates match.

We note that the isentropic relationships (Eqs. 3.17-3.20) are valid only if there is no shock inside of the nozzle. This can be guaranteed as long as the following inequity holds:

$$\frac{P_b}{P_e} < \frac{2\gamma}{\gamma+1}\mathbf{M}_e^2 - \frac{\gamma-1}{\gamma+1} \tag{3.22}$$

where P_b is the back pressure (ambient pressure), and P_e is the gas pressure at the exit of the nozzle. For the experimental Diamond Jet hybrid gun system, our calculations show that the right hand side of the above equation is about 5, and therefore no shock will ever occur inside of the nozzle as long as the exit pressure is larger than one fifth of the back pressure; a condition which is always satisfied under industrial operating conditions.

We have applied the above modeling procedure and equations to analyze the Diamond Jet HVOF process [111], which is similar to the one shown in Figure 1.3 but whose nozzle has only a convergent part. The combustion products considered in our numerical simulation are Ar, CO, CO_2, H, H_2, H_2O, NO, N_2, O, O_2, and OH etc. It is worth pointing out that C_3H_6 is not part of the products under normal operating

Table 3.2: Comparison of computational and experimental results for a Diamond Jet process [111].

Case	O_2 $scfh$	C_3H_6 $scfh$	Air $scfh$	N_2 $scfh$	P^e_{eq} $psia$	P^c_{eq} $psia$	error %
1	635	185	790	29.4	69.7	68.7	-1.4
2	635	185	395	29.4	59.7	56.1	-6.0
3	879	185	795	29.4	76.7	77.6	1.2
4	347	110	632	29.4	44.7	44.8	0.2

conditions. For the given four different operating conditions, the combustion pressures predicted by the above procedure are all within 6% of the experimentally measured values (see table 3.2); this result is more accurate than the one obtained with the two step chemical kinetics model [111] and implies that the combustion model should take into account the dissociation of the combustion products.

At the exit of the nozzle, the Reynolds number based on the diameter and the gas velocity is about 3×10^4, and the flow is fully turbulent. Depending on the magnitude of the gas pressure at the exit of the air cap and of the back pressure, the flow outside of the nozzle may be under-expanded, ideally expanded or over-expanded. Usually the velocity and temperature of the gas in the free jet are lower than the ones at the nozzle exit. [63, 20] From the exit of the nozzle to a position whose distance is not larger than the potential core length (L_{pc}), the gas velocity and temperature can be considered almost constant[127]. Further downstream, the gas velocity and temperature decay rapidly because of the entrainment of the surrounding air. This decay of the gas velocity and temperature can be described by the following empirical formulas: [127]:.

$$\frac{v}{v_e} = 1 - \exp\left(\frac{\alpha}{1 - x/L_{pc}}\right) \tag{3.23}$$

and

$$\frac{T - T_a}{T_e - T_a} = 1 - \exp\left(\frac{\beta}{1 - x/L_{pc}}\right) \tag{3.24}$$

where x is the axial distance from the exit of the gun barrel ($x > L_{pc}$) and α and β are parameters obtained from experimental measurements. L_{pc} is a function of the mach number at the exit of the gun barrel (M_e) and of the barrel diameter (D) of the following form[127]:

$$L_{pc}/D = 3.5 + 1.0\mathrm{M}_e^2 \tag{3.25}$$

3.2 Modeling of particle velocity, temperature and melting degree in the Diamond Jet hybrid HVOF thermal spray process

The particle trajectories and temperature histories in the gas field are computed by the momentum and heat transfer equations. Since the acceleration and deceleration of particles in the moving gas in the HVOF process are dominated by the drag force [109], other forces applied on the particles can be neglected and the particle motion can be adequately described by the following two first-order ordinary differential equations:

$$\begin{aligned} m_p \frac{dv_p}{dt} &= \frac{1}{2} C_D \rho_g A_p (v_g - v_p)|v_g - v_p|, \quad v_p(0) = v_{p0} \\ \frac{dx_p}{dt} &= v_p, \quad x_p(0) = 0 \end{aligned} \tag{3.26}$$

where m_p is the mass of the particle, v_p is the axial velocity of the particle, A_p is the projected area of the particle on the plane perpendicular to the flow direction, ρ_g is the density of the gas, C_D is the drag coefficient, and x_p is the position of the particle. The absolute sign in the relative velocity between particle and gas implies that a particle is accelerated if its velocity is less than that of the gas and decelerated otherwise. In order to take into consideration the fact that many powders used in

the HVOF process are not spherical, a formula for the drag coefficient C_D, which accounts for the particle shape using the concept of sphericity ϕ (defined as the ratio of the surface area of a sphere with equivalent volume to the actual surface area of the particle) is used in this work, which has the following form [18, 39]:

$$\frac{C_D}{K_2} = \frac{24}{ReK_1K_2}\left[1 + 0.1118(ReK_1K_2)^{0.6567}\right] + \frac{0.4305}{1 + 3305/ReK_1K_2} \tag{3.27}$$

where K_1 and K_2 are two sphericity-related factors. The local Reynolds number (Re) for this two phase flow problem is defined based on the relative velocity $Re = d_p \mid v_g - v_p \mid \rho_g/\eta_g$, where d_p is either the particle diameter if the particle is spherical or an appropriate equivalent diameter if the particle is not spherical and η_g is the gas viscosity.

In the HVOF process, the Biot number of the particles ($Bi = hL/\lambda_p$, h is the heat transfer coefficient, L is a characteristic dimension defined by the ratio of particle volume to its surface area, and λ_p is the thermal conductivity of the particle) is typically less than 0.1 [18], which means that the particles are heated with negligible internal resistance and that the temperature gradients inside them can be neglected[40]. Consequently, the equation describing the heat transfer between a single particle and the gas reduces to a first-order ordinary differential equation. Depending on the value of particle temperature, different equations are used. With the assumption of negligible particle vaporization, the particle heating can be described as follows:

$$hA'_p(T_g - T_p) = \begin{cases} m_p c_{p_p}\dfrac{dT_p}{dt}, & (T_p \neq T_m) \\ \Delta H_m m_p \dfrac{df_p}{dt}, & (T_p = T_m) \end{cases} \tag{3.28}$$

where T_p is the temperature of the particle, A'_p is the surface area of the particle, T_m is the melting point of the particle, ΔH_m is the enthalpy of melting and f_p is the melting ratio, or the ratio of the melted mass to the total mass of the particle

$(0 \leq f_p \leq 1)$. The heat transfer coefficient h is computed by the Ranz-Marshall empirical equation[6]:

$$\frac{hd_p}{\bar{\lambda}_g} = Nu = 2 + 0.6Re^{\frac{1}{2}}Pr^{\frac{1}{3}} \tag{3.29}$$

where the Prandtl number (Pr) is calculated by $Pr = \bar{c}_{p_g}\bar{\eta}_g/\bar{\lambda}_g$.

In the above equations, the viscosity and thermal conductivity of each species are calculated by the following formulas[46]:

$$\begin{aligned} \ln(\eta) &= b_1 \ln(T) + b_2/T + b_3/T^2 + b_4 \\ \ln(\lambda) &= c_1 \ln(T) + c_2/T + c_3/T^2 + c_4 \end{aligned} \tag{3.30}$$

where $b_1, \ldots, b_4$, $c_1, \ldots, c_4$ are constants for a specific species. For gas mixtures, the average viscosity and thermal conductivity are calculated by the following mixing rules [46]:

$$\begin{aligned} \bar{\eta} &= \sum_i \frac{x_i \eta_i}{x_i + \sum_{j \neq i} x_i \psi_{ij}} \\ \bar{\lambda} &= \sum_i \frac{x_i \lambda_i}{x_i + \sum_{j \neq i} x_i \varsigma_{ij}} \end{aligned} \tag{3.31}$$

where the interaction coefficients ψ_{ij} and ς_{ij} are obtained from the following formulas:

$$\begin{aligned} \psi_{ij} &= \frac{1}{4}\left[1 + \left(\frac{\eta_i}{\eta_j}\right)^{1/2}\left(\frac{M_j}{M_i}\right)^{1/4}\right]^2 \left[\frac{2M_j}{M_i + M_j}\right]^{1/2} \\ \varsigma_{ij} &= \psi_{ij}\left[1 + \frac{2.41(M_i - M_j)(M_i - 0.142M_j)}{(M_i + M_j)^2}\right] \end{aligned} \tag{3.32}$$

At each step, we integrate Eqs. 3.26 and 3.28 with a small enough time-step such that the gas velocity, gas temperature, and the local Reynolds number can all be considered constant over this interval. After one integration step, we update the gas velocity and gas temperature according to the new particle position and then apply the same strategy for the next time-step. This methodology was proposed by Crowe and Stock [29] and was found to be computationally economical and accurate. To

account for the particle melting behavior, we modified this approach and check the molten state of the particle at each time-step and applied different formulas for the particle heating. Specifically, the iterative formulas for particle velocity, position and temperature are:

$$\begin{aligned} v_p^{i+1} &= v_g^i - (v_g^i - v_p^i)\exp(-\Delta t/\tau_p) \\ x_p^{i+1} &= x_p^i + v_p^i \Delta t \\ T_p^{i+1} &= T_g^i - (T_g^i - T_p^i)\exp(-\Delta t/\omega_p), \quad (T_p^i, T_p^{i+1} > T_m \text{ or } T_p^i, T_p^{i+1} < T_m) \\ f_p^{i+1} &= f_p^i + \frac{c_{p_p}(T_g - T_m)}{\Delta H_m}\frac{\Delta t}{\omega_p}, \quad (0 < f_p^i, f_p^{i+1} < 1) \end{aligned} \tag{3.33}$$

where $\tau_p = \dfrac{4\rho_p d_p^2}{3\eta_g C_D Re}$ and $\omega_p = \dfrac{\rho_p c_p d_p^2}{6Nu\lambda_g}$. In the four possible phase transition points, in which the current step and the next step correspond to different particle molten states, the successive formulas for particle temperature and melting ratio take the following form:

1. $T_p^i < T_m$ $(f_p^i = 0)$, $T_p^{i+1} > T_m$, from totally solid state to partially melted state

$$\begin{aligned} f_p^{i+1} &= f_p^i + \frac{c_{p_p}(T_p^{i+1} - T_m)}{\Delta H_m} \\ T_p^{i+1} &= T_m \end{aligned} \tag{3.34}$$

2. $T_p^i > T_m$ $(f_p^i = 1)$, $T_p^{i+1} < T_m$, from totally liquid state to partially melted state

$$\begin{aligned} f_p^{i+1} &= f_p^i + \frac{c_{p_p}(T_p^{i+1} - T_m)}{\Delta H_m} \\ T_p^{i+1} &= T_m \end{aligned} \tag{3.35}$$

3. $T_p^i = T_m$ $(0 < f_p^i < 1)$, $T_p^{i+1} > T_m$, from partially melted state to totally liquid state

$$\begin{aligned} T_p^{i+1} &= T_m + \frac{\Delta H_m(f^{i+1} - 1)}{c_{p_p}} \\ f_p^{i+1} &= 1 \end{aligned} \tag{3.36}$$

4. $T_p^i = T_m$ $(0 < f_p^i < 1)$, $T_p^{i+1} < T_m$, from partially melted state to totally solid state

$$\begin{aligned} T_p^{i+1} &= T_m + \frac{\Delta H_m f^{i+1}}{c_{p_p}} \\ f_p^{i+1} &= 0 \end{aligned} \tag{3.37}$$

To reduce the computation time and to maintain accuracy at the same time, a time varying time-step is used of the following form:

$$\Delta t = \min\{\tau_p/100, \omega_p/100, \Delta x_{max}/v_p\} \tag{3.38}$$

where Δx_{max} is chosen to be 10^{-4} m, which is the maximum flight distance in each time interval. The first two constraints guarantee that the gas velocity and temperature will change little in each time-step.

3.3 Analysis of gas and particle behavior in the Diamond Jet hybrid HVOF thermal spray process

3.3.1 Analysis of the gas dynamics without air

Initially, we only included propylene and oxygen as feed to the system and tested the influence of combustion pressure and oxygen/fuel ratio on the gas temperature, velocity, density, and momentum flux (ρu^2) in the internal field. The reasons are the following: (1) the influence of the process parameters on the gas dynamics and the particle infight behavior is apparent in this simplified case; (2) a bijection of pressure and equivalence ratio to fuel and oxygen flow rates is possible, and calculation starting from either side is equivalent to the other, which facilitates the numerical calculation; and (3) there are many HVOF processes whose feed consists of only fuel and oxygen (i.e., without air); see, for example, Gu et al [48]. and Yang and Eidelman [139] etc. The process model was based on the assumptions of negligible injection

gas velocity, instantaneous equilibrium under constant enthalpy and pressure in the injection interface, and frozen isentropic flow during passage through the nozzle. To account for the dissociation of gaseous products, the model included nine species (CO, CO_2, H, H_2, H_2O, O, O_2, and OH etc.) in the product mixture. The equilibrium temperature and composition of combustion was solved by minimizing the total Gibbs free energy, and the gas properties during passage through the nozzle were determined by standard laws governing compressible flows described in subsection 3.1.2.

In Figure 3.5(a), the combustion pressure is fixed to be 9 *bar* and the equivalence ratio varies from 0.5 to 1.6. In this range, it is found that there is a peak in each of the temperature vs. equivalence ratio plot. As the equivalence ratio increases, the temperature at the entrance, the throat and the exit increase first, reaching a maximum value, and then decrease. However, the equivalence ratio associated with each peak temperature is about 1.2 (or fuel rich system), which is somewhat different from a fuel/air system [83], whose optimal value is close to 1.05. It can also be seen that as the equivalence ratio increases from 0.5 to 1.6, the gas velocity both at the throat and at the exit increase by about 22-23%, while the gas density decreases by about 33%. As a result, the momentum flux keeps almost constant at these two positions. In Figure 3.5(b), the equivalence ratio is kept at 1.0 and the combustion pressure varies from 5 to 15 *bar*. In the combustion pressure range of interest, it is found that both gas velocity and gas temperature change little (about 2% and 5%, respectively), however, the gas density and momentum flux change almost linearly with respect to the combustion pressure, by about 190% and 200%, respectively. We also computed 3D profiles of gas properties under different combustion pressures and equivalence ratios, as shown in Figures 3.1, 3.2 and 3.3. Further analysis reveals the following:

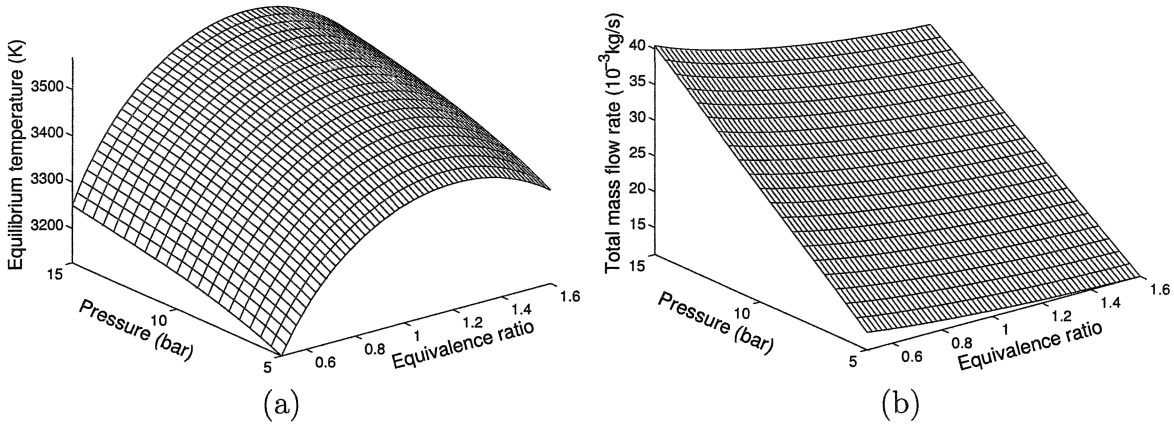


Figure 3.1: Profiles of (a) equilibrium temperature and (b) total mass flow rate with respect to P and φ. Operating conditions: P = 5 - 15 *bar* and φ = 0.5 - 1.6.

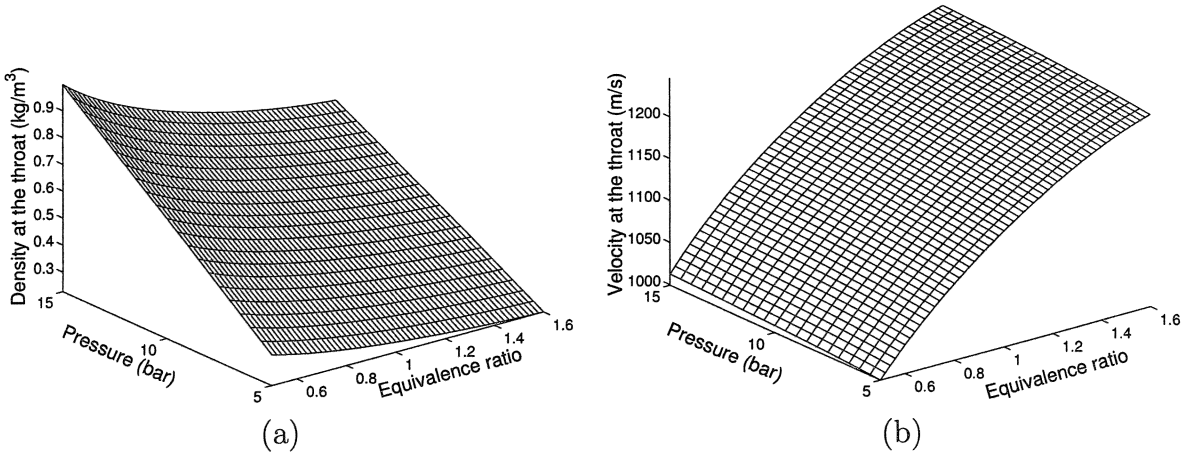


Figure 3.2: Profiles of (a) gas density and (b) velocity at the throat with respect to P and φ. Operating conditions: P = 5 - 15 *bar* and φ = 0.5 - 1.6.

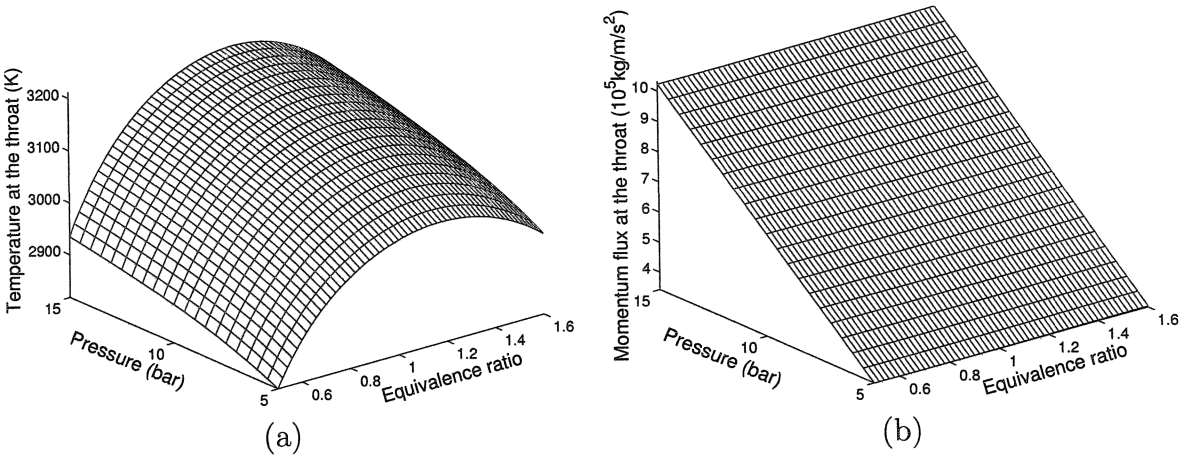


Figure 3.3: Profiles of (a) temperature and (b) momentum flux at the throat with respect to P and φ. Operating conditions: P = 5 - 15 *bar* and φ = 0.5 - 1.6.

1. At a fixed pressure, there is a peak in the equilibrium temperature vs. equivalence ratio plot, whose value is about 1.2. It is worth noting that the peak flame temperature occurs not at stoichiometric, but at a fuel rich condition. This is because the equilibrium temperature is determined not only by the heat generated by the exothermic reaction process, but also by the heat capacity of the product mixture as well. As the equivalence ratio becomes slightly above 1, the gas temperature increases further with the equivalence ratio; this is because the heat capacity of products decreases more rapidly than the heat released. Beyond the equivalence ratio associated with the peak temperature (about 1.2), the heat generated falls more rapidly than does the heat capacity, and the temperature decreases. On the other hand, when the equivalence ratio is fixed, the equilibrium temperature increases with pressure. The primary cause of the equilibrium temperature variation with pressure is the product dissociation because higher pressure favors larger molecules (Le Chatelier's principle). Further increase in pressure results in an increase in H_2O with respect to H_2 and O and helps to

increase temperature.

2. The higher the equivalence ratio, the smaller the total mass flow rate is needed to achieve the same combustion pressure to choke the flow. On the other hand, under the same equivalence ratio, the combustion pressure increases linearly with the total mass flow rate. These observations can be explained by the following equation:

$$\dot{m}_g = \rho_g v_g A = \mathbf{M} P \sqrt{\frac{\gamma \bar{M}_{pr}}{R T_g}} A = \frac{\mathbf{M} P \gamma A}{a} \tag{3.39}$$

Note that the combustion process tends to increase the total number of moles in the product mixture and to decrease the average molecular weight. In the fuel rich case, the total amount of dissociation becomes significant and the molecular weight decreases continuously as φ increases. Referring to Figure 3.4, when φ increases from 0.5 to 1.6 with a fixed P, while T varies less than 10%, $\bar{M}_{pr}$ decreases about 30% following a nearly linear function, and as a consequence, M_{pr}/T decreases monotonically. Therefore, $\dot{m}_g$ decreases monotonically as φ increases. When the combustion pressure increases with a fixed φ, both $\bar{M}_{pr}$ and T increase slightly because the product dissociation is suppressed. Because $\sqrt{\bar{M}_{pr}/T}$ varies less than 2% in the pressure range of interest, the total mass flow rate of gas is roughly proportional to the combustion pressure. Eq. 3.39 also indicates that the pressure can be increased by (1) increasing the total mass flow rate of the gas, and (2) increasing the equivalence ratio.

3. The gas density at the nozzle throat can increase by increasing the combustion pressure and decreasing the equivalence ratio. This can be explained by the expression $\rho = \gamma P/a^2$. However, the gas velocity at the nozzle throat, where the Mach number is one, is mainly a function of the equivalence ratio and changes little with the combustion pressure, as previously discussed.

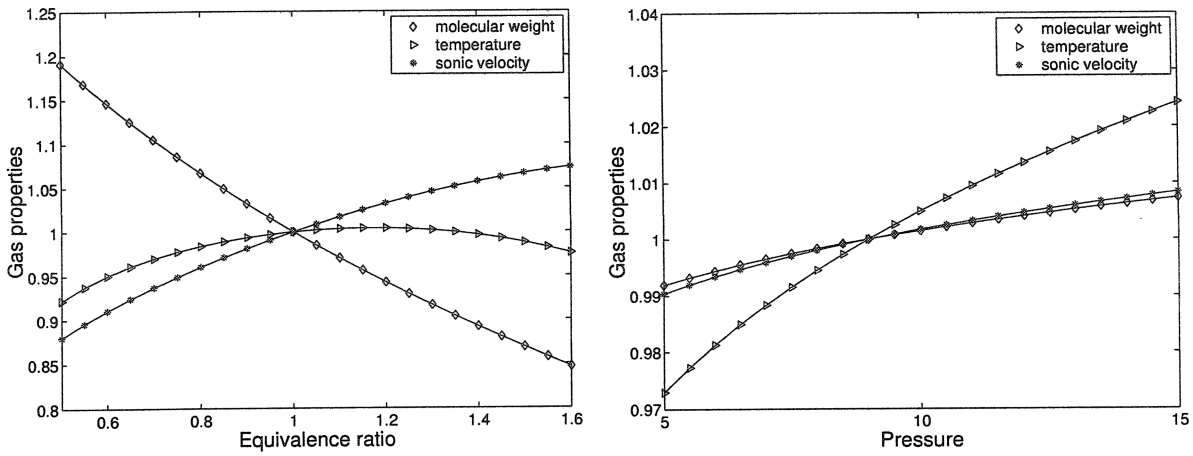


Figure 3.4: Normalized average molecular weight, temperature, and sonic velocity at the throat of the nozzle under operating conditions: (a) $P = 5$ - 15 *bar*, $\varphi = 1.0$, and (b) $P = 9$ *bar*, $\varphi = 0.5$ - 1.6. Normalization is done with respect to the corresponding gas properties under operating conditions: $P = 9$ *bar* and $\varphi = 1.0$ (Table 3.3).

4. The momentum flux at the throat of the nozzle is independent of the equivalence ratio and is a linear function of the combustion pressure. The influence of pressure on momentum flux can be explained by the following equation:

$$\rho_g v_g^2 = \rho_g \mathbf{M}^2 a^2 = \rho_g \mathbf{M}^2 \left(\sqrt{\gamma P/\rho_g}\right)^2 = \mathbf{M}^2 \gamma P \qquad (3.40)$$

where γ is nearly a constant and $\mathbf{M}$ mainly depends on the geometrical configuration of the nozzle. As a consequence, the momentum flux is a nearly linear function of the gas pressure. Equation 3.40 is also applicable to the HVOF systems which include air in the feed stream.

Because the drag force, which is the dominant force that determines the motion of the particles in the gas field, is approximately proportional to the gas momentum flux, and the gas temperature, whose difference from the particle temperature provides the driving force for particle heating, it follows from the above analysis that particle

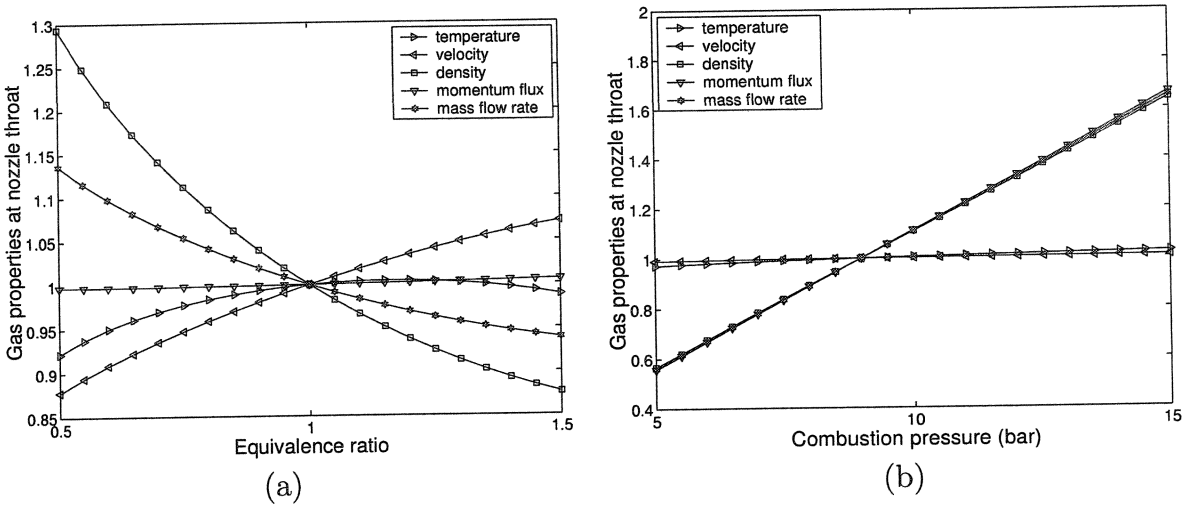


Figure 3.5: Normalized gas temperature, velocity, momentum flux, and mass flow rate in the internal field under operating conditions: (a) P = 5 - 15 bar, φ = 1.0 and (b) P = 9 bar, φ = 0.5 - 1.6. Normalization is done with respect to the corresponding gas properties under operating conditions: P = 9 bar and φ = 1.0 (Table 3.3).

Table 3.3: Gas properties under operating conditions: P = 9 bar and φ =1.0.

Properties	Inlet	Throat	Exit
Temperature (K)	3486.7	3120.7	2222.6
Velocity (m/s)	–	1147.0	2150.8
Density (kg/m^3)	0.7535	0.4688	0.1073
Momentum flux $(10^5 kg \cdot m/s^2)$	–	6.1673	4.9627
Mass flow rate $(10^{-3} kg/s)$	21.65	21.65	21.65
Average molecular weight $(10^{-3} kg/mol)$	24.15	24.15	24.15

temperature and velocity can be nearly independently adjusted by manipulating the equivalence ratio and the combustion pressure, respectively.

3.3.2 Analysis of gas dynamics including the air stream

Motivated by the conclusions drawn from the above parametric analysis, we included air in the feed stream to the HVOF process; this makes the process analysis more difficult. Assuming the air is composed by O_2, N_2, and Ar only, the reaction formula becomes

$$\varphi C_3H_6 + 4.5O_2 + x[N_2 + 1/78Ar] \Rightarrow \sum_{i \in pr} \xi_i (PR)_i \tag{3.41}$$

where x can be any number from 0 to 16.7, corresponding to the cases of pure oxygen as oxidant and pure air as oxidant, respectively. Obviously, in this case, the equilibrium temperature is not only dependent on φ, but also on x. Furthermore, because the pressure depends on the temperature, the average molecular weight and the mass flow rate (Eq. 3.39), the air stream plays an important role in achieving a high pressure.

Figure 3.6 shows the combustion pressure and equilibrium temperature under different total mass flow rates and equivalence ratios for a fixed $x = 3.97$. It can been seen that the process behavior is very similar to the one without air if x is kept constant (compare Figure 3.6 and Figure 3.1). The pressure contour in Figure 3.6(a) shows that the total mass flow rate required to achieve the same combustion pressure decreases as the equivalence ratio increases. The total mass flow rate increases linearly with pressure when the equivalence ratio is fixed. The equilibrium temperature is significantly dependent on the equivalence ratio, but varies slightly with the total mass flow rate. This also implies that pressure variations do not significantly affect the equilibrium temperature.

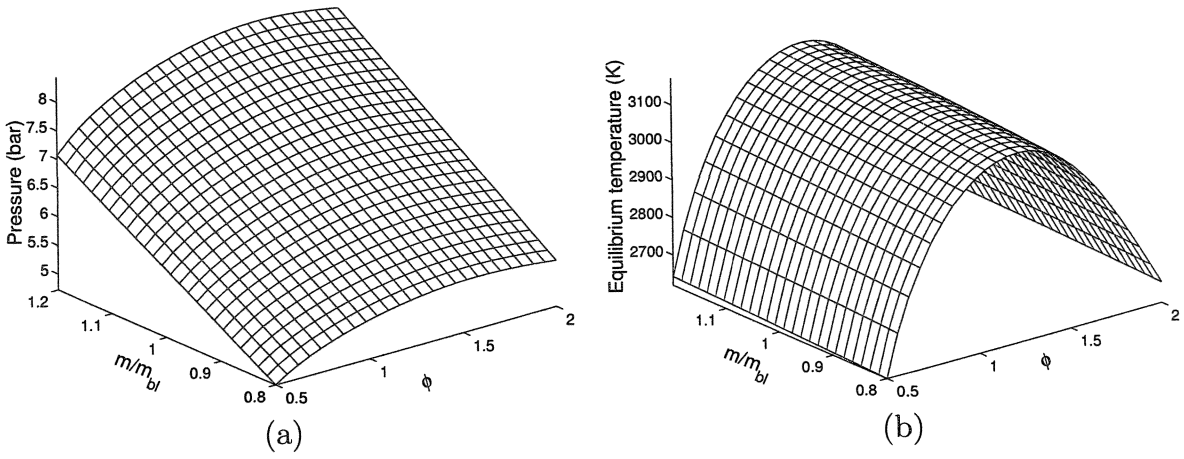


Figure 3.6: Profiles of (a) pressure and (b) equilibrium temperature with respect to φ and m/m_{bl}. Operating conditions: x the same as the one in the baseline condition (Propylene: 176 $scfh$ (standard cubic feet per hour), Oxygen: 578 $scfh$, Air: 857 $scfh$, Nitrogen: 28.5 $scfh$), total mass flow rate varying from 0.8 to 1.2 times the one of the baseline value (18.1 g/s), and φ = 0.5 - 2.0.

Figure 3.7 shows the combustion pressure and equilibrium temperature under different equivalence ratios and oxygen/nitrogen ratios with a fixed total mass flow rate that is equal to the one in the baseline condition. It can been seen that as the fraction of air in the whole reactant mixture increases, both pressure and temperature drop. As x varies from 0 (pure oxygen as oxidant) to 16.7 (pure air as oxidant), the equivalence ratio corresponding to the peak equilibrium temperature decreases from 1.23 to 1.05 (see Figure 3.8); this result provides a way to optimally manipulate the relative flow rate of oxygen to air.

We tested the gas dynamics under nine different operating conditions shown in Table 3.4. The baseline condition is recommended by the manufacturer. The simulation results are given in Table 3.5. Under the baseline conditions, the pressure at the exit of the air cap calculated by the proposed procedure is 0.63 bar, which implies

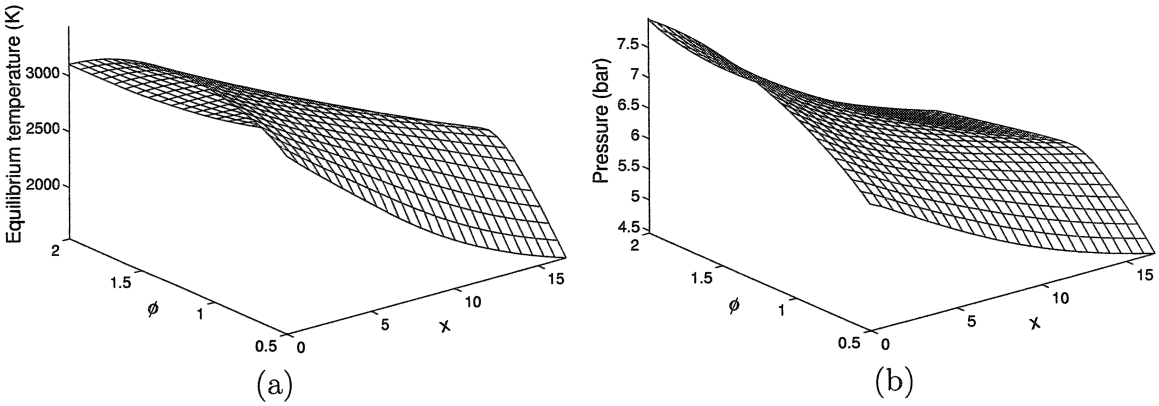


Figure 3.7: Profiles of (a) equilibrium temperature and (b) pressure with respect to φ and x. Operating conditions: total mass flow rate the same as the one in the baseline condition, $\varphi = 0.5$ - 2.0, and $x = 0$ - 16.7.

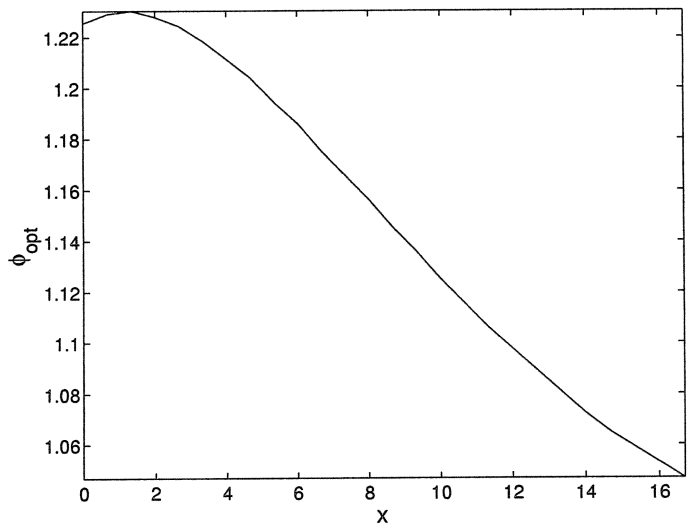


Figure 3.8: Profile of optimal equivalence ratio corresponding to the peak temperature of the gas with respect to x. Operating conditions: total mass flow rate the same as the one in the baseline condition, $x = 0$ - 16.7.

Table 3.4: Nine different gas flow rates.

Case	O_2 $scfh$	C_3H_6 $scfh$	Air $scfh$	N_2 $scfh$	$\dot{m}$ kg/s	φ	x
1 (baseline)	578.0	176.0	857.0	28.5	18.10	1.045	3.969
2 ($Air\uparrow$ 33%)	578.0	176.0	1139.8	28.5	20.98	0.969	4.895
3 ($Air\downarrow$ 33%)	578.0	176.0	574.2	28.5	15.22	1.134	2.885
4 ($O_2\uparrow$ 33%)	768.7	176.0	857.0	28.5	20.24	0.835	3.171
5 ($O_2\downarrow$ 33%)	387.3	176.0	857.0	28.5	15.95	1.396	5.303
6 ($C_3H_6\uparrow$ 33%)	578.0	234.1	857.0	28.5	18.95	1.390	3.969
7 ($C_3H_6\downarrow$ 33%)	578.0	117.9	857.0	28.5	17.24	0.700	3.969
8 ($\dot{m}\uparrow$ 33%)	768.7	234.1	1139.8	37.9	24.07	1.045	3.969
9 ($\dot{m}\downarrow$ 33%)	387.3	117.9	574.2	19.1	12.13	1.045	3.969

that the flow outside of the gun is overexpanded. The manufacturer, Sulzer Metco measured a gauge pressure of -4 *psig* (-0.3 *bar*, or the absolute pressure is about 0.7 *bar*) at the nozzle exit under the same operating conditions [101], which validated the model and assumption applied in this work. In fact, the overexpanded flow condition gives a slightly higher gas velocity.

In the nine different operating conditions, the equilibrium temperature is a function of the total mass flow rate, as well as a function of φ and x. For instance, cases 1, 6, 7, 8, 9 have the same x (about 4.0), under which the equivalence ratio associated with the peak temperature is around 1.2 according to our previous discussion. Equilibrium temperature in case 7 is the lowest because its equivalence ratio is only 0.7. Although the equivalence ratios in cases 2 and 6 are quite different, the temperatures are almost the same. This is because these two equivalence ratios are located in opposite sides of the optimal equivalence ratio and the total mass flow rates differ slightly. Temperatures are quite different in cases 5 and 6 although the equivalence ratios are very close because the mass flow rates are different. Note that a higher mass flow rate favors higher pressure, and accordingly, higher equilibrium temperature. Case 3

Table 3.5: Calculated gas properties for different operating conditions.

Case	P_{eq} bar	T_{eq} K	M_{pr} $10^{-3}kg/mol$	T_t K	ρ_t kg/m^3	v_t m/s	$(\rho v^2)_t$ $10^5 kg/m/s^2$
1 (baseline)	6.79	3128	26.1	2812	0.428	1050	4.72
2 ($Air\uparrow$ 33%)	7.66	3056	26.8	2747	0.509	1023	5.33
3 ($Air\downarrow$ 33%)	5.89	3197	25.0	2874	0.349	1083	4.09
4 ($O_2\uparrow$ 33%)	7.47	3112	26.8	2802	0.487	1032	5.19
5 ($O_2\downarrow$ 33%)	5.98	3008	25.0	2693	0.376	1054	4.18
6 ($C_3H_6\uparrow$ 33%)	7.34	3128	24.4	2805	0.433	1087	5.11
7 ($C_3H_6\downarrow$ 33%)	6.05	2925	27.9	2630	0.436	982	4.21
8 ($\dot{m}\uparrow$ 33%)	9.06	3159	26.1	2842	0.567	1054	6.30
9 ($\dot{m}\downarrow$ 33%)	4.52	3084	26.0	2772	0.288	1045	3.15

has the lowest x and an equivalence ratio close to the optimal one, as a consequence; its equilibrium temperature is the highest, compare to cases 1 and 2, even when the total mass flow rate is low.

On the other hand, the combustion pressure under the above operating conditions is roughly a linear function of the total mass flow rate and changes little with the gas composition. This is because the average molecular weight of the reaction product mixture is 24-28$\times 10^{-3}$ kg/mol, and the temperature is 2.9-3.1$\times 10^3$ K. Consequently, the sonic velocity does not vary much and the pressure is proportional to the total mass flow rate (which is in agreement with Eq. 3.39).

3.3.3 Analysis of particle velocity, temperature and melting ratio

In the fabrication of nanostructured coatings, it is crucial to maintain high particle temperature at the point of impact on the substrate and to prevent particles from being superheated at the same time, because it is precisely the small grain size that contributes to the superior qualities of nanostructured coatings [18]. It is also of great importance to maintain high particle velocity at the point of impact on substrate

Table 3.6: Thermophysical properties of powder particles.

Powder	Ni
Density (kg/m^3)	8900
Specific heat$(J/kg/K)$	471
Melting point (K)	1727
Latent heat (J/kg)	3×10^5
Diameter (μm)	1-100

since the higher the particle velocity, the denser the coating. We simulated the Diamond Jet hybrid HVOF process model under the baseline operating conditions given in Table 3.4 for Nickel (particle properties are given in Table 3.6) and the results for the in-flight particle velocity, temperature and melting ratio are shown in Figure 3.9. Particles of small sizes may reach very high velocities during flight, however, their velocities drop more sharply than those of larger particles because of their smaller momentum inertias. Furthermore, they may be heated to the melting point in a short time and be fully melted during flight, however, they may eventually be in a coexistence state of liquid and solid or even in a solid state after a long enough distance. Smaller particles tend to change their temperatures easily because of their smaller thermal inertias. For particles of large sizes, however, their period for acceleration and heating are both longer, and their velocity (or temperature) profiles become nearly flat as they approach the same velocity (or temperature) of the gas. In addition, they may not reach the melting point and be in solid state during the entire flight. However, particles of medium sizes may become partially melted during flight.

To further understand the behavior of particles in the HVOF process, we also plotted the velocity, temperature and melting ratio at the 0.254 m standoff as a function of particle size, shown in Figure 3.10 (note the configuration of each figure

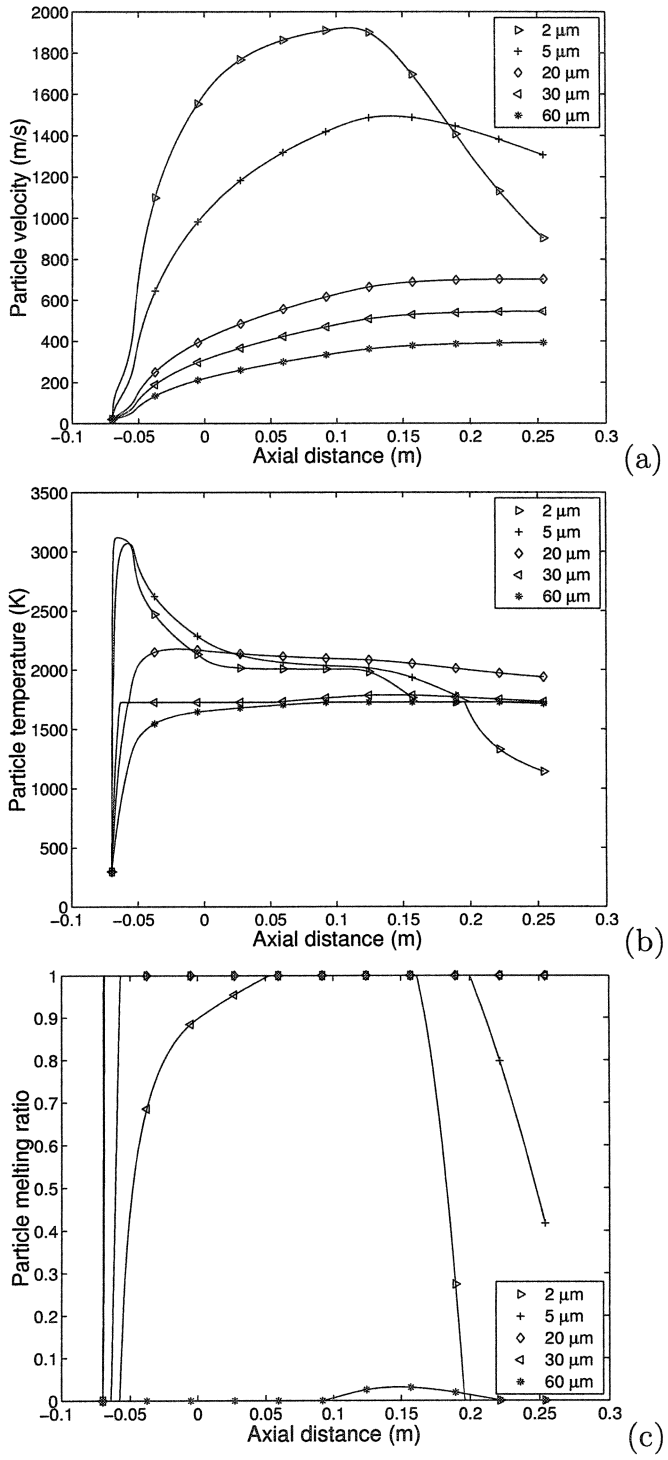


Figure 3.9: Profiles of particle velocity, temperature, and melting ratio along the flow field ($x = 0$ corresponds to the nozzle exit).

may vary with different spray distances). Under the baseline operating conditions, particles in the size range of 9 - 30 μm hit the substrate as liquid droplets. Particles of sizes larger than 49 μm or less than 5 μm are in solid state at the point of impact on substrate. Other particles, however, when reach the substrate, are in a semi-molten state (where both liquid and solid coexist). It is worth pointing out that, although both very small particles and very big particles hit the substrate in partially molten state or even solid state, their microstructure is not the same because the former ones have been fully melted during flight.

Figure 3.11 shows the influences of particle injection velocity and spray distance on the profiles of particle velocity and temperature and flight time. It is shown that both disturbances have a minimal effect on particle velocity. However, their influence on particle temperature and melting behavior, can not be neglected. This behavior can be explained by the changes of residence time of particles in the gas flow field. An increase in the particle injection velocity will result in a decrease of particle residence time, especially in the high temperature zone. This is why larger size particles are affected to a larger extent. An increase in the spray distance, however, has a greater influence on the temperature of smaller particles. This is because larger particles have greater thermal inertia and do not change their temperature very much after they reach the gas temperature.

3.4 Summary

This chapter presents control-relevant modeling of an industrial high velocity oxygen-fuel (HVOF) thermal spray process (Diamond Jet hybrid gun, Sulzer Metco, Westbury, NY). The process model describes the evolution of the gas thermal and velocity fields, the motion and temperature of agglomerate particles of different sizes, and

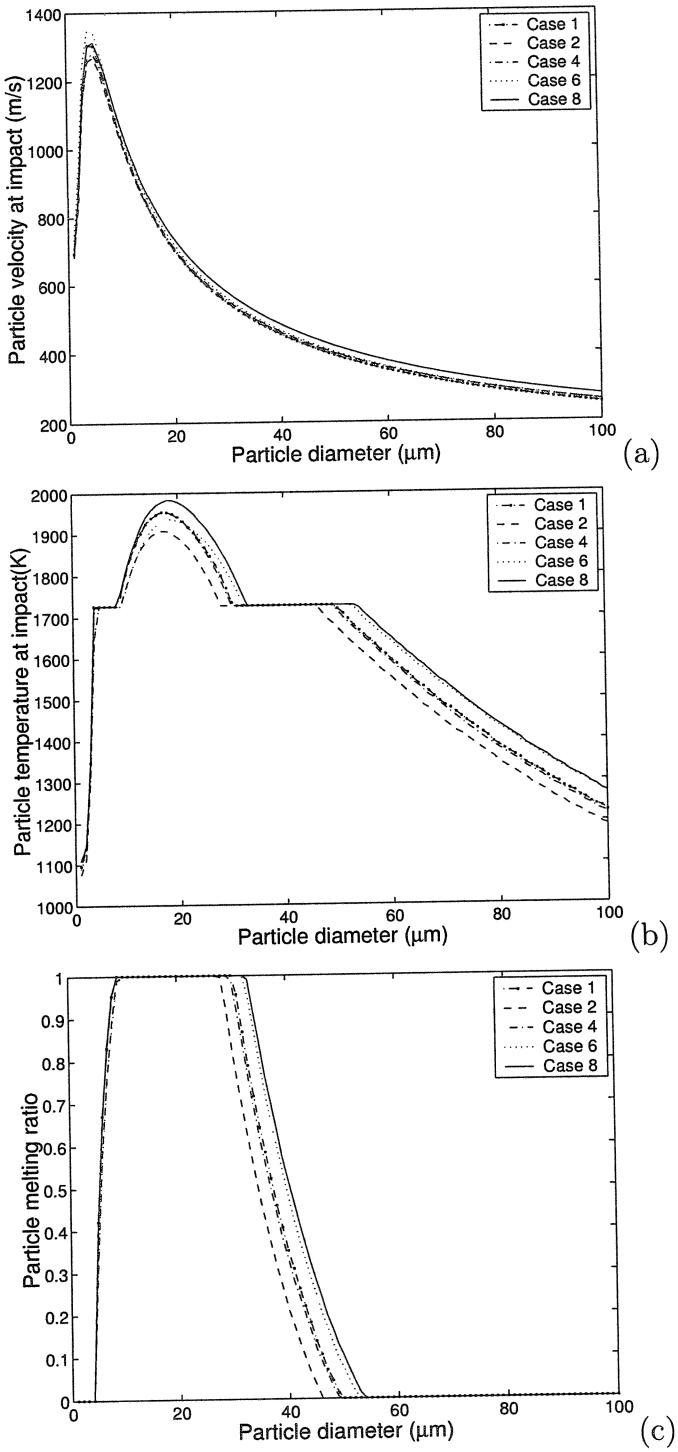


Figure 3.10: Velocity, temperature and melting ratio at the 0.254 m standoff (point of impact on substrate) as a function of particle size.

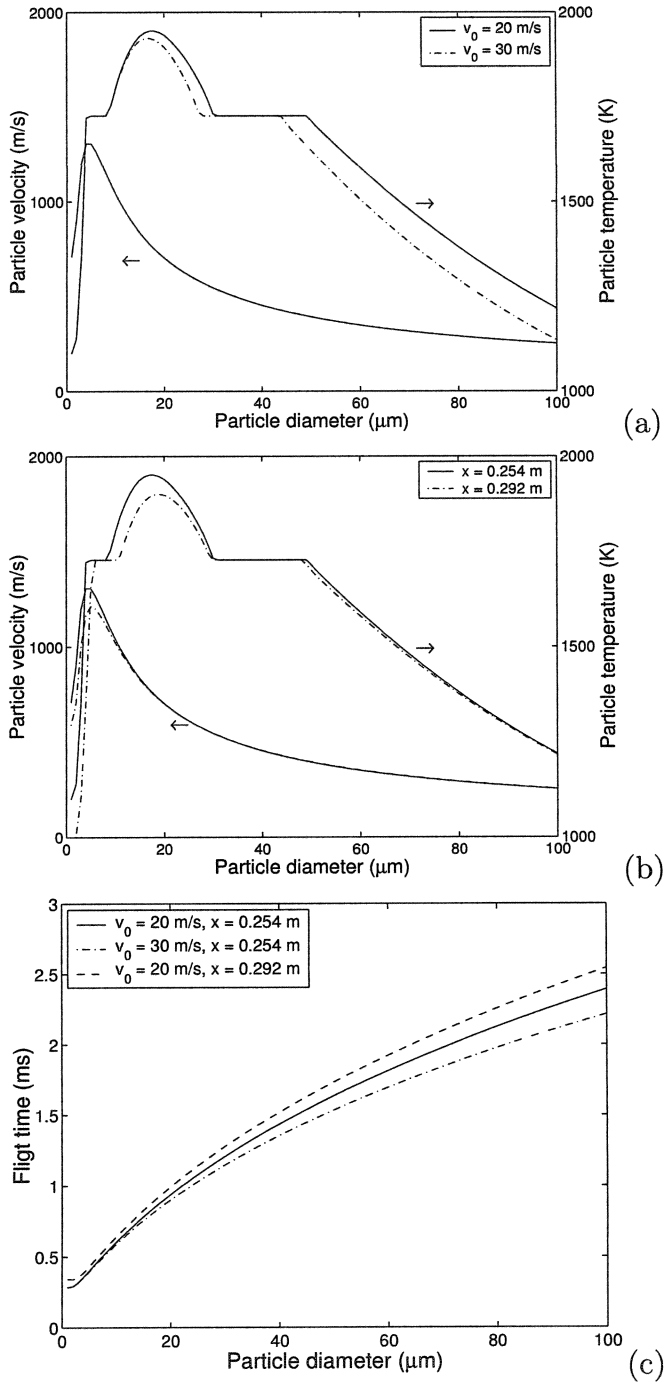


Figure 3.11: Effect of disturbances on operating conditions (particle injection velocity and spray distance) on particle velocity, temperature and flight time.

explicitly accounts for the effect of powder size distribution. In addition to providing useful insight into the in-flight behavior of different-size particles, the model was used to make a comprehensive parametric analysis of the HVOF process. This analysis allowed a systematic characterization of the influence of controllable process variables such as combustion pressure, oxygen/fuel ratio, as well as the effect of powder size distribution, on the values of particle velocity, temperature and melting ratio at the point of impact on substrate. Specifically, the study shows that the particle velocity is primarily influenced by the combustion pressure, the particle temperature (and melting ratio) is strongly dependent on the fuel/oxygen ratio, and both particle velocity and particle temperature (and melting ratio) are strong functions of particle size. In particular, particles of moderate sizes (around 20 μm) have larger velocities and temperatures than both smaller and bigger ones. These findings are consistent with existing experimental studies and set the basis for the formulation of the control problem for this HVOF thermal spray process.

Chapter 4

Diamond Jet Hybrid HVOF Thermal Spray Process: Rule-based Modeling and Analysis of Coating Microstructure

This chapter[1] focuses on computational modeling and simulation of microstructure of coatings produced by an industrial high velocity oxygen-fuel (HVOF) thermal spray process (Diamond Jet hybrid gun, Sulzer Metco, Westbury, NY). Based on the understanding of coating structure and mechanisms of pore formation inside of the coating obtained from experimental studies, a stochastic simulation procedure is used to explore the evolution of the microstructure of the coatings. In the coating growth model, the velocity, temperature and degree of melting of particles hitting on the substrate are determined by a previously developed mathematical model [87] describing gas and particle behavior, and the complex characteristics of the thermally sprayed coatings are captured by applying certain basic rules that encapsulate the main phys-

[1]Chapter 4 is based on [119].

ical features of the deposition process. In addition to providing useful insight into the pore formation and coating growth, the model is used to make a comprehensive parametric analysis, which allows us to systematically characterize the influence of operating conditions, such as the gas flow rate, spray distance, as well as the effect of particle size, on the particle melting behavior, coating porosity, surface roughness and deposition efficiency. Comparison of simulation results and experimental studies shows that the proposed model can reasonably predict the relationship between macroscopic processing conditions and coating microstructure.

4.1 Introduction

In order to improve coating repeatability and process performance, much experimental work has been done in the last decade to study the effect of key process parameters such as gas flow rate, fuel/oxygen ratio, and spray distance, on the physical and mechanical properties of HVOF thermally sprayed coatings [25, 30, 43, 47, 54, 96, 89]. The optimization of process parameters involved in these works relies on the conventional Taguchi method, which uses a set of orthogonal arrays that stipulates the way of conducting the minimal number of experiments that could give the full information of all the factors affecting the coating performance parameters [30]. This approach is expensive but reliable for a specific HVOF thermal spray process. However, a lack of fundamental understanding of the dynamics of the gas and particle behavior as well as of the microscopic deposition process significantly restrict its applicability because, the experimentally derived "optimal" solution may be questionable when it is applied to another thermal spray process in which some important parameters, such as the nozzle configuration, powder or fuel type, etc., are different [16]. Mathematical modeling, on the other hand, provides an efficient and versatile alternative to quantify

the effect of each one of the key process parameters on coating properties.

In the last decade, significant efforts have been made to simulate the evolution of coating microstructure using mathematical models. For example, stochastic simulation has been applied to model the stochastic deposition and coating growth process in plasma spray [15, 26, 72]. These stochastic models are based on certain rules that govern the splat formation, coating growth and pore formation. Parametric analysis has been made based on these models to study how the coating microstructure and physical properties such as the porosity and roughness, are affected by various process parameters, including the gun scanning velocity, spray angle [15], particle size, gas temperature and velocity [26]. However, the particle temperature, velocity and degree of melting profiles in the plasma spray process are very different from the corresponding profiles in the HVOF thermal spray, and thus, these models cannot be used to predict coating microstructure in the HVOF thermal spray process. Recently, continuum type and stochastic models have been developed to simulate the coating microstructure formation [42, 103] in the HVOF thermal spray process; the continuum type models involve partial differential equations governing particle deformation and spreading. However, in these works, the particles at the point of impact on the substrate are assumed to be fully melted and the important effect of degree of particle melting (i.e., most particles hit the substrate in semi-molten state) is not accounted for in the heat balance that describes the evolution of particle temperature and the formation of coating microstructure.

In order to develop a methodology to precisely control the coating micro- or nanostructure which determines the coating mechanical and physical properties by manipulating macro-scale operating conditions, the link between the macroscopic operating conditions and the coating microstructure should be established and the relationship

between particle size and melting behavior and coating porosity needs to be explored. In this work, we focus on the modeling of microstructure of coatings produced by an industrial HVOF thermal spray process (Diamond Jet hybrid gun, Sulzer Metco, Westbury, NY). Based on the understanding of coating structure and mechanisms of pore formation inside of the coating obtained from experimental studies [91, 92, 93], stochastic simulation is used to explore the microstructure evolution behavior of the coatings on the substrate. In the coating growth model, the velocity, temperature and degree of melting of powders hitting on the substrate are determined by a previously developed mathematical model describing gas and particle behavior [87], and the complex characteristics of the thermally sprayed coatings are captured by applying several basic rules that encapsulate the main physical features of the deposition process. In addition to providing useful insight into the pore formation and coating growth, the model is used to make a comprehensive parametric analysis, which allows us to systematically characterize the influence of operating conditions, such as the gas flow rate, spray distance, as well as the effect of particle size, on the particle melting behavior, coating porosity, surface roughness and deposition efficiency. Comparison of simulation results and experimental studies shows that the proposed model can provide good predictions of the relationship between macroscopic processing conditions and coating microstructure.

4.2 Characteristics of deposition and coating growth

Thermally sprayed coatings consist of lamellar splats interspersed with pores. The splats, which are the fundamental building blocks of the coating, are formed by the impact, deformation, spreading and solidification of individual droplets. The pores, however, are formed by the interaction of the droplets and the previously-deposited

coating surface. In this section, several characteristics involved in the deposition and coating growth process, including deformation, pore formation and surface roughness, will be described.

4.2.1 Deformation

In the HVOF thermal spray process, each individual particle is accelerated and heated up in a burning gas flame, and then impinges onto the substrate in a molten, partially-molten or solid state. At impact, the sudden stagnation of the powder particles leads to a pressure build-up at the particle-surface interface, and deformation occurs. As the particles splash on the substrate, they are also quenched to the substrate temperature in a very short time. For the particle deformation process, if a particle is fully melted, it is assumed that the droplet becomes a cylinder as a result of deformation [97] (see Figure 4.1(a)). The splat flattening degree ξ is defined by the following equation:

$$\xi = \frac{D}{d_p} = \frac{2}{d_p}\sqrt{\frac{A}{\pi}} \tag{4.1}$$

where D and A are the estimated diameter and area of the splat, respectively, and d_p is the particle diameter prior to impact. The analysis of Madejski [97] shows that ξ depends on several dimensionless parameters characterizing the impact and spreading processes, including: the Reynolds number ($Re = d_p v_p/\nu_p$, where ν_p is the kinematic viscosity of the droplets), which represents the viscous dissipation of the inertia forces, the Weber number ($We = d_p v_p^2 \rho_p/\sigma_p$, where σ_p is surface tension of the droplets), which quantifies the conversion of the kinetic energy into surface energy, and the Peclet number ($Pe = v_p d_p/\varepsilon_p$, where ε_p is the thermal diffusivity of the solidified layer), which expresses the freezing rate [97]. Under the operating conditions typically employed in the HVOF thermal spray process, solidification is insignificant before the deformation is complete, and therefore the flattening ratio can

be expressed as a function of We and Re as follows [97]:

$$\frac{3\xi^2}{We} + \frac{1}{Re}\left(\frac{\xi}{1.2941}\right)^5 = 1 \tag{4.2}$$

The above equation is valid for $We > 100$ and $Re > 100$. When the surface tension effects are negligible, which is usually true for particles with size larger than 10 μm, Eq. 4.2 can be further simplified to:

$$\xi = 1.2941 Re^{0.2} \tag{4.3}$$

If a particle is partially melted, our modeling procedure assumes that the unmelted part will form a hemisphere with the equivalent volume and the melted part will form a ring around this hemisphere (see Figure 4.1(b)), whose flattening ratio can be calculated using the same formula.

4.2.2 Pore formation

Porosity, which is defined as the ratio of the volume of the pores inside the coating to the total volume of the coating, is one of the most important quality parameters of the coatings produced by the HVOF thermal spray process. Experimental studies have shown that a lamellar microstructure is consistently observed on cross sections of a coating, and pores are distributed in the lamellar structure, regardless of the processing conditions [109]. However, the amount, size and distribution of pores in the thermally sprayed coatings are dependent to a large extent on the processing conditions. These variables, which significantly affect thermal conductivity and mechanical properties of the coatings, can be controlled more efficiently if an in-depth understanding of the fundamental mechanisms of porosity formation is established. In this sense, estimation of coating porosity is one of the main objectives of this work.

Liu *et al.* [91, 92, 93] proposed several possible mechanisms of pore formation in the

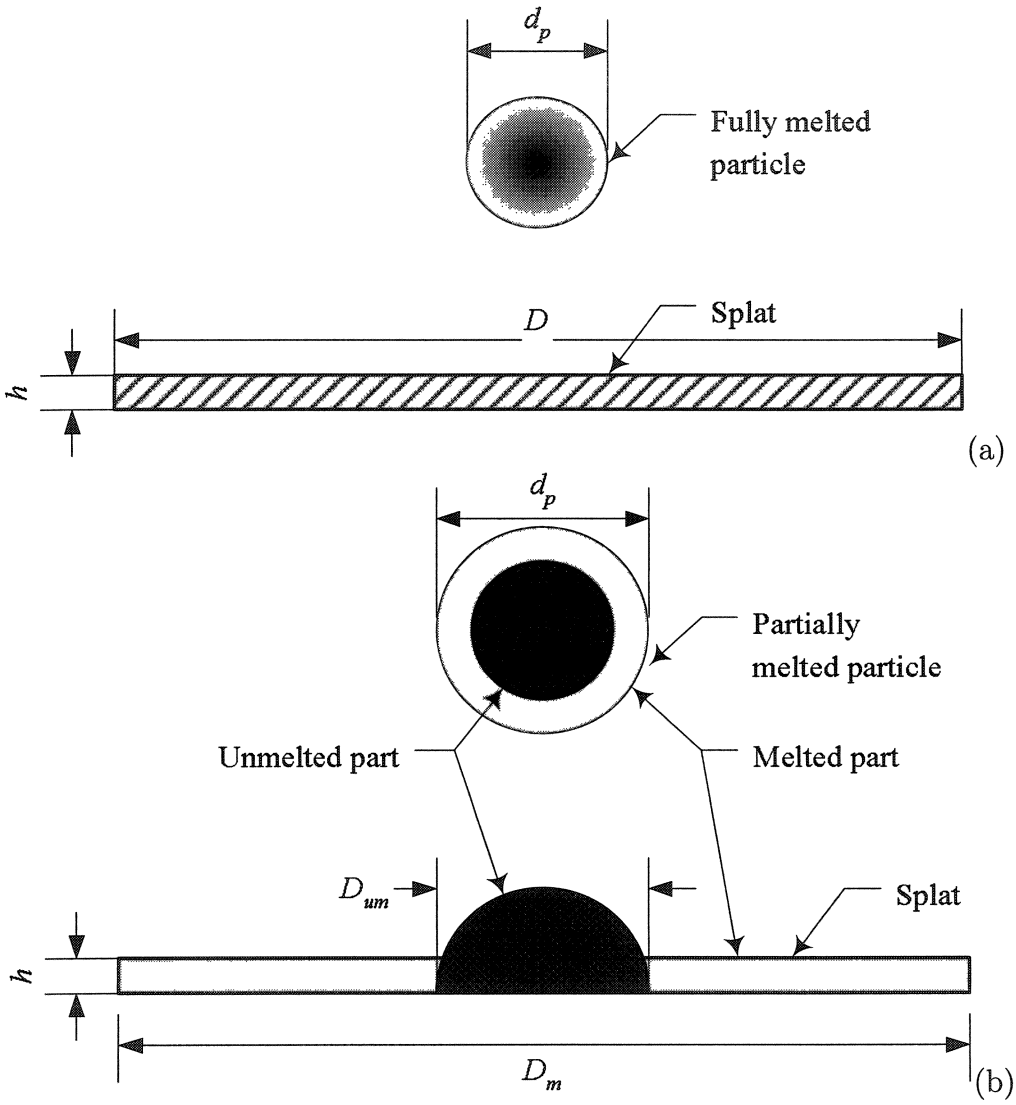


Figure 4.1: Deformation of (a) fully melted particle and (b) partially melted particle upon impact on the substrate.

coating microstructure based on their experimental investigations. Five major types of pores are classified (see Figured 4.2). The first one is a macro-pore type, whose size is comparable to the droplet size. It is primarily formed in the vicinity of solidified particles, unmelted or partially melted particles as a result of unfree spreading of subsequent droplets around these slightly flattened particles. The remaining four types of pores are all of micro-pore type, whose size is much smaller than the size of the droplets. Specifically, they are formed by: (1) solidification of voids caused by droplet/droplet and droplet/liquid-surface-layer interactions; (2) separation of liquid from the solid/liquid interface or liquid ejection or rebounding (detached liquid may entrap voids); (3) presence of cavities in droplets before impact; and (4) extraneous inclusions and dispersoids (e.g., carbides, nitrides and oxides) that may be present in droplets. The occurrence of each mechanism depends on the processing conditions. For example, when the degree of melting of the particles at impact is low and there are many solid particles in the sprayed powder at the point of impact on substrate, the first two mechanisms may be dominant. When the deposition layers are thin and the resultant rate of heat extraction in the deposited material is high, mechanism 3 becomes important. If there is a large amount of extraneous particles in the droplets, mechanism 5 will be significant. Because the spray powder used in the current study is nickel, the powder particles are dense and it can be assumed that there is no reaction of carbides or oxides inside them. Therefore, pores formed by mechanisms 4 and 5 can be neglected. Mechanisms 1, 2 and 3 will be included in the microstructure model and their relative importance will vary depending on the operating conditions.

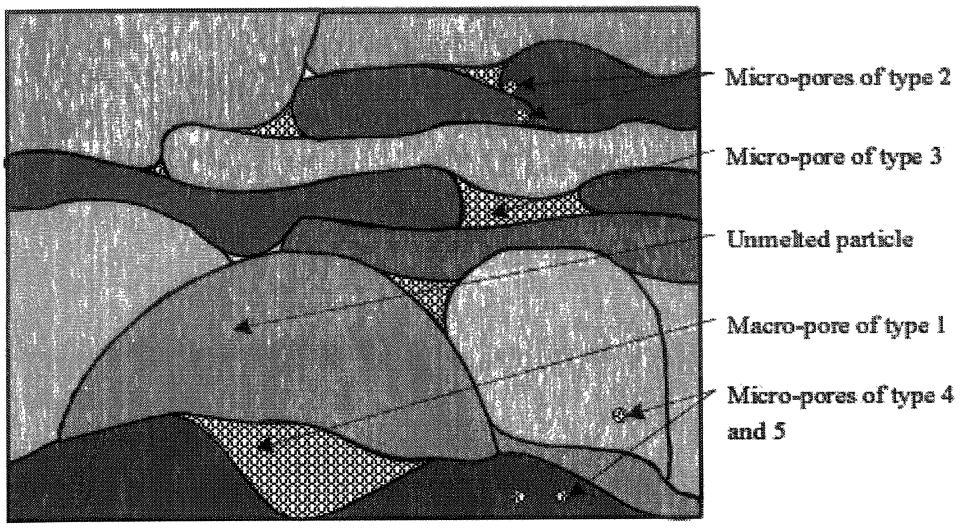


Figure 4.2: Schematic of the five types of pores.

4.2.3 Surface roughness

The roughness of a coating surface is another important factor that affects coating quality. A smooth surface can enhance the coating performance in terms of abrasion, wear, and corrosion resistance. In this work, the roughness is defined as the arithmetic mean of the absolute difference between the surface height of each gird and the average surface height:

$$R_a = \frac{\sum_{i=1}^{n} |h(i) - h_m|}{n} \tag{4.4}$$

where R_a is the roughness, n is the number of grid points used in the model, $h(i)$ is the surface height of grid point i, and h_m is the average surface height calculated by using the expression $\sum_{i=1}^{n} h(i)/n$.

The surface roughness is primarily dependent on the substrate properties as well as the particle size and chemical and physical states of the particles at the point of impact on the substrate. This work considers that the substrate is smooth and does not account for the effect of substrate roughness on the coating properties.

However, it should be noted that the substrate surface is usually roughened before coating processing. Such a treatment can increase the bonding strength between the thermally sprayed coating and the substrate. Mellali *et al.* [99] have concluded that the particle adhesion/cohesion on the surface increases with substrate roughness at least for the well-molten particles.

4.3 Computer simulation of coating formation

Because of the polydisperse nature of the powder size distribution and the stochastic nature of the deposition process, a stochastic simulation method, which is based on random number generation and rule-based modeling of coating formation, is used to explore the particle behavior in the deposition and coating formation processes. In this section, the modeling procedure, coating growth rules, and modeling settings will be presented. While the proposed model will be applied to a coating sprayed by the Diamond Jet hybrid HVOF thermal spray process, the modeling methodology is applicable to coatings sprayed with other HVOF thermal spray processes.

4.3.1 Simulation procedure

The procedure followed for the simulation of coating microstructure is based on the sequential modular method, which is shown in Figure 4.3. At the beginning of each simulation run, the process operating conditions (such as the mass flow rate of oxygen, fuel and air) and the particle size distribution parameters are specified. After the initialization, the simulation repeats a process in which individual particles hit on the surface of the coating, until the coating thickness reaches the desired set-point value. The size of each particle is chosen by using a random number generator according to a lognormally-distributed particle size distribution of the following form [27]:

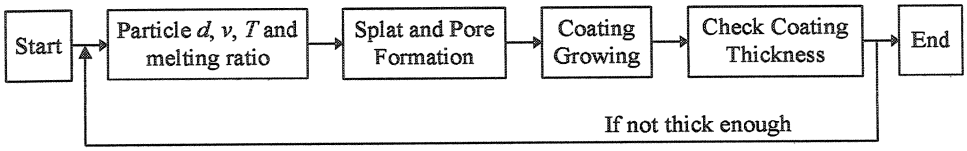


Figure 4.3: Modeling procedure for coating microstructure.

$$f(d_p) = \frac{1}{\sqrt{2\pi}\sigma d_p} \exp\left[-\frac{(\ln d_p - \mu)^2}{2\sigma^2}\right] \tag{4.5}$$

where $f(d_p)$ is the size distribution function, μ and σ^2 are two dimensionless parameters corresponding to the mean and the variance of $\ln d_p$, which obeys the normal distribution. For particles that are lognormally distributed, μ and σ can be determined by the following formulas:

$$\begin{aligned} \mu &= \ln \sqrt[3]{d_{10} d_{50} d_{90}} - 1.831 \left(\ln \sqrt{\frac{d_{90}}{d_{10}}}\right)^2 \\ \sigma &= 0.781 \ln \sqrt{\frac{d_{90}}{d_{10}}} \end{aligned} \tag{4.6}$$

where d_{10}, d_{50} and d_{90} are three characteristic diameters which can be obtained experimentally [77].

Once the particle size is determined, the particle velocity, temperature and melting ratio at the point of impact on the substrate are calculated by using the HVOF thermal spray process model developed in Chapter 3 [87]. The hitting position of the particle on the substrate is also determined by a random number. The program then simulates how each individual particle hits on the substrate and forms a splat. For the simulation of splat accumulation, we consider that the coating formation process is a sequence of independent discrete events of each individual particle hitting on the previously formed coating layer. After all the parameters of a particle before hitting the previously deposited coating layer, such as the melting ratio, the flattening ratio etc., are determined, the particle is added to the already-formed coating layer

based on certain rules, which will be discussed in subsection 4.3.2 below. When the coating thickness reaches its set-point value, the program saves the configuration of the simulated coating section and calculates the coating porosity, surface roughness and deposition efficiency. The deposition efficiency is defined as the ratio of the volume of particles deposited on the substrate to the total volume of particles sprayed by the HVOF process.

To increase the efficiency of the computation, the model only simulates the cross section of the coating that is perpendicular to the substrate, i.e., simulation of coating growth in two dimensions. The point of impact of a particle on the substrate is determined by two random variables, corresponding to its two dimensional position on the coating surface. The first one represents its position in the x-coordinate (x_p), calculated from a reference point on the simulated section to the center of the splat. The second one stands for its position in the y-coordinate (y_p), calculated from the position where the splat is cut by the cross section to the center of the splat (see Figure 4.4). Specifically,

$$\begin{cases} x_p &= uL + L/2 \\ y_p &= wD \end{cases} \tag{4.7}$$

where u and w are two independent and uniformly distributed random variables in the interval [-0.5, 0.5], L is the length of the simulated coating section and D is the diameter of the splat. Note uniformly but not normally distributed variables are used to describe splat position because the thermal spray gun may move in general back and forth. After the point of impact of a particle on the substrate is determined, the splat is added on the previously deposited coating layer and pores may be formed, depending on the conditions of the previously-deposited coating layer.

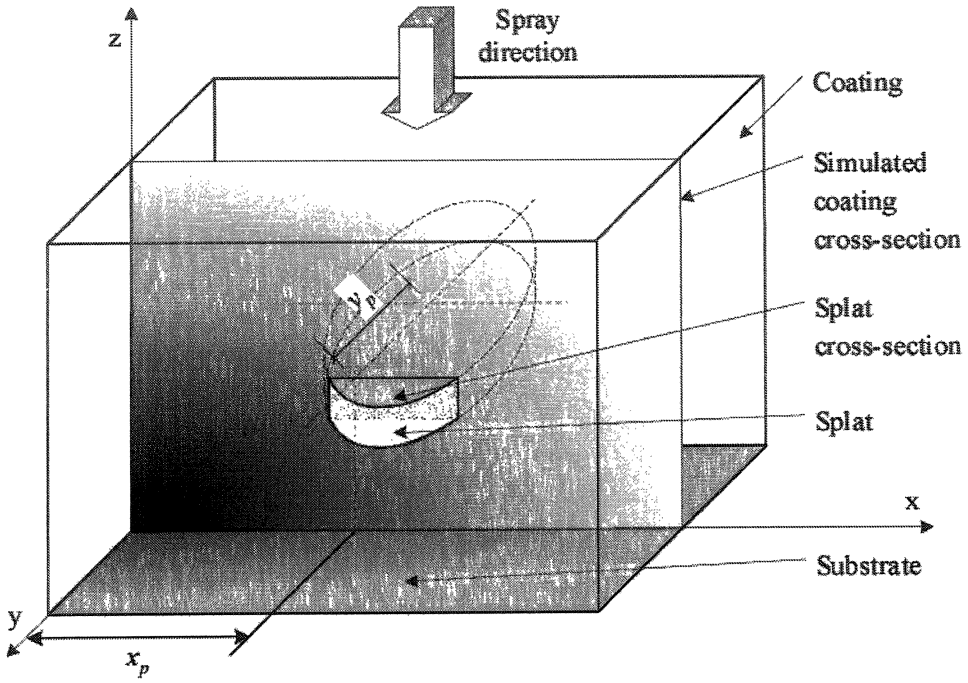


Figure 4.4: Sketch of the splat position used in the model.

4.3.2 Coating growth rules

There are several different events which may take place when a particle hits on the substrate. The occurrence of each event depends on the physical state of the sprayed particle and the condition of the previously deposited layer at the hitting point. The rules governing the geometric shape of the splats and the formation of the pores are described as follows.

1. If a particle at the point of impact on the substrate is partially melted, the unmelted part will form a hemisphere on the previously deposited layer and the melted part will form a ring around this hemisphere (see Figure 4.1(b)). Furthermore, if the unmelted part of the particle hits at the point of the previously deposited layer that is formed by an unmelted particle, it will bounce off, and a hole will be formed in the center of the disk. Otherwise, the hemisphere will hit

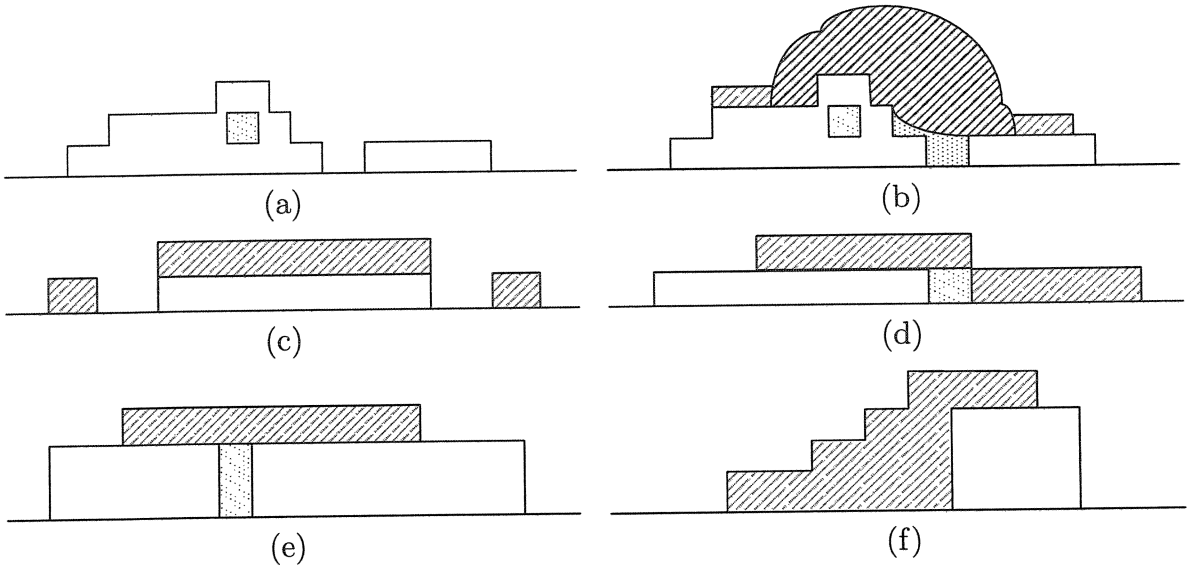


Figure 4.5: Splat formation rules (shaded area corresponds to added splat and dotted area corresponds to pore formation) - (a) coating surface before impact of partially melted particle, (b) coating structure after impact of partially melted particle, (c) splat breaking up, (d) pore formation at the corner of a step, (e) pore formation in a gap and (f) splat pileup on a step.

on the surface and macro-size pores may form under the hemisphere. Figures 4.5(a) and (b) show the coating layer before and after a partially melted particle hits on the surface. It is shown that one pore is formed as the unmelted particle covers the gap. This kind of pore formation is consistent with the first type of pore formation mentioned in the subsection 4.2.2.

2. When a particle hits the substrate, the melted part will fit on the surface as much as possible. The splat will spread outwards, after the impact region of the particle fits on the surface, without forming a new pore. The impact region is determined by the size and the cross-sectional position of the particle.

3. During the splat spreading, if the splat comes to a vertical drop, the program will calculate the ratio of the splat that has not been settled down. If the step

does not continue with a gap (shown in Figure 4.5(e)) that can be covered by the splat, the splat will break (Figure 4.5(c)) or cover the corner at the step (Figure 4.5(d)) according to the ratio and the height of the step. Otherwise, the gap will be covered by the splat (Figure 4.5(e)), and a pore will be formed. Pores formed in this way fall into the second and third categories of pore formation mechanism mentioned in the subsection 4.2.2.

4. If the splat encounters a dead end (Figure 4.5(f)), it first fills the available space, and then it flows over the outer surface if the volume of the remaining splat is big enough.

To successfully simulate the coating microstructure, several important parameters are used in these rules. According to the situations that these parameters are used, there are 5 groups of parameters: (a) two parameters are used to determine how deep the unmelted part of the particle will hit into the gap (Figure 4.5(b)) based on the width of the gap, and therefore, these two parameters decide the size of a macro-sized pore; (b) in the third rule, when a splat meets a vertical drop step (Figure 4.5(c) and (d)), the ratio of the step height to the splat thickness determines whether the splat will break; (c) if the splat breaks when it meets a vertical drop step (Figure 4.5(c)), the distance that it breaks away is determined by an equation (which involves three adjustable parameters) that accounts for the thickness of the splat, the length of the splat that breaks and the height of the step; (d) if the splat does not break when it meets a vertical drop step (Figure 4.5(d)), a pore will form at the corner of the step (the size of the pore is decided by a parameter, which is the slope of the splat covering the corner); (e) in the fourth rule, a necessary parameter is the slope of the bulk formed by the splat at the dead end (Figure 4.5(f)). All these parameters were carefully selected based on the consideration of their physical meaning and were

tuned to provide results of important coating variables (like coating porosity) which are consistent with the available experimental results [43, 54].

Based on these parameters, these four basic rules control how each particle hits and deforms on the substrate to form a lamellar-structured coating. Based on the simulated coating structure, the coating porosity and roughness can be calculated. Specifically, the coating porosity P is calculated by the following equation:

$$P = \frac{n_1}{n_1 + n_2} \tag{4.8}$$

where n_1 is the number of void grids under the simulated coating surface, and n_2 is the number of grids occupied by splats under the simulated coating surface. The deposition efficiency η is calculated by the following equation:

$$\eta = \frac{V_1}{V_1 + V_2} \tag{4.9}$$

where V_1 is the volume of particles that are added to the coating, and V_2 is the volume of solid particles that are bouncing off by hitting on the surface formed by unmelted particles. Note that all partially-melted and fully-melted particles stick onto the surface independently of the nature of the coating layer at the hitting position.

4.3.3 Simulation settings

The simulation model is based on the operation of the Diamond Jet Hybrid gun, whose geometric configuration can be found in the Chapter 3 [87]. Table 4.1 lists the baseline operating conditions (recommended by the manufacturer), typical particle size distribution and the dimension of the simulated coating section. Especially, the three characteristic diameters (d_{10}, d_{50} and d_{90}) are listed as a reference for the lognormal distribution of the powder particles. When particles with different sizes are used

Table 4.1: Operating conditions for the Diamond Jet hybrid thermal spray process in the simulation.

Flow rate of oxygen, O_2	=	578	$scfh$
Flow rate of propylene, C_3H_6	=	176	$scfh$
Flow rate of air, Air	=	857	$scfh$
Spray distance, L	=	245	mm
Characteristic diameter, d_{50}	=	45	μm
Particle injection velocity, v_{p_0}	=	20	m/s

Table 4.2: Thermophysical properties of powder particles.

Powder	=	Nickel	
Density	=	8.9×10^3	kg/m^3
Melting temperature	=	1727	K
Heat capacity	=	471	$J/kg/K$
Latent heat of melting	=	3×10^5	J/kg
Liquid kinematic viscosity	=	6.2×10^{-7}	m^2/s

in the simulation, these three characteristic diameters are varied proportionally, i.e. only one characteristic diameter is needed to describe a certain lognormal distribution of particles. Therefore, we only mention d_{50} to characterize the size distributions of the various powder used in this work. The physical properties of the particles used for coating formation are listed in Table 4.2.

The model simulates a section of the coating. The section is assumed to be a rectangle and is discretized by a 8192 $\times$ 4096 mesh. The size of each grid in the mesh is 0.1 $\times$ 0.1 μm. Such a grid size is around half of the height of the splat which is formed by a fully melted particle, whose diameter is 40 μm, under the baseline operating conditions. According to the mathematical model describing gas and particle behavior [87], particles whose size is smaller than about 8 μm are mostly fully unmelted. Based on this fact, a grid size of 0.1 μm is small enough to carry

out a simulation of coating growth with reasonable computing power. Each splat formed by a particle hitting on the previously formed coating surface is discretized to a combination of grids, and is placed on the coating surface by following certain rules (see section 3.2). The splat with a thickness less than 0.1 μm is rounded to 0.1 μm. Eq. 4.10 shows the relationship between the ratio of splat diameter (D) to thickness (h) and the flattening degree (ξ):

$$\frac{D}{h} = 1.5\xi^3 \tag{4.10}$$

Usually, ξ is around 8 according to our calculations, which means that the splat diameter D is around 768 times the splat thickness h. Considering such a high particle deformation, a smaller grid size will not be able to substantially improve the accuracy of the computed results, this point has been verified by running representative simulations with different grid size.

4.4 Simulation results and discussions

4.4.1 Microstructure of coatings made of particles of different molten states

Under normal operating conditions, the gas temperature at the exit of the gun is around 2000 K, which is several hundred Kelvin higher than the melting point of the nickel particle. However, simulation results [87] show that even at such a high temperature, only particles in a certain size range, about 10 - 40 μm, can be fully melted, while others, either too small or too large, are in a coexistence state of liquid and solid or even in a solid state at the point of impact on substrate. The very small particles, although they may be totally melted during flight, are not in a fully molten state at impact because they are cooled down quickly in the free jet

due to the gas temperature decay and their small thermal inertias. Experiments of Zhang et al. [141] also shows that particles at the point of impact on the substrate may be in different molten states (fully melted, partially melted or solid) due to different sizes and different trajectories in the HVOF thermal spray process. Figure 4.6 shows the simulated configuration of the coating sections that are perpendicular to the substrate, for particles with different molten states. The simulated section in Figure 4.6(a) is formed by particles that are all fully melted (ideal case, in which the particle velocity is calculated based on the baseline operating conditions, and the particle melting ratio is assumed to be one), while the one in Figure 4.6(b) is formed by particles with nonuniform molten states (some particles may be partially melted or even unmelted, in which case the particle velocity, temperature and degree of melting are calculated based on the baseline operating conditions). The ideal lamellar structure of the thermally sprayed coating can be easily seen in Figure 4.6(a). However, such a lamellar structure is disturbed by the unmelted part of the particles, as shown in Figure 4.6(b). It is also shown that large unmelted particles affect the coating surface dramatically, thus, leading to high coating roughness. To show the pore size and distribution inside of the coating, we draw the Figure 4.6(b) again by ignoring the difference between each splat; the result is shown in Figure 4.6(c). The white dots in Figure 4.6(c) represent the pores. He *et al.* [52] and Totemeier *et al.* [131] have observed similar coating microstructures in their experiments. It can be concluded from this comparison that the particle melting behavior plays a very important role in the coating microstructure evolution and should be accounted for in the simulation model.

The effect of particle melting behavior on the coating porosity was studied by analyzing the simulation results. Figure 4.7 shows the comparison of the coating

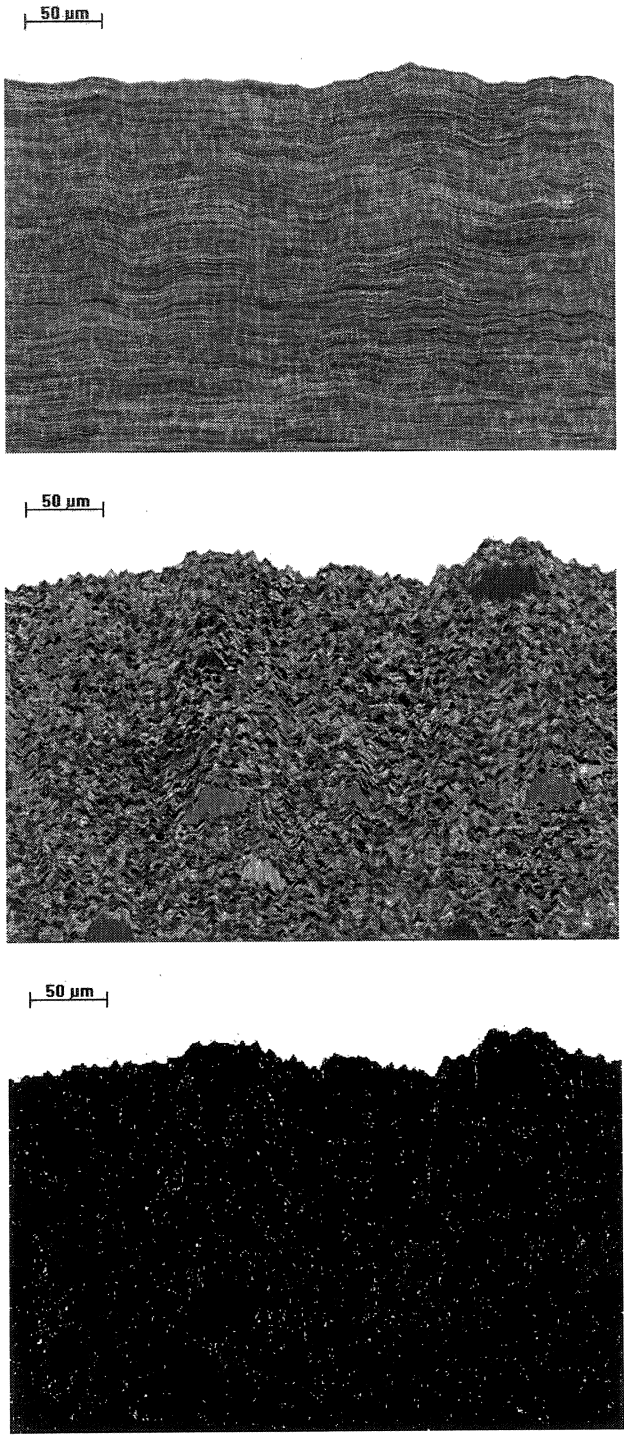


Figure 4.6: Simulated coating section using fully-melted particles and partially-melted particles.

porosity simulated by two different models. One model considers the particle melting behavior, i.e. the melting ratio of each particle is calculated by a mathematical model [87] considering the particle size and operating conditions. Another model assumes that all particles are fully melted, while other parameters, such as the particle velocity, are calculated by the same mathematical model [87]. The comparison shows the importance of considering the particle melting behavior, which has not been included in previous coating simulation models [72, 103, 42]. For the model considering that all the particles are fully melted, the coating porosity decreases monotonically as the particle size (d_{50}) increases, shown as the dashed line in Figure 4.7. However, the simulated coating porosity accounting for the particle melting behavior will decrease first and then increase, as the particle size (d_{50}) increases, shown as the solid line in the same figure. The existence of a minimum porosity can be explained by the existence of the maximum particle melting ratio for particles with different size, Figure 4.8. Several experimental studies [54, 43] have proved that a better particle melting condition can lead to a lower coating porosity. It is also found that the error band increases as bigger particles are used in the simulation. Such a phenomenon can be explained by the formation of more macro-pores when larger particles are used for the coating formation. Simulations show that the number of macro-pores is usually less than 50 inside one simulated coating section. Under operating conditions in which macro-pores strongly influence the coating porosity (e.g. large particles are used for the coating formation), a small change of the number of macro-pores will strongly influence the coating porosity.

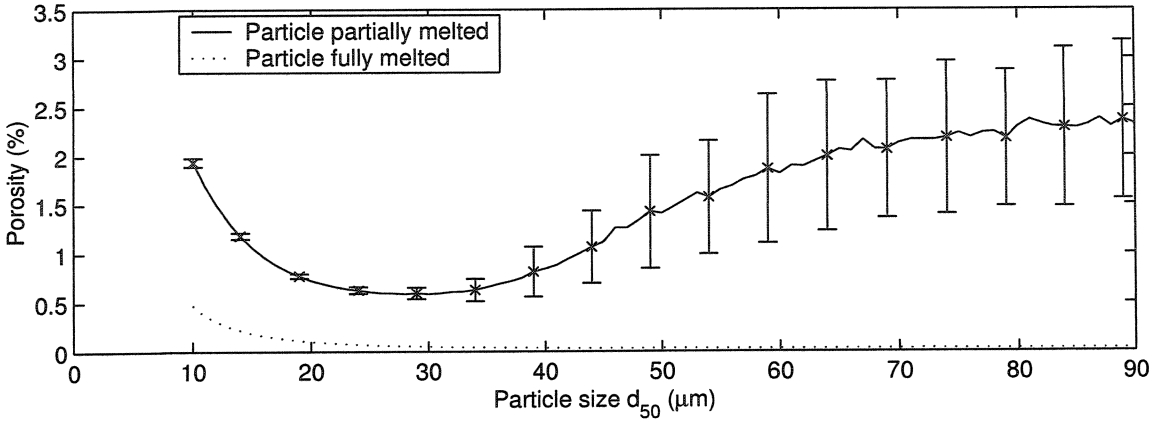


Figure 4.7: Comparison of simulation results for fully melted and partially melted particles under baseline operating conditions.

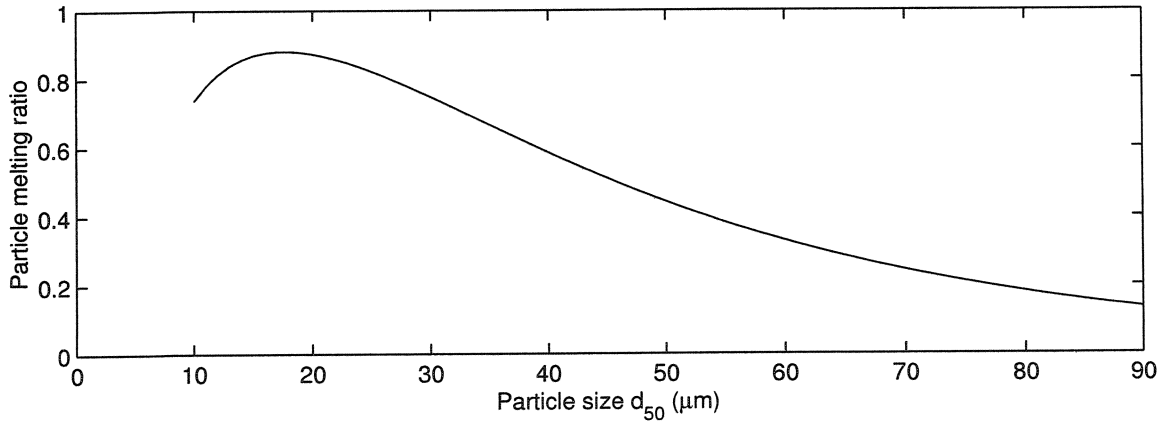


Figure 4.8: The melting ratio of particles with different size under baseline operating conditions.

4.4.2 Influence of operating conditions on coating properties

In addition to providing useful insight into coating formation and growth, the developed model is used to make a comprehensive parametric analysis, which allows us to systematically characterize the influence of operating conditions and the effect of particle size on the coating porosity and deposition efficiency. The parametric analysis of macroscopic operating conditions on coating microstructure is based on the "one-factor-at-a-time" method, i.e. each time only one processing parameter is varied from 55% to 150% of its baseline condition value while the other parameters are fixed. The influence of particle size on coating microstructure is also studied by varying powder size distribution parameters, e.g. d_{50} (whose corresponding cumulative weight function is 0.5), from 20 to 60 μm. The simulated results in the following figures are the average of over sufficient repeated runs of simulations performed under the same operating conditions to obtain a convergent average value and make the variance small enough. The effect of variations of the process parameters is compared with available experimental data.

Effect of oxygen flow rate

Figure 4.9 shows the influence of oxygen flow rate and particle size on the particle melting ratio, coating porosity, surface roughness and deposition efficiency. Figure 4.9(a) reveals that the particle melting ratio increases significantly and becomes almost flat when the oxygen flow rate increases from its lower bound (318 $scfh$) to its upper bound (867 $scfh$); this behavior can be explained by the discussion in Chapter 3 or [87]. When the oxygen flow rate is small, the equivalence ratio is very far away from its optimal value. As the oxygen flow rate increases, the equivalence ratio becomes close to its optimal value, and the combustion pressure increases (due

to an increase in the total mass flow rate of the gas) at the same time. This leads to an increase of the gas temperature, and therefore, the particle temperature goes up sharply. However, after the oxygen flow rate exceeds a critical value in which the equivalence ratio departs significantly from its optimal value, the gas temperature slightly decreases. This is because the effect of an increase in the combustion pressure partially compensates for the effect of a decrease in the equivalence ratio. Accordingly, the coating porosity decreases very fast initially, and then approaches a nearly constant value as the oxygen flow rate spans its entire range of variation, for particles of small size (Figure 4.9(b)). This implies that for small particles, a good particle melting condition (i.e., higher degree of particle melting) helps to decrease coating porosity. For particles of large size, the coating porosity is large, which can be explained by the low melting ratio of large particles at the point of impact on substrate, which results in big pores formed in the coating structure. We should also notice the effect of particle size on the coating porosity. Figure 4.9(b) shows that a coating formed by a powder with $d_{50} = 30\ \mu m$ has a lower porosity than the coating formed by a powder with $d_{50} = 20\ \mu m$. The roughness of the coating increases with the particle size, but it is not affected much by the oxygen flow rate, as shown in Figure 4.9(c). This is because the coating roughness is controlled by the unmelted part of the particles, whose amount does not change much when the oxygen flow rate changes. The effect of oxygen flow rate on the deposition efficiency is similar to the one on particle melting ratio, as shown in Figure 4.9(d). When the oxygen flow rate is less than 500 $scfh$, higher oxygen flow rates and smaller particle size lead to higher degree of particle melting and higher deposition efficiency.

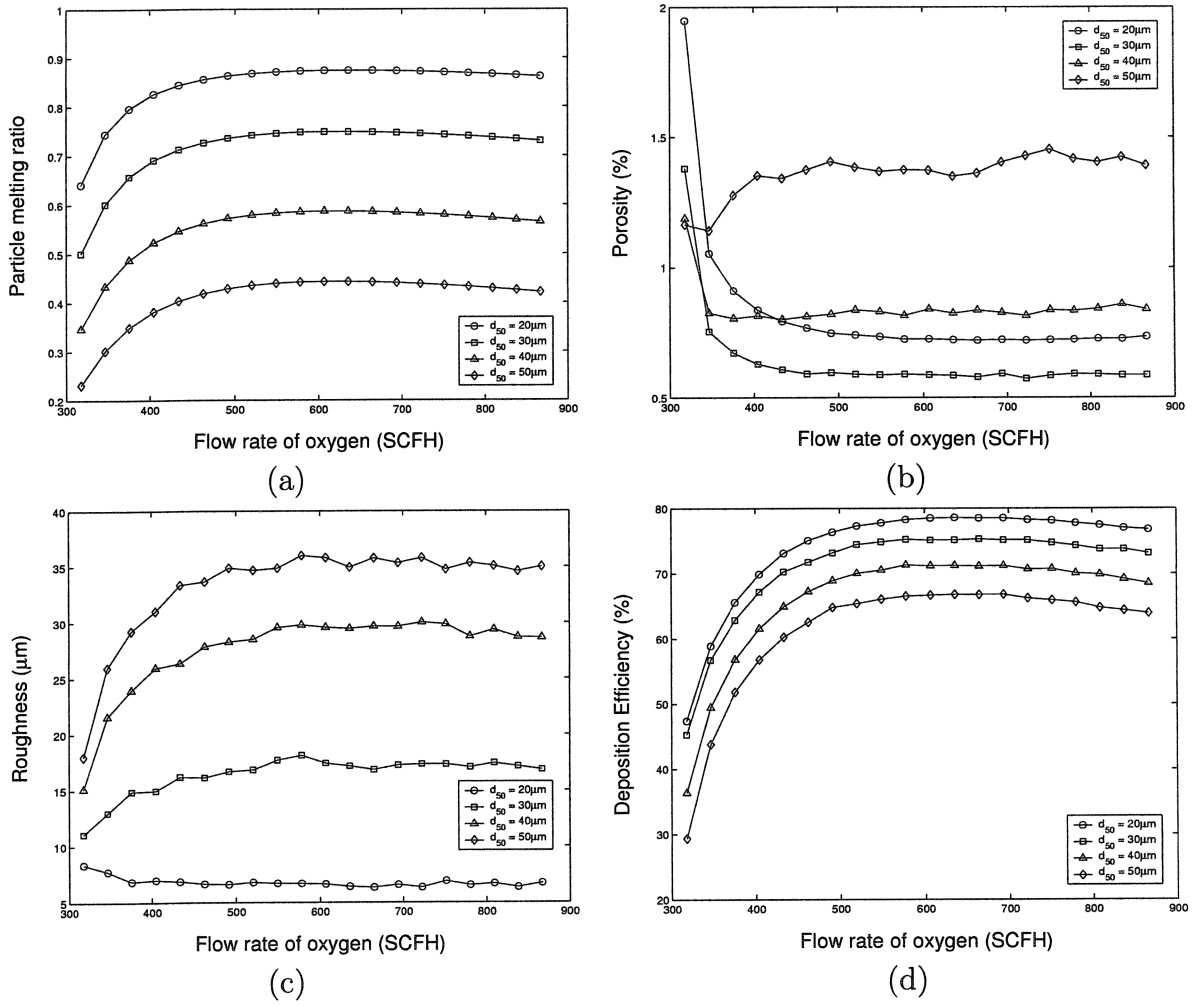


Figure 4.9: The effect of oxygen flow rate on (a) particle melting behavior, (b) coating porosity, (c) surface roughness and (d) deposition efficiency.

Effect of fuel flow rate

Compared to the influence of oxygen flow rate, variation in the fuel flow rate has more obvious effects on coating properties, as shown in Figure 4.10. For example, a peak in the fuel flow rate vs. particle melting ratio can be clearly seen in Figure 4.10(a). This is because the total mass flow rate does not increase much in the range of interest (because the flow rate of fuel is small compared to those of oxygen and air) and the gas temperature is only a function of the equivalence ratio. For particles of different size, the maximum melting ratio occurs when the fuel flow rate is about 210 $scfh$, whose corresponding equivalence ratio is about 1.2. Accordingly, as the fuel flow rate increases, the coating porosity decreases first and then increases, and the lowest coating porosity is achieved when the fuel flow rate is around 210 $scfh$. This fact further substantiates the point that a good particle melting condition (i.e., high degree of particle melting) is beneficial to achieve a lower coating porosity. However, it is not the only factor affecting the coating porosity. Figure 4.10(b) shows that a coating formed by a powder with $d_{50} = 30\ \mu m$ has a lower porosity than a coating formed by a powder with $d_{50} = 20\ \mu m$, although smaller particles have better melting condition than bigger ones. This is similar to the observation in Figure 4.9(b). Once again, the roughness of the coating increases with the particle size, and the relationship between the coating roughness and the fuel flow rate is not so strong (Figure 4.10(c)). Consistent with the variation of particle melting ratio, the deposition efficiency is shown to increase first and then decrease as the fuel flow rate increases (Figure 4.10(d)).

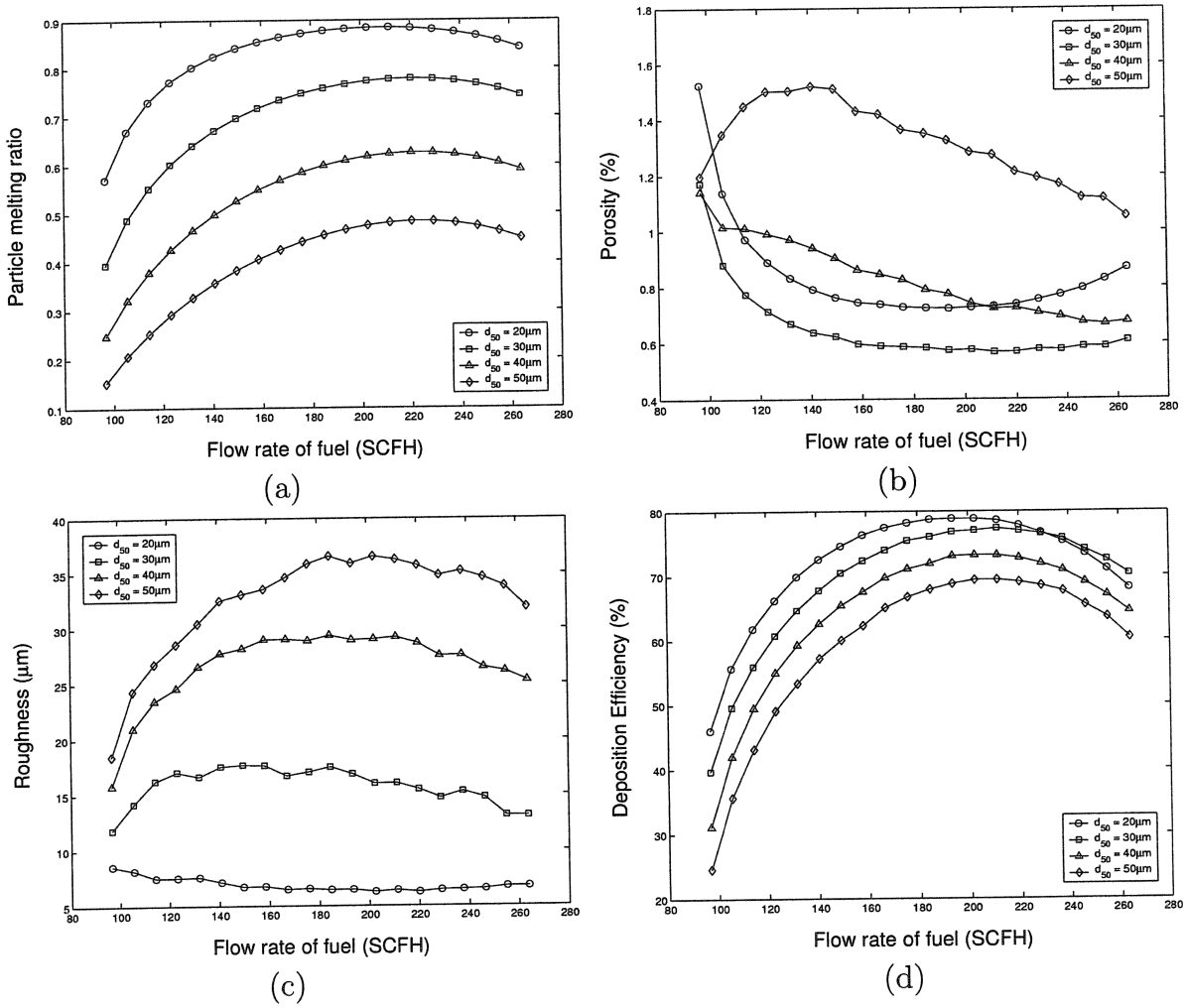


Figure 4.10: The effect of fuel flow rate on (a) particle melting behavior, (b) coating porosity, (c) surface roughness and (d) deposition efficiency.

Effect of air flow rate

The effect of air, which partially functions as coolant in the HVOF thermal spray process, can be seen in Figure 4.11. As the air flow rate increases, the particle melting ratio at the point of impact on the substrate decreases (Figure 4.11(a)). Correspondingly, the porosity of coatings deposited by different size particles increases, as shown in Figure 4.11(b). Regardless of the change of air flow rate, the coating roughness is almost proportional to the particle size (Figure 4.11(c)). A higher air flow rate will lead to a lower deposition efficiency (Figure 4.11(d)). Moreover, an increase in the particle size will decrease the deposition efficiency.

Effect of total mass flow rate

The effect of total mass flow rate can be seen in Figure 4.12. According to Figure 4.12(a), the relative ratio of fuel, oxygen and air flow rate is kept at the baseline condition, while the total mass flow rate varies from 50% to 150% of its baseline condition. For different particle size, the particle melting ratio changes almost linearly with the total mass flow rate. Such a dependence is different from the corresponding effect of the fuel flow rate and of the oxygen flow rate. The increase in degree of particle melting is caused by an increase in the combustion pressure, and therefore, gas temperature [87]. Note that as the total mass flow rate increases, the particle velocity at the point of impact will also increase [87]. From Figure 4.12(b), it can be seen that the coating porosity decreases slowly as the total mass flow rate changes. This is caused by an increase in both degree of particle melting and impact velocity. The deposition efficiency increases dramatically as the total mass flow rate increases. Again, the coating formed by powder particles with mean size $d_{50} = 30\ \mu m$ has the lowest porosity and almost the highest deposition efficiency, as shown in Figure

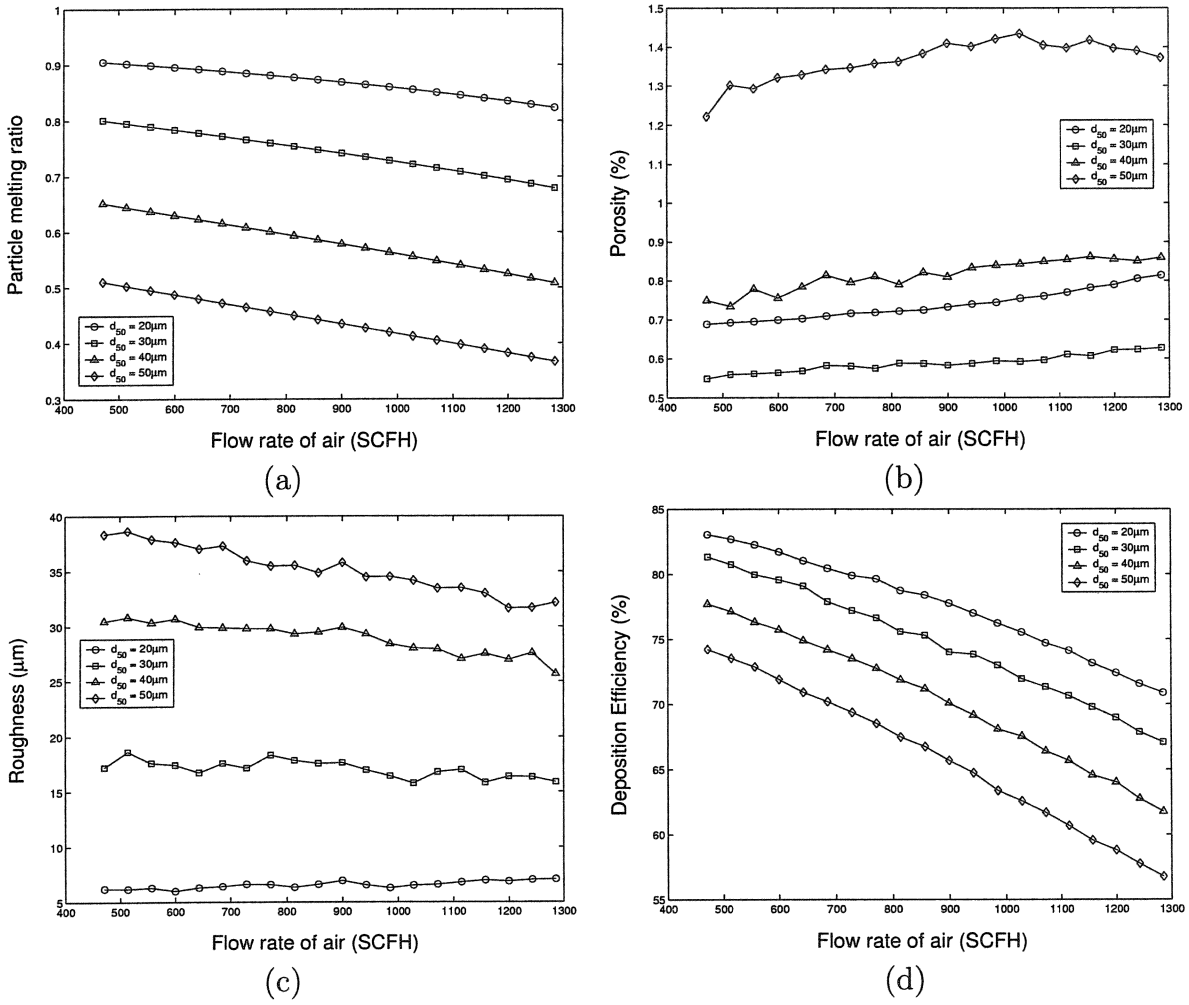


Figure 4.11: The effect of air flow rate on (a) particle melting behavior, (b) coating porosity, (c) surface roughness and (d) deposition efficiency.

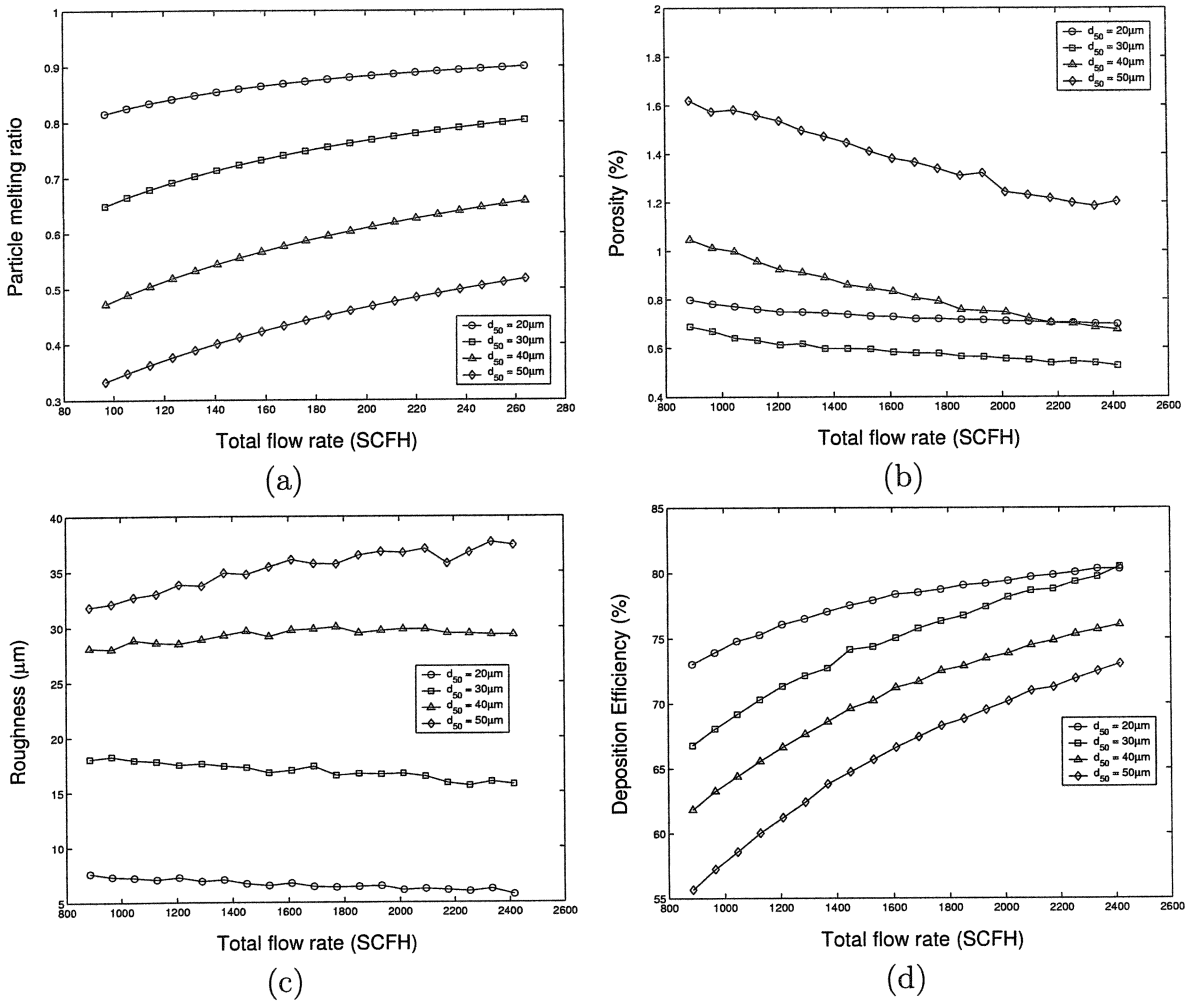


Figure 4.12: The effect of total mass flow rate on on (a) particle melting behavior, (b) coating porosity, (c) surface roughness and (d) deposition efficiency.

4.12(d). Also, the coating roughness is mainly a function of the particle size, and is almost independent of the total mass flow rate.

Effect of spray distance

The spray distance has the most complicated effect on the particle melting behavior and coating porosity. Figure 4.13(a) shows that the particle melting ratio decreases as the spray distance increases. Furthermore, the melting ratio of smaller particles

drops much faster than bigger ones. For instance, the melting ratio of particles with $d_{50} = 20\ \mu m$ becomes even lower than that of the bigger particles ($d_{50} = 40\ \mu m$) at large spray distances. As a result, the coating porosity generally increases as the spray distance increases, as shown in Figure 4.13(b). Among all particle sizes of interest, the porosity of coatings produced by particles with $d_{50} = 20\ \mu m$ increases the fastest as the spray distance increases, and becomes even the largest at a large spray distance. Figure 4.13(c) shows that the coating roughness is high at small spray distances, when the particle melting ratio is high, and decreases as the spray distance increases, especially for large particles. One possible reason for this behavior is that the deposition efficiency is less than 50% for large spray distances (shown in Figure 4.13(d)). Such a low deposition efficiency lead to the result that the increase of the amount of unmelted particles bouncing off the surface outweighs the increase of the amount of unmelted particles caused by the decrease of particle melting ratio. Since only the melted part of particles and small unmelted particles are deposited on the surface, small coating roughness can be achieved at long spray distances. Such a phenomenon can also be observed in Figure 4.9(c) and 4.10(c). When the deposition efficiency is less than 50% , which is caused by low flow rate of oxygen and fuel, the coating roughness is also considerable low. Figure 4.13(d) also shows that the deposition efficiency decreases very fast because the particle melting ratio decreases significantly as the spray distance increases. Specifically, comparing the curves for small particles ($d_{50} = 20\ \mu m$) in Figure 4.13(a) and 4.13(d), we can see that at large spray distances, the deposition efficiency for particles with $d_{50} = 20\ \mu m$ becomes the smallest among all the particles of interest and their melting ratio is even less than that of larger particles. Such a result substantiates the conclusion that the particle melting condition has the strongest effect on the deposition efficiency.

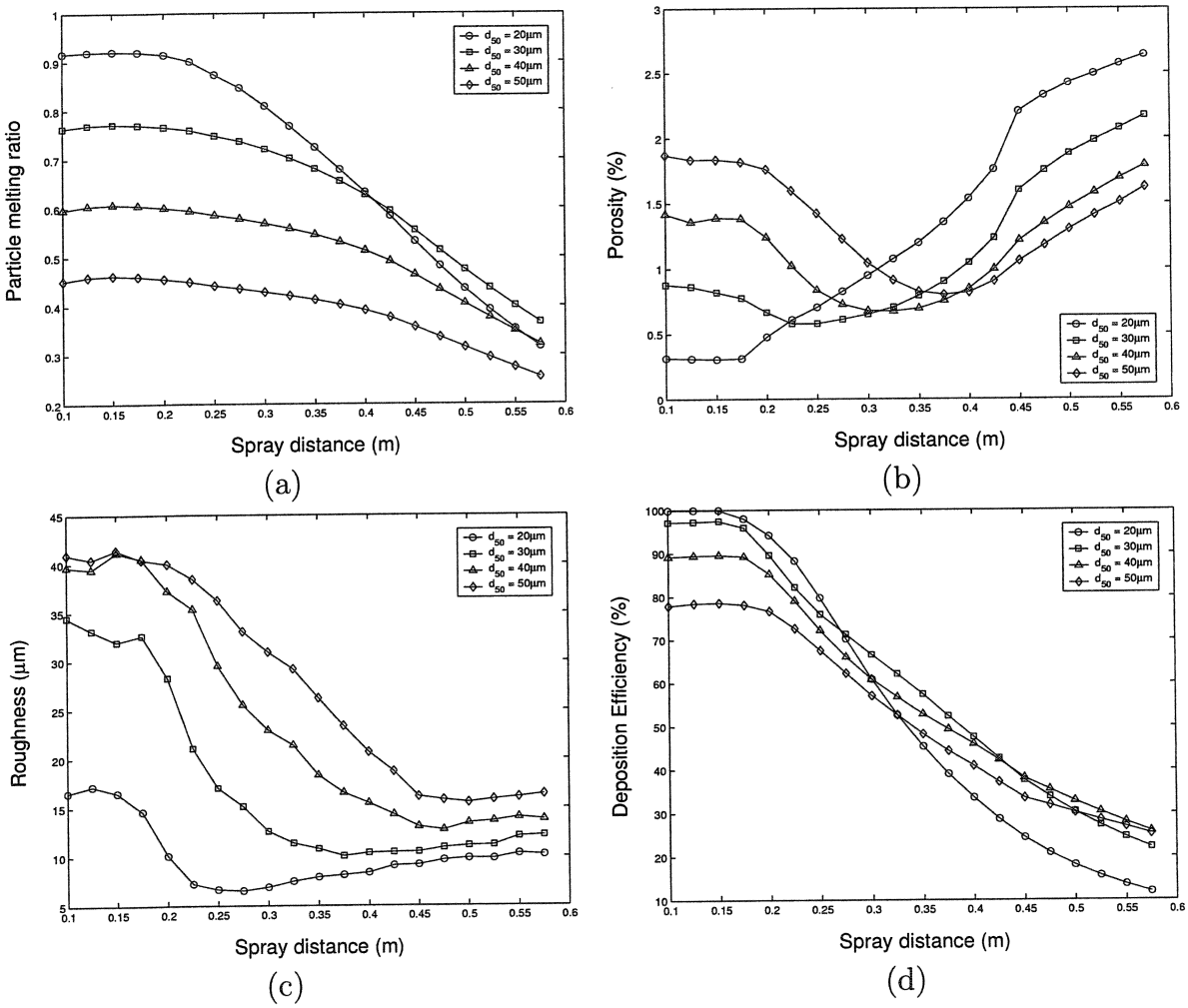


Figure 4.13: The effect of spray distance on on (a) particle melting behavior, (b) coating porosity, (c) surface roughness and (d) deposition efficiency.

Table 4.3: Experimental systems for parametric analysis.

Reference	HVOF System	Fuel	Powder	Size (μm)
Hearley et al. [54]	UTP TopGun	Propylene	NiAl	15-45
de Villers Lovelock et al. [30]	JP-5000	Kerosene	WC-17%Co	16-45
Gil and Staia [43]	JP-5000	Kerosene	NiWCrBSi	22-66
Lih et al. [89]	A3000	Propylene	CrC/20NiCr	
Lugscheider et al. [96]	Diamond Jet Hybrid	Hydrogen or Propane	MCrAlY	
Gourlaouen et al. [47]	Diamond Jet Hybrid	Propylene	Stainless Steel	
Swank et al. [126]	JP-5000	Kerosene	Inconel 718	15-63

4.4.3 Comparison of stochastic simulation results and experimental studies

The influence of operating conditions on coating microstructure and deposition efficiency have been experimentally studied by various groups [30, 43, 47, 54, 96, 89]. The gun type and corresponding fuel and powder used in these HVOF thermal spray processes are listed in Table 4.3. In this subsection, we attempt to put into perspective our simulation results described above with respect to the available experimental results.

The important effect of equivalence ratio (which affects to a large extent the degree of particle melting) on coating porosity has been analyzed by several experimental studies. For instance, the porosity of the inert gas atomized (IGA) NiAl coatings produced by the UTP TopGun HVOF gun is 2% when the equivalence ratio is 1.26, which is close to the optimal one [87]. When the equivalence ratio is maintained at 1.68, which is far away from the optimal one, the porosity is 2.54% (or 3.38%) as

a result of increasing fuel flow rate (or decreasing oxygen flow rate) [54]. Although the equivalence ratio is the same in the last two cases, the coating porosity is higher when the total mass flow rate is lower, which validates the conclusion in subsection 4.4.2. By conducting experiments of NiWCrBSi coating processing using a JP-5000 HVOF thermal spray system, Gil and Staia [43] pointed out that the best coating properties are achieved at an equivalence ratio between 1.1 and 1.2, which is very close to our prediction. Note although liquid fuel (kerosene) is used in this process, the relationship between the equivalence ratio and the combustion temperature (see analysis in the work of Swank et al. [125]) is very similar to the Diamond Jet hybrid HVOF thermal spray process studied in our work [87].

One of the main conclusions of our study is that a better particle melting condition (higher degree of particle melting, which occurs under a fuel-rich condition) will increase the deposition efficiency. This conclusion is substantiated by the experiments of Hearley et al. [54]. It is found from their studies that when the equivalence ratio gets close to the optimal one and the total gas flow rate increases, the deposition efficiency also increases. Sakaki and Shimizu [116] have also drawn such a conclusion based on their experiment studies. By analyzing the effects of gun size on HVOF thermal spray, they found that a higher degree of particle melting will lead to a higher deposition efficiency.

4.5 Summary

Based on the discussion of the influence of operating conditions on coating microstructure and deposition efficiency, the following main conclusions can be drawn.

1. Particle melting behavior plays a very important role in coating microstructure. A high degree of particle melting tends to achieve a low coating porosity and

a high deposition efficiency. This requires the system to be operated under a fuel-rich condition ($\varphi = 1.2$ for the Diamond Jet Hybrid thermal spray process).

2. Particle size has a significant effect on coating porosity. Particles of mean size (d_{50}) around 35 μm tend to achieve the lowest coating porosity among all the particles of interest under various operating conditions, including the fuel-rich condition. Furthermore, the larger the particle size, the higher the coating surface roughness.

In summary, the comparison of simulation results and available experimental data shows that the stochastic simulation model developed here can be used to properly predict the effects of process parameters, including the particle size, spray distance, flow rate of oxygen, fuel and air, on the microstructure of coatings produced by the Diamond Jet hybrid HVOF thermal spray process.

Chapter 5

Diamond Jet Hybrid HVOF Thermal Spray Process: Model-based Estimation and Control of Particle Velocity and Melting

This chapter[1] focuses on the feedback control of the Diamond Jet hybrid HVOF thermal spray process. Based on the modeling of gas and particle behavior and coating microstructure evolution and available experimental studies, the control problem is formulated as the one of regulating volume-based averages of the velocity, temperature and degree of melting at the point of impact on the substrate (these are the variables that directly influence coating microstructure and porosity, which, in turn, determine coating strength and hardness) by directly manipulating the flow rate of fuel, oxygen and air at the entrance of the HVOF thermal spray gun, through which the chamber

[1]Chapter 5 is based on [87, 86].

pressure and the fuel/oxygen ratio can be adjusted. A feedback control system is developed and applied to a detailed mathematical model of the process. Closed-loop simulations demonstrate that the proposed controller is effective in driving the controlled outputs (the particle velocity and melting ratio at the point of impact on the substrate) to desired set-point values and is also robust with robust with respect to disturbances in spray distance and particle injection velocity, and variations in powder size distribution.

We note that in practice, it is difficult to directly measure the degree of melting of individual particles and consequently, the average degree of melting of the entire particle size distribution. To overcome this limitation, we propose an estimation scheme to obtain real-time estimates of particle velocity, temperature and degree of melting. The proposed estimation scheme is based on the modeling equations which describe the evolution of particle temperature, velocity and degree of melting coupled with the available gas phase measurements. Then, a feedback control system, which directly uses the estimation scheme, is designed to regulate the volume-based average of the particle velocity and degree of melting by manipulating the inlet gas flow rates to the process. The proposed estimation/control structure is applied to a fundamental model of the industrial HVOF thermal spray process and its performance and robustness properties are tested through simulations.

5.1 Feedback control of HVOF thermal spray process

5.1.1 Control problem formulation and controller design for the Diamond Jet hybrid HVOF thermal spray process

Based on model predictions (see Chapters 3 and 4) and available experimental observations, the control problem for the HVOF process is formulated as the one of

regulating the volume-based averages of melting ratio and velocity of particles at the impact on substrate (these are the variables that directly influence coating microstructure and porosity) by manipulating the flow rates of propylene, oxygen and air at the entrance of the HVOF thermal spray gun. From the analysis in the previous sections, it follows that the gas momentum flux, which is approximately proportional to the drag force, and the gas temperature, whose difference between the particle temperature provides the driving force for particle heating, can be almost independently adjusted by manipulating the combustion pressure and the equivalence ratio. To develop a feedback controller that can be readily implemented in practice, the manipulation of combustion pressure and equivalence ratio is realized by adjusting the flow rate of propylene, $u_1(t)$, oxygen, $u_2(t)$, and air $u_3(t)$. Owing to the almost decoupled nature of the manipulated input/controlled output pairs, two proportional integral (PI) controllers are used to regulate the process. Specially, the controllers have the following form:

$$\begin{aligned} \dot{\zeta}_i &= y_{sp_i} - y_i, \;\; \zeta_i(0) = 0, \;\; i = 1, 2 \\ u_i' &= K_{c_i}\left[(y_{sp_i} - y_i) + \frac{1}{\tau_{c_i}}\zeta_i\right] + u_{0_i}', \;\; i = 1, 2 \\ \{u_1, u_2, u_3\} &= f(u_1', u_2', x) \end{aligned} \tag{5.1}$$

where y_{sp_i} is the desired set-point value and y_i is the value of the output obtained from the measurement system (y_1 is the volume-based average of particle velocity and y_2 is the volume-based average of particle melting ratio). u_1' is the combustion pressure and u_2' is the equivalence ratio. K_{c_i} is the proportional gain and τ_{c_i} is the integral time constant of the ith controller. The third equation makes use of the process model. To keep the problem simple, the ratio of air to oxygen (or x) is fixed. We note that the relationship between the gas temperature and the equivalence ratio is not monotonic. Beyond the optimal equivalence ratio (about 1.2 for $x = 3.97$), the gas temperature decreases as the equivalence ratio increases. Therefore, K_{c_2} and τ_{c_2}

should be replaced by $-K_{c_2}$ and $-\tau_{c_2}$ when the equivalence ratio is above this value. The design of a model-based feedback control system, employing nonlinear control techniques for particulate processes, [21, 22, 35, 25, 64, 65, 66] as well as applications of the control system to an experimental system, will be the subject of future work.

Regarding the practical implementation of the proposed control system (see Figure 5.1 for a schematic) on the Diamond Jet hybrid HVOF thermal spray, we note that the chamber pressure and the equivalence ratio can be readily manipulated in real-time by adjusting the mass flow rates of fuel, oxygen and air. The velocity and temperature of individual particles can be measured experimentally using non-intrusive optical techniques, for example, Laser Doppler Velocimetry, [38] Particle Imaging Velocimetry, [71, 130] and Two Color Pyrometry [124, 49, 36] etc. However, it is not possible to directly measure the degree of melting of individual particles and consequently, the average degree of melting of the entire particle size distribution. To overcome this limitation, one needs to use an estimation scheme based on the modeling equations that describe the evolution of particle temperature, velocity and degree of particle melting coupled with the available gas phase measurements to estimate average particle melting ratio at the point of impact on the substrate. The estimates obtained by this model can be further improved through comparison with the particle temperature measurements at various locations across the free jet. In the simulation section, we have included a closed-loop simulation in the presence of measurement errors to evaluate the effect of such errors in closed-loop performance; the detailed development of an estimation scheme for particle melting ratio is the subject of future work. The controller then obtains information from the measurement system, and makes decisions, which are sent to the controlled valves (total flow of gases to the process and oxygen/fuel ratio), to adjust the manipulated input variables until

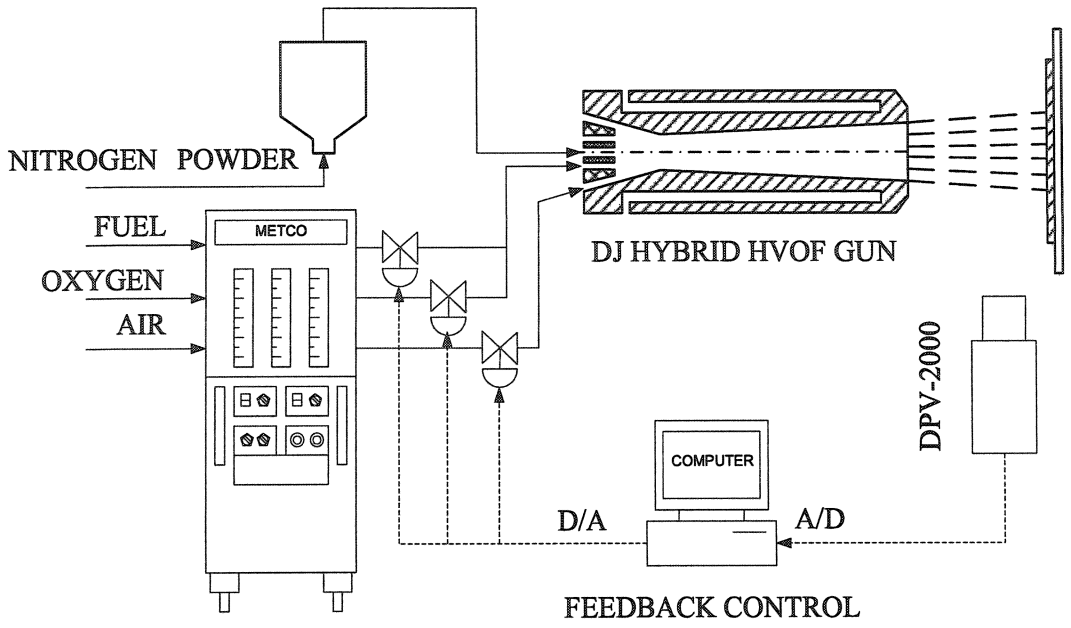


Figure 5.1: Schematic of the proposed feedback control system.

the deviation of the controlled outputs from their corresponding set-point values falls within a tolerable region. One of the great advantages of feedback control is that it can compensate for the effect of disturbances in the process operating conditions.

5.1.2 Simulation results of HVOF process model under feedback control

In this subsection, simulation runs of the closed-loop system are presented. The outputs $y_1(t)$ and $y_2(t)$ are computed by averaging the individual particle velocity and melting ratio data obtained from the process model. To account for the powder size distribution, we first fit a lognormal distribution and calculate the size range in order to capture more than 99wt% of all the particles. We then divide this size range into 100 intervals to perform the integration (Further increase on the number of discretization intervals did not change the accuracy of the computed results). [84, 83] This requires solving simultaneously 400 ordinary differential equations for each process simulation. The powder used is Nickel and all the other parameters used in

Table 5.1: Process and controller parameters used in the closed-loop simulation.

K_{c_1}	=	5×10^{-3}	
K_{c_2}	=	0.1	
τ_1	=	5×10^{-2}	
τ_2	=	5×10^{-2}	
d_{10}^*	=	15	μm
d_{50}	=	35	μm
d_{90}	=	77	μm
ϕ	=	1.0	

* powders are assumed to be lognormally distributed, and d_{10}, d_{50}, and d_{90} are three characteristic diameters whose corresponding cumulative weight function values are 0.1, 0.5, 0.9.

the closed-loop system simulations are shown in Table 5.1.

Several simulation runs of the process model under the feedback controller were performed to evaluate the ability of the controller to: a) drive the melting ratio and velocity of particles at the point of impact on substrate to desired set-point values, b) attenuate the effect of disturbances on process operating conditions, and c) compensate for the effect of measurement errors. The first simulation studies the behavior of the closed-loop system in the presence of changes in the set-point. Initially, the process is assumed to operate at the baseline condition, and at time $t =$ 10 *sec*, the average particle velocity set-point value increases by 5% and the average particle melting ratio set-point value decreases by 5%. Figure 5.2 shows how the controlled outputs and manipulated inputs as well as the total mass flow rate and the equivalence ratio respond in the case of requesting such changes in the set-point values. The feedback controller drives the controlled outputs to the new set-points in about 10 *sec* (note that 10 *sec* is the time needed for the controlled outputs to reach the new set-point values, not the time for the particles to hit the substrate,

which is on the order of 10^{-3} *sec*). In a typical HVOF process, the powder feed rate is in the range 20-80 g/min and the thickness of a coating is about 100 - 300 μm [109]. The deposition efficiency of HVOF process is around 70% [126]. Considering the deposition of a coating on a 0.5 m × 0.5 m substrate, the deposition time can be estimated by the following formula:

$$t = \frac{200 \times 10^{-6} m \times 0.5m \times 0.5m \times 8900 kg/m^3}{50 \times 10^{-3} kg/min \times 0.7} = 12.7\ min \qquad (5.2)$$

For a coating with a larger area, the deposition time is even longer, which means that the controller is quite effective (compared with a typical time needed for a full coating) and validates the feasibility of implementation of feedback control on the HVOF process. Note that in the first 0.8 *sec*, the liquid ratio increases when the equivalence ratio decreases. This is because in this time period the mass flow rate and the pressure increase by 22% and 21% while the equivalence ratio decreases by 6%. As a result, the increase in gas temperature resulting from the increased pressure outweighs its decrease resulting from the lower equivalence ratio.

To demonstrate that the proposed formulation of the control problem, which explicitly accounts for the effect of powder size distribution, leads to a solution of the control problem that is superior (with respect to the control action needed to achieve the desired control objectives) to a solution that assumes a monodisperse powder size distribution, the two PI controllers are also implemented on the process model using the same controlled outputs but assuming that the velocity and temperature measurements are based on a single particle whose size is taken to be $d_p = 35\ \mu m$, which is equal to the d_{50} value of the powder size distribution used in our simulation. The corresponding controlled and manipulated variables are given in Figure 5.3. The results show that the desired objectives of 5% change in the set-point values are not achieved (compare the controlled output profiles of Figure 5.2, where the desired

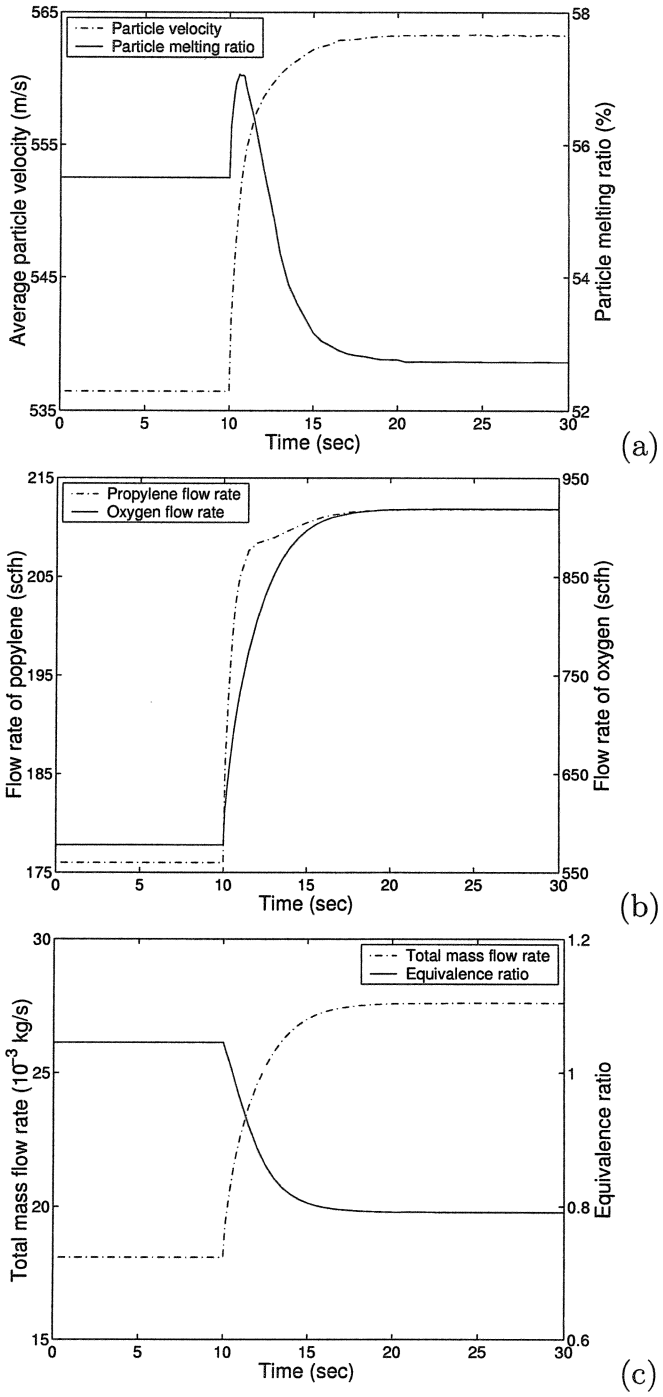


Figure 5.2: Profiles of (a) controlled outputs (average particle velocity and melting ratio), (b) manipulated inputs (flow rate of propylene, oxygen and air), and (c) total mass flow rate and equivalence ratio, under the request of 5% increase in average particle velocity and 5% decrease in the melting ratio - Control problem formulation accounts for the effect of powder size distribution.

set-point change is achieved); this occurs because, as it has been previously shown, [84] the behavior of an individual particle is insufficient to represent that of the entire powder size distribution. This makes clear the need to account for the effect of powder size distribution in the control problem formulation and solution.

To test the robustness of the proposed control problem formulation and of the feedback controller, the problem of controlling the HVOF process in the presence of disturbances was studied. Figures 5.4 and 5.5 show the controlled output and manipulated input profiles in the presence of disturbance (20% increase and 20% decrease, respectively) in the spray distance which occurs at t = 10 *sec.* Without control, the process jumps to a new steady state in a very short time (owing to the very short time of particle fight), the particle velocity in both cases drop instantaneously. The reason is that the particles are usually accelerated first and then decelerated in the external field and therefore there is an optimal spray distance. Nevertheless, the disturbances in spray distance do not have a significant effect on particle velocity because the velocity profile of particles is almost flat as they reach the gas velocity. However, the melting ratio of particles at the point of impact on substrate decreases in the former case and increases in the latter case, which can be explained by the change in residence time of particles in the gas flame. Such variations in the molten state of the particle may have a detrimental effect on the coating microstructure evolution. Under feedback control, the manipulated inputs drive the process outputs to their original steady state values in 10 - 25 *sec.* It is also interesting to see how the controller responds to compensate for this velocity decrease. While it is intuitively expected that the mass flow rate increases in the latter case to increase the particle velocity, the total mass flow rate in the former case decreases to drive the particle velocity to its original value. This is because the equivalence ratio increases all the

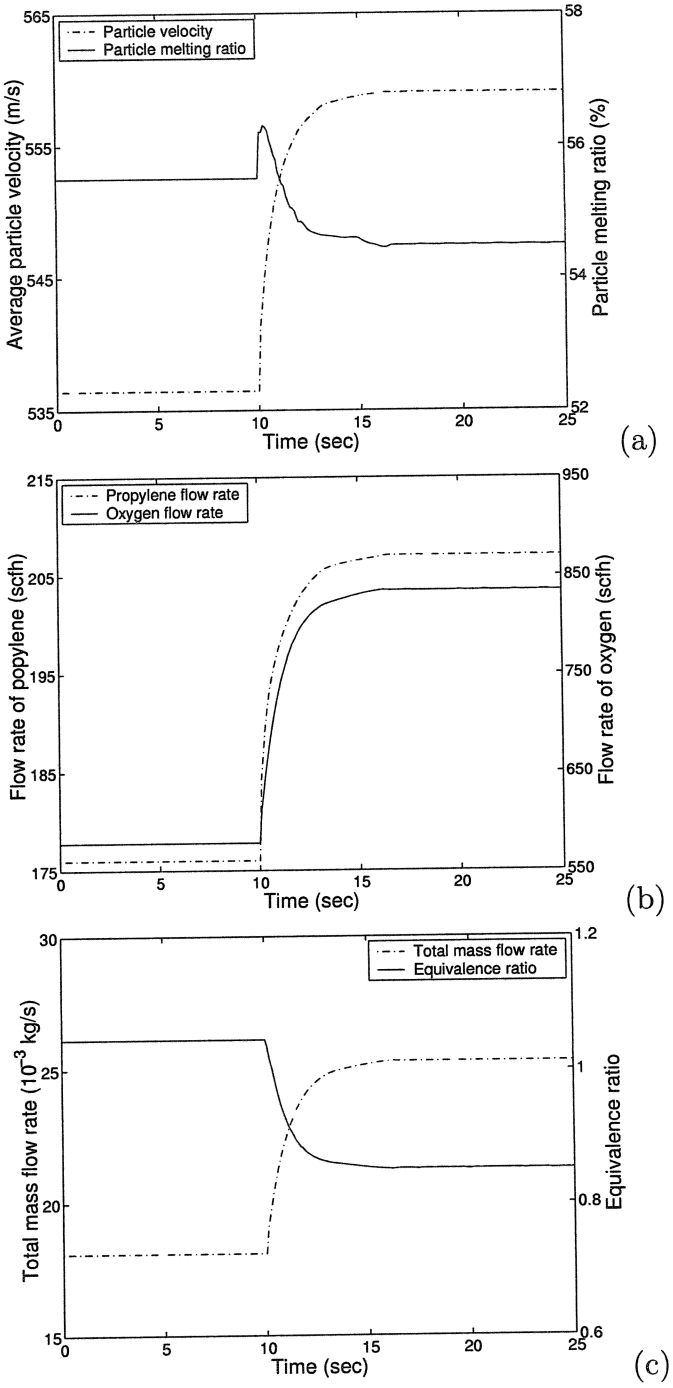


Figure 5.3: Profiles of (a) controlled outputs (average particle velocity and melting ratio), (b) manipulated inputs (flow rate of propylene, oxygen and air), and (c) total mass flow rate and equivalence ratio, under the request of 5% increase in average particle velocity and 5% decrease in the melting ratio - Control problem formulation does not account for the effect of powder size distribution.

time and the pressure increases even as the total mass flow rate decreases.

Figures 5.6 and 5.7 show the controlled output and manipulated input profiles in the presence of disturbances (10% increase and 20% decrease, respectively) in initial particle velocity at t = 10 *sec.* Without control, the system jumps to a new steady state in a very short time. While the particle velocity changes little in both cases, the particle melting behavior varies a lot. The changes of particle temperature in both cases can be explained by the residence time of particles in the flame gas, which is caused by the variation of the particle velocity along the flight, although the particle velocity at the point of impact remains nearly the same. Under feedback control, the manipulated inputs drive the process outputs to their original steady state values in about 20 *sec.*

Another source of disturbance to the process operation, especially in an industrial environment, is the variation of the size distribution of the powder during the operation of the HVOF process. This may have a significant influence on the particle velocity and particle temperature at the point of impact on the substrate based on the analysis of the previous sections. In the following simulation, it is assumed that the process is at steady state in the first 100 *sec* and then the powder size distribution changes gradually (specifically, in the following calculation, μ increases according to the expression $\mu = \mu_0[1 + 0.03(1 - e^{-t/100})]$ and σ^2 is kept constant). Figure 5.8 shows the controlled outputs and the manipulated inputs as well as the total mass flow rate and the equivalence ratio in the presence of such a variation in the powder size distribution. Under feedback control, both particle velocity and melting ratio fluctuate in a very narrow range around the desired set-point values. We note that φ changes rather sharply compared to the change in $\dot{m}_{Fuel}$ and $\dot{m}_{O_2}$ because both $\dot{m}_{Fuel}$ and $\dot{m}_{O_2}$ have an influence on φ ($\varphi = \dot{m}_{Fuel}/\dot{m}_{O_2} \times 4.5$). For example, φ will go up

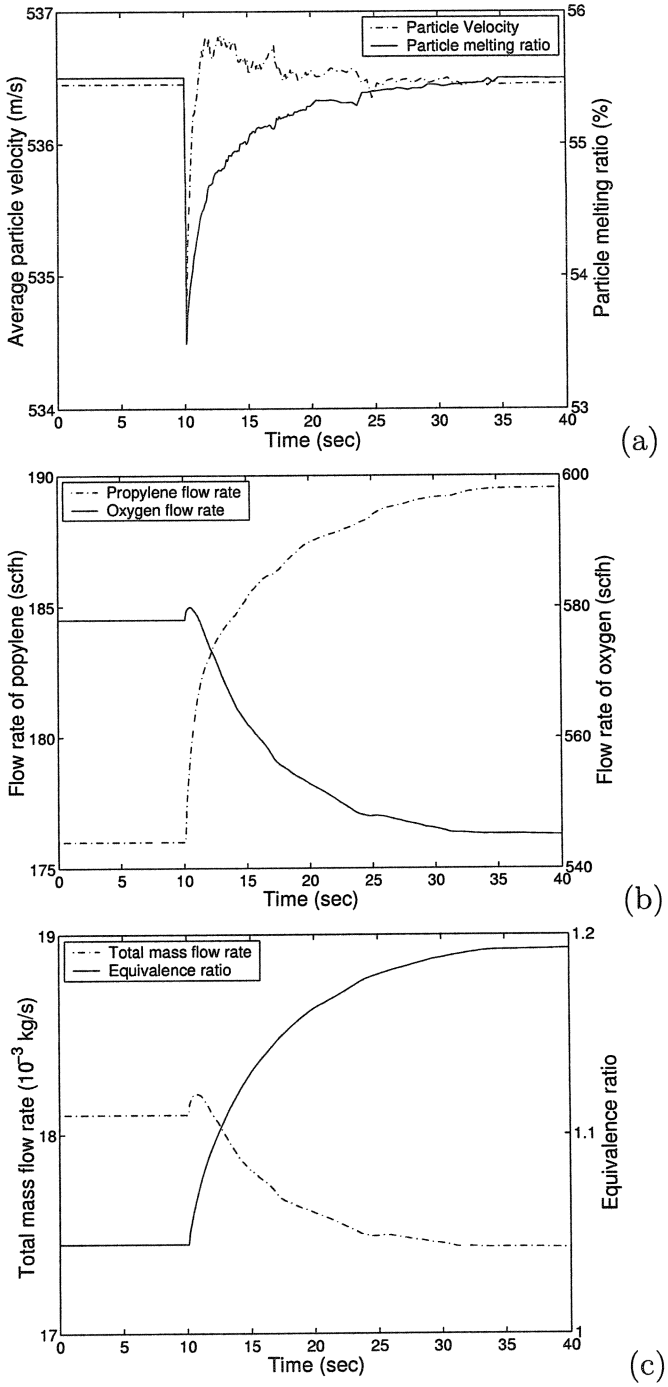


Figure 5.4: Profiles of (a) controlled outputs (average particle velocity and melting ratio), (b) manipulated inputs (flow rate of propylene, oxygen and air), and (c) total mass flow rate and equivalence ratio, in the presence of disturbance (20% increase) in the spray distance.

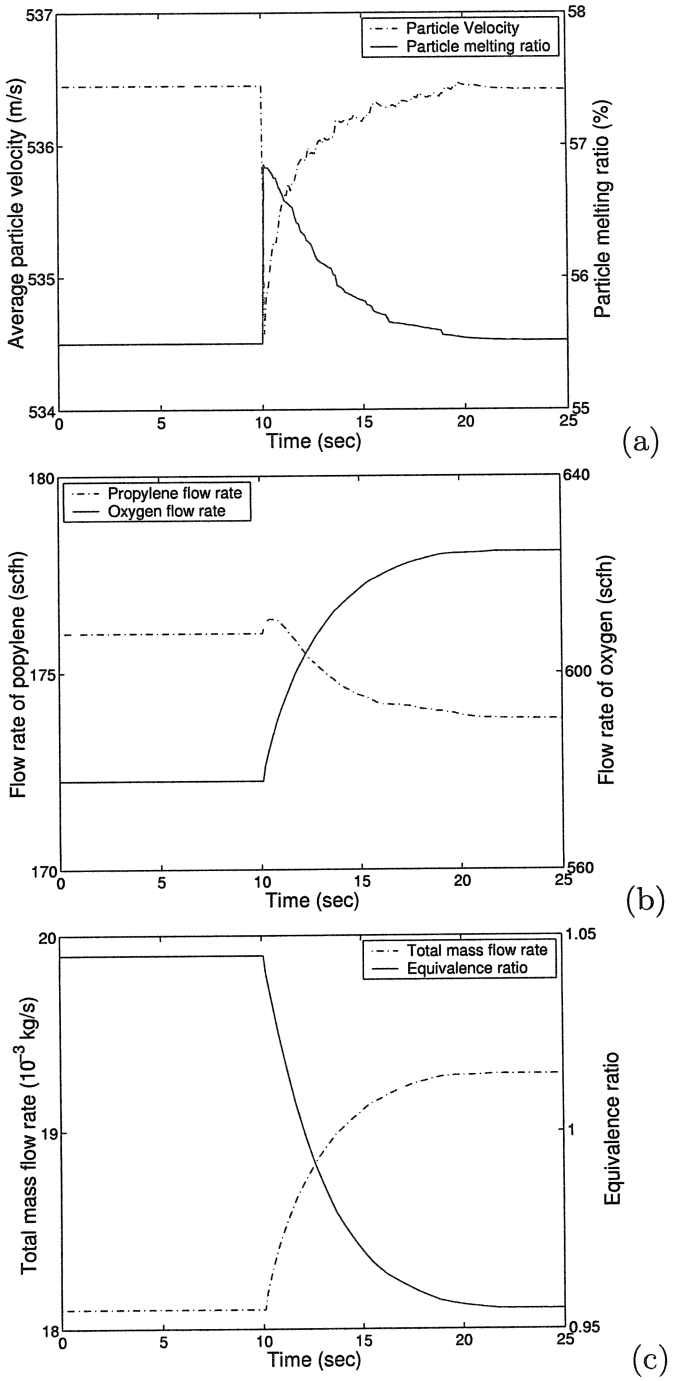


Figure 5.5: Profiles of (a) controlled outputs (average particle velocity and melting ratio), (b) manipulated inputs (flow rate of propylene, oxygen and air), and (c) total mass flow rate and equivalence ratio, in the presence of disturbance (20% decrease) in the spray distance.

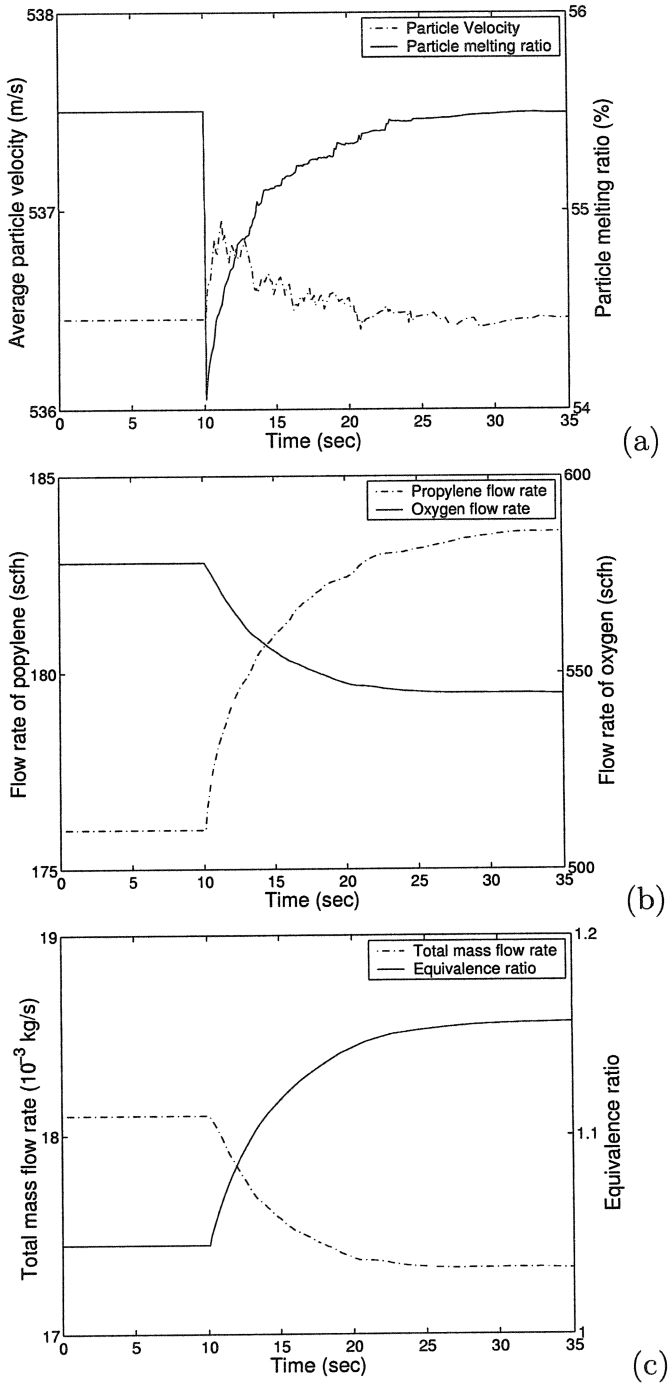


Figure 5.6: Profiles of (a) controlled outputs (average particle velocity and melting ratio), (b) manipulated inputs (flow rate of propylene, oxygen and air), and (c) total mass flow rate and equivalence ratio, in the presence of disturbance (10% increase) in particle injection velocity.

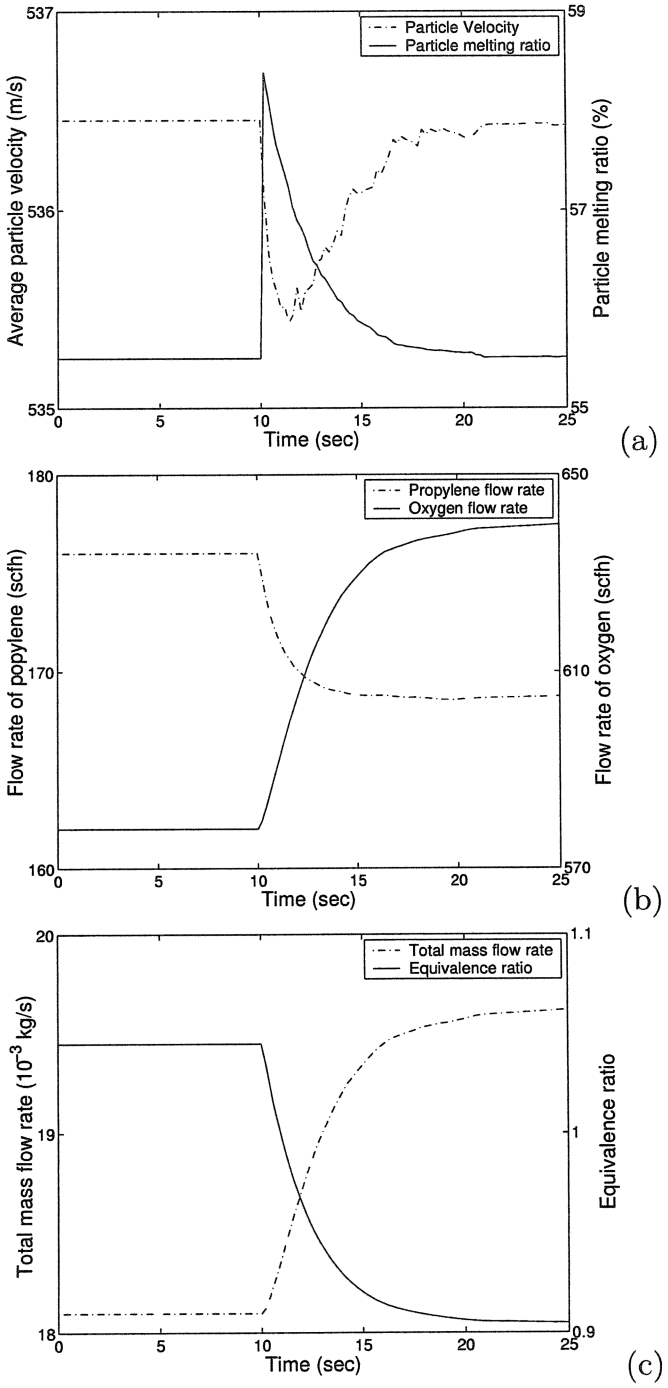


Figure 5.7: Profiles of (a) controlled outputs (average particle velocity and melting ratio), (b) manipulated inputs (flow rate of propylene, oxygen and air), and (c) total mass flow rate and equivalence ratio, in the presence of disturbance (20% decrease) in particle injection velocity.

sharply if $\dot{m}_{Fuel}$ increases while $\dot{m}_{O_2}$ decreases and go down sharply in the opposite case. When no control is used, in which case the flow rate of each stream is kept constant, both velocity and melting ratio of particles decrease with time, which may have an undesirable effect on the resulting coating properties.

To demonstrate that the proposed formulation of the control problem is robust with respect to measurement errors, we implemented the developed control system on the process model under the request of 5% increase in average particle melting ratio set-point value and 5% decrease in the average particle velocity set-point value at time $t = 10$ *sec* but assuming that there are errors in the values of average velocity and degree of melting used in the controller. In the closed-loop simulation, we assume that the estimation errors follow an exponentially-decaying function with an initial error of 10%. The corresponding controlled and manipulated variables are given in Figure 5.9. The results show that the desired control objective of 5% change in the set-point values is eventually achieved (compare the controlled output profiles of Figures 5.2 and 5.9); this demonstrates that the proposed formulation of the control problem is robust with respect to measurement errors.

5.2 Model-based estimation and control of particle velocity and melting ratio in HVOF thermal spray

5.2.1 Real-time estimation of volume-averaged particle velocity and melting ratio

The velocity, temperature (or degree melting) of particles at the point of impact on the substrate are two key parameters that determine the coating thermal and mechanical properties. However, most of the online measurements, including particle size, velocity and temperature using Laser Doppler Velocimeter, Two Color Pyrom-

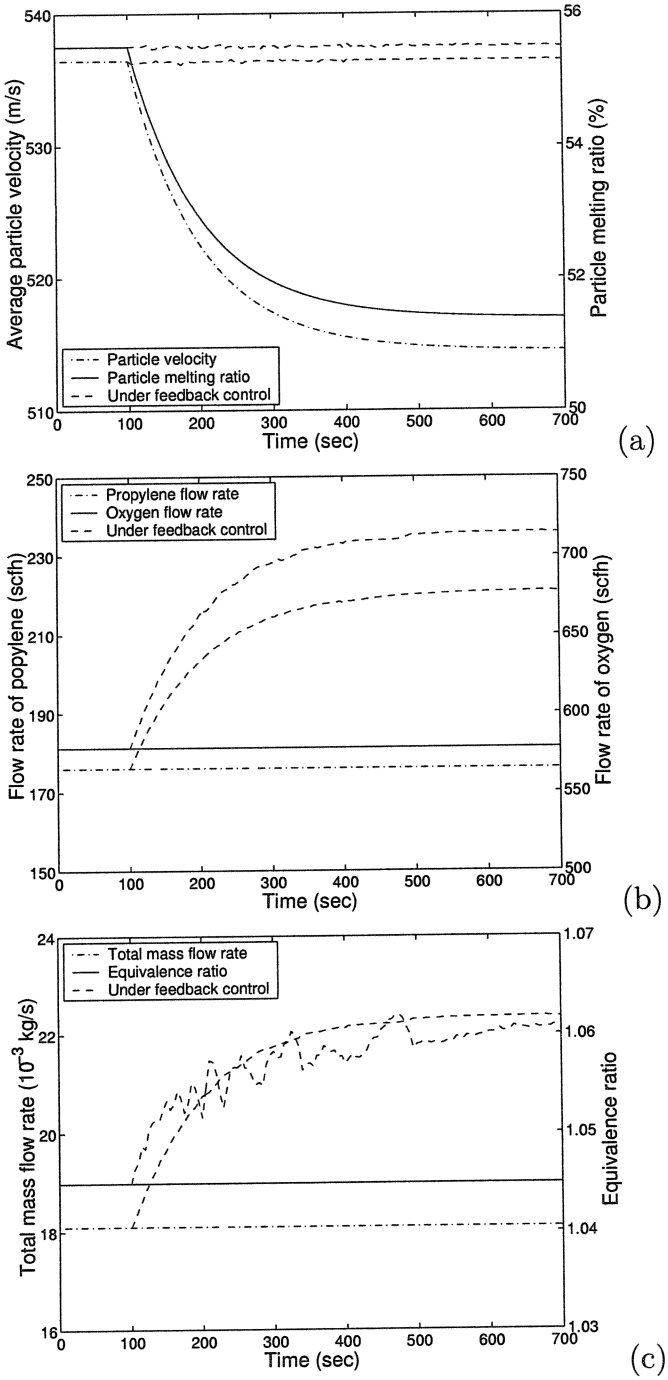


Figure 5.8: Profiles of (a) controlled outputs (average particle velocity and melting ratio), (b) manipulated inputs (flow rate of propylene, oxygen and air), and (c) total mass flow rate and equivalence ratio, in the presence of disturbance (10% increase) in particle injection velocity.

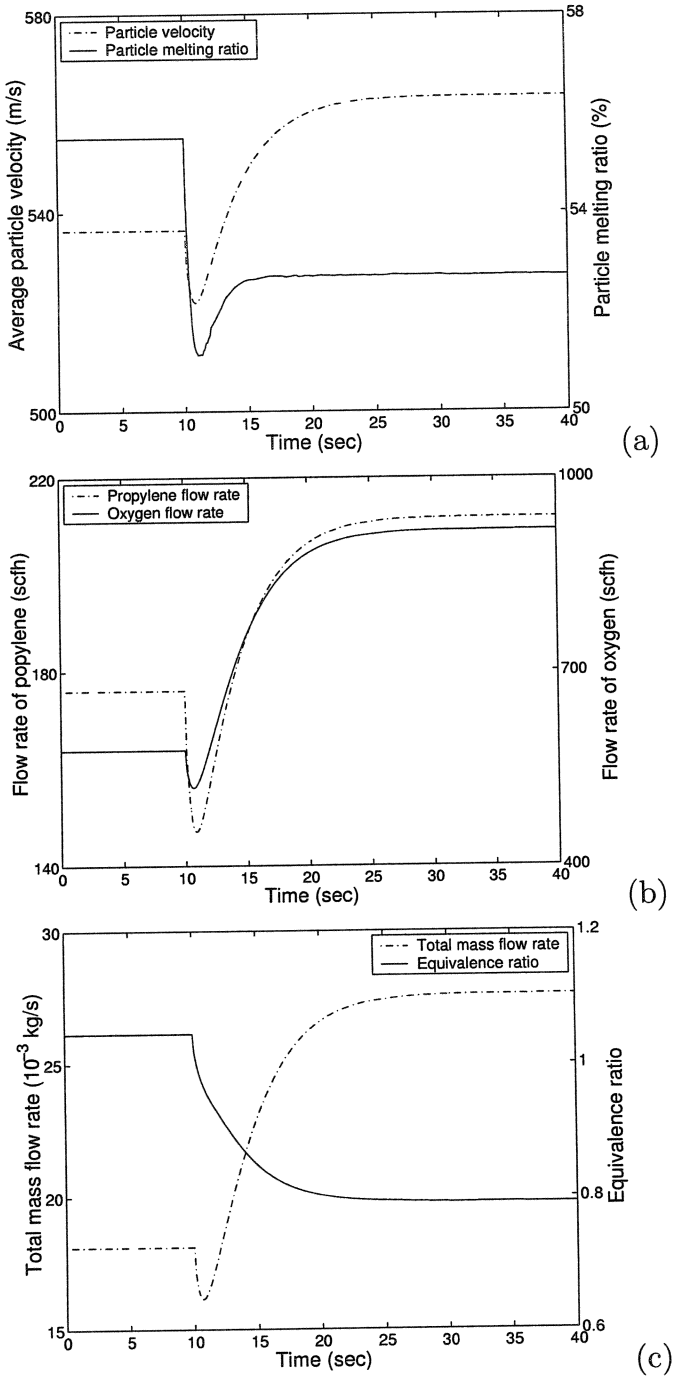


Figure 5.9: Profiles of (a) controlled outputs (average particle velocity and melting ratio), (b) manipulated inputs (flow rate of propylene, oxygen and air), and (c) total mass flow rate and equivalence ratio, under the request of 5% increase in average particle velocity and 5% decrease in the melting ratio - Closed-loop simulation in the presence of measurement error.

eter, etc. [38, 71, 36] can only give histogram counts properties and the relationship between particle velocity, temperature and particle size is implicit. Moreover, it is very difficult to directly measure the degree of melting of individual particles and consequently, the average degree of melting of the entire particle size distribution. To overcome this limitation, one needs to use an estimation scheme based on the modeling equations that describe the evolution of particle temperature, velocity and degree of particle melting coupled with the available gas phase measurements to estimate average particle melting ratio and velocity at the point of impact on the substrate.

In an industrial environment, where the presence of measurement noise cannot be ignored, it is desirable to estimate the states of the system with as little uncertainty as possible in the presence of noise. This entails the implementation of a real-time estimator to alleviate the effect of measurement noise. In the present work, it is assumed that the gas velocity and temperature are measured by N Rayleigh scattering based sensors placed downstream of the gun exit (Figure 5.10). To account for measurement noise, the measured gas velocity and temperature at various locations in the free jets are described by:

$$\begin{aligned} v'_g(x_i) &= \bar{v}_g(x_i) + R_v \\ T'_g(x_i) &= \bar{T}_g(x_i) + R_T \end{aligned} \tag{5.3}$$

where $\bar{v}_g(x_i)$ and $\bar{T}_g(x_i)$ are the model predicted gas velocity and temperature at the i-th location, and $v'_g(x_i)$ and $T'_g(x_i)$ are the corresponding measured values. R_v and R_T are two independent random numbers which obey Gaussian distribution. In the computer simulation, both of them are assumed to have a zero mean and a variance of 150^2. An adaptive filter is used in this work to reject the stochastic fluctuations contained in the gas phase measurements. Specifically, the adaptive filter is a second-

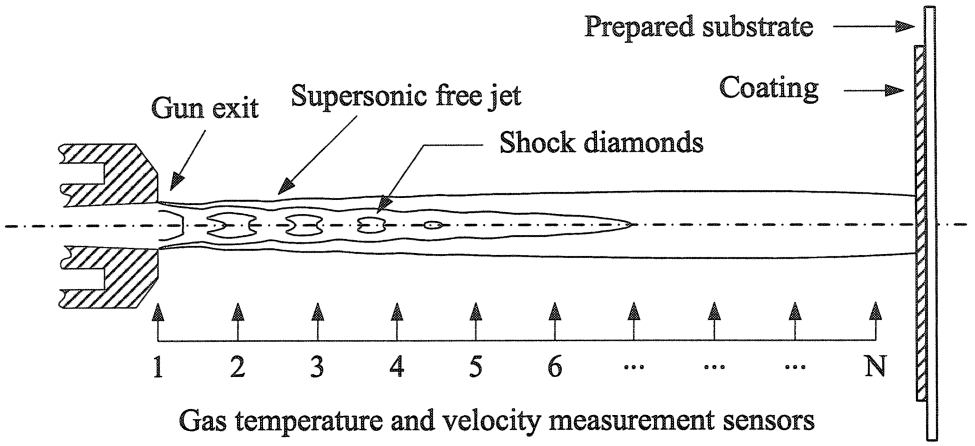


Figure 5.10: Diagram of the gas phase measurement system.

order dynamical system with the following representation:

$$\begin{aligned} \frac{d\hat{y}_i}{dt} &= \xi_i \\ \frac{d\xi_i}{dt} &= \frac{K_i}{\tau_i}(y_i - \hat{y}_i) - \frac{1}{\tau_i}\xi_i \end{aligned} \tag{5.4}$$

where y_i is the gas velocity (or temperature) measurements at the i-th location, $\hat{y}_i$ is the corresponding filter output, K_i is the filter gain and τ_i is the filter time constant. To accelerate the response of the filter and avoid large overshoot, τ is set to be $0.5/K$. The filter gain is adaptively adjusted according to the following law:

$$K(t) = K_0 \frac{|\int_{t-\Delta t}^{t} y(t)dt - \int_{t-2\Delta t}^{t-\Delta t} y(t)dt|}{\Delta t^2} + K_s \tag{5.5}$$

to achieve both fast tracking of the dynamics of the outputs and efficient noise rejection, where K_0 is a constant, K_s is the steady-state gain for the adaptive filter and Δt is the time interval between two updates of K.

Interpolation is applied to the set of gas phase measurements ($v_g(x_i)$ and $T_g(x_i)$) to determine the profiles of gas velocity and temperature across x. For instance, the gas properties at position x_p can be calculated as the weighted sum of the measured

values as follows:

$$\begin{aligned} \hat{v}_g(x_p) &= \sum_{i=1}^{N} \alpha(i)\hat{v}_g(x_i) \\ \hat{T}_g(x_p) &= \sum_{i=1}^{N} \beta(i)\hat{T}_g(x_i) \end{aligned} \tag{5.6}$$

where $\alpha(i)$ and $\beta(i)$ are coefficients that can be determined using standard techniques, for example, the Lagrangian interpolation method [112]. Using the expression of gas velocity and temperature of Eq. 5.6, we can construct the following equations:

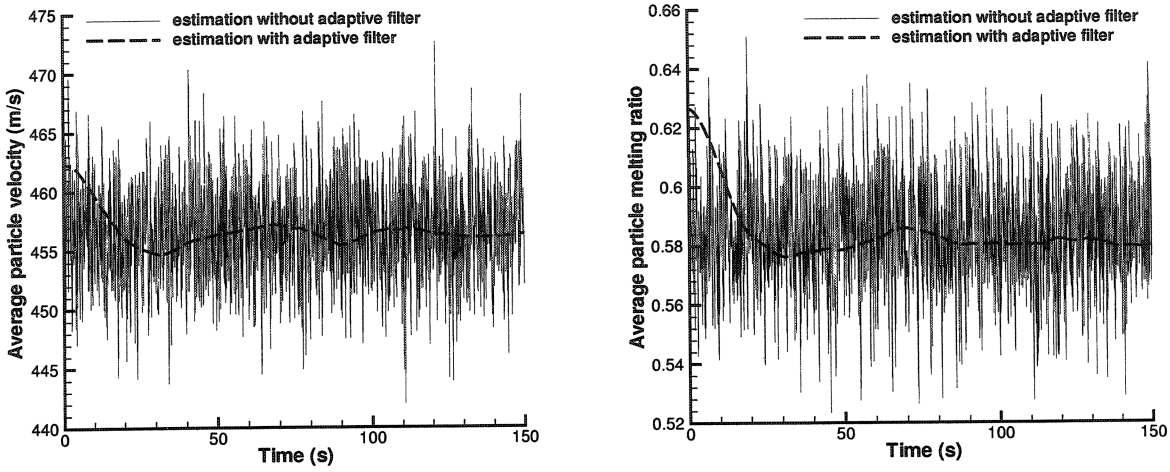
$$\begin{aligned} m_p\frac{d\hat{v}_p}{dt} &= \frac{1}{2}C_D\rho_g A_p(\sum_{i=1}^{N}\alpha(i)\hat{v}_g(x_i) - \hat{v}_p)|\sum_{i=1}^{N}\alpha(i)\hat{v}_g(x_i) - \hat{v}_p|, \hat{v}_p(0) = v_{p0} \\ \frac{d\hat{x}_p}{dt} &= \hat{v}_p, \hat{x}_p(0) = 0 \\ m_p c_{p_p}\frac{d\hat{T}_p}{dt} &= hA'_p(\sum_{i=1}^{N}\beta(i)\hat{T}_g(x_i) - \hat{T}_p) + S_h, \ (\hat{T}_p \neq T_m), \hat{x}_p = T_{p0} \\ \Delta H_m m_p\frac{d\hat{f}_p}{dt} &= hA'_p(\sum_{i=1}^{N}\beta(i)\hat{T}_g(x_i) - \hat{T}_p) + S_h, \ (\hat{T}_p = T_m), \hat{f}_{p0} = 0 \end{aligned} \tag{5.7}$$

from which the estimates of velocity, temperature and melting degree of each individual particle in the whole gas flow/thermal field can be obtained. The estimated average particle properties are then readily calculated using Eq. 2.32.

Figure 5.11 shows the estimates of particle velocity and melting ratio, obtained with (dashed line) and without (solid line) the use of filtering of the gas velocity and temperature measurement measurements. Clearly, the filter is quite effective in alleviating the effect of the measurement noise on the estimates of particle velocity and degree of melting.

5.2.2 Model-based control of particle velocity and melting degree

To formulate the control problem, we follow the strategy proposed in [87]. Specifically, the volume-based average of particle velocity and degree of melting can be



(a) (b)

Figure 5.11: (a) Average particle velocity and (b) particle melting ratio at the point of impact on the substrate under noise in the measurements of gas phase - simulation with and without adaptive filter.

almost independently regulated by manipulating the pressure in the chamber and the equivalence ratio (fuel/oxygen ratio divided by its value at stoichiometric condition), respectively. To develop a feedback controller that can be readily implemented in practice, the manipulation of the combustion pressure and the equivalence ratio is realized by adjusting the flow rate of propylene, $u_1(t)$, oxygen, $u_2(t)$, and air $u_3(t)$ to the process. Owing to the almost decoupled nature of the manipulated input/controlled output pairs, two proportional-integral controllers are used to regulate the process of the following form:

$$\begin{aligned} u_i' &= K_{c_i}\left[(y_{sp_i} - y_i) + \frac{1}{\tau_{c_i}}\int_0^t (y_{sp_i} - y_i)dt\right] + u_{0_i}', \quad i = 1,2 \\ \{u_1, u_2, u_3\} &= f(u_1', u_2', w) \end{aligned} \tag{5.8}$$

where y_{sp_i} is the desired set-point value and y_i is the value of the output obtained from the model-based estimator developed in the previous section(y_1 is the volume-based

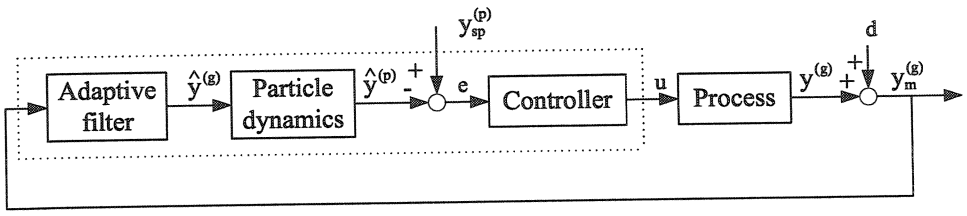


Figure 5.12: Diagram of the closed-loop system under the proposed estimator/controller structure.

average of particle velocity and y_2 is the volume-based average of melting ratio). u_1' is the combustion pressure, u_2' is the equivalence ratio, and w is the air/oxygen ratio. K_{c_i} is the proportional gain and τ_{c_i} is the integral time constant. The manipulated inputs, which are the fuel, oxygen, and air flow rates to the process, are then determined by solving the gas temperature and velocity equation. To keep the problem simple, a fixed w (air/oxygen ratio) is used in the closed-loop simulation. It has been shown that the relationship between the gas temperature and the equivalence ratio is not monotonic. Beyond the optimal equivalence ratio (about 1.2), the gas temperature decreases as the equivalence ratio increases [87]. Therefore, K_{c_2} should be replaced by $-K_{c_2}$ if the initial equivalence ratio is beyond this value. The diagram of the closed-loop system under the developed estimator/control structure is shown in Figure 5.12. The parameters used in the closed-loop simulation are given in Table 5.2.

Several closed-loop simulation runs were performed to evaluate the ability of the proposed estimator/controller structure to: (a) regulate the average particle velocity and degree of melting at the point of impact on substrate to desired set-point values, and (b) attenuate the effect of disturbances on process operating conditions. In all the simulations, the adaptive filter is applied to the gas temperature and velocity measurements at all times and the process is operated under the conditions shown in Table 5.3 for 50 seconds, which is long enough for the controlled output estimates to

Table 5.2: Estimator and controller parameters used in the closed-loop simulation.

K_s	K_0	K_{c_1}	K_{c_2}	τ_{c_1}	τ_{c_2}
1.0	12.0	10^{-3}	10^{-2}	0.05	0.05

converge to constant values. At time t = 50 *sec*, a change in the set-point value (or disturbance) is made and the controller is implemented. To evaluate the performance of the feedback controller, the results of open-loop simulation in which the manipulated inputs are kept on constant values are also presented in the following figures. In the first simulation, we study the behavior of the closed-loop system in the presence of changes in the set-point. Specifically, at t = 50 *sec*, the set-point values of the average particle velocity and the average particle melting ratio change to 500 m/s and 0.65, respectively and the controller is implemented. Figure 5.13 shows how the controlled outputs, manipulated inputs as well as the pressure and the equivalence ratio evolve in the case of requesting such changes in the set-point values. The controller drives the controlled outputs to the new set points in less than 1 minute, which is much less than the typical time needed for coating deposition (this time is usually several tens of minutes). The simulation results show that the controller is quite effective in driving the controlled outputs to desired set-point values and validates the feasibility of implementing real-time feedback control on the HVOF process.

Figure 5.14 shows the profiles of the controlled outputs and the manipulated inputs as well as of the pressure and equivalence ratio in the presence of a 30% sudden increase in the spray distance occurring at t = 50 *sec*. Without control, the particle velocity drops and the melting ratio increases. This is because both the particle velocity and the degree of particle melting increase first and then decrease in the free jet. However, the optimal spray distance for maximum particle velocity and

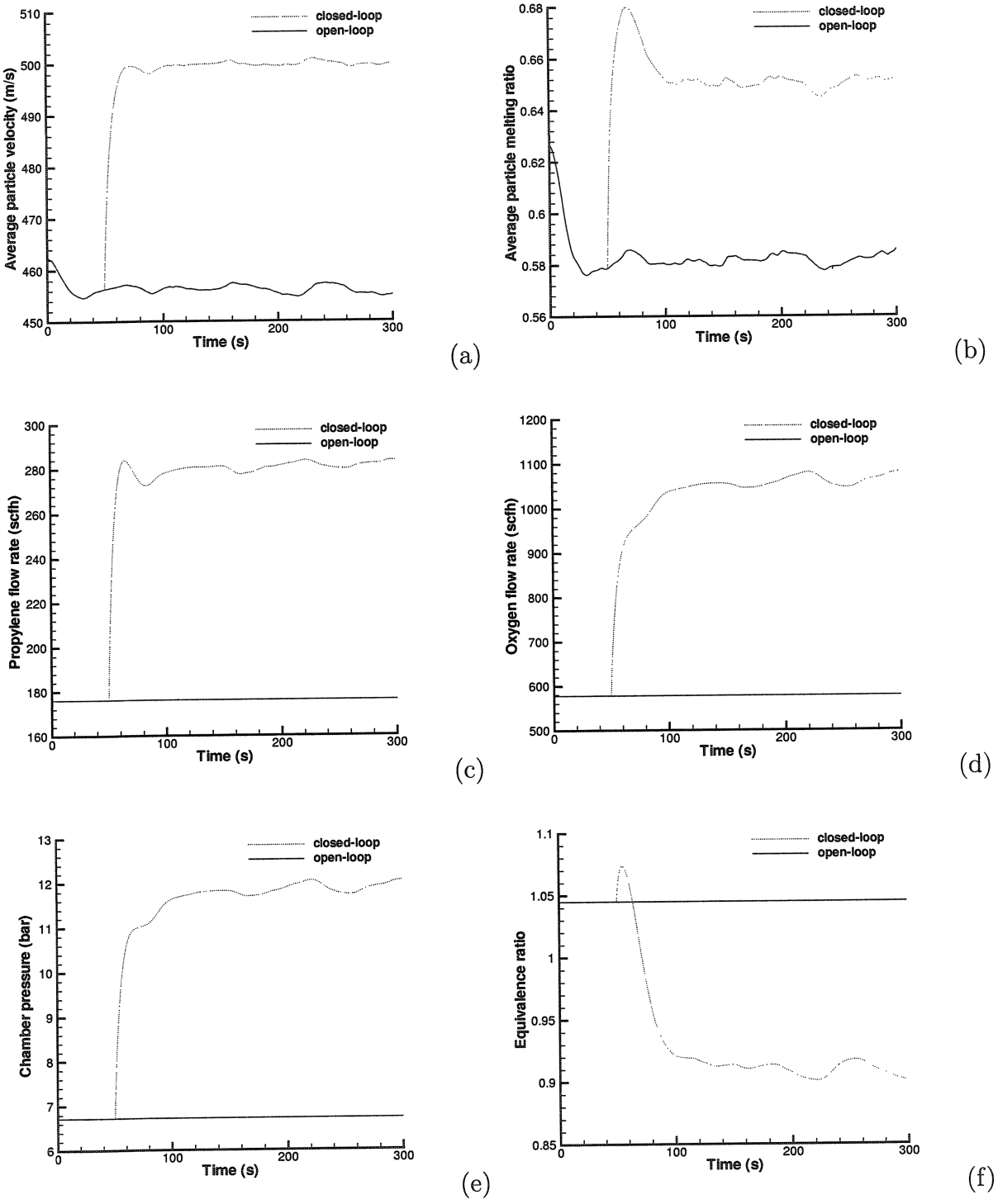


Figure 5.13: Profiles of (a) average particle velocity, (b) average particle melting ratio, (c) gas flow rates of propylene, (d) gas flow rates of oxygen, (e) combustion pressure and (f) equivalence ratio under the request of set-point change in the average particle velocity and average particle melting ratio.

Table 5.3: Operating conditions.

Powder	=	WC-12%Co	
Oxygen flow rate	=	578	$scfh$
Propylene flow rate	=	176	$scfh$
Air flow rate	=	876	$scfh$
Nitrogen flow rate	=	28.5	$scfh$
Spray distance	=	8	$inch$
d_{10}	=	5	μm
d_{50}	=	15	μm
d_{90}	=	45	μm

the one for maximum particle melting ratio are usually different. If the initial spray distance is in between of these two locations, a change in the spray distance might have different effects on particle velocity and melting ratio. Under feedback control, the manipulated inputs drive the controlled outputs to their original steady state values in a very short time.

Figure 5.15 shows the profiles of the controlled outputs and manipulated inputs as well as of the pressure and equivalence ratio in the presence of variation in the powder size (in the simulation, the characteristic sizes describing particle size distribution, d_{10}, d_{50}, d_{90}, increase with time according to the expression $d_p = d_{p_0}[1+0.03(1-e^{-t/100})]$). When no control is used, both the velocity and the melting ratio of particles decrease with time, which may have an detrimental effect on the resulting coating properties. Under feedback control, both the particle velocity and the melting ratio fluctuate in a narrow range around the desired set-point values.

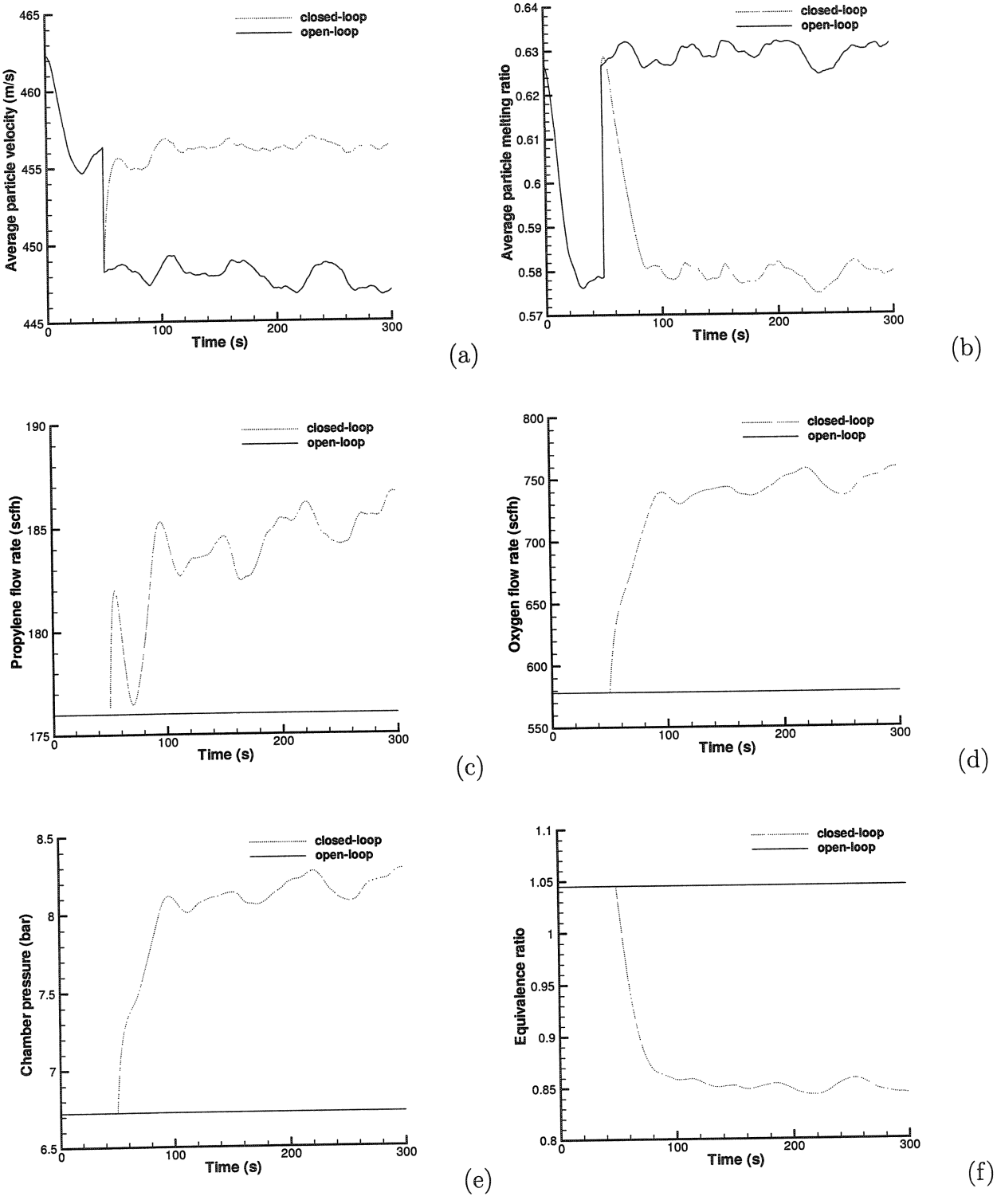


Figure 5.14: Profiles of (a) average particle velocity, (b) average particle melting ratio, (c) gas flow rates of propylene, (d) gas flow rates of oxygen, (e) combustion pressure and (f) equivalence ratio, in the presence of a 30% decrease in the spray distance.

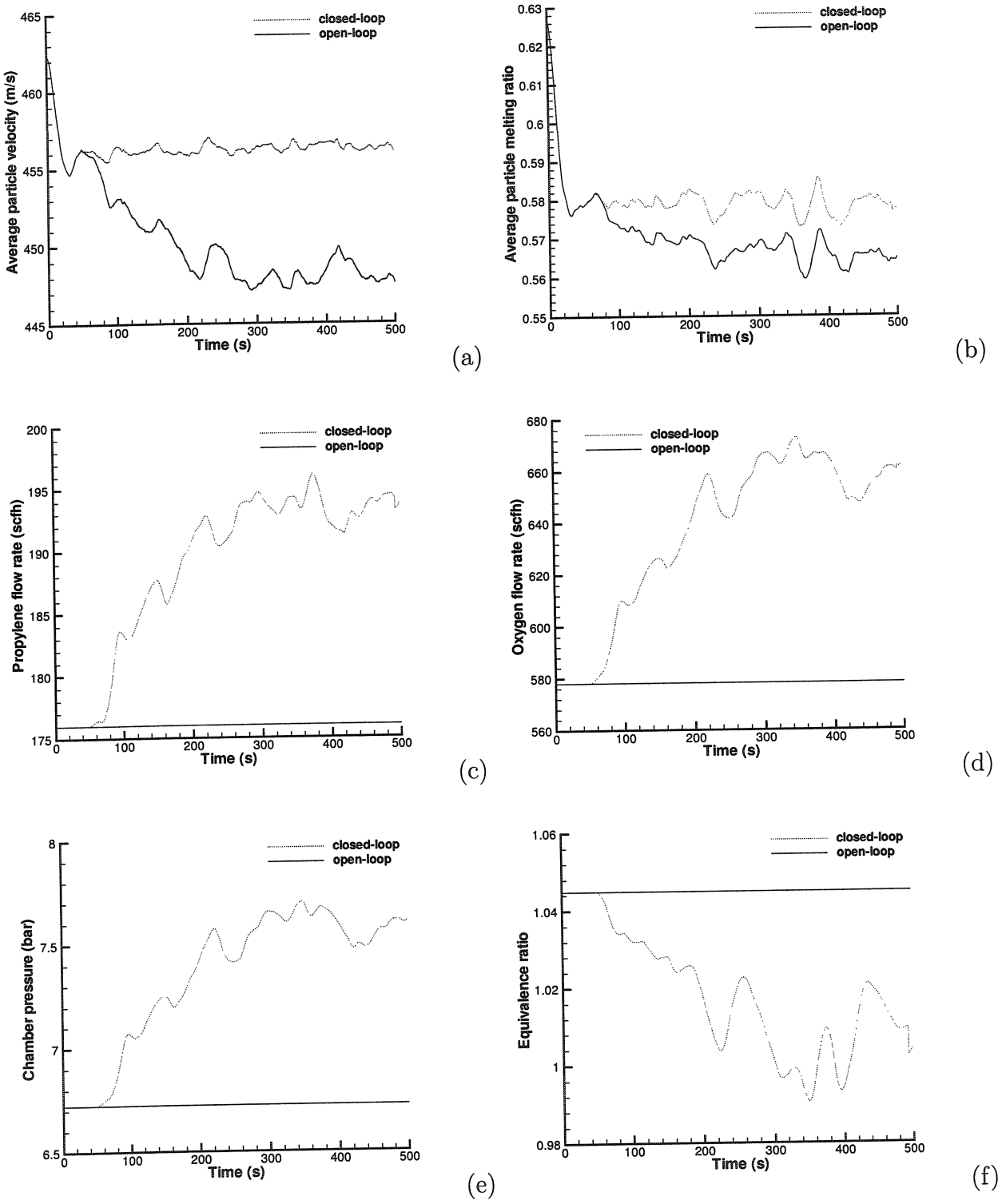


Figure 5.15: Profiles of (a) average particle velocity, (b) average particle melting ratio, (c) gas flow rates of propylene, (d) gas flow rates of oxygen, (e) combustion pressure and (f) equivalence ratio, in the presence of 3% increase in the powder size.

5.3 Summary

We have developed a control system for the HVOF thermal spray process which targets the control of particle velocity and degree of melting at the point of impact on the substrate by manipulating the gas flow rate at the entrance of the gun. Based on the difficulty in real-time measurements of volume-based particle properties, we have proposed an estimation scheme based on gas phase measurements and the momentum transfer and heat transfer equations to estimate the volume-based average of particle velocity and melting degree at the point of impact on the substrate. A feedback control system, which directly uses the estimation scheme, has been designed to regulate the volume-based average of the particle velocity and degree of melting by manipulating the inlet gas flow rates to the process. The proposed estimation/control structure has been applied to a fundamental model of the industrial Diamond Jet hybrid HVOF thermal spray process and its performance and robustness properties have been successfully tested through simulations.

Chapter 6

Control of HVOF Thermal Spray Process: Application to the Processing of WC-Co Coatings

This chapter[1] presents the control of HVOF thermal spray processing of WC-12%Co coatings. The behavior of the open-loop system and the closed-loop system are tested through simulations.

6.1 Gas and Particle behavior

To study the gas and particle behavior, we followed the procedure proposed in Chapter 3. The modeling structure is shown in Figure 6.1 and detailed procedure is given in Chapter 3.

The particle trajectories and temperature histories in the gas field are computed

[1]Chapter 6 is based on [88].

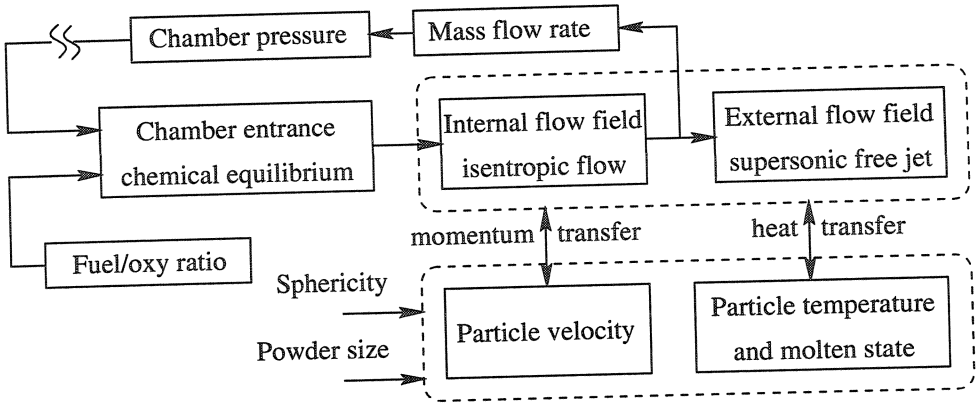


Figure 6.1: Modeling procedure of the gas and particle field.

by the following momentum and heat transfer equations:

$$
\begin{aligned}
m_p \frac{dv_p}{dt} &= \frac{1}{2} C_D \rho_g A_p (v_g - v_p)|v_g - v_p| \\
\frac{dx_p}{dt} &= v_p \\
m_p c_{p_p} \frac{dT_p}{dt} &= \begin{cases} hA'_p(T_g - T_p) + S_h, & (T_p \neq T_m) \\ 0, & (T_p = T_m) \end{cases} \\
\Delta H_m m_p \frac{df_p}{dt} &= \begin{cases} hA'_p(T_g - T_p) + S_h, & (T_p = T_m) \\ 0, & (T_p \neq T_m) \end{cases}
\end{aligned}
\tag{6.1}
$$

where m_p is the mass of the particle, t the time, v_p the axial velocity of the particle, A_p the projected area of the particle on the plane perpendicular to the flow direction, ρ_g the density of the gas, C_D the drag coefficient, x_p the position of the particle, T_p the temperature of the particle, A'_p the surface area of the particle, T_m the melting point of the particle, ΔH_m the enthalpy of melting, f_p the mass fraction of melted part in the particle ($0 \leq f_p \leq 1$) and S_h the source term including heat transfer due to radiation ($\varepsilon\sigma A'_p(T_g^4 - T_p^4)$) and oxidation. The above equations describing particle velocity, position, temperature and degree of particle melting are solved by the 4th order Runge-Kutta method. The thermodynamic and transport properties of the

Table 6.1: Baseline operating conditions.

Gas	Propylene	Oxygen	Air	Nitrogen
Volume Flow rate ($scfh$)	176	578	857	28.5
Mass Flow rate ($10^{-3}kg/s$)	2.596	6.495	8.727	0.280

mixture are calculated using the formulas provided in [46]. Note that in the HVOF thermal spray processing of particles consisting of carbides with binding metals, such as the WC-Co powders used in this work, only the latter may experience a molten state because the gas temperature in a conventional HVOF thermal spray process is not high enough to melt the carbides, whose melting point is very high (i.e. 2870 ^{0}C for tungsten carbide) [122]. In such a case, the particle melting equation in Eq. 6.1 should be modified such that only the fusion of metals might occur in the gas thermal field. In the present work, the melting degree of particles represents the one of the binder (Cobalt) instead of the whole particulate phase.

The gas phase dynamics under the baseline operating conditions (shown in Table 6.1) is solved numerically and the calculated gas equilibrium composition is listed in Table 6.2. It is shown that even under the fuel rich condition ($\varphi = 1.045$), propylene does not show up in the combustion product mixture. Instead, the fraction of oxygen (O plus O_2) is about 5.5%. Due to the existence of oxygen in the internal flow field and the entrainment of air in the external flow field, the powder particles may be oxidized, and their temperatures can be increased due to the exothermic oxidation reaction.

The calculated gas properties in the internal flow field and profiles of gas velocity, temperature and density are shown in Table 6.3 and Figure 6.3. The gas properties at the entrance of the gun is calculated based on the equilibrium model. It is shown that

Table 6.2: Calculated gas equilibrium composition under baseline conditions.

Species	Coefficient	Species	Coefficient
CO	0.13431	OH	0.04198
CO_2	0.13796	O_2	0.04158
H	0.01468	C_3H_6	0
H_2	0.02753	Ar	0.00442
H_2O	0.21642	N_2	0.35118
O	0.01348	NO	0.01645

Table 6.3: Calculated gas properties in the internal flow field.

Parameter	Entrance	Throat	Exit
Pressure (bar)	6.72	3.80	0.62
Temperature (K)	3127	2811	2006
Velocity (m/s)	172	1040	1946
Density (kg/m^3)	0.69	0.43	0.10
Mach number	0.16	1.00	2.21

the highest temperature of propylene combustion under the baseline condition is a little higher than 3100 K and a high pressure of 6.7 bar is maintained in the chamber. However, as the combustion gases pass through the convergent divergent nozzle, the thermal energy is partially converted to kinetic energy. As a consequence, the gas velocity increases from subsonic to supersonic and both pressure and temperature decrease. In particular, the pressure at the exit of the gun is less than one atmosphere, which implies the flow outside of the gun will be overexpanded. This conclusion has been validated by experimental measurements [101].

The calculated gas thermodynamic and transport properties in the internal and external flow fields under the baseline conditions are shown in Table 6.4. As the gas temperature decreases, the gas heat capacity, viscosity and thermal conductivity increase. As a result, the Prandtl number is almost constant (about 0.7). It should

Table 6.4: Calculated gas thermodynamic and transport properties in the internal and external flow fields under the baseline operating conditions.

Heat capacity, $\bar{c}_{p_g}$	=	$1.4 - 1.7 \times 10^3$	$J/kg/K$
Viscosity, $\bar{\eta}_g$	=	$4.5 - 9.4 \times 10^{-5}$	$kg/m/s$
Thermal conductivity, $\bar{\lambda}_g$	=	$0.09 - 0.23$	$W/m/K$
Prandtl number, Pr	=	$0.68 - 0.74$	
Isentropic ratio, γ	=	$1.23 - 1.28$	

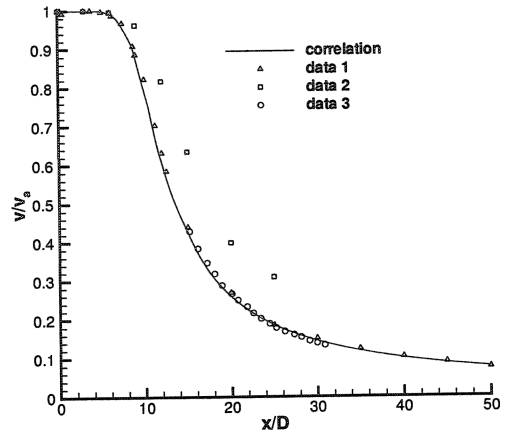
be noted that the isentropic ratio of the exhaust gas mixture is about 1.25, which is less than that of the air (about 1.4).

Regarding the supersonic free jet in the external flow field, it is quite complex and is modeled by taking advantage of the experimentally measured data of supersonic free jets [125, 62, 63, 73, 126]. The data is correlated using formulas of the following form [127]:

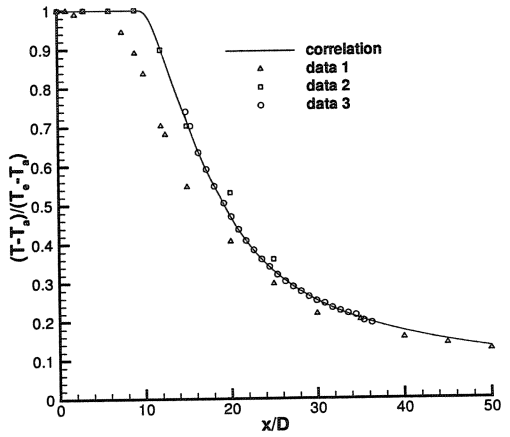
$$\overline{gp} = 1 - \exp\left(\frac{\alpha}{1 - \bar{x}/\beta}\right) \tag{6.2}$$

where $\overline{gp}$ refers to normalized gas properties (v/v_e, $(T - T_a)/(T_e - T_a)$ and $(\rho - \rho_a)/(\rho_e - \rho_a)$, where subscripts a and e stand for atmospheric condition and nozzle exit condition, respectively) and $\bar{x}$ is the normalized axial distance from the exit of the nozzle ($\bar{x} = x/D$, where D is the diameter of the nozzle exit). Piecewise constant expression for α and β are used to make the curve smooth. The results are shown in Figure 6.2. It can be seen that the correlation formulas fit well the experimental data obtained from a similar HVOF thermal spray process [125, 126].

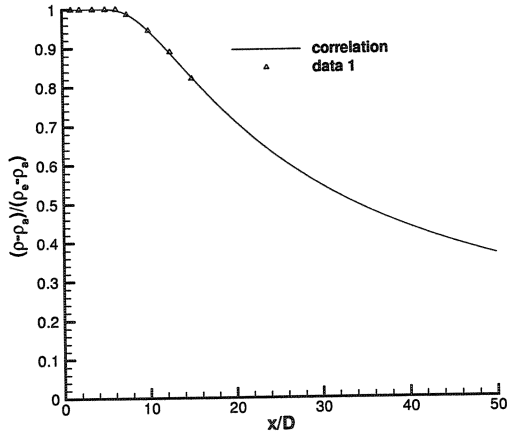
Due to the one dimensional model and the frozen flow assumption, the gas temperature is the highest at the chamber entrance and decreases monotonically in the axial direction. However, the gas temperature in the centerline usually increases sharply and then decreases because of the carrier gas, (see, e.g., [19, 85]). Although this stage



(a)

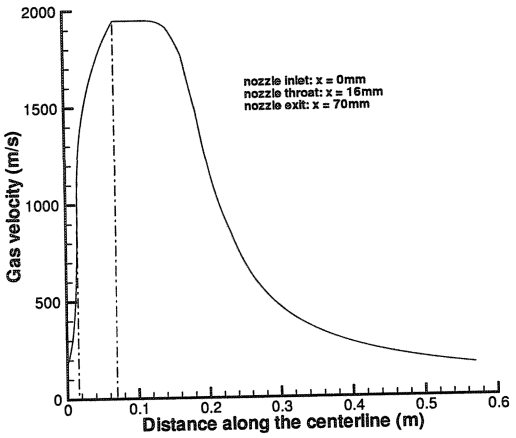


(b)

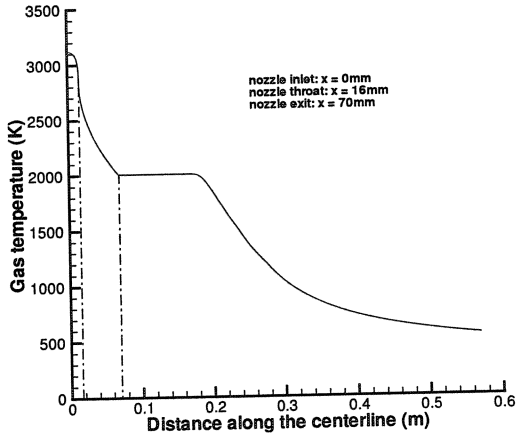


(c)

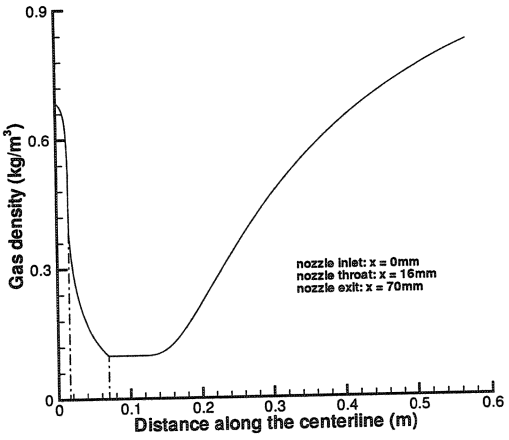
Figure 6.2: Correlation of (a) gas velocity, (b) temperature and (c) density in the supersonic free jet. data 1 - mach number=1.8, ρ_e/ρ_{air} = 3.7 [62, 63], data 2 - mach number = 2.0, data 3 - mach number = 2.0 [73], ρ_e/ρ_{air} = 7-8 [125, 126].



(a)



(b)

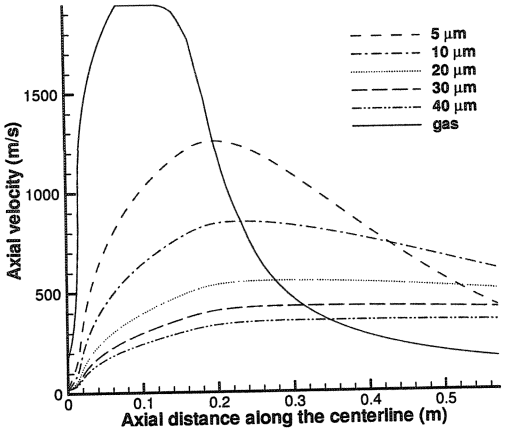


(c)

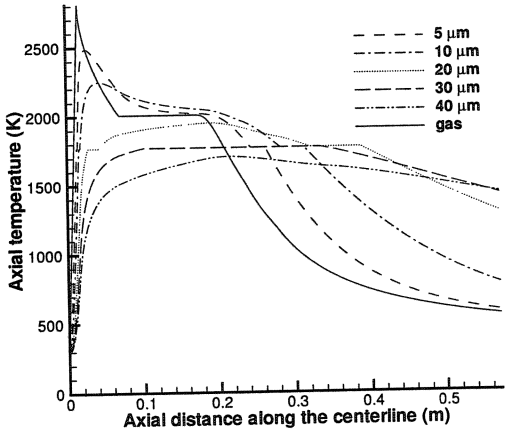
Figure 6.3: Profiles of (a) gas velocity, (b) temperature and (c) density along the centerline.

is short, it plays an important role in particle heating because the particle residence time is relative long in this region. To reasonably predict the particle temperature, we assume the gas temperature increases linearly in the entire convergent part of the nozzle, from room temperature at the nozzle entrance to the calculated throat temperature at the nozzle throat. The resulting profiles of particle velocity, temperature and melting ratio are shown in Figure 7.11. It can be seen that particles of small sizes may reach very high velocities during flight, however, their velocities drop more sharply than those of larger particles because of their smaller momentum inertias. Furthermore, they may be heated to the melting point in a short time and be fully melted during flight, however, they may eventually be in a coexistence state of liquid and solid or even in a solid state after a long enough distance. Smaller particles tend to change their temperatures easily because of their smaller thermal inertias. For particles of large sizes, however, the periods for acceleration and heating are both longer, and the velocity (or temperature) profile becomes nearly flat as it approaches the same velocity (or temperature) of the gas. In addition, their temperature may not reach the melting point, and therefore, they remain in solid state during the entire flight. However, particles of medium sizes may become partially melted during flight.

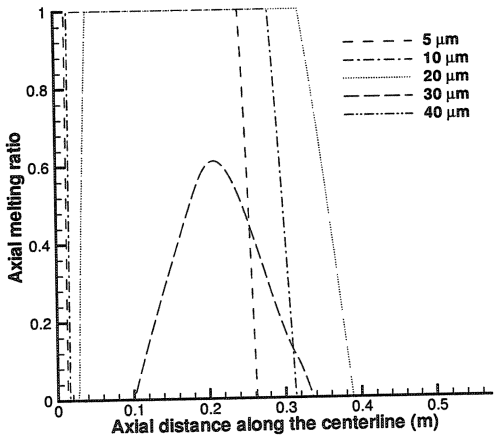
To further understand the behavior of particles in the HVOF process, we also plotted the velocity, temperature and melting ratio at the 8 inch (0.203 m) standoff (default spray distance) as a function of particle size, shown in Figure 6.5 (note that the configuration of each figure may vary with different spray distances). It is shown that particles in the size range 4 - 38 μm hit the substrate in a semi-molten state (where both liquid and solid coexist). Other particles, either smaller or larger, are in a solid state. It is worth pointing out that, although both very small particles and



(a)



(b)



(c)

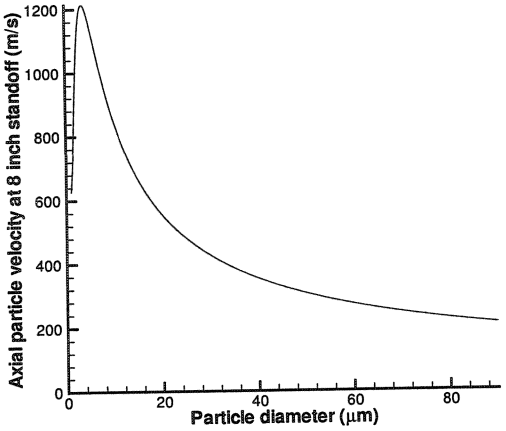
Figure 6.4: Profiles of (a) particle velocity, (b) temperature and (c) degree of melting along the centerline.

very big particles hit the substrate in partially molten state or even solid state, their microstructure is not the same because the former ones have been fully melted during flight.

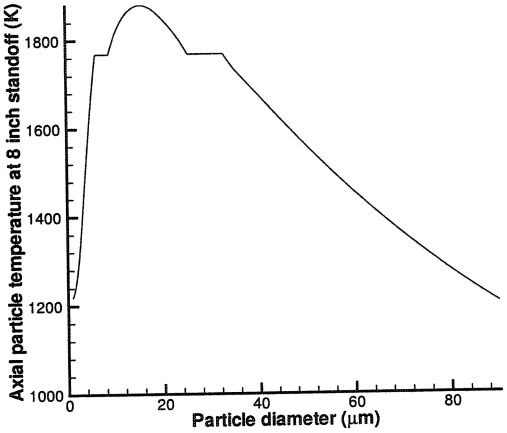
6.2 Closed-loop simulations

In this subsection, simulation runs of the closed-loop system are presented. The outputs $y_1(t)$ and $y_2(t)$ are computed by averaging the individual particle velocity and liquid fraction data obtained from the process model. To account for the powder size distribution, we first fit a lognormal distribution and calculate the size range in order to capture more than 99wt% of all the particles. We then divide this size range into 100 intervals to perform the integration (Further increase on the number of discretization intervals did not change the accuracy of the computed results) [83, 84, 87]. This requires solving simultaneously 400 ordinary differential equations for each process simulation. The parameters used in the closed-loop system simulations are shown in Table 6.5.

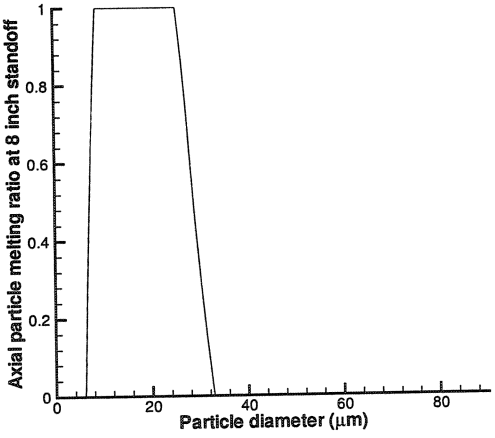
Several simulation runs of the process model under the feedback controller were performed to evaluate the ability of the controller to: a) regulate the velocity and melting ratio of particles at the point of impact on substrate to desired set-point values, b) attenuate the effect of disturbances on process operating conditions, and c) compensate for the effect of measurement errors. The first simulation studies the behavior of the closed-loop system in the presence of changes in the set-point. Initially, the process is assumed to operate under the baseline conditions, and at time t = 10 sec, the average particle velocity set-point value increases by 5% and the average particle melting set-point value increases by 5%. Figure 6.6 shows how the controlled outputs and manipulated inputs evolve in the case of requesting such changes in the



(a)



(b)



(c)

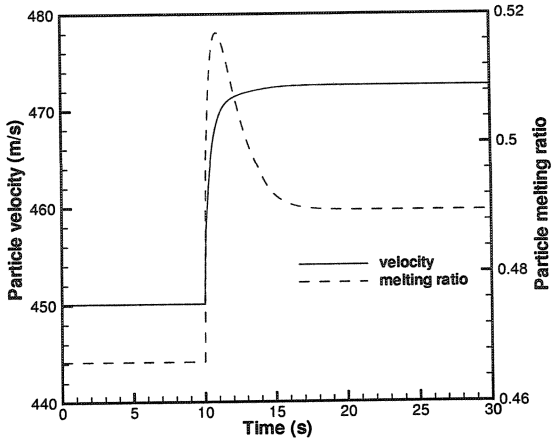
Figure 6.5: (a) Particle velocity, (b) temperature and (c) degree of melting at the 8 *inch* (0.203 m) standoff (point of impact on substrate) as a function of particle size.

Table 6.5: Parameters used in the closed-loop simulation.

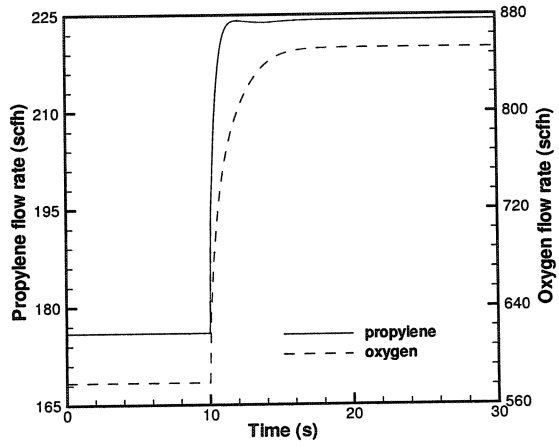
K_{c_1}	=	1×10^{-2}	
K_{c_2}	=	0.1	
τ_1	=	5×10^{-2}	
τ_2	=	5×10^{-2}	
ρ_p	=	14320	kg/m^3
c_{p_p}	=	295.4	$J/kg/K$
T_m^*	=	1768	K
ΔH_m	=	4.2×10^5	J/kg
ε	=	0.4	
d_{10}	=	5	μm
d_{50}	=	15	μm
d_{90}	=	45	μm
φ	=	1.0	

set-point values. The feedback controller drives the controlled outputs to the new set points in about 5 sec, which means that the controller is quite effective and validates the feasibility of implementation of real-time feedback control on the HVOF process.

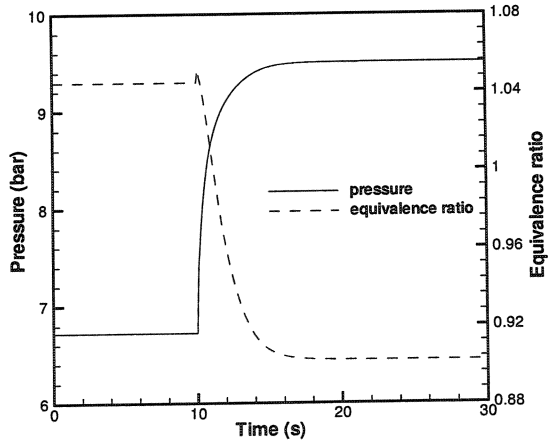
To test the robustness of the proposed control problem formulation and of the feedback controller, the problem of controlling the HVOF process in the presence of disturbances was studied. Figures 6.7-6.8 show the controlled output and manipulated input profiles in the presence of disturbances (10% increase and 10% decrease, respectively) in the spray distance which occurs at t = 10 sec. Without control, the particle velocity in both cases drops instantaneously. The reason is that the particles are usually accelerated first and then decelerated in the external field, and therefore there is an optimal spray distance. Nevertheless, the disturbances in spray distance do not have a significant effect on particle velocity because the velocity profile of particles is almost flat as they reach the gas velocity. However, the melting ratio of particles at the point of impact on substrate decreases when the spray distance



(a)



(b)



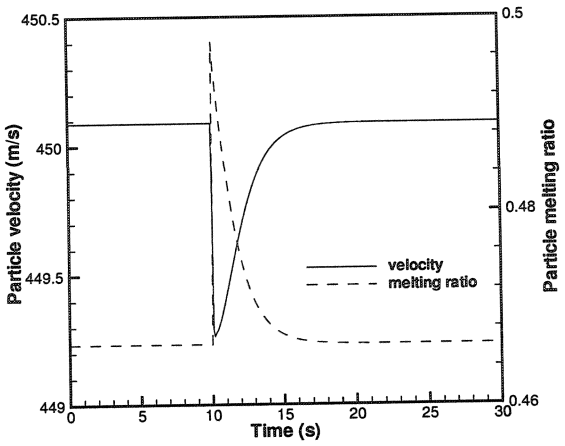
(c)

Figure 6.6: Profiles of (a) controlled outputs (average particle velocity and melting ratio), (b) manipulated inputs (flow rate of propylene, oxygen and air), and (c) pressure and equivalence ratio under the request of 5% increase in particle velocity and 5% increase in melting ratio.

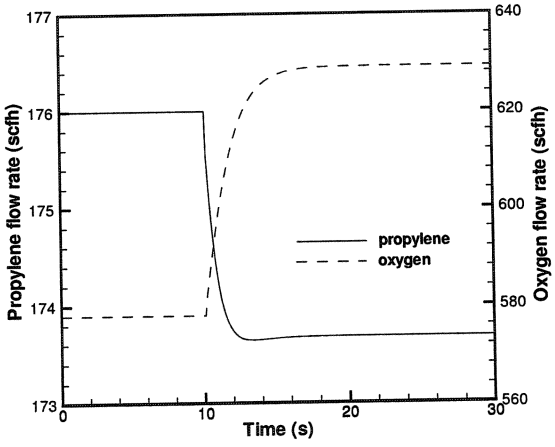
increases, and increases when the spray distance decreases. This can be explained by the change of particle residence time in the gas flame. Such variations in the molten state of the particle may have a detrimental effect on the coating microstructure and properties. Under feedback control, the manipulated inputs drive the process outputs to their original steady state values in 10 sec for the first case. However, for the second case, although the particle velocity reaches its desired set-point value eventually, the objective of particle melting ratio is not achieved. This is because the initial operating condition is very close to the optimal one ($\varphi \approx 1.2$) and the particle temperature cannot be increased further.

Another source of disturbance to the process operation, especially in an industrial environment, is the variation of the size distribution of the powder during the operation of the HVOF process. This may have a significant influence on the particle velocity and particle temperature at the point of impact on the substrate based on the analysis of the previous sections. In the following simulation, it is assumed that the process is at steady-state in the first 100 sec and then the powder size distribution changes gradually (specifically, in the following calculation, the characteristic sizes describing lognormal distribution, d_{10}, d_{50}, d_{90} increases according to the expression $d_p = d_{p_0}[1 + 0.03(1 - e^{-t/100})]$). Figure 6.9 shows the controlled output and the manipulated input profiles in the presence of such a variation in the powder size distribution. Under feedback control, both particle velocity and liquid fraction fluctuate in a very narrow range around the desired set-point values. When no control is used, in which case the flow rate of each stream is kept constant, both velocity and melting ratio of particles decrease with time, which may have an undesirable effect on the resulting coating properties.

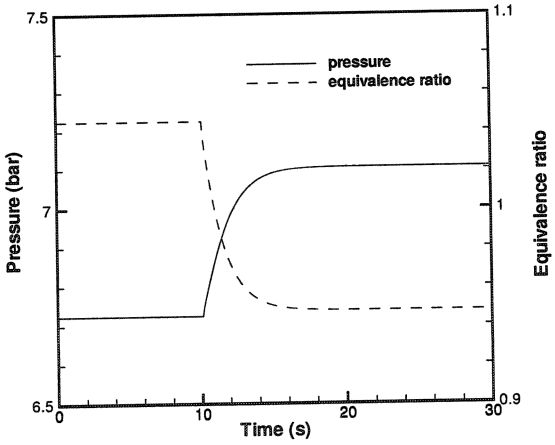
To demonstrate that the proposed formulation of the control problem is robust



(a)

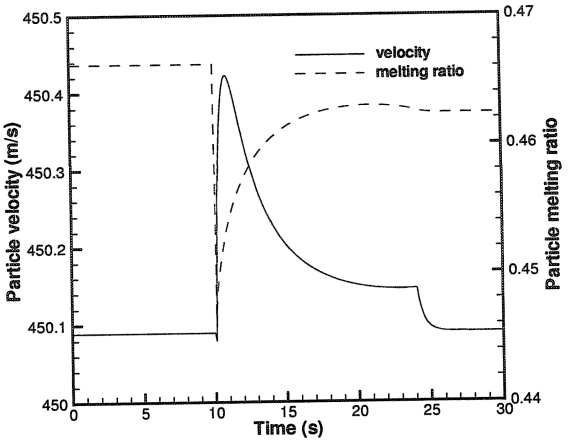


(b)

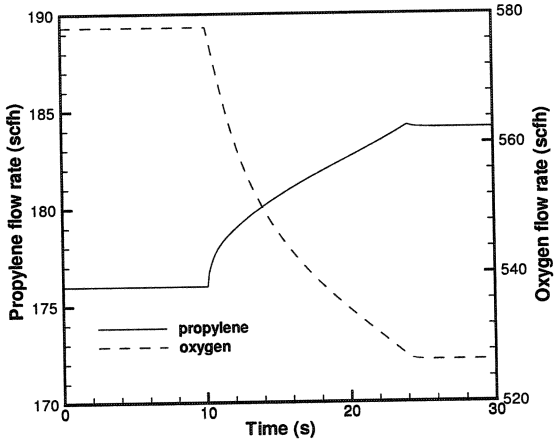


(c)

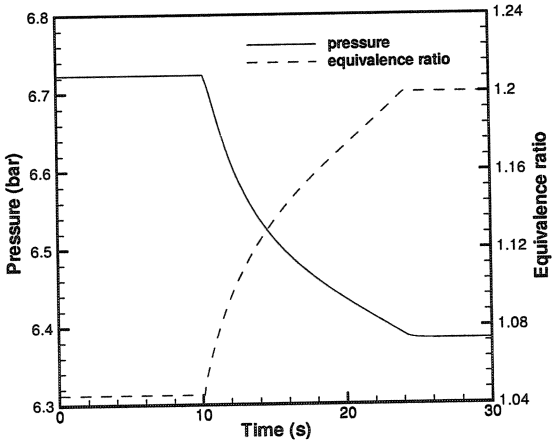
Figure 6.7: Profiles of (a) controlled outputs (average particle velocity and melting ratio), (b) manipulated inputs (flow rate of propylene, oxygen and air), and (c) pressure and equivalence ratio in the presence of 10% decrease in spray distance.



(a)

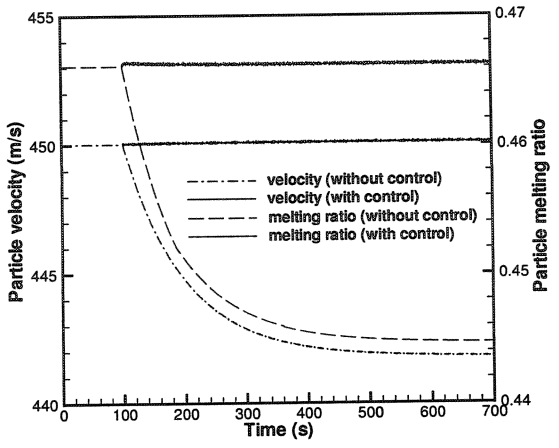


(b)

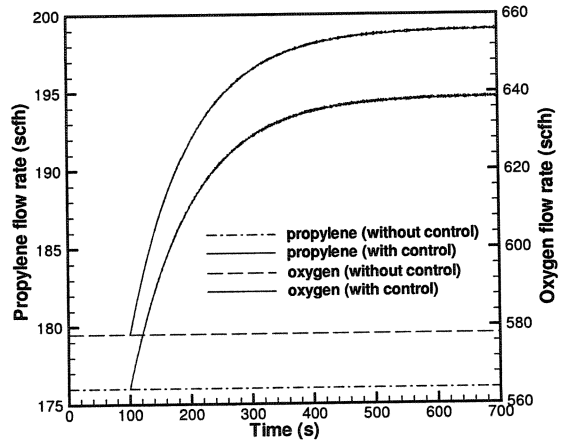


(c)

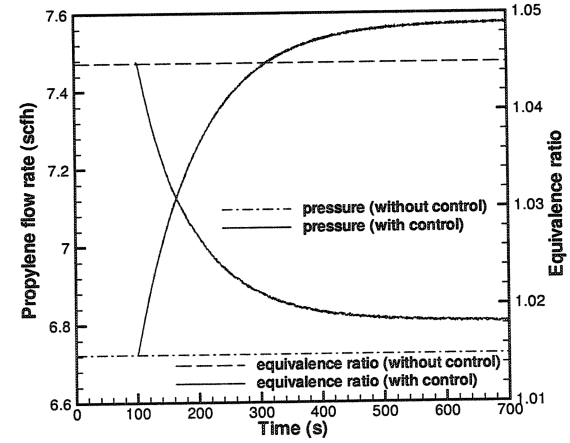
Figure 6.8: Profiles of (a) controlled outputs (average particle velocity and melting ratio), (b) manipulated inputs (flow rate of propylene, oxygen and air), and (c) pressure and equivalence ratio in the presence of 10% increase in spray distance.



(a)



(b)



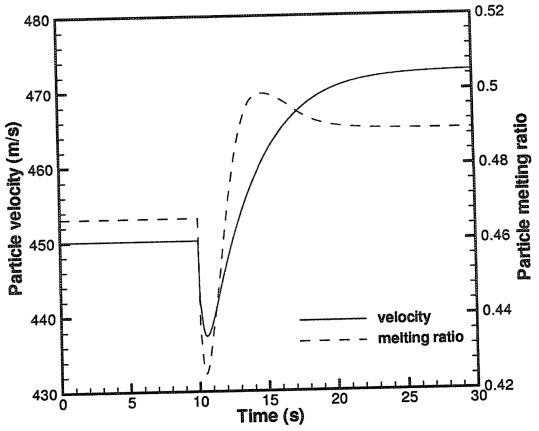
(c)

Figure 6.9: Profiles of (a) controlled outputs (average particle velocity and melting ratio), (b) manipulated inputs (flow rate of propylene, oxygen and air), and (c) pressure and equivalence ratio in the presence of variation in powder size distribution.

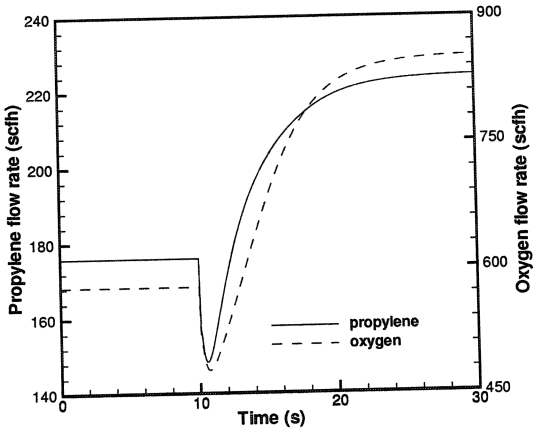
with respect to measurement errors, we implemented the developed control system on the process model under the request of 5% increase in average particle melting ratio set-point value and 5% increase in the average particle velocity set-point value at time $t = 10$ sec but assuming that there are errors in the values of average velocity and degree of melting used in the controller. In the closed-loop simulation, we assume that the estimation errors follow an exponentially-decaying function with an initial error of 10%. The corresponding controlled and manipulated variables are given in Figure 6.10. The results show that the desired control objective of 5% change in the set-point values is eventually achieved (compare the controlled output profiles of Figures 6.6 and 6.10); this demonstrates that the proposed formulation of the control problem is robust with respect to measurement errors. The readers may refer to [86] for model-based estimation and control of particle velocity and melting in the HVOF thermal spray process.

6.3 Summary

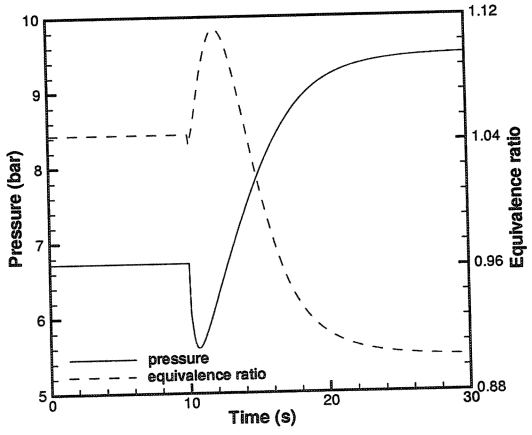
This work presents the modeling and control of HVOF thermal spray processing of WC-Co coatings. The simulation results show that the particle melting degree and the particle velocity, which play very important roles in the coating microstructure formation, can be adjusted by the equivalence ratio and the chamber pressure. The control problem is then formulated as the one of regulating volume-based averages of particle velocity and melting degree at the point of impact on substrate by manipulating the gas flow rate of air, oxygen and fuel at the entrance of the thermal spray gun, through which the pressure and oxygen/fuel ratio can be independently adjusted. A feedback control system is developed and applied to a detailed mathematical model of the process. Closed-loop simulations show that the proposed feedback controller is ef-



(a)



(b)



(c)

Figure 6.10: Profiles of (a) controlled outputs (average particle velocity and melting ratio), (b) manipulated inputs (flow rate of propylene, oxygen and air), and (c) pressure and equivalence ratio under the request of 5% increase in particle velocity and 5% increase in melting ratio - Closed-loop simulation in the presence of measurement error.

fective in driving the controlled outputs to the desired set-point values and attenuates the effect of various external disturbances in the operating environment.

Chapter 7

CFD Modeling and Analysis of HVOF Thermal Spray Process

This chapter[1] focuses on multiscale modeling and analysis of the HVOF thermal spray process. A hybrid (deterministic/stochastic) fundamental model is proposed to model the major physicochemical processes involved in an industrial HVOF thermal spray process (Diamond Jet hybrid gun, Sulzer Metco, Westbury, NY). The model includes continuum type differential equations that describe the evolution of gas and particle temperature and velocity, and a rule-based stochastic simulator that predicts the evolution of coating microstructure. On the macroscopic gas/particle dynamics side, the Reynolds and Favre-averaged Navier-Stokes equations and energy balance equations are solved with the renormalization group (RNG) k-ϵ turbulence model, and the particle trajectories, temperature histories and melting degrees are determined using the 4th order Runge-Kutta method. On the microscopic particle deposition process, the formation of coating microstructure is captured by certain rules that encapsulate the main physical features of particle deposition, deformation, solidification and coating

[1]Chapter 7 is based on [85].

growth. Based on the proposed model, a detailed comprehensive parametric analysis is carried out to study the relationship between the key process parameters and the particle inflight behavior as well as the resulting coating properties.

7.1 Introduction

The last two decades have witnessed the wide application of the High Velocity Oxygen-Fuel (HVOF) thermal spray technology as a means of processing coatings of cermets, metallic alloys and composites. Using the thermal energy produced by the combustion of fuel with oxygen to heat and propel the powder particles, which subsequently hit the substrate in a molten/semi-molten state and with a high velocity, the HVOF thermal spray provides a highly efficient way of coating processing to modify the surface properties of a substrate to extend product life, increase performance and reduce maintenance costs. Recently, there is an increasing interest in the HVOF thermal spray processing of nanostructured coatings, which owes to its unique process characteristics - very high gas/particle velocity and relatively low gas/particle temperature, when compared to those in plasma spray process. On the one hand, the extremely high particle velocity helps to densify the coating and to increase the deposition rate. On the other hand, the very short residence time in the relatively low temperature gas flame makes the powder particles highly plastic and superheating or vaporization is prevented [17, 19, 84, 83, 86].

Generally speaking, the physical properties of a thermally sprayed coating are strongly influenced by the microstructure of the deposit, which, in turn, depends to a large extent on the physical and chemical states of particles at the point of impact on the substrate, such as velocity, temperature, degree of melting and oxidant content. These variables, however, are strongly dependent on several key process parameters

including the fuel/oxygen ratio, total gas flow rate, spray distance and powder size distribution [87]. In order to improve coating performance, much experimental work has been done in the last decade to study the effect of these key process parameters on the physical and mechanical properties of HVOF thermally sprayed coatings (e.g., [30, 43, 47, 54, 96, 89]). The optimization of process parameters involved in these works usually relies on the conventional Taguchi method, which uses a set of orthogonal arrays that stipulates the way of conducting the minimal number of experiments that could give the full information of all the factors affecting the coating performance parameters [30]. This approach is expensive but reliable for a specific HVOF thermal spray process. However, a lack of fundamental understanding of the dynamics of the gas and particle behavior as well as of the microscopic deposition process significantly restrict its applicability because, the experimentally derived "optimal" solution may be questionable when it is applied to another thermal spray process in which some important parameters, such as the nozzle configuration, powder or fuel type, etc., are different [17]. It is in this context that the computational fluid dynamical (CFD) analysis of gas dynamics and particle inflight behavior within a HVOF thermal spray system is of great importance. Coordination between theoretical CFD modeling and experimental efforts will be mutually benefit to both investigations. The experiments provide validation of the theoretical process model, and in turn, a validated process model predicts the direction where further experiments can be done to improve process performance.

From a modeling point of view, the HVOF thermal spray process is very complex because it involves combustion, turbulence, compressible flow, multiphase interactions, subsonic/supersonic transitions and droplet deformation and solidification etc. There are four main physicochemical process occurring in the HVOF thermal/flow

field: transformation of gas chemical energy into thermal energy by the combustion of the fuel, conversion of gas thermal energy into kinetic energy of the burning gases by passing through the nozzle, transfer of momentum and heat from the gas to the powder particles, and conversion of particle kinetic and thermal energy into internal energy. It is widely acknowledged that the higher the particle velocity, the denser the coating. In order to transfer as much kinetic energy as possible to the particulate phase from the gas phase, the flow is typically maintained at supersonic conditions outside of the torch. This is realized by the so called "Laval nozzle", or convergent-divergent nozzle. In the convergent section, the flow is accelerated continuously and reaches sonic velocity at the throat of the nozzle. As long as a enough nozzle pressure ratio (NPR) is maintained, the flow will be further accelerated to supersonic sonic velocity in the divergent section. At the throat of the nozzle, the flow is choked, and therefore, the mach number is one [114]. Some types of HVOF thermal spray gun has only a truncated nozzle, for example, Diamond Jet (DJ), Praxair HV2000, etc. and the flow at the exit of the torch is sonic. In the external flow field, the free jet adjusts to the ambient pressure by a series of expansion and compression waves alternatively occurring along the centerline axis. During expansion, the flow is accelerated and the gas temperature and pressure decrease. During compression, the flow is decelerated and the gas temperature and pressure increase. Depending on the values of the pressure at the gun exit and ambient pressure, the flow condition at the exit of the gun may be underexpanded ($P_e > P_a$), ideally expanded ($P_e = P_a$) or overexpanded ($P_e < P_a$). At underexpanded flow conditions, the free jet expands immediately upon entering the ambient environment and is accelerated further during expansion. At overexpanded flow conditions, the opposite process occurs. Previous studies of CFD modeling and analysis of several different HVOF thermal spray processes are summarized in Table 7.1. Most of them have underexpanded flow at the exit of the gun

Table 7.1: Summary of previous CFD modeling work.

References	Gun type	Combustion model	Exit condition
[111, 120, 110]	Metco DJ	two-step reduced kinetics with eddy dissipation model	M=1, underexpanded
[14]	Tafa JP-5000	equilibrium with finite reaction kinetics	M=2, underexpanded
[106, 107]	Metco DJ	infinite reaction rate with equilibrium chemistry	M=1, underexpanded
[139]	Tafa JP-5000	instanetateous equilibrium in the chamber and frozen flow along the nozzle and barrel	M=2, underexpanded
[50]	Metco DJ rotating wire	infinite reaction rate with equilibrium chemistry	M=1.7, underexpanded
[95]	Metco DJ rotating wire	finite reaction rate with equilibrium stoichiometry	M=1.7, underexpanded
[48]	Praxair HV2000	finite reaction rate with equilibrium stoichiometr	M=2, underexpanded
[19, 18]	Metco DJ Hybrid	infinite reaction rate with equilibrium chemistry	M=2, underexpanded (under baseline conditions)
[32]	Metco DJ Hybrid	four-step reduced kinetics with eddy dissipation model	M=2, overexpanded

except [32]. However, in a Diamond Jet hybrid HVOF thermal spray process (Sulzer Metco, Westbury, NY), which is of interest in this work, it is designed to have overexpanded flow conditions at the exit of the torch [101] in order to achieve a higher gas velocity. Moreover, the particle melting behavior, which plays a very important role in the formation of coating microstructure [87, 119], has never being tried by existing CFD investigations. Finally, multi-scale modeling of the HVOF thermal spray process, which includes the macroscopic two-phase flow and the microscopic deposition process, is rare in the literature.

Motivated by the above, in this work, we focus on the multi-scale modeling and

analysis of gas dynamics, particle inflight behavior and coating microstructure formation in the industrial Diamond Jet hybrid HVOF thermal spray process. The gas thermal and flow fields are solved by Eulerian approach and the particle velocity, temperature and degree of melting by Lagrangian approach. On the gas dynamics side, we solve the Reynolds and Favre-averaged Navier-Stokes equations. Due to the high Reynolds number and the large pressure gradient in the nozzle, the renormalization group (RNG) k-ϵ turbulence model is used with the non-equilibrium wall function treatment to enhance the prediction of the wall shear and heat transfer. The eddy dissipation model, which assumes the reaction rate is limited by the turbulent mixing rate, is employed to address the chemistry issues. The governing mass, momentum and energy balance equations together with the idea gas state equation are solved at first using a first-order upwind scheme to get to a convergent solution and then a second-order upwind scheme to capture the shock diamonds that occur in the external flow field. On the particle dynamics side, we solve the equations that describe the particle trajectories, temperature histories and melting degrees using the 4th order Runge-Kutta method. The formation of coating microstructure is modelled by stochastic simulation, in which certain basic rules are applied to encapsulate the main physical features involved in the deposition process. Based on the proposed model, a detailed comprehensive parametric analysis is carried out to study the relationship between the key process parameters and the particle inflight behavior as well as the resulting coating properties.

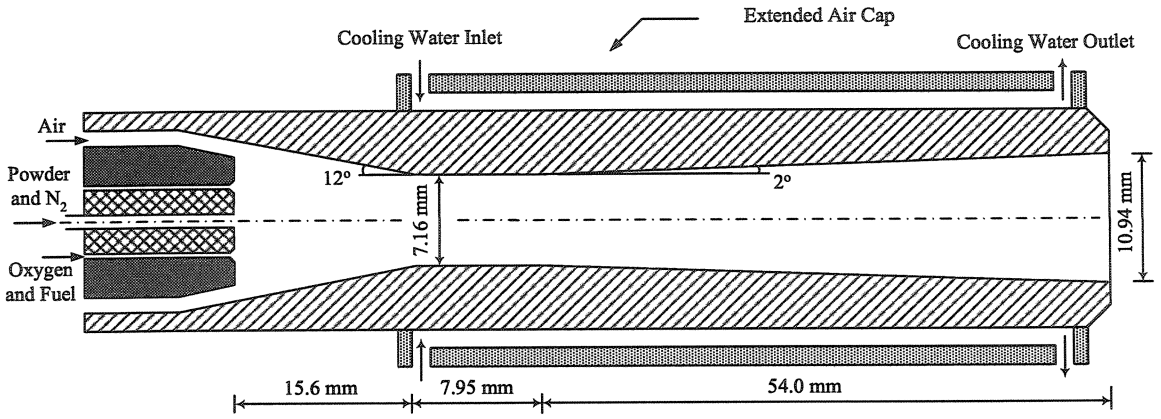


Figure 7.1: Schematic diagram of the Diamond Jet Hybrid Thermal Spray Gun.

7.2 Fluid dynamics

7.2.1 Torch geometry

Figure 7.1 shows a schematic diagram of the Diamond Jet hybrid gun. The fuel gases (typically propylene or hydrogen), which are thoroughly mixed with oxygen through a siphon system, are fed to the air cap, where they react to produce high temperature combustion gases. The exhaust gases, together with the air injected from the annular inlet orifice, expand through the nozzle to reach supersonic velocity. The air cap is cooled by both water and air ("hybrid") to prevent from being melted. The powder particles are injected from the central inlet hole using nitrogen as the carrier gas. Consequently, rapid momentum and heat transfer between the gas and the powder particles leads to acceleration and heating of the powder particles. The molten or semi-molten particles exit the air cap and move towards the substrate. The particles hit the substrate, cool and solidify, forming a thin layer of dense and hard coating.

The convergent-divergent nozzle consists of three zones: (1) convergent zone: a conical channel with a convergent half angle of 12 degree and a diameter of 15.9 mm at the beginning and 7.16 mm at the end. (2) cylindrical zone: a cylindrical channel

with a diameter of 7.16 *mm* and a length of 7.95 *mm*. (3) divergent zone: a conical channel with a divergent half angle of 2 degree and a diameter of 7.16 *mm* at the beginning and 10.94 *mm* at the end. The powders are injected into the torch in the centerline with with nitrogen as the carrier gas through a circular tube with a radius of 0.75 *mm*. The premixed fuel and oxygen enter the torch through an annulus with an inner radius of 4.02 *mm* and a width of 0.53 *mm*. The air is injected into the torch through an annulus with an inner radius of 6.68 *mm* and a width of 1.27 *mm*.

7.2.2 Governing equations

In the macroscopic HVOF flow filed, the three major physicochemical processes - transformation of chemical energy into thermal energy by the combustion of the fuel, conversion of thermal energy into kinetic energy of the burning gases by passing through the nozzle, and transfer of momentum and heat from the gases to the powder particles, are actually coupled together. To simplify the analysis, the process model used in this work is based on the one-way coupling assumption, i.e., the existence of particles has a minimal influence on the gas dynamics while the particle in-flight behavior is dependent on the gas thermal/flow field. This assumption is reasonably accurate because the particle loading in the HVOF thermal spray process is typically less than 4% [139]. In addition, in order to make the reactive flow process much easier to handle, a commonly used assumption that the chemical reaction rate is much faster than the time-scale associated with the gas dynamics [17], is employed here. Based on this, the eddy dissipation model (will be shown later) with a stoichiometry derived from an instantaneous equilibrium code [87] is employed to model combustion. Regarding the role of the air stream, it is assumed that all the oxygen coming from the air participates in the reaction, as did in several previous papers [32, 47, 111, 87].

Gourlaouen et al. [47] pointed out that the airflow mixing with the oxygen/propylene mixture is more effective in the currently used Diamond Jet hybrid gun (which is the process under consideration in this work) than the previous Diamond Jet gun, as implied by the "water-cooled" (not "air-cooled") nozzle. It is also assumed that all the combustion gases obey ideal gas law.

The governing equations for the HVOF thermal spray process are conservation of mass, momentum and energy. The direct solution of these conservation equations for such a high-Reynolds-number turbulent compressible flow is far beyond the current computation capacity. However, by applying Reynold or Favre averaging, these equations can be simplified such that the small-scale turbulent fluctuations do not have to be directly simulated, and consequently, the computation efforts can be significantly reduced. In Reynolds or Favre averaging, the solution variables are decomposed into the mean (time-averaged or density-averaged) and fluctuating components:

Reynolds (or time) averaging

$$\phi = \bar{\phi} + \phi', \text{ with } \bar{\phi} = \frac{1}{\Delta t}\int_{t_0}^{t_0+\Delta t} \phi \, dt \text{ and } \bar{\phi}' = 0 \tag{7.1}$$

Favre (or density) averaging

$$\phi = \tilde{\phi} + \phi'', \text{ with } \tilde{\phi} = \frac{\overline{\rho\phi}}{\bar{\rho}} \text{ and } \tilde{\phi}'' = 0 \tag{7.2}$$

Substituting expressions of this form for the variables into the instantaneous continuity and momentum equations, and taking a time average of pressure and density and density average of all the other quantities yield the following equations written in the Cartesian tensor form:

$$\frac{\partial \bar{\rho}}{\partial t} + \frac{\partial}{\partial x_i}(\bar{\rho}\tilde{v}_i) = 0 \tag{7.3}$$

and

$$\frac{\partial}{\partial t}(\bar{\rho}\tilde{v}_i) + \frac{\partial}{\partial x_j}(\bar{\rho}\tilde{v}_i\tilde{v}_j) = -\frac{\partial \bar{p}}{\partial x_i} + \frac{\partial}{\partial x_j}\left[\mu\left(\frac{\partial \tilde{v}_i}{\partial x_j} + \frac{\partial \tilde{v}_j}{\partial x_i} - \frac{2}{3}\delta_{ij}\frac{\partial \tilde{v}_l}{\partial x_l}\right)\right] + \frac{\partial}{\partial x_j}(-\overline{\rho v_i'' v_j''}) \tag{7.4}$$

where ρ is the density, p is the pressure, x is the coordinate, μ is the molecular viscosity, δ_{ij} is the Kronecker delta and i, j and l are the indices. $-\overline{\rho v_i'' v_j''}$ is the Reynolds stress term representing the the effect of turbulence, which can be related to the mean velocity gradients according to the Boussinesq hypothesis [56]:

$$-\overline{\rho v_i'' v_j''} = \mu_t\left(\frac{\partial \tilde{v}_i}{\partial x_j} + \frac{\partial \tilde{v}_j}{\partial x_i}\right) - \frac{2}{3}\left(\bar{\rho}k + \mu_t\frac{\partial \tilde{v}_l}{\partial x_l}\right)\delta_{ij} \tag{7.5}$$

where μ_t is the turbulent viscosity and k is the turbulence kinetic energy.

Due to the high Reynolds number and the large pressure gradient in the nozzle, the RNG $k-\epsilon$ turbulence model is used with the non-equilibrium wall function treatment to enhance the prediction of the wall shear and heat transfer. The RNG $k-\epsilon$ turbulence model has the following form:

$$\frac{\partial}{\partial t}(\bar{\rho}k) + \frac{\partial}{\partial x_i}(\bar{\rho}\tilde{v}_i k) = \frac{\partial}{\partial x_j}\left[\alpha_k(\mu + \mu_t)\frac{\partial k}{\partial x_j}\right] + G_k - \bar{\rho}\epsilon - Y_M \tag{7.6}$$

and

$$\frac{\partial}{\partial t}(\bar{\rho}\epsilon) + \frac{\partial}{\partial x_i}(\bar{\rho}\tilde{v}_i\epsilon) = \frac{\partial}{\partial x_j}\left[\alpha_\epsilon(\mu + \mu_t)\frac{\partial \epsilon}{\partial x_j}\right] + C_{1\epsilon}\frac{\epsilon}{k}G_k - C_{2\epsilon}\bar{\rho}\frac{\epsilon^2}{k} - R_\epsilon \tag{7.7}$$

where ϵ is the turbulence dissipation rate, G_k is the generation of turbulence kinetic energy due to the mean velocity gradients ($G_k = \mu_t S^2$, where $S = \sqrt{2S_{ij}S_{ij}}$ and $S_{ij} = \frac{1}{2}\left[\frac{\partial v_j}{\partial x_i} + \frac{\partial v_i}{\partial x_j}\right]$), Y_M is the contribution of the fluctuating dilatation in compressible turbulence to the overall dissipation rate ($Y_M = 2\rho\epsilon\mathbf{M}_t^2$, where $\mathbf{M}_t$ is the turbulent Mach number calculated by $\mathbf{M}_t = \sqrt{k}/a$ and a is the sonic velocity), R_ϵ is the additional term in the ϵ equation calculated by:

$$R_\epsilon = \frac{C_\mu\eta^3(1-\eta/\eta_0)}{(1+\beta\eta^3)}\rho\frac{\epsilon^2}{k} \tag{7.8}$$

with $\eta = Sk/\epsilon$ and η_0=4.38, β=0.012. $C_{1\epsilon}$ =1.42, $C_{2\epsilon}$ =1.68, and α_k and α_ϵ are the inverse effective Prandtl numbers for k and ϵ, which are computed by the following formula derived from the RNG theory:

$$\left|\frac{\alpha - 1.3929}{\alpha_0 - 1.3929}\right|^{0.6231} \left|\frac{\alpha + 2.3929}{\alpha_0 + 2.3929}\right|^{0.3679} = \frac{\mu}{\mu + \mu_t} \tag{7.9}$$

In the high Reynolds number limit ($\frac{\mu}{\mu + \mu_t} \ll 1$), $\alpha_k = \alpha_\epsilon = 1.393$.

The energy conservation is described by

$$\begin{aligned} &\frac{\partial}{\partial t}(\bar{\rho}E) + \frac{\partial}{\partial x_i}\left[\tilde{v}_i(\bar{\rho}E + \bar{p})\right] \\ = &\frac{\partial}{\partial x_j}\left[\alpha c_p(\mu + \mu_t)\frac{\partial T}{\partial x_j} + \tilde{v}_i(\mu + \mu_t)\left(\frac{\partial \tilde{v}_j}{\partial x_i} + \frac{\partial \tilde{v}_i}{\partial x_j} - \frac{2}{3}\delta_{ij}\frac{\partial \tilde{v}_l}{\partial x_l}\right)\right] + S_E \end{aligned} \tag{7.10}$$

where T is the temperature, E the total energy per unit mass, S_E is the source term and α is calculated from Eq. 7.9 but with $\alpha_0 = 1/Pr$, where Pr is the Prandtl number.

7.2.3 Eddy dissipation Model

The combustion of hydrogen is a very complex process. As the temperatures goes beyond 2000 K, CO_2 and H_2O will dissociate into a number of species with light molecular weight due to strong thermal atomic vibration [19]. Previous studies have shown that the model which does not account for the dissociation of combustion products will overpredict the combustion temperature [48, 87, 106]. To accurately model the combustion process with tolerable computational efforts, several assumptions were usually made to address the chemistry issues, which can be classified into the following three categories: (1) reduced kinetics [111, 120, 110, 32], (2) infinite reaction rate with equilibrium chemistry [106, 107, 139, 50, 19, 18], and (3) finite reaction rate with equilibrium chemistry [14, 95, 48]. Generally speaking, the finite rate chemistry model is better than the infinite rate one since the latter may result in solution instabilities

[95]. The eddy dissipation model, which assumes that reactions occur infinitely fast and the reaction rate is limited by the turbulent mixing rate of fuel and oxidant, is employed in this work. In many practical situations like the HVOF thermal spray process, the eddy-dissipation model describes the limiting rate and thus a knowledge of accurate Arrhenius rate data, is not needed. This conclusion has been validated by experimental observations [32]. Based on the fact that the residence time of gas in the combustion chamber (convergent section of the nozzle) is much longer than the subsequent parts, it is assumed that most of the reaction occurs in the chamber and the reaction moves forward following an equilibrium chemistry model. Assuming the air is composed of oxygen and nitrogen only, the reaction considered in this work is of the following form:

$$\begin{aligned} & \varphi C_3H_6 + 4.5O_2 \\ = \; & \xi_1 CO + \xi_2 CO_2 + \xi_3 H + \xi_4 H_2 + \xi_5 H_2O + \xi_6 O + \xi_7 OH + \xi_8 O_2 \end{aligned} \tag{7.11}$$

As we pointed out before, the stoichiometric coefficients of each component in the above reaction formula are determined using an instantaneous equilibrium model. However, it is worth noting that the fraction of each species in the combustion gas mixture relies on the combustion pressure, which, in turn, is dependent on the gas flow rate of oxygen, propylene, air and carrier gas at the entrance of torch. Therefore, iteration is needed to guarantee that the pressure used in deriving the stoichoimetry in Eq. 7.11 is consistent with the pressure eventually determined by CFD modeling. To have a good starting point, we use at first a one dimensional model [87] to calculate the combustion pressure based on the flow rate of each gas stream at the entrance of the HVOF torch, and then solve the stoichiometric coefficient involved in Eq. 7.11 using a chemical equilibrium code with the the combustion pressure equal to the partial pressure of oxygen and propylene [46]. Typically speaking, the pressure obtained by model in [87] is close to the one solved by CFD simulation and the work of trial and

error can be significantly reduced.

7.3 Particle dynamics

As we mentioned before, due to the very low particle loading, the coupling between the gas phase and the particulate phase is one-way, i.e., the fluid influences the particles via momentum transfer and heat transfer, but the particles have no influence on the gas phase. Therefore, the particle trajectories, temperature histories and melting degrees can be solved after the gas thermal/flow field is determined. Particle coagulation in the HVOF thermal spray process has not been reported in the literature, which might be explained by the following argument. Based on the analysis of Crowe et al. [28], the average interparticle spacing ratio in a gas flow field can be estimated by:

$$\frac{L_d}{d_p} = \left[\frac{\pi}{6}\frac{1+\kappa}{\kappa}\right]^{1/3} \tag{7.12}$$

where L_d is the distance between two particles and κ is the particle/gas mass flow rate ratio divided by the particle/gas density ratio. Usually the particle loading is about 4%, the density ratio is about 10^{3-4}, therefore L_d/d_p is about 20-50, which implies that the individual powder particles can be considered isolated from each other. Therefore, in this work, we assume that particle coagulation is negligible and the powder size distribution does not change during flight.

Firstly, the motion of particles in the gas flow field is governed by Newton's law, which can be written as

$$m_p\frac{dv_p}{dt} = \sum_i F_i \tag{7.13}$$

In typical HVOF thermal spray conditions, the major force acting on a particle is the drag force, and other forces, such as the basset history term, gravitational force,

thermophoresis force, and forces caused by pressure gradient and added mass etc., can be neglected [111, 109]. Therefore, the equation of particle motion has the following form:

$$m_p \frac{dv_p}{dt} = \frac{1}{2} C_D \rho_g A_p (v_g - v_p)|v_g - v_p|, \quad v_p = v_{p0} \tag{7.14a}$$

$$\frac{dx_p}{dt} = v_p, \quad x_p = x_{p0} \tag{7.14b}$$

where m_p is the mass of the particle, v_p is the axial velocity of the particle, t is the time, A_p is the projected area of the particle on the plane perpendicular to the flow direction, ρ_g is the density of the gas, C_D is the drag coefficient, and x_p is the position of the particle. The absolute sign in the relative velocity between particle and gas implies that a particle is accelerated if its velocity is less than that of the gas and decelerated otherwise. In order to take into consideration the fact that many powders used in the HVOF process are not spherical, a formula for the drag coefficient C_D, which accounts for the particle shape using the concept of sphericity ϕ (defined as the ratio of the surface area of a sphere with equivalent volume to the actual surface area of the particle) is used in this work, which has the following form [39]:

$$\frac{C_D}{K_2} = \frac{24}{ReK_1K_2}\left[1 + 0.1118(ReK_1K_2)^{0.6567}\right] + \frac{0.4305}{1 + 3305/ReK_1K_2} \tag{7.15}$$

where K_1 and K_2 are two sphericity-related factors. The local Reynolds number (Re) for this two phase flow problem is defined based on the relative velocity $Re = d_p \mid v_g - v_p \mid \rho_g/\mu_g$, where d_p is either the particle diameter if the particle is spherical or an appropriate equivalent diameter if the particle is not spherical and μ_g is the gas viscosity. The above formula for drag coefficient is recommended by Cheng et al. [18].

In the HVOF thermal spray process, the Biot number of the particles (ratio of heat transportation coefficient on boundary to internal heat conductance) is typically less

than 0.1 for good heat conducting materials (see analysis in subsection 7.4.2), which means that the particles are heated with negligible internal resistance and that the temperature gradients inside them can be ignored [40]. Consequently, the equation describing the heat transfer between a single particle and the gas reduces to a first-order ordinary differential equation. Depending on the value of particle temperature, different equations are used. With the assumption of negligible particle vaporization, the particle heating can be described as follows:

$$m_p c_{p_p} \frac{dT_p}{dt} = \begin{cases} hA'_p(T_g - T_p) + S_h, & (T_p \neq T_m) \\ 0, & (T_p = T_m) \end{cases}, \quad T_p = T_{p_0} \tag{7.16a}$$

$$\Delta H_m m_p \frac{df_p}{dt} = \begin{cases} hA'_p(T_g - T_p) + S_h, & (T_p = T_m) \\ 0, & (T_p \neq T_m) \end{cases}, \quad f_p = f_{p_0} \tag{7.16b}$$

where T_p is the temperature of the particle, A'_p is the surface area of the particle, T_m is the melting point of the particle, ΔH_m is the enthalpy of melting and f_p is the ratio of the melted mass to the total mass of the particle ($0 \leq f_p \leq 1$). S_h is the source term including heat transfer due to radiation ($\varepsilon\sigma A'_p(T_g^4 - T_p^4)$) and oxidation. The heat transfer coefficient h is computed by the Ranz-Marshall empirical equation [6]:

$$h = \frac{\lambda_g}{d_p}\left[2 + 0.6Re^{\frac{1}{2}}Pr^{\frac{1}{3}}\right] \tag{7.17}$$

where the Prandtl number (Pr) is calculated by $Pr = c_{p_g}\mu_g/\lambda_g$. The thermodynamic and transport properties of the mixture are calculated using the formulas provided in [46]. Note that in the HVOF thermal spray processing of particles consisting of carbides with binding metals, such as the WC-Co powders used in this work, only the latter may experience a molten state because the gas temperature in a conventional HVOF thermal spray process is not high enough to melt the carbides, whose melting point is very high (i.e. 2870 ^{0}C for tungsten carbide) [122]. In such a case, the particle melting equation in Eq. 7.16 is modified such that only the fusion of metals

might occur in the gas thermal field. In the present work, the melting degree of particles represents the one of the binder (Cobalt) instead of the whole particulate phase. Since the gas properties, such as temperature, velocity, and viscosity etc. are all functions of x_p, if we let $\vec{y} = [v_p, x_p, T_p, f_p]$, Eq. 7.14 and 7.16 can be converted to $\frac{d\vec{y}}{dt} = g(\vec{y})$, $\vec{y}(0) = \vec{y}_0$. This initial value problem can be easily solved by the 4th order Runge-Kutta method provided that the gas fluid/thermal field is known.

7.4 Results and discussion

7.4.1 Analysis of gas dynamics

The process model of gas dynamics was implemented into Fluent, a commercial CFD software, and was solved by Finite Volume method. The computational domain is shown in Figure 7.2. Due to the symmetric geometry of the torch, a one-half, two-dimensional grid is used. In prescribing the boundary conditions, the flow is radially symmetric at the centerline, in addition, at the openings of each delivery tube, the mass flow rate of oxygen, propylene, air and nitrogen are specified. The walls in the torch are all assumed to be maintained at the constant temperature of 400 K. In the external flow field, the radial extent of the computational domain is chosen to 50 mm (more than 9 times the radius of the torch exit), which is sufficiently far from the jet outer radius and thus pressure far-field conditions can be applied at the outer boundaries. At the outer boundary which is 0.3 m far away from the torch exit, a pressure outlet boundary condition is specified. Finally, the atmospheric pressure is assumed to be 1 atm. The computational grid consists of 30 radial and 80 axial nodes inside the torch and 45 radial and 200 axial nodes outside the torch. The grid is highly clustered near the exit of the torch in order to capture the shock diamonds in the external flow field and lowly clustered in the far field. The gas pressure, velocity

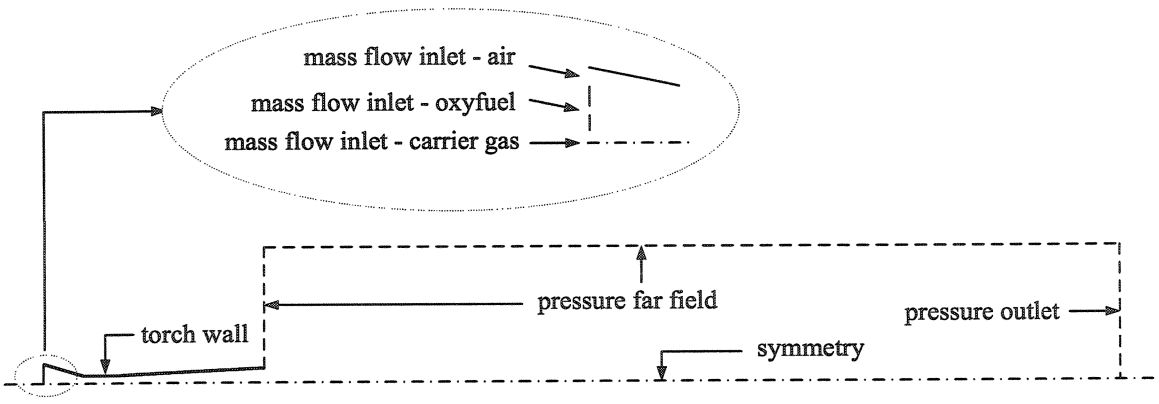


Figure 7.2: Computational domain and boundary conditions.

and temperature in the computational domain is initially patched using linear field functions to accelerate convergence. The governing mass, momentum and energy balance equations together with the idea gas state equation are solved at first using a first-order upwind scheme to get to a convergent solution and then a second-order upwind scheme to capture the shock diamonds that occur in the external flow field. The baseline gas flow rates of oxygen, propylene, air and carrier gas used in the CFD simulation is shown in the first row of Table 7.2, which is the recommended flow rate for the processing of Tungsten Carbides. It can be found out that the equivalence ratio (fuel/oxygen ratio divided by its stoichiometric value) is 1.045 and propylene is in excess. We first use a one-dimensional process model [87] to calculate the chamber pressure and then use a chemical equilibrium program code developed by Gordon and McBride [46] to get the reaction formula under a partial pressure of oxygen and propylene. Subsequently, we run the CFD simulation and compare the final pressure with the one used for deriving the reaction formula. Trial and error shows that the chamber pressure is about 6.0 atm and the partial pressure of oxygen and propylene is about 3.4 atm, under which the equilibrium stoichiometry is:

$$\begin{aligned} 1C_3H_6 + 4.307O_2 \quad \Rightarrow \quad & 1.903CO + 1.097CO_2 + 0.382H + 0.432H_2 \\ & +2.004H_2O + 0.388O + 0.745OH + 0.698O_2 \end{aligned} \tag{7.18}$$

Table 7.2: Specified gas flow rate for parametric analysis of Diamond Jet Hybrid HVOF gun.

Case	Propylene $(scfh)$	Oxygen $(scfh)$	Air $(scfh)$	Nitrogen $(scfh)$	$\dot{m}$ (g/s)	φ
1 (Baseline)	176	578	857	28.5	18.10	1.045
2	176	578	428	28.5	13.73	1.186
3	176	867	857	28.5	21.35	0.756
4	264	867	1286	28.5	27.01	1.045

Note propylene does not show up at the right hand side of the reaction formula under normal operating conditions. Furthermore, O_2 shows up in the right hand side of the reaction because it is not completely consumed under equilibrium condition.

The simulated contours and centerline profiles of static pressure, mach number, axial velocity and temperature in the internal and external fields are shown in Figure 7.3. In the combustion chamber (convergent section of the air cap), reaction of the pre-mixed oxygen and propylene results in an increase of gas temperature to higher than 3000 K and a high pressure of 6 atm is maintained. As the exhaust gases expand the convergent-divergent nozzle, the pressure decreases and the gas velocity increases continuously. At the throat of the nozzle, the Mach number is around 1. The gas is accelerated to supersonic velocity in the divergent section of the nozzle, and reaches a Mach number of 2 at the exit of the nozzle.

As we stated before, depending on the magnitude of the total temperature and total pressure at the chamber as well as the temperature and velocity at the nozzle exit, the flow condition at the exit of the nozzle may be underexpanded, ideally expanded or overexpanded. Our simulation shows that the pressure at the exit of the air cap is 0.6 atm, which implies the flow condition is actually overexpanded. The manufacturer, Sulzer Metco measured a gauge pressure of -4 $psig$ (-0.3 atm, or

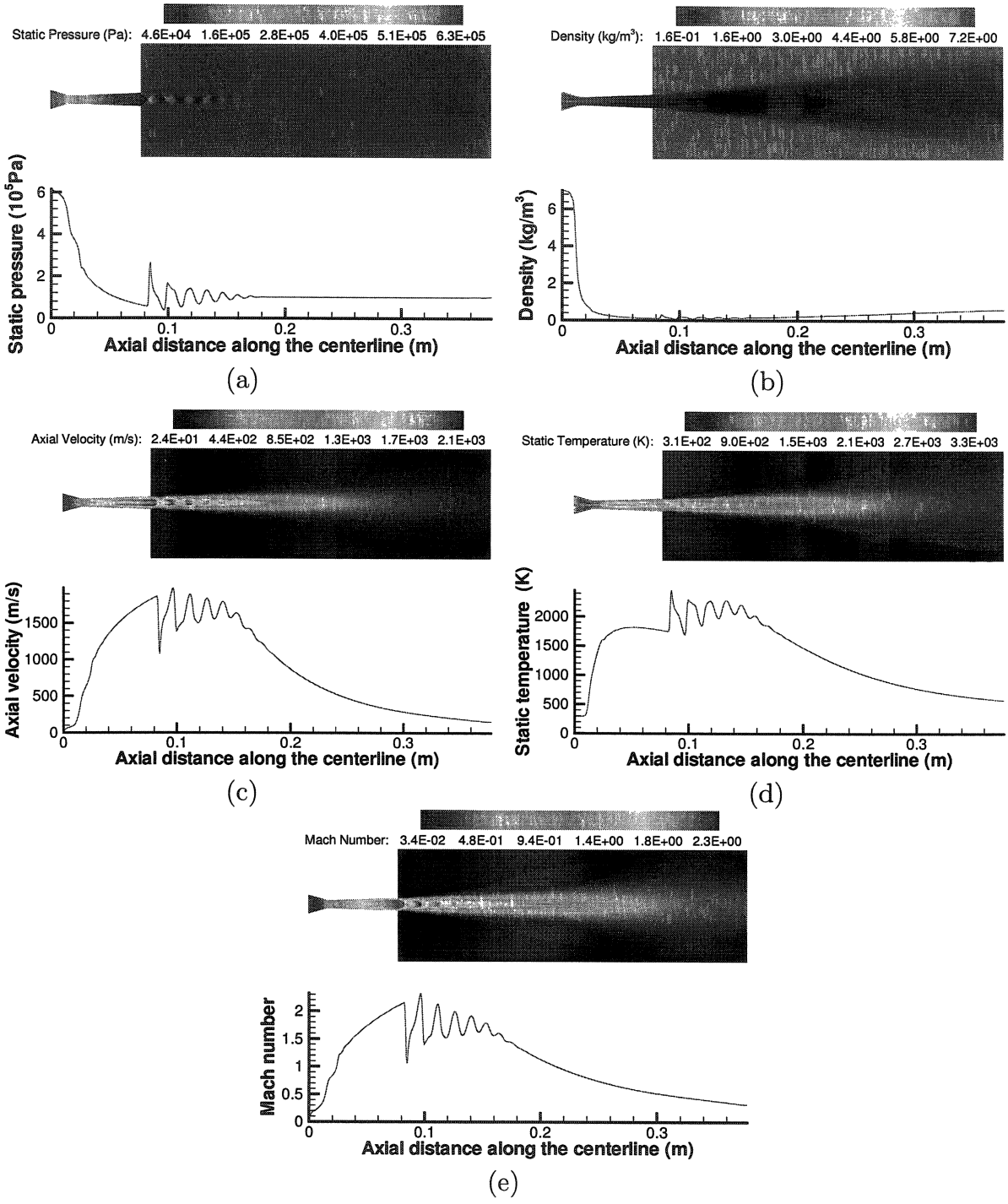


Figure 7.3: Contours of flooded gas properties (upper plot) and centerline profiles of gas properties (lower plot) - (a) static pressure (b) density (c) axial velocity (d) static temperature and (e) mach number.

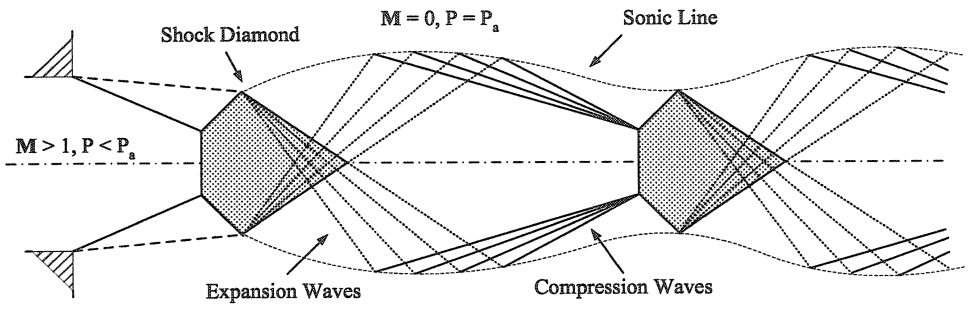


Figure 7.4: Schematic of wave structure in the overexpanded jet.

the absolute pressure is about 0.7 atm) at the nozzle exit under the same operating conditions [101], which partially validates the model assumptions applied in this work. In fact, the overexpanded flow condition gives a slightly higher gas velocity, and more kinetic energy can be transferred to the powders. The overexpanded flow pattern involved in the HVOF thermal spray process can be illustrated by Figure 7.4. At the exit of the nozzle, the shock front begins obliquely as a conical surface and is cut off by a "Mach shock disc" perpendicular to the axis. Behind the incident and Mach shock front, a reflected shock front and a jet boundary develop. As the reflected shock front meets the jet boundary, reflected expansion waves develop. These reflected expansion waves converge before reaching the opposite boundaries and give rise to shock fronts, which meet the jet boundary again and the whole process repeats. This periodic jet pattern is eventually blurred and dies out due to the action of viscosity at the jet boundary.

We note that although the gas temperature inside of the torch is very high, its value in the centerline, however, is less than that outside of the torch. This also implies that the external thermal field plays a very important role in particle heating. The contour of gas temperature in the external field is given in Figure 7.5. It is shown that the gas temperature is relatively low as it exits from the torch (about 1800 K). However, passing through the first shock leads to a sharp increase in the

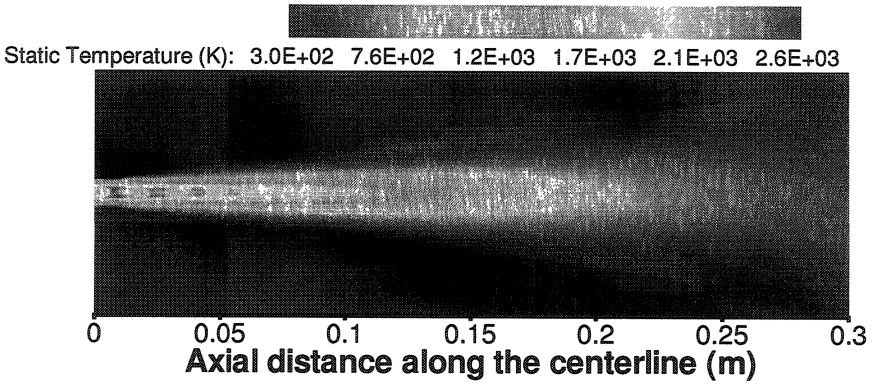


Figure 7.5: Contour of static temperature outside of the torch.

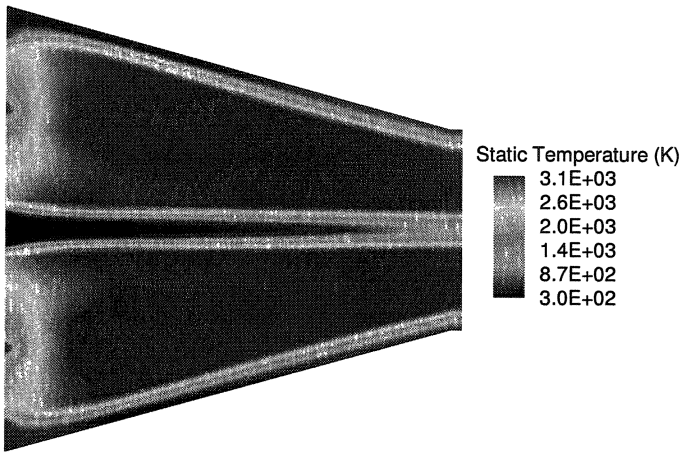


Figure 7.6: Contour of static temperature in the combustion chamber.

gas temperature (about 2600 K). The location of the first shock is 7 mm, which is a little higher than the reported measured value (5 mm) in which a similar operating condition but with a lower flow rate of propylene and nitrogen is used [32].

A previous study of Power et al. [111, 110] has shown the cooling effect of air in the former Diamond Jet gun (without extended air cap). This unique behavior can also be observed in the current Diamond Jet hybrid gun (with the extended air cap). It can be easily seen in Figure 7.6 that the hot flame is surrounded by the cooling air around the torch wall, thus protecting the hardware from being overheated.

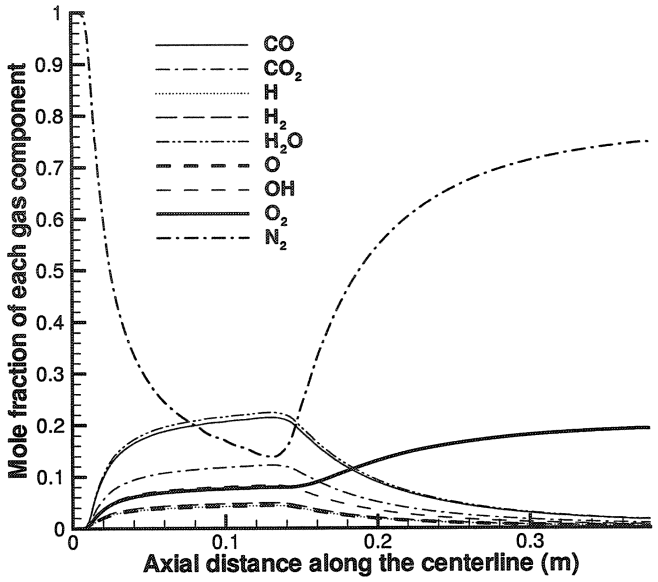


Figure 7.7: Mole fraction of each gas component along the centerline.

The solved mole fraction of each gas component is shown in Figure 7.7. In the first 1 cm, only nitrogen exists in the centerline, which comes from the carrier gas. Due to turbulent mixing, the mole fraction of nitrogen decreases gradually and the mole fraction of all the other species increases as the gas mixture passes through the convergent divergent nozzle. In the supersonic free jet, because of the entrainment of the air from the external environment, the mole fraction of both nitrogen and oxygen increases and eventually reaches a value of 0.75 and 0.20, at the 0.3 m standoff. It is also shown that the mole fraction of propylene is no more than 10^{-6} along the centerline, which implies propylene is almost exhausted by the combustion process, although the process is under fuel-rich condition. Instead, it is shown that the mole fraction of oxygen molecule and oxygen atom in the entire flow field is about 0.1 - 0.2, which implies the oxygen may have a differentiable influence on the particle composition and temperature at impact via particle oxidation.

Based on the proposed CFD model, a parametric analysis is performed to study the effect of gas flow rate on the gas dynamics, and the simulation results under different gas flow rates (see Table 7.2) are shown in Figure 7.8. The reaction formulas determined by the iterative procedure proposed in section 7.2.3 and used in the eddy-dissipation model for these four cases are shown in Table 7.3. Generally speaking, as the mass flow rate increases, the pressure will increase, which might be explained by the following equation:

$$\dot{m}_g = \rho_t v_t A_t = \frac{P_0}{\sqrt{T_0}} A_t \left[\frac{\gamma \bar{M}_{pr}}{R} \left(\frac{2}{\gamma+1} \right)^{(\gamma+1)/(\gamma-1)} \right]^{1/2} \tag{7.19}$$

where m_g is total mass rate, $\bar{M}_{pr}$ is the average molecular weight of the gas mixture after reaction, and T_0 and P_0 are the stagnation temperature and stagnation pressure, respectively. Since $\sqrt{T_0}$ varies much less than m_g, the pressure is approximately in proportion to the total mass flow rate. As the pressure increases, the equilibrium temperature of the reaction will go up if the equivalence ratio (fuel/oxygen ratio divided by its stoichiometric value) is kept the same. However, it is important to note that the flame temperature is primarily dependent on the equivalence ratio and high temperatures are achieved at equivalence ratios close to 1.2 [87], which may explain the fact that the gas temperature in case 2 is higher than the one in the other cases, although the total mass flow rate is the lowest. However, one of the most prominent consequences of increasing the total gas flow rate is that the velocity and temperature in the free jet can be maintained at high levels for a longer distance, which will certainly enhance the momentum transfer and heat transfer between the gas phase and the particulate phase. For example, in the last case, where the air, oxygen and fuel flow rates are 50% higher than those in the baseline conditions, the flow outside of the torch is nearly ideally expanded. As a result, both the centerline velocity and temperature are relatively constant inside the potential core of the jet,

Table 7.3: Reaction formula obtained from equilibrium chemistry.

Case	P	Reactants		Products							
	(bar)	C_3H_6	O_2	CO	CO_2	H	H_2	H_2O	O	OH	O_2
1	3.4	1	4.307	1.903	1.097	0.382	0.432	2.004	0.388	0.745	0.698
2	3.6	1	3.795	2.085	0.915	0.433	0.544	1.918	0.302	0.643	0.413
3	4.7	1	5.949	1.417	1.583	0.248	0.245	2.183	0.538	0.899	1.860
4	5.7	1	4.307	1.860	1.140	0.322	0.406	2.059	0.344	0.747	0.670

whose length is about 8.5 times the diameter of the torch exit. In addition, a relative low flow rate of the carrier gas will shorten the length of the initial cool zone in the chamber, which will certainly increase the particle temperature and in turn, affects the coating properties.

In [87, 88], we developed a simplified one dimensional mathematical model for the Diamond Jet hybrid thermal spray process. A comparison of the results obtained by the one dimensional model and the CFD model (see Figure 7.9) shows that the velocity and temperature predicted by the one dimensional model is higher than those predicted by the CFD model, especially in the convergent part of the torch. This can be explained by the large gradient of velocity, temperature and density in the combustion chamber, due to the mixing of the cold air and nitrogen and the high temperature combustion gases. In the chamber, a one dimensional model is insufficient to capture the multi-dimensional behavior of the gas phase, especially the temperature and the density (see Figures 7.3 and 7.6 for details). Moreover, because the flow at the exit of the torch is overexpanded but not ideally expanded, the velocity and temperature decay model derived from experiments cannot accurately describe the gas properties in the shock waves, where the centerline velocity and temperature fluctuate sharply. Finally, a one dimensional model cannot incorporate the influence of the substrate on the gas flow/thermal field, which will be shown in

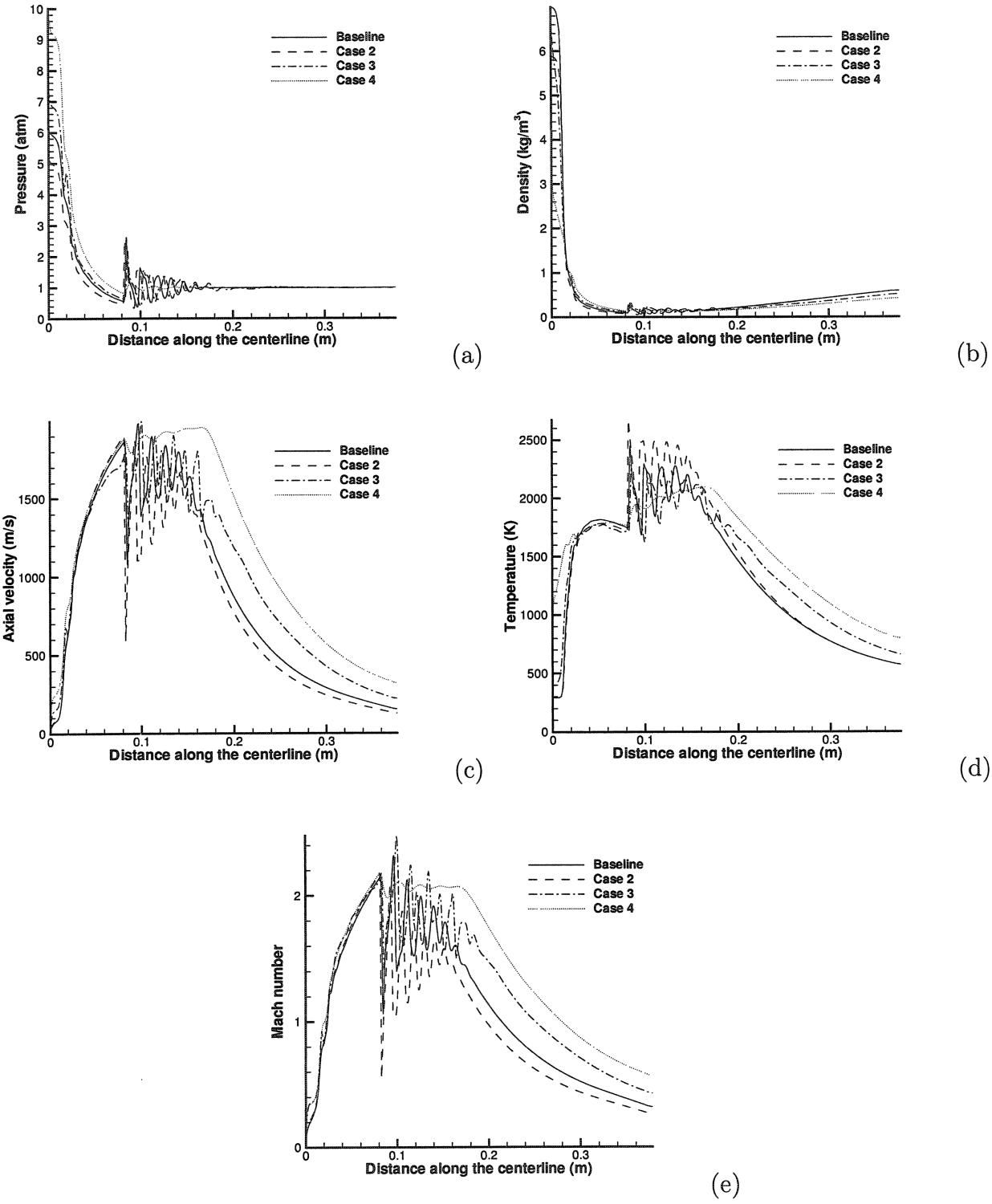
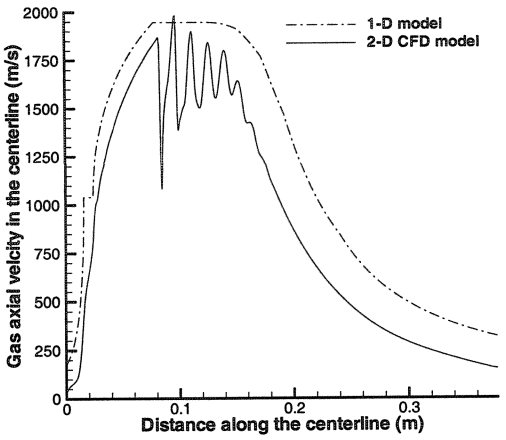


Figure 7.8: Influence of gas flow rates on gas properties - (a) static pressure, (b) density, (c) axial velocity, (d) static temperature, and (e) mach number in the centerline.

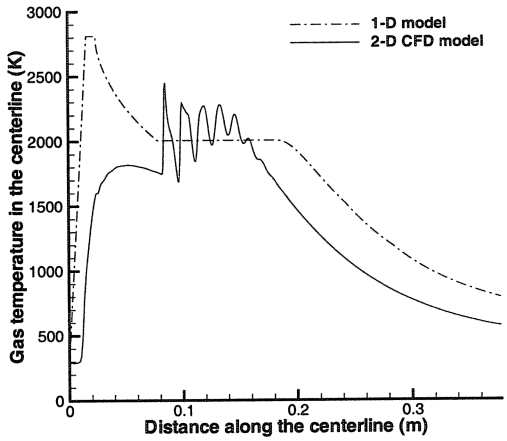
the next subsection. However, the relationship between particle inflight behavior and gas flow rate, spray distance etc, can still be reasonably predicted by the simplified one dimensional model. Moreover, from a control point of view, a one dimensional model is more tractable and its solution time is comparable to the evolution of the process.

7.4.2 Analysis of particle inflight behavior

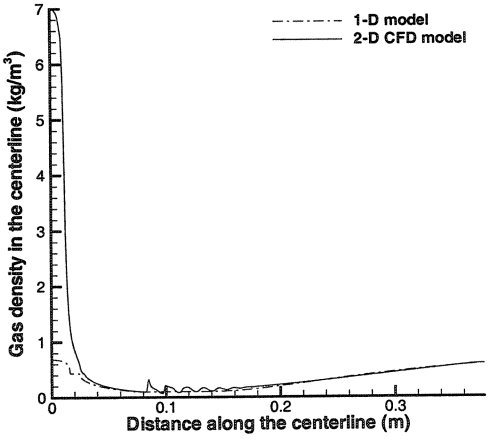
The particle temperature plays an important role in the formation of coating microstructure. Especially, in the fabrication of nanostructured coatings, it is crucial to maintain high particle temperature at the point of impact on the substrate and to prevent particles from being superheated at the same time, because it is precisely the small grain size that contributes to the superior qualities of nanostructured coatings [18]. It is also of great importance to maintain high particle velocity at the point of impact on substrate since the higher the particle velocity, the denser the coating. To solve the particle properties in the gas field, it is important to note that when the substrate is placed downstream of the free jet, the gas flow pattern will be changed because the jet will have a zero axial velocity component at the point of impact on the substrate. To illustrate this, we run two other simulations with the pressure outlet boundary condition set to be wall and all the other boundary condition kept the same. The simulation results are shown in Figure 7.10. It is shown that at long spray distances, such as 0.3 m, the substrate has a minimal influence on both the thermal and the flow field. This is because the gas velocity and temperature are relatively low when the spray distance is long. However, as the spray distance becomes shorter, the interaction between the gas and the plate will have a differential effect on the gas phase, especially the gas velocity.



(a)

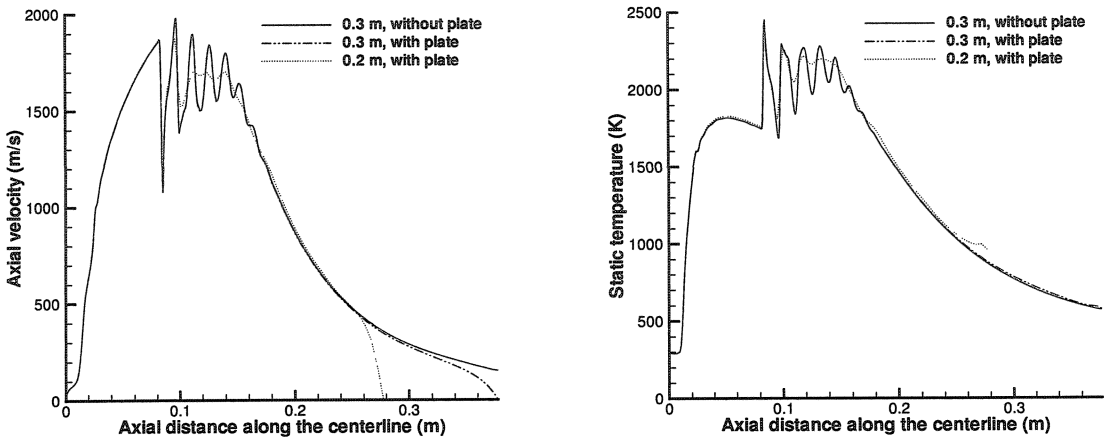


(b)



(c)

Figure 7.9: Comparison of (a) axial velocity, (b) temperature, and (c) density of gas phase in the centerline using a simplified one dimensional model [87, 88] and the CFD model [85].



(a) (b)

Figure 7.10: Influence of substrate on (a) axial velocity and (b) static temperature in the centerline.

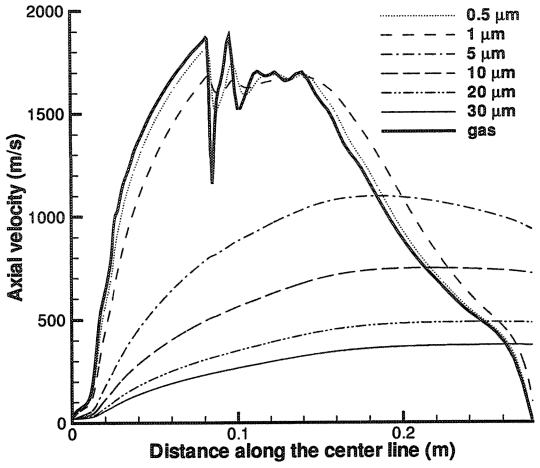
The particle inflight behavior is then solved (particle thermophysical properties are given in Table 7.4.2) under the baseline flow rates given in Table 7.2 and a spray distance of 0.2 m, and the results are shown in Figure 7.11. The profiles of gas velocity and temperature are also given in the same figure for reference. It is shown that particles of small sizes may reach very high velocities during flight, however, their velocities drop more sharply than those of larger particles because of their smaller momentum inertias. For example, a particle with a diameter of 0.5 μm may reach a velocity of about 1800 m/s during flight, however, its velocity decays very sharply and it is eventually trapped by the gas stream. For a different type of particle with a smaller density (Nickel, for example), the maximum size of particles that will fully track the gas stream may be even larger. Moreover, in the shock waves, where the gas velocity oscillates very sharply, the velocity profile of small particles crosses the one of the gas and the former are flat with respect to the axial distance at the point of intersection. On the other hand, particles of small sizes may be heated to the

Table 7.4: Thermophysical properties of WC-12%Co particles [122].

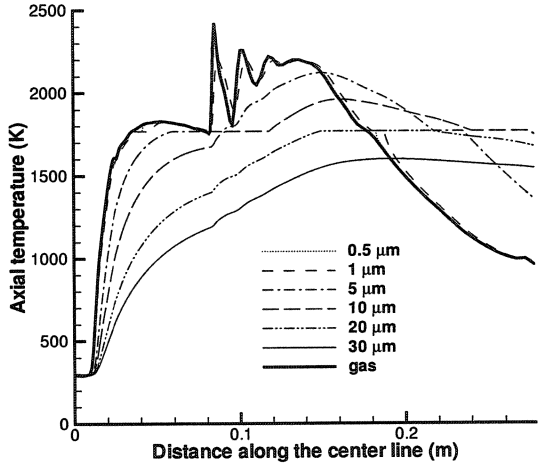
Density, ρ_p	=	14320	kg/m^3
Heat capacity, c_{p_p}	=	295.4	$J/kg/K$
Latent heat of fusion, ΔH_m	=	4.2×10^5	J/kg
Surface emissivity, ε	=	0.4	
Melting temperature of Cobalt, T_m	=	1768	K

melting point in a short time and be fully melted during flight, however, they may eventually be in a coexistence state of liquid and solid or even in a solid state after a long enough distance. Smaller particles tend to change their temperatures easily because of their smaller thermal inertias. The smaller the particle size is, the easier its temperature varies. For particles of large sizes, however, their period for acceleration and heating are both longer, and their velocity (or temperature) profiles become nearly flat as they approach the same velocity (or temperature) of the gas. Moreover, they may not reach the melting point and keep the solid state along the whole flow field. However, particles of medium sizes may become partially melted during flight.

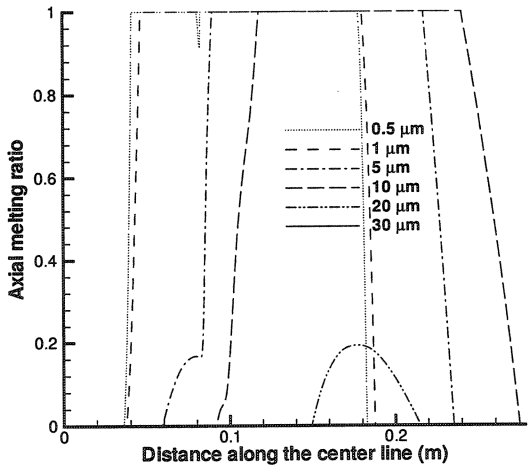
To further understand the behavior of particles in the HVOF process, we also plotted the velocity, temperature and melting ratio at the differential spray distances as a function of particle size, shown in Figure 7.12. Under all spray distances, it can be consistently observed that there is a peak in each of the v_p vs. d_p curve. As the particle diameter increases, the particle velocity increases first, reaching the peak value, and then decreases gradually. On the whole, the change in the spray distance has an stronger influence on small particles than big ones. As the spray distance increases, the velocity of small particles at the point of impact on the substrate decreases, which is caused by the velocity decay of the free jet. However, the velocity of large particles



(a)



(b)



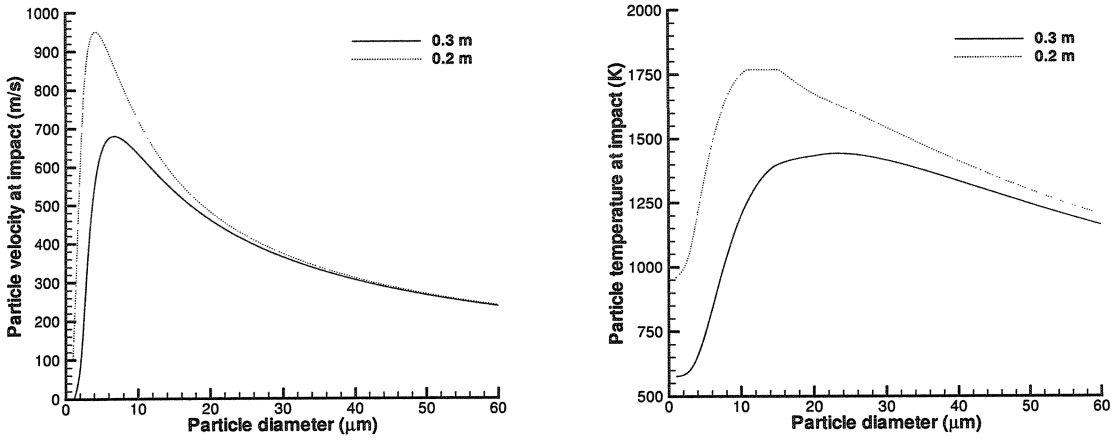
(c)

Figure 7.11: Profiles of (a) particle velocity, (b) temperature and (c) melting ratio along the centerline.

may increase a little as the spray distance increases, although it is hard to discern from the figure. If ignoring this very small change in the velocity of large particles, it can almost be concluded that the spray distance has a negligible influence on the impact velocity of large particles. This is because, as the particle velocity becomes to equal to or larger than the gas velocity, the drag force becomes very small for large particles and their velocity change little. However, the change in the spray distance may have a broader and stronger influence on the particle temperature. At a short spray distance (5 *inch*, for example), particles of several micrometers may be fully melted. However, as the spray distance increases, they may be partially melted or even in a solid state at impact because they solidify as a result of the temperature decay of the free jet. For particles in the range of 10 - 20 μm, although a change in the spray distance has a negligible influence on their velocity, its strong effect on their temperature can be easily observed. The influence of the spray distance on the particle temperature can be explained by the change of the residence time of particles in the gas flame.

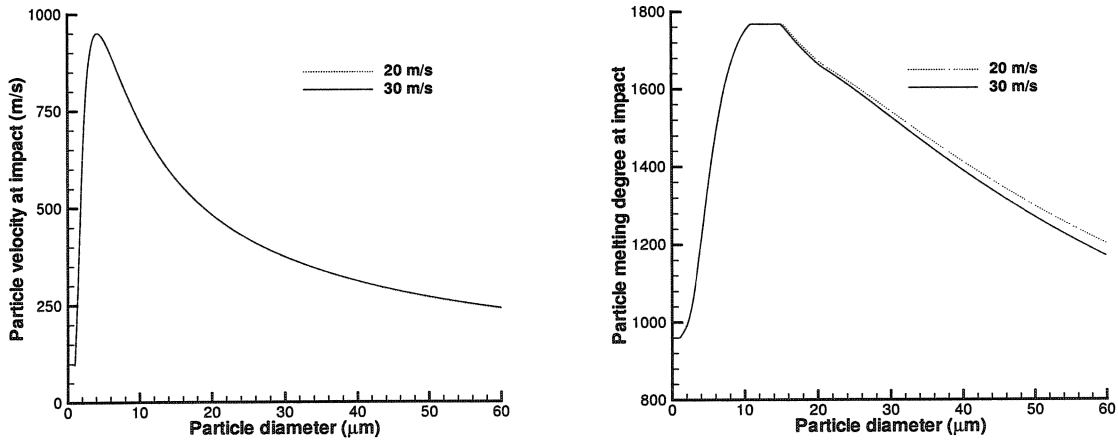
Figure 7.13 shows the influences of particle injection velocity on the profiles of particle velocity and temperature. It can be seen that the injection velocity has a negligible influence on the impact velocity for particles in the whole size range of 1 - 60 μm. It also has a negligible effect on the temperature of small particles at the point of impact on the substrate. The influence of injection velocity on particle temperature becomes visible as the particle diameter goes beyond 30 μm.

The above phenomena can be further explained by the following mathematical analysis. Firstly, it is interesting to observe that for large particles ($d_p \approx 20\ \mu m$ in this case), the particle velocity profile becomes almost flat after an acceleration stage, where $v_p \ll v_g$ holds. Note that since $Re = d_p|v_g - v_p|\rho_g/\mu_g$, Eq. 7.14a can be written



(a) (b)

Figure 7.12: (a) velocity and (b) temperature of particles of different sizes under 20 m/s injection velocity and different spray distances.



(a) (b)

Figure 7.13: (a) velocity and (b) temperature of particles of different sizes under 0.2 m spray distance and different injection velocities.

as:

$$\frac{dv_p}{dt} = \frac{3\mu_g C_D Re}{4\rho_p d_p^2}(v_g - v_p) \tag{7.20}$$

Dividing Eq. 7.14a by Eq. 7.14b, one can derive

$$\frac{dv_p^2}{dx_p} = \frac{3\mu_g C_D Re}{2\rho_p d_p^2}(v_g - v_p) \tag{7.21}$$

Because the maximum velocity that the particles can achieve (especially for large particles) in the HVOF flow field is mainly decided by the initial acceleration stage when $v_p \ll v_g$ holds (this is because when the particle velocity approaches the gas velocity, the drag force term becomes small and the particle velocity profile becomes almost flat). Approximating $(v_g - v_p)$ by v_g, Eq. 7.21 can be analytically solved to yield:

$$v_p = \sqrt{\int_0^{x_p} \frac{3\mu_g C_D Re}{2\rho_p d_p^2} v_g dx_p + v_{p0}^2} \tag{7.22}$$

For particles in the HVOF gas field, the Reynolds number based on the relative velocity is typically less than 10^3, and C_D can be approximately calculated by $18.5/Re^{0.6}$ [6]. Therefore,

$$v_p = \sqrt{\int_0^{x_p} \frac{28 v_g^{1.4} \rho_g^{0.4} \mu_g^{0.4}}{\rho_p d_p^{1.6}} dx_p + v_{p0}^2} \tag{7.23}$$

If one checks the magnitude of the first term and the second one under the square root in Eq. 7.25 it can be found that v_{p0}^2 can be almost neglected. The following parameters are used to estimate these terms: $v_g = 10^3\ m/s$, $\rho_g = 10^{-1}\ kg/m^3$, $\mu_g = 10^{-5} kg/m/s$, $\rho_p = 10^4\ kg/m^3$, $d_p = 10^{-5}\ m$, $x_p = 10^{-2}\ m$, it can be easily figured out that $\int_0^{x_p} \frac{28 v_g^{1.4} \rho_g^{0.4} \mu_g^{0.4}}{\rho_p d_p^{1.6}} dx_p = 10^5\ m^2/s^2$. If $v_{p0} = 30\ m/s$, v_{p0}^2 will be just 1% of the aforementioned integral. Therefore, Eq. 7.25 can be further simplified to be

$$v_p = \sqrt{\int_0^{x_p} \frac{28 v_g^{1.4} \rho_g^{0.4} \mu_g^{0.4}}{\rho_p d_p^{1.6}} dx_p} \tag{7.24}$$

Several conclusions can be drawn from the above analysis. Firstly, a very short flight distance of the particles will compensate for the effect of the change in particle injection velocity. Secondly, the initial particle velocity has a negligible effect on maximum velocity that particle can achieve. Finally, the velocity profile of particles are almost the same after the initial acceleration stage, even if the injection velocities are different.

Furthermore, as a particle falls into the Stokes region ($Re \leq 2$), where $C_D = 24/Re$ holds, the characteristic time for particle motion $\tau = \dfrac{4\rho_p d_p^2}{3\mu_g C_D Re} = \dfrac{\rho_p d_p^2}{18\mu_g}$ is a constant. An analytic solution of Eq. 7.20 yields

$$v_p = e^{-\frac{t}{\tau}} \left[v_{p0} + \int_0^t e^{\frac{t}{\tau}} \frac{v_g}{\tau} dt \right] \tag{7.25}$$

Consider a very small time step Δt, the formula of updating particle velocity is

$$\begin{aligned} v_p^{i+1} &= e^{-\frac{\Delta t}{\tau}} \left[v_p^i + \int_0^{\Delta t} e^{\frac{t}{\tau}} \frac{v_g}{\tau} dt \right] \\ &= e^{-\frac{\Delta t}{\tau}} \left[v_p^i + e^{\frac{t}{\tau}} v_g |_0^{\Delta t} - \int_{v_g^i}^{v_g^{i+1}} e^{\frac{t}{\tau}} dv_g \right] \\ &= v_g^{i+1} - (v_g^i - v_p^i) e^{-\frac{\Delta t}{\tau}} - e^{-\frac{\Delta t}{\tau}} \int_{v_g^i}^{v_g^{i+1}} e^{\frac{t}{\tau}} dv_g \end{aligned} \tag{7.26}$$

Apply Taylor expansion on v_g and ignore all the terms containing derivatives of second order and higher, i.e. $v_g^{i+1} = v_g^i + \dfrac{dv_g}{dt}|_{v_g^i} \Delta t$, the above equation can be further simplified as:

$$v_p^{i+1} = v_g^{i+1} - (v_g^i - v_p^i) e^{-\frac{\Delta t}{\tau}} - \frac{dv_g}{dt}|_{v_g^i} \tau (1 - e^{-\frac{\Delta t}{\tau}}) \tag{7.27}$$

It can be concluded from the above equation that the smaller the characteristic time τ, the easier the particle velocity varies. In particular, for very small τ, or particles of small size or density, $e^{-\frac{\Delta t}{\tau}} \approx 0$ and therefore, $v_p^{i+1} = v_g^{i+1} - \dfrac{dv_g}{dt}|_{v_g^i} \tau$, which implies the particles will be fully tracked by the gas stream if the gas velocity

does not change sharply. Moreover, If v_g is constant, the above equation reduces to $v_p^{i+1} = v_g - (v_g - v_p^i)e^{-\frac{\Delta t}{\tau}}$ or $v_p = v_g - (v_g - v_{p0})e^{-\frac{t}{\tau}} \approx v_g(1 - e^{-\frac{t}{\tau}})$ if $v_{p0} \ll v_g$, which is usually cited in the literature.

Similar analysis can be made on particle heating equation. Note in Eq. 7.16 we used a first order ODE to describe particle heating, which holds only when the Biot number (the ratio of thermal internal resistance to surface film resistance) is less than 0.1. This can be verified by the following analysis:

$$Bi = \frac{hd_p/6}{\lambda_p} = \frac{Nu\lambda_g/6}{\lambda_p} \tag{7.28}$$

For tungsten carbide, $\lambda_p = 10^{1\sim2}\ W/m/K$, since $Nu = 10^{0\sim1}$, $\lambda_g = 10^{-(1\sim2)}\ W/m/K$, the Biot number is much less than 0.1. In addition, the ratio of heat transfer due to convection to that due to radiation can be calculated by:

$$\frac{J_{cov}}{J_{rad}} = \frac{h(T_g - T_p)}{\varepsilon\sigma(T_g^4 - T_p^4)} = \frac{Nu\lambda_g}{d_p\varepsilon\sigma(T_g^2 + T_p^2)(T_g + T_p)} \tag{7.29}$$

Setting $Nu = 10^{0\sim1}$, $\lambda_g = 10^{-(1\sim2)}\ W/m/K$, $d_p = 10^{-5}\ m$, $T_g = 10^3\ K$, $T_p = 10^3\ K$, $\varepsilon = 0.4$, $\sigma = 5.67 \times 10^{-8}$, one can figure out $J_{cov}/J_{rad} \approx 10^2$, which shows radiation only accounts for no more than several percent of the total heat flux. If ignoring the particle melting behavior, one can derive that

$$\frac{dT_p}{dt} = \frac{6\lambda_g Nu(T_g - T_p)}{d_p^2\rho_p c_{p_p}} \tag{7.30a}$$

$$\frac{dT_p}{dx} = \frac{6\lambda_g Nu(T_g - T_p)}{d_p^2\rho_p c_{p_p} v_p} \tag{7.30b}$$

$$\frac{dT_p}{dv_p} = \frac{8\lambda_g Nu(T_g - T_p)}{c_{p_p}\mu_g C_D Re(v_g - v_p)} \tag{7.30c}$$

By setting $\varpi = \frac{d_p^2\rho_p c_{p_p}}{6\lambda_g Nu}$ to be the characteristic time for particle heating, it can be derived from Eq. 7.30a that

$$T_p^{i+1} = T_g^{i+1} - (T_g^i - T_p^i)e^{-\frac{\Delta t}{\varpi}} - \frac{dT_g}{dt}|_{T_g^i}\varpi(1 - e^{-\frac{\Delta t}{\varpi}}) \tag{7.31}$$

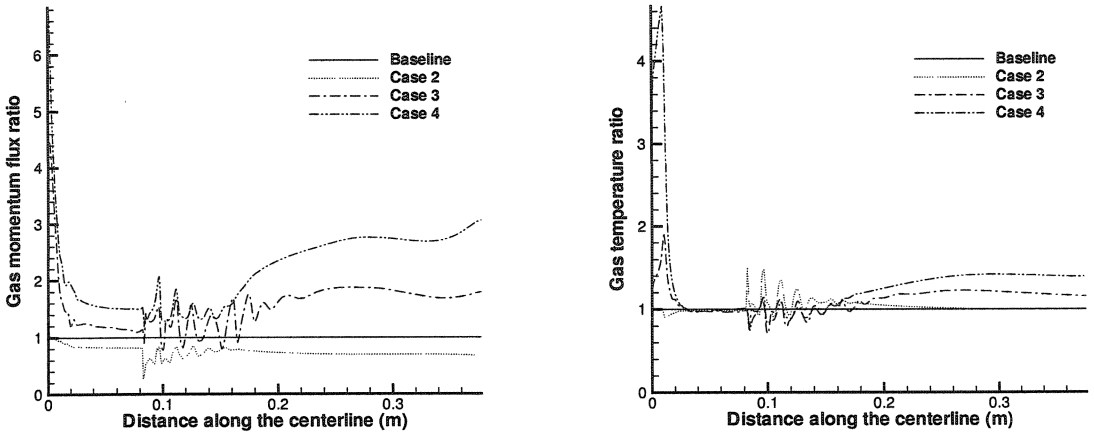
which implies $T_p^{i+1} = T_g^{i+1} - \frac{dT_g}{dt}|_{T_g^i}\varpi$ for very small ϖ, or particles of small size, density or heat capacity. Moreover, Eq. 7.30b shows that an increase of particle velocity will lead to a decrease of particle temperature if the spray distance is fixed.

In addition, we note that

$$\frac{\varpi}{\tau} = \frac{c_{p_p}\mu_g C_D Re}{8\lambda_g Nu} = \frac{2.3\mu_g c_{p_p} Re^{0.4}}{\lambda_g Nu} \tag{7.32}$$

is typically less than one, which means the particle temperature is easier to vary than the particle velocity. Furthermore, v_p/T_p can be increased by increasing v_g/T_g and decreased by decreasing v_g/T_g, which can be used to regulate the relative magnitude of the particle velocity and temperature. Note the gas velocity is typically low in the convergent part of the nozzle, the particle heating can be significantly improved if the gas temperature is maintained at high levels.

To study the influence of gas flow rates on the particle inflight behavior, it is important to note that the gas momentum flux ($\rho_g v_g^2$) is approximately proportional to the drag force (when the effect of the drag coefficient is neglected) and the gas temperature, whose different between the particle temperature provides the driving force for particle. We also plotted the influence of gas flow rates on these two key parameters based on the simulation results in subsection 7.4.1 and the results are shown in Figure 7.14. It is clear that the momentum flux increases with the total mass flow rate and the temperature in the free jet is highly dependent on the equivalence ratio and the total flow rate as well. Therefore, in industrial applications, it is beneficial to increase the total mass flow rate, and to keep the equivalence ratio close to 1.2, wherever it is possible. This conclusion can be substantiated by the simulation results of particle inflight behavior at a standoff of 0.2 m under various gas flow rates, which are shown in Figure 7.15. Typically speaking, the particle velocity increases as the total mass flow rates increases, since high gas momentum flux can be achieved



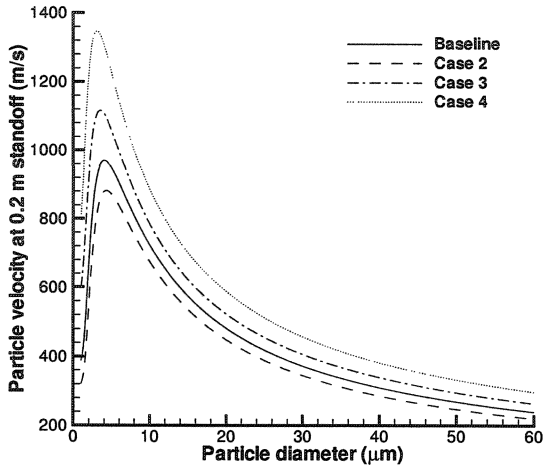
(a) (b)

Figure 7.14: (a) gas momentum flux and (b) gas temperature along the centerline under different gas flow rates. Normalization is done with respective to the corresponding properties under baseline gas flow rates.

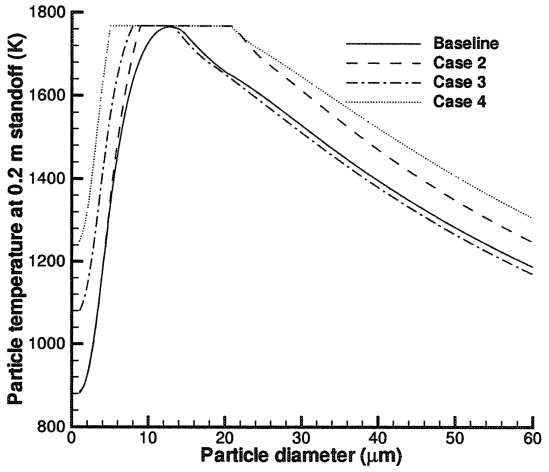
at high gas flow rates, especially in the free jet. The same trend is observed for the particle temperature and degree of melting. However, it is worth noting that the total mass flow rate is not the sole factor affecting particle temperature. For example, the total gas flow rate is the lowest in case 2. However, the particle temperature achieved in this case is even higher than the one in cases 1 and 3, which clearly show that the equivalence ratio is a key parameter that can be manipulated to adjust particle temperature and degree of melting.

7.4.3 Analysis of coating microstructure formation

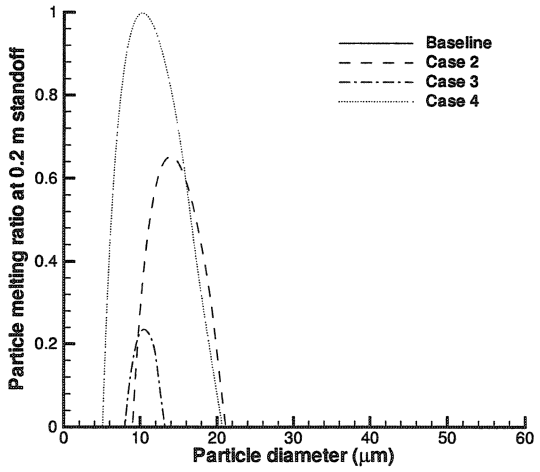
At impact, the particle kinetic energy might be partially converted to thermal energy and the particle temperature and melting degree will increase due to collision with the coating surface. If 100% conversion efficiency is assumed, the increase in the particle



(a)



(b)



(c)

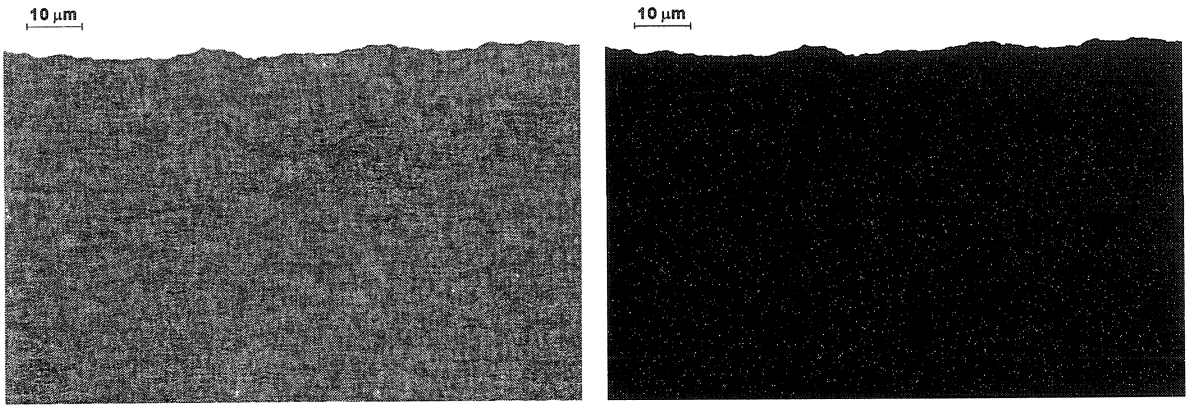
Figure 7.15: (a) velocity and (b) temperature of particles of different sizes at 0.2 m standoff under different gas flow rates.

temperature and melting degree can be estimated by the following equations:

$$\frac{1}{2}m_p v_p^2 = \int_{T_1}^{T_2} m_p c_{p_p} dT + \int_{f_{p_1}}^{f_{p_2}} \Delta H_m m_p df_p \tag{7.33}$$

where T_1, f_{p_1} and T_2, f_{p_2} are the temperature and melting ratio before and after impact, respectively.

Based on this approximation, the coating build-up is modeled using stochastic simulation. In the simulation, the coating cross section is assumed to be a rectangle and is discretized using a 8192 $\times$ 4096 mesh. The size of each grid in the mesh is 0.1 $\times$ 0.1 μm. The particles are assumed to lognormally distributed with $d_{10} = 4$ μm, $d_{50} =$ 12 μm, and $d_{90} = 36$ μm. If all the particles are fully melted, which is the ideal case, the ideal lamellar coating microstructure is captured (see Figure 7.16). However, both our CFD simulations and analyses as well as the experiments [141] show that particles at the point of impact on the substrate may be in different molten states (fully melted, partially melted or solid) due to different sizes and different trajectories in the HVOF flow field. When this fact is taken into account, the ideal coating microstructure is found to be disturbed by the unmelted part of particles. Figures 7.17 and 7.18 show the simulated configuration of the coatings deposited under the first (baseline) and the forth conditions, respectively. It is also shown that unmelted particles affect the coating surface dramatically, thus, leading to a higher porosity and roughness. A comparison of microstructure of coatings fabricated under different flow rates show that when the particle melting ratio is not high, many large particles are bounced off as they hit the substrate. As a result, the deposited coating has a high porosity, for example, 4.6% under the baseline conditions as compared to 1.1% under the conditions in case 4. However, when the particle melting ratio is high, the unmelted particles or the unmelted part of partially melted particle have a high probability to be attached to the previous deposited coating instead of being bounced off (compare



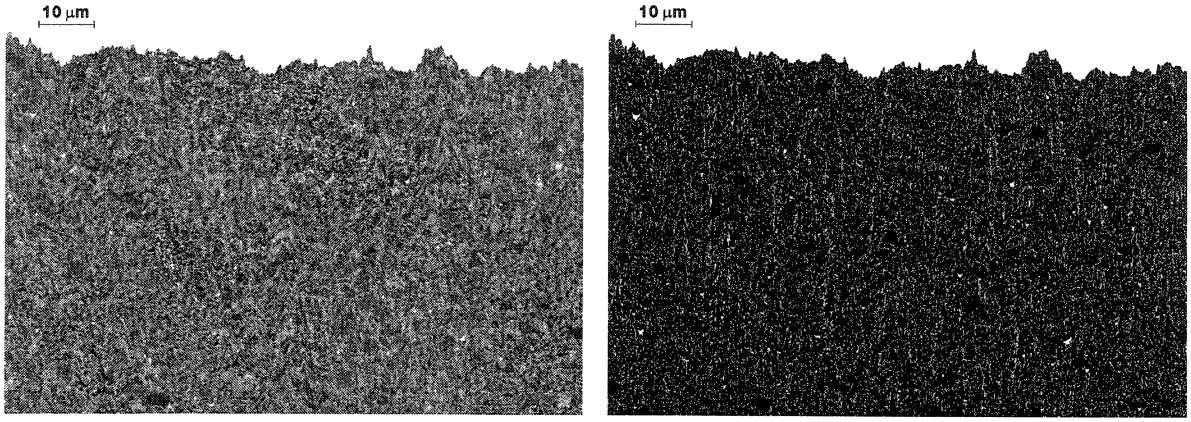
(a) (b)

Figure 7.16: (a) Simulated coating microstructure and (b) pore distribution in the coatings made of fully melted particles (ideal case).

Figure 7.17(a) and 7.18(a)).

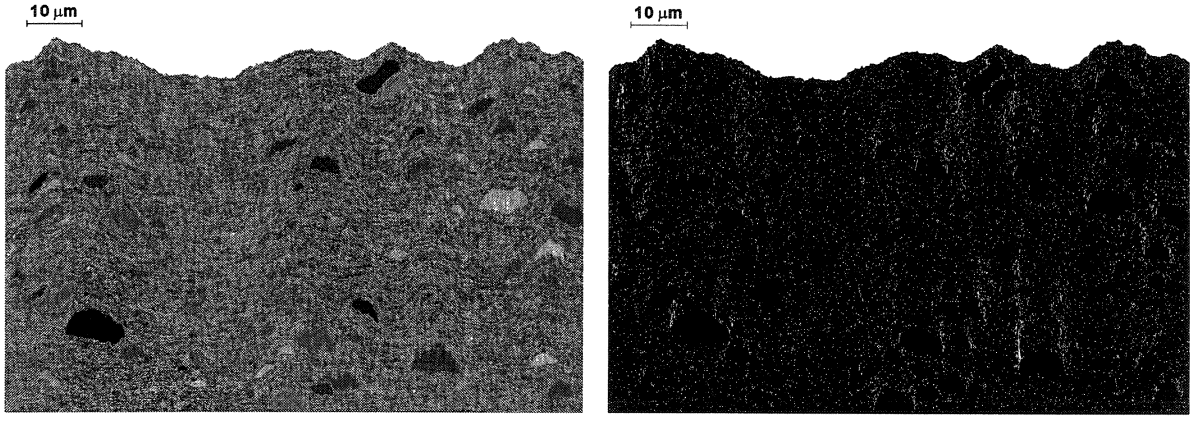
7.5 Summary

A multi-scale modeling framework of HVOF thermal spray process is developed and applied to the processing of WC-12%Co particles using a representative process. A particle laden supersonic reacting flow with overexpanded flow condition at the exit of the nozzle is solved using CFD simulation and the formation of coating microstructure is captured by rule-based stochastic simulation. The simulation result show that coating microstructure is sensitive to particle states at the point of impact and entail the precise control of the process parameters to suppress coating variability. The reader may refer to [84, 87, 88, 86] and the book [25] to see discussions of control of HVOF thermal spray processes.



(a) (b)

Figure 7.17: (a) Simulated coating microstructure and (b) pore distribution in the coatings made of particles of nonuniform molten states, which are deposited under the baseline conditions.



(a) (b)

Figure 7.18: (a) Simulated coating microstructure and (b) pore distribution in the coatings made of particles of nonuniform molten states, which are deposited under the conditions in case 4.

Chapter 8

Conclusions

8.1 Conclusions

In this work, we developed a multiscale modeling and control framework for the HVOF thermal spray processing of nanostructured coatings. In the modeling part, we developed a comprehensive multiscale model, which includes continuum type differential equations that describe the evolution of gas and particle temperature and velocity, and a rule-based stochastic simulator that predicts the evolution of coating microstructure. On the macroscopic gas/particle dynamics side, the Reynolds and Favre-averaged Navier-Stokes equations and energy balance equations are solved with the renormalization group (RNG) k-ϵ turbulence model to capture the complex fluid/thermal behavior, and the particle trajectories, temperature histories and melting degrees are determined using the 4th order Runge-Kutta method. On the microscopic particle deposition process, the formation of coating microstructure is captured by certain rules that encapsulate the main physical features of particle deformation, solidification and coating growth. Based on the proposed model, a detailed comprehensive parametric analysis is carried out to study the relationship between

the key process parameters and the particle inflight behavior as well as the resulting coating properties. Specifically, the modeling and analysis work shows the following:

1. The principle of the HVOF thermal spray process is to utilize the thermal energy released from an exothermic reaction to achieve supersonic velocity and then propel and heat the powder particles in the high temperature high velocity gas stream. In our current work, up to seven shock diamonds have been successfully captured in the supersonic free jet, which is very close to the experimentally observed values (about eight) [17]. This result is superior to others reported in the literature [111, 120, 110, 14, 106, 107, 139, 50, 95, 48, 19, 18, 32], in which only 2-5 shock diamonds were captured. Moreover, in the Diamond Jet hybrid HVOF thermal spray process, the compressed air injected from the annular inlet orifice forms a thin cool layer which separates the hardware from the high temperature flame gases. The cooling effect of air is a unique characteristic of the Diamond Jet hybrid HVOF thermal spray process, which has been successfully captured by CFD simulations in this work.

2. Particles in the HVOF thermal spray process are not uniformly accelerated or heated, i.e., particles of moderate sizes usually achieve highest velocities, temperatures and melting degrees. Small particles, due to their small momentum inertia, may follow the gas stream and not stick on the substrate. (Note that the existence of the substrate will change that pattern of the supersonic free jet. In the vicinity of substrate, the gas velocity in the axial direction decreases to zero and the gas flows in parallel to the substrate.) They are most likely in a solid state upon impact, although they might experience a fully molten state during flight. Particles with sizes larger than 50 μm, however, are hard to be either accelerated (or heated up) or decelerated (or cooled down). The nonuniform

acceleration and heating of particles of different sizes have been validated by experiments [52, 70, 141].

3. The particle velocity and melting degree play a very important role in the formation of coating microstructure. The higher the particle velocity, the larger the flattening ratio and the denser the coating. Moreover, a high degree of particle melting tends to decrease the coating porosity and increase the deposition efficiency (see also [102]). Therefore, to improve process performance, both the velocity and melting degree of particles at the point of impact on the substrate should be maintained above certain levels. However, for the processing of nanostructured coatings, the particle melting ratio should not be too high since it is the nanocrystalline structure preserved in most of the particles deposited on the substrate that leads to the unique characteristics of nanostructured coatings [19].

4. Chamber pressure and fuel/oxygen ratio are two key parameters directly related to the gas momentum flux (ρu^2) and gas temperature, which provide driving forces for particle motion and particle heating. To enhance momentum transfer, the chamber pressure should be maintained as high as possible, however, the pressure in the chamber maintained is usually limited by the maximum reservoir pressure. Moreover, an increase in the total mass flow rate typically results in an increase in the chamber pressure. And, increasing the total mass flow rate tends to lengthen the potential core in the supersonic free jet, or both gas velocity and temperature are maintained at high values for a longer distance, which enhances momentum and heat transfer. However, the relationship between the fuel/oxygen ratio and the gas temperature is not monotonic. The maximum gas temperature is usually achieved at the equivalence ratio around 1.1-1.2, a fuel

rich condition.

Based on the comprehensive process model, a simplified one dimensional model, which is computationally tractable (from a control point of view) while capable of capturing the dominant characteristic occurring within the HVOF thermal spray process, is developed. The control problem is then formulated as the one of regulating volume-based averages of the melting ratio and velocity of the particles at the point of impact on the substrate (these are the variables that directly influence coating microstructure and porosity, which, in turn, determine coating strength and hardness) by directly manipulating the flow rate of fuel, oxygen and air at the entrance of the HVOF thermal spray gun. A feedback control system is developed and applied to the fundamental process model. Closed-loop simulations demonstrate that the particle velocity and melting ratio at the point of impact on substrate reach the desired set-point values in a short time, which validates the feasibility of real-time implementation of feedback control on the HVOF thermal spray system. It is shown that the proposed formulation of the control problem (which accounts for the effect of powder size distribution) leads to a solution of the control problem that is superior (with respect to the achievement of the desired control objectives) to a solution that assumes a monodisperse powder size distribution. It is also demonstrated that the proposed control problem formulation and the feedback control system are robust with respect to disturbances in spray distance and particle injection velocity, and variations in powder size distribution. However, we note that in practice, it is difficult to directly measure the degree of melting of individual particles and consequently, the average degree of melting of the entire particle size distribution. To overcome this limitation, we have proposed an estimation scheme to obtain real-time estimates of particle velocity, temperature and degree of melting. The proposed estimation scheme is based on

the modeling equations which describe the evolution of particle temperature, velocity and degree of melting coupled with the available gas phase measurements. Then, a feedback control system, which directly uses the estimation scheme, is designed to regulate the volume-based average of the particle velocity and degree of melting by manipulating the inlet gas flow rates to the process. The proposed estimation/control structure is applied to a fundamental model of the industrial HVOF thermal spray process and its performance and robustness properties are tested through simulations.

8.2 Future work

A more comprehensive CFD model should be developed for HVOF thermal spray systems which takes into account reactions, transport, phase change and microstructure development phenomena taking place in the process. The model should include the gas dynamics of in the torch and in the free jet, particle injection and the interaction (heat and momentum transfer) between the injected particles and the turbulent gas flow inside the outside the barrel, particle interaction with the barrel walls, phase change of the nanosize powders, droplet motion, distribution and impact on the substrate, microstructure development, and dependence of coated material end-properties on microstructure. Since most of the factors have been taken into account in our present work, this comprehensive model to be developed will focus on the three dimensional tracking of particles in the gas flow/thermal field and the interaction between particles and gas, especially the heating and melting of particles during flight. Moreover, the impact of particles on the substrate and the interaction between melted parts and unmelted ones of the splats will be explored. The detailed model will be used to predict the dependence of the thermal and mechanical properties of the nanostructured coatings on the size, velocity, temperature and molten state of the droplets

which hit on the substrate, along with the consolidation rate of the sprayed droplets. In addition, the model will predict the dependence of these parameters on the heat and momentum transfers between the flame and the particles of the nanopowder, and on the other hand by the morphology, size and injection velocity distribution of the particles. Moreover, the relationship of the nature, roughness and temperature of the substrate and the previously deposited layers on the impact, flattening, cooling and solidification of the droplets will be explicitly modeled.

3-D particle tracking: Most of the previous modeling work is based on the one dimensional particle tracking, in which case the particle properties are only functions of particle size and axial position. However, because of the stochastic behavior of particle motion due to injection velocity distribution, collision of wall, turbulence of the gas phase, particles of the same size may take totally different trajectories during flight and have different melting experience. Therefore, the properties of particles at the point of impact will be not only size dependent but also spatially distributed. The 3-D particle tracking will provide a more accurate description of the evolution of velocity, temperature and melting degree of particles in the HVOF gas flow field.

Interaction between melted parts and unmelted parts in coating microstructure evolution: Most previous studies of particle deposition and coating growth rely on the assumption of fully molten state of particles on the substrate. However, both experiments [52, 70, 141] and numerical modeling [87, 85] have shown that particles at the point of impact on the substrate may be in different molten states (fully melted, partially melted or solid) due to different sizes and different trajectories in the HVOF thermal spray process. We first included the nonuniform molten states of particles upon impact on the substrate [119]. However, the rules governing the coating growth, for example, the threshold for particle bouncing off, the interaction between

the melted parts and the unmelted parts of the splats, can be further improved to have more accurate predictions. Moreover, further efforts should be devoted to the modeling of solid particle impingement and the microstructural evolution, particularly the grain growth behavior, and chemical reactions during impingement.

Model validation: Model validation should be conducted in collaboration with Sulzer Metco, the manufacturer of the Diamond Jet hybrid HVOF thermal spray gun. Comparison between the CFD predicted gas phase data such as pressure, velocity, temperature, mach number and density etc. and the corresponding experimental measurements will point out various modeling assumptions and equations that have been suggested in the literature to improve the process model. Based on the validated process model, a comprehensive parametric analysis will be made to find out the key parameters that affect coating microstructure, including particle velocity, temperature, melting degree, and oxidant content etc. This model would allow precise simulation of HVOF thermal spray processes using any combination of carries gases and nanostructured powders under any operating conditions, which would facilitate testing of different operating conditions with minimum cost compared to expensive laboratory or pilot-scale testing.

We note that although a comprehensive CFD model is adequate to capture the reaction, transport, phase change, microstructure development phenomena involved in the HVOF thermal spray process, however, from a control point of view, such a model is computationally untractable because its solution time can not be comparable to the evolution of the process dynamics. Therefore, a well-characterized, simplified model that is capable of capturing the dominant gas and particle dynamics should be developed and validated. Combination of experimental data and model predictions will determine whether some mechanisms in the thermal spray process may be neglected

in the models used for controller design in order to simplify the controller design task. This can be done by running a bunch of comprehensive CFD simulations under different gas flow rates and equivalence ratios and applying interpolation method to estimate the gas thermal and flow characteristics in a certain range. Our preliminary study has shown that the gas dynamics can be adequately described by the weighted sum of several characteristic functions, thus the gas flow/thermal field can be reasonably estimated in a very short time. Based on the reduced model, model-based estimation and control algorithms will be then synthesized which use the information from the measurements and the simulator to manipulate external variables to achieve the desired performance specifications.

To develop a practical control system for the HVOF thermal spray process, it is also important to note several physical constraints on this process. Firstly, although it is found that an increase in the total gas flow rate leads to an increase in the gas momentum flux and the flame temperature, which is beneficial to the particle in-flight behavior, especially the degree of particle melting, and eventually, the coating microstructure. However, It should be noted that the reservoir pressure of the inlet gases limits the increase of pressure in the combustion chamber. Secondly, the flame temperature cannot increase unboundedly. Although the gas temperature increases a little as the total gas flow rate increases, the flame temperature is almost a sole function of the equivalence ratio, and the highest temperature is achieved at an optimal equivalence ratio around 1.2. If the process is operated under or around this optimal conditions, it will be difficult to further increase the particle temperature and melting ratio by changing the total mass flow rate and the equivalence ratio. One possible way to solve this is to adjust the spray distance. This leads to the development of control systems with switching scheme (see, for example, [100, 34, 33]). Thirdly, significant

uncertainty in the parameters of the process model (time-varying unknown process parameters such as unknown reaction rates, heat transfer coefficients, heat of reaction, etc.) and external disturbances (arbitrary variations in the concentration and temperature of inlet streams), and large dead-times in the measurement instruments and the control actuators should be accounted for in the synthesis of controllers for implementation into practice.

Bibliography

[1] L. Ajdelsztajn, J. Lee, K. Chung, F. L. Bastian, and E. J. Lavernia. Synthesis and nanoindentation study of high-velocity oxygen fuel thermal-sprayed nanocrystalline and near-nanocrystalline Ni coatings. *Metall. Mater. Trans. A*, 33:647–655, 2002.

[2] S. Annavarapu, D. Apelian, and A. Lawley. Spray casting of steel strip: Process analysis. *Metall. Trans. A*, 21:3237–3256, 1990.

[3] M. Benaissa, M. JoseYacaman, T. D. Xiao, and P. R. Strutt. Microstructural study of hollandite-type MnO_2 nano-fibers. *Appl. Phys. Lett.*, 70:2120–2122, 1997.

[4] F. Biancaniello, J. J. Conway, P. I. Espina, G. E. Mattingly, and S. D. Ridder. Particle size measurement of inert-gas-atomized powder. *Materials Sci. & Eng.*, A124:9–14, 1990.

[5] F. Biancaniello, C. Presser, and S.D. Ridder. Real-time particle size analysis during inert gas atomization. *Materials Sci. & Eng.*, A124:21–29, 1990.

[6] R. B. Bird, W. E. Stewart, and E. N. Lightfoot. *Transport Phenomena.* John Wiley & Sons, New York, USA, 1960.

[7] C. M. Bouko, T. H. Le, and H. Henein. Ensemble and single particle laser probe sizing results for gas atomized zinc powders. *Particle & Particle systems characterization*, 10:266–270, 1993.

[8] M. Bussmann, J. Mostaghimi, and S. Chandra. On a three-dimensional volume tracking model of droplet impact. *Physics of Fluids*, 11:1406–1417, 1999.

[9] W. D. Cai and E. J. Lavernia. Sensors and techniques used to monitor processing parameters during spray atomization and deposition. *J. Mater. Sci.*, 30:1125–1138, 1995.

[10] W. D. Cai and E. J. Lavernia. Modeling of porosity during spray forming. *Mat. Sci. Eng. A*, 226:8–12, 1997.

[11] W. D. Cai and E. J. Lavernia. Numerical simulation of porosity evolution during spray forming of Ta-2.5 wt% Fe. *J. Mater. Synth. Proces.*, 5:39–44, 1997.

[12] R. C. Cammarata. Surface and interface stress effects on interfacial and nanostructured materials. *Mater. Sci. & Eng.*, A237:180–184, 1997.

[13] B. M. Cetegen and W. Yu. In-situ particle temperature, velocity, and size measurements in DC arc plasma thermal sprays. *J. Therm. Spray Techn.*, 8:57–67, 1999.

[14] C. H. Chang and R. L. Moore. Numerical simulation of gas and particle flow in a high-velocity oxygen-fuel (HVOF) torch. *J. Therm. Spray Techn.*, 4:358–366, 1995.

[15] Y. Chen, G. Wang, and H. Zhang. Numerical simulation of coating growth and pore formation in rapid plasma spray tooling. *Thin Solid Films*, 390:13–19, 2001.

[16] D. Cheng, G. Trapaga, J. W. McKelliget, and E. J. Lavernia. Mathematical modeling of high velocity oxygen fuel thermal spraying: an overview. *Key Eng. Mat.*, 197:1–25, 2001.

[17] D. Cheng, G. Trapaga, J. W. McKelliget, and E. J. Lavernia. Mathematical modelling of high velocity oxygen fuel thermal spraying of nanocrystalline materials: an overview. *Modelling Simul. Mater. Sci. Eng.*, 11:R1–R31, 2003.

[18] D. Cheng, Q. Xu, G. Trapaga, and E. J. Lavernia. The effect of particle size and morphology on the in-flight behavior of particles during high-velocity oxyfuel thermal spraying. *Metall. Mat. Trans. B*, 32:525–535, 2001.

[19] D. Cheng, Q. Xu, G. Trapaga, and E. J. Lavernia. A numerical study of high-velocity oxygen fuel thermal spraying process. part I: Gas phase dynamics. *Metall. Mat. Trans. A*, 32:1609–1620, 2001.

[20] T. S. Cheng, J. A. Wehrmeyer, R. W. Pitz, O. Jarrett, and G. B. Northam. Raman measurement of mixing and finite-rate chemistry in a supersonic hydrogen-air diffusion flame. *Combustion and Flame*, 99:157–173, 1994.

[21] T. Chiu and P. D. Christofides. Nonlinear control of particulate processes. *AIChE J.*, 45:1279–1297, 1999.

[22] T. Chiu and P. D. Christofides. Robust control of particulate processes using uncertain population balances. *AIChE J.*, 46:266–280, 2000.

[23] T. Chraska and A. H. King. Interfaces in rapidly solidified zirconia-yttria. *Mat. Sci. Forum*, 294:779–782, 1999.

[24] P. D. Christofides. Control of nonlinear distributed process systems: recent developments and challenges. *AIChE J.*, 47:514–518, 2001.

[25] P. D. Christofides. *Model-Based Control of Particulate Processes.* Kluwer Academic Publishers, Particle Technology Series, Netherlands, 2002.

[26] S. Cirolini, J. H. Harding, and G. Jacucci. Computer simulation of plasma-sprayed coatings I coating deposition model. *Surf. Coat. Tech.*, 48:137–145, 1991.

[27] E. L. Crow and K. Shimizu. *Lognormal Distributions: Theory and Applications.* Marcel Dekker, New York, USA, 1988.

[28] C. T. Crowe, M. Sommerfeld, and Y. Tsuji. *Multiphase Flows with Droplets and Particles.* CRC Press, Boca Raton, FL, USA, 1997.

[29] C. T. Crowe and D. E. Stock. A computer solution for two-dimensional fluid-particle flows. *International Journal for Numerical Methods in Engineering*, 10:185–196, 1976.

[30] H. L. de Villiers Lovelock, P. W. Richter, J. M. Benson, and P. M. Young. Parameter study of HP/HVOF deposited WC-Co coatings. *J. Therm. Spray Techn.*, 7:97–107, 1998.

[31] L. DelCastillo, Y. Wu, H. M. Hu, and E. J. Lavernia. The mechanism of porous column formation during spray forming. *Metall. Mater. Trans. A*, 30:1381–1389, 1999.

[32] A. Dolatabadi, J. Mostaghimi, and V. Pershin. Effect of a cylindrical shroud on particle conditions in high velocity oxy-fuel spray process. *J. Mater. Process. Tech.*, 137:214–224, 2003.

[33] N. El-Farra and P. D. Christofides. Coordinated feedback and switching for control of hybrid nonlinear processes. *AIChE J.*, 49:2079–2098, 2003.

[34] N. El-Farra, P. Mhaskar, and P. D. Christofides. Hybrid predictive control of nonlinear systems: Method and applications to chemical processes. *Int. J. Rob. & Non. Contr.*, 14:199–225, 2004.

[35] N. H. El-Farra, T. Chiu, and P. D. Christofides. Analysis and control of particulate processes with input constraints. *AIChE J.*, 47:1849–1865, 2001.

[36] J. R. Fincke, D. C. Haggard, and W. D. Swank. Particle temperature measurement in the thermal spray process. *J. Therm. Spray Techn.*, 10:255–266, 2001.

[37] J. R. Fincke, W. D. Swank, R. L. Bewley, D. C. Haggard, M. Gevelber, and D. Wroblewski. Diagnostics and control in the thermal spray process. *Surf. Coat. Tech.*, 146-147:537–543, 2001.

[38] J. R. Fincke, W. D. Swank, and C. L. Jeffrey. Simultaneous measurement of particle size, velocity and temperature in thermal plasmas. *IEEE Trans. Plasma Sci.*, 18:948–957, 1990.

[39] G. H. Ganser. A rational approach to drag prediction of spherical and nonspherical particles. *Powder Technol.*, 77:143–152, 1993.

[40] C. J. Geankoplis. *Transport Processes and Unit Operations, 3rd ed.* Prentice-Hall, New Jersey, USA, 1993.

[41] M. Gell. The potential for nanostructured materials in gas turbine engines. *Nanostructured Materials*, 6:997–1000, 1995.

[42] R. Ghafouri-Azar, J. Mostaghimi, S. Chandra, and M. Charmchi. A stochastic model to simulate the formation of a thermal spray coating. *J. Therm. Spray Techn.*, 12:53–69, 2003.

[43] L. Gil and M. H. Staia. Influence of HVOF parameters on the corrosion resistance of NiWCrBSi coatings. *Thin Solid Films*, 420–421:446–454, 2002.

[44] S. L. Girshick and C. P. Chiu. Numerical study of MGO powder synthesis by thermal plasma. *Journal of Aerosol Science*, 21:641–650, 1990.

[45] N. G. Glumac, Y. J. Chen, and G. Skandan. Diagnostics and modeling of nanopowder synthesis in low pressure flames. *J. Therm. Spray Techn.*, 13:2572–2579, 1998.

[46] S. Gordon and B. J. McBride. Computer program for calculation of complex chemical equilibrium compositions and applications. NASA Reference Publication 1311, Lewis Research Center, Cleveland, Ohio, USA, 1994.

[47] V. Gourlaouen, E. Verna, and P. Beaubien. Influence of flame parameters on stainless steel coatings properties. In *Thermal Spray: Surface Engineering Via Applied Research, Proceedings of the International Thermal Spray Conference*, pages 487–493, Montreal, QC, Canada, 2000.

[48] S. Gu, C. N. Eastwick, K. A. Simmons, and D. G. McCartney. Computational fluid dynamic modeling of gas flow characteristics in a high-velocity oxy-fuel thermal spray system. *J. Therm. Spray Techn.*, 10:461–469, 2001.

[49] T. C. Hanson, C. M. Hackett, and G. S. Settles. Independent control of HVOF particle velocity and temperature. *J. Therm. Spray Techn.*, 11:75–85, 2002.

[50] B. Hassan, A. R. Lopez, and W. L. Oberkampf. Computational analysis of a three-dimensional high-velocity oxygen fuel (HVOF) thermal spray torch. *J. Therm. Spray Techn.*, 7:71–77, 1998.

[51] J. He, M. Ice, and E. J. Lavernia. Synthesis and characterization of nanostructured Cr3C2-NiCr. *Nanostructured Materials*, 10:1271–1283, 1998.

[52] J. He, M. Ice, and E. J. Lavernia. Particle melting behavior during high-velocity oxygen fuel thermal spraying. *J. Therm. Spray Techn.*, 10:83–93, 2001.

[53] J. H. He, M. Ice, S. Dallek, and E. J. Lavernia. Synthesis of nanostructured WC-12 pct Co coating using mechanical milling and high velocity oxygen fuel thermal spraying. *Metall. Mater. Trans. A*, 31:541–553, 2000.

[54] J. A. Hearley, J. A. Little, and A. J. Sturgeon. The effect of spray parameters on the properties of high velocity oxy-fuel NiAl intermetallic coatings. *Surf. Coat. Tech.*, 123:210–218, 2000.

[55] H. Henein, P. L. Meyer D. J. Holve, and M. A. Kuhni. On-line measurement of powder size distribution in zinc atomization. *Int. J. Powder Metall.*, 28:149–165, 1992.

[56] J. O. Hinze. *Turbulence.* McGraw-Hill, USA, 1975.

[57] K. Hollis and R. Neise. Analysis of the nonthermal emission signal present in a molybdenum particle-laden plasma-spray plume. *J. Therm. Spray Techn.*, 7:383–391, 1998.

[58] K. Hollis and R. Neiser. Particle temperature and flux measurement utilizing a non-thermal signal correction process. *J. Therm. Spray Techn.*, 7:392–402, 1998.

[59] B. Huang, R. J. Perez, and E. J. Lavernia. Grain growth of nanocrystalline Fe-Al alloys produced by cryomilling in liquid argon and nitrogen. *Mat. Sci. Eng. A.*, 255:124–132, 1998.

[60] G. M. Jiang, H. Henein, and M. W. Siege. Overview - intelligent sensors for atomization. *Int. J. Powder Metall.*, 26:253–268, 1990.

[61] H. G. Jiang, M. L. Lau, and E. J. Lavernia. Grain growth behavior of nanocrystalline Inconel 718 and Ni powders and coatings. *Nanostructured Materials*, 10:169–178, 1998.

[62] L. Y. Jiang and J. P. Sislian. LDV measurements of mean velocity components and turbulence intensities in supersonic high-temperature exhaust plumes. *AIAA Paper*, 93 - 3069, 1993.

[63] L. Y. Jiang and J. P. Sislian. Velocity and density measurements in supersonic high-temperature exhaust plumes. *AIAA J.*, 36:1216–1222, 1998.

[64] A. Kalani and P. D. Christofides. Nonlinear control of spatially-inhomogeneous aerosol processes. *Chem. Eng. Sci.*, 54:2669–2678, 1999.

[65] A. Kalani and P. D. Christofides. Modeling and control of a titania aerosol reactor. *Aer. Sci. & Tech.*, 32:369–391, 2000.

[66] A. Kalani and P. D. Christofides. Simulation, estimation and control of size distribution in aerosol processes with simultaneous reaction, nucleation, condensation and coagulation. *Comp. & Chem. Eng.*, 26:1153–1169, 2002.

[67] J. Karthikeyan, C. C. Berndt, S. Reddy, J. Y. Wang, A. H. King, and H. Herman. Nanomaterial deposits formed by DC plasma spraying of liquid feedstocks. *J. Amer. Cer. Soc.*, 81:121–128, 1998.

[68] J. Kartikeyan, C. C. Berndt, J. Tikkanen, J. Y. Wang, A. H. King, and H. Herman. Nanomaterial powders and deposits prepared by flame spray processing of liquid precursors. *Nanostructured Materials*, 8:61–74, 1997.

[69] D. Katoshevski and J. H. Seinfeld. Analytical solution of the multicomponent aerosol general dynamic equation - without coagulation. *Aer. Sci. & Tech.*, 27:541–549, 1997.

[70] K. A. Khor, H. Li, and P. Cheang. Significance of melt-fraction in hvof sprayed hydroxyapatite particles, splats and coatings. *Biomaterials*, 25:1177–1186, 2004.

[71] R. Knight, R. W. Smith, and Z. Xiao. Particle velocity measurements in HVOF and APS systems. In *Thermal Spray Industrial Applications, Proceedings of 7th National Thermal Spray Conference*, pages 331–336, 1994.

[72] O. Knotek and R. Elsing. Monte carlo simulation of the lamellar structure of thermally sprayed coatings. *Surf. Coat. Tech.*, 32:261–271, 1987.

[73] N. T. Lagen and J. M. Seiner. Evaluation of water cooled supersonic temperature and pressure probes for application to 2000 F flows. NASA Technical Memorandum 102612, Langley Research Center, 1990.

[74] M. L. Lau, V. V. Gupta, and E. J. Lavernia. Mathematical modeling of particle behavior of nanocrystalline Ni during high velocity oxy-fuel thermal spray. *Nanostructured Materials*, 10:715–722, 1998.

[75] M. L. Lau, V. V. Gupta, and E. J. Lavernia. Particle behavior of nanocrystalline 316-stainless steel during high velocity oxy-fuel thermal spray. *Nanostructured Materials*, 12:319–322, 1999.

[76] M. L. Lau, J. He, R. Schweinfest, M. Rhle, C. G. Levi, and E. J. Lavernia. Synthesis and characterization of nanocrystalline Cu-Al coatings. *Materials Science and Engineering A*, 347:231–242, 2003.

[77] M. L. Lau, H. G. Jiang, W. Nuchter, and E. J. Lavernia. Thermal spraying of nanocrystalline Ni coatings. *Physica Status Solidi A - Applied Research*, 166:257–268, 1998.

[78] M. L. Lau, E. Strock, A. Fabel, C. J. Lavernia, and E. J. Lavernia. Synthesis and characterization of nanocrystalline Co-Cr coatings by plasma spraying. *Nanostructured Materials*, 10:723–730, 1998.

[79] W. Lauterborn, A. Judt, and E. Schmitz. High-speed off-axis holographic cinematography with a copper-vapor-pumped dye laser. *Optics Letters*, 18:4–6, 1993.

[80] E. J. Lavernia and Y. Wu. *Spray Atomization and Deposition.* Wiley, New-York, 1996.

[81] T. Le, R. Stefaniuk, H. Henein, and J. Huot. Measurement and analysis of melt flowrate in gas atomization. *Int. J. Powder Metall.*, 35:51–59, 1999.

[82] Z. H. Lee, M. M. Hu, E. J. Lavernia, and D. R. White. The mechanism of porous column formation during spray forming. *Metall. Mater. Trans. A*, 30:1679–1682, 1999.

[83] M. Li and P. D. Christofides. Modeling and Analysis of HVOF Thermal Spray Process Accounting for Powder Size Distribution. *Chem. Eng. Sci.*, 58:849–857, 2003.

[84] M. Li and P. D. Christofides. Feedback control of HVOF thremal spray process accounting for powder size distribution. *J. Therm. Spray Techn.*, 13:108–120, 2004.

[85] M. Li and P. D. Christofides. Multiscale modeling and analysis of HVOF thermal spray process. *Chem. Eng. Sci.* submitted, 2004.

[86] M. Li, D. Shi, and P. D. Christofides. Model-based estimation and control of particle velocity and melting in HVOF thermal spray. *Chem. Eng. Sci.* in press, 2004.

[87] M. Li, D. Shi, and Christofides P. D. Diamond jet hybrid HVOF thermal spray: Gas-phase and particle behavior modeling and feedback control design. *Ind. & Eng. Chem. Res.*, 43:3632–3652, 2004.

[88] M. Li, D. Shi, and Christofides P. D. Modeling and control of HVOF thermal spray processing of WC-Co coatings. *Powder Technol.* to appear, 2004.

[89] W. C. Lih, S. H. Yang, C. Y. Su, S. C. Huang, I. C. Hsu, and M. S. Leu. Effects of process parameters on molten particle speed and surface temperature and the properties of HVOF CrC/NiCr coatings. *Surf. Coat. Tech.*, 133, 2000.

[90] R. S. Lima, A. Kucuk, and C. C. Berndt. Integrity of nanostructured partially stabilized zirconia after plasma spray processing. *Mat. Sci. Eng. A*, 313:75–82, 2001.

[91] H. Liu, E. J. Lavernia, and R. H. Rangel. Numerical simulation of substrate impact and freezing of droplets in plasma spray processes. *J. Phys. D: Appl. Phys.*, 26:1900–1908, 1993.

[92] H. Liu, E. J. Lavernia, and R. H. Rangel. Numerical stimulation of impingement of molten Ti, Ni, and W droplets on a flat substrate. *J. Therm. Spray Techn.*, 2:369–378, 1993.

[93] H. Liu, E. J. Lavernia, and R. H. Rangel. Modeling of molten droplet impingement on a nonflat surface. *Acta Metall. Mater.*, 43:2053–2072, 1995.

[94] H. M. Liu, R. H. Rangel, and E. J. Lavernia. Modeling of reactive atomization and deposition processing of NI_3AL. *Acta Metall. Mater.*, 42:3277–3289, 1994.

[95] A. R. Lopez, B. Hassan, W. L. Oberkampf, R. A. Neiser, and T. J. Roemer. Computational fluid dynamics analysis of a wire-feed, high-velocity oxygen fuel (HVOF) thermal spray porch. *J. Therm. Spray Techn.*, 7:374–382, 1998.

[96] E. Lugscheider, C. Herbst, and L. Zhao. Parameter studies on high-velocity oxy-fuel spraying of MCrAlY coatings. *Surf. Coat. Tech.*, 108-109:16–23, 1998.

[97] J. Madejski. Solidification of droplets on a cold surface. *Int. J. Heat Mass Transfer*, 19:1009–1013, 1976.

[98] P. Marthur, S. Annavarapu, D. Apelian, and A. Lawley. Spray casting: An integral model for process understanding and control. *Mat. Sci. Eng. A*, 142:261–276, 1991.

[99] M. Mellali, P. Fauchais, and A. Grimaud. Influence of substrate roughness and temperature on the adhesion/cohesion of alumina coatings. *Surf. Coat. Tech.*, 81:275–286, 1996.

[100] P. Mhaskar, N. El-Farra, and P. D. Christofides. Hybrid predictive control of process systems. *AIChE J.*, 50:1242–1259, 2004.

[101] D. Mills. Personal communication, sulzer metco, 2003.

[102] C. Moreau and L. Leblanc. Optimization and process control for high performance thermal spray coatings. *Key Eng. Mat.*, 197:27–57, 2001.

[103] J. Mostaghimi, S. Chandra, R. Ghafouri-Azar, and A. Dolatabadi. Modeling thermal spray coating processes: a powerful tool in design and optimization. *Surf. Coat. Tech.*, 163-164:1–11, 2003.

[104] R. Mueller, R. Jossen, S. E. Pratsinis, M. Watson, and M. K. Akhtar. Zirconia nanoparticles made in spray flames at high production rates. *J. Am. Ceram. Soc.*, 87:197–202, 2004.

[105] R. Mueller, L. Madler, and S. E. Pratsinis. Nanoparticle synthesis at high production rates by flame spray pyrolysis. *Chem. Eng. Sci.*, 58:1969–1976, 2003.

[106] W. L. Oberkampf and M. Talpallikar. Analysis of a high-velocity oxygen-fuel (HVOF) thermal spray torch part 1: Numerical formulation. *J. Therm. Spray Techn.*, 5:53–61, 1996.

[107] W. L. Oberkampf and M. Talpallikar. Analysis of a high-velocity oxygen-fuel (HVOF) thermal spray torch part 2: Computational results. *J. Therm. Spray Techn.*, 5:62–68, 1996.

[108] D. Oliver and R. Enikov. Micro-particles temperature measurements in a plasma jet. *Vacuum*, 58:244–249, 2000.

[109] L. Pawlowski. *The Science and Engineering of Thermal Spray Coatings.* John Wiley & Sons, Chichester, England, 1995.

[110] G. D. Power, T. J. Barber, and L. M. Chiappetta. Analysis of a high velocity oxygen-fuel (HVOF) thermal torch. In *the 28th AIAA/SAE/ASME/ASEE Joint Propulsion Conference and Exhibit,* AIAA92-3598, Nashville, Tennessee, 1992.

[111] G. D. Power, E. B. Smith, T. J. Barber, and L. M. Chiappetta. Analysis of a combustion (HVOF) spray deposition gun. Report 91-8, United Technologies Research Center, East Hartford, Connecticut, USA, 1991.

[112] W. H. Press, S. A. Teukolsky, W. T. Vetterling, and B. P. Flannery. *Numerical recipes in C++ : the art of scientific computing, 2nd ed.* Cambridge University Press, New YorK, USA, 1997.

[113] D. E. Reisner, A. J. Salkind, P. R. Strutt, and T. D. Xiao. Nickel hydroxide and other nanophase cathode materials for rechargeable batteries. *Journal of Power Sources*, 65:231–233, 1997.

[114] J. A. Roberson and C. T. Crowe. *Engineering Fluid Dynamics, 6th ed.* John Wiley & Sons, New York, USA, 1997.

[115] Biancaniello F. S., P. I. Espina, G. E. Mattingly, and S. D. Rider. A flow visualization study of supersonic inert gas-metal atomization. *Mat. Sci. Eng. A*, 119:161–168, 1989.

[116] K. Sakaki and Y. Shimizu. Effect of the increase in the entrance convergent section length of the gun nozzle on the high-velocity oxygen fuel and cold spray process. *J. Therm. Spray Techn.*, 10:487–496, 2001.

[117] S. K. Sampath, D. G. Kanhere, and R. Pandey. Electronic structure of spinel oxides: zinc aluminate and zinc gallate. *Journal of Physics-Condensed Matter*, 11:3635–3644, 1999.

[118] A. K. Sandrowitz, J. M. Cooke, and N. G. Glumac. Flame emission spectroscopy for equivalence ratio monitoring. *Applied Spectroscopy*, 52:658–662, 1998.

[119] D. Shi, M. Li, and P. D. Christofides. Diamond jet hybrid HVOF thermal spray: Rule-based modeling of coating microstructure. *Ind. & Eng. Chem. Res.*, 43:3653–3665, 2004.

[120] E. B. Smith, G. D. Power, T. J. Barber, and L. M. Chiappetta. Application of computational fluid dynamics to the HVOF thermal spray gun. In *Proceedings of the International Thermal Spray Conference & Exposition*, pages 805–810, Orlando, Florida, 1992.

[121] V. V. Sobolev and J. M. Guilemany. Dynamic processes during high velocity oxyfuel spraying. *international materials reviews*, 41:13–32, 1996.

[122] V. V. Sobolev, J. M. Guilemany, J. C. Garmier, and J. A. Calero. Modelling of particle movement and thermal behavior during high velocity oxy-fuel spraying. *Surf. Coat. Tech.*, 63:181–187, 1994.

[123] H. D. Steffens, H. Kern, and M. Fathi-Torbaghan. An expert system for diagnosis of low pressure plasma spraying. In *Proceedings of Conference on Thermal Spray Technology*, pages 67–74, Cincinnati, OH, 1989.

[124] W. D. Swank, J. R. Fincke, and D. C. Haggard. A particle temperature sensor for monitoring and control of the thermal spray process. In *Proceedings of the 8th National Thermal Spray Conference*, pages 111–116, Houston, Texas, 1995.

[125] W. D. Swank, J. R. Fincke, D. C. Haggard, and G. Irons. HVOF gas flow field characteristics. In *Proceedings of the 7th National Thermal Spray Conference*, pages 313–318.

[126] W. D. Swank, J. R. Fincke, D. C. Haggard, G. Irons, and R. Bullock. HVOF particle flow field characteristics. In *Proceedings of the 7th National Thermal Spray Conference*, pages 319–324, Boston, Massachusetts, 1994.

[127] H. H. Tawfik and F. Zimmerman. Mathematical modeling of the gas and powder flow in HVOF systems. *J. Therm. Spray Techn.*, 6:345–352, 1997.

[128] V. L. Tellkamp, S. Dallek, D. Cheng, and E. J. Lavernia. Grain growth behavior of a nanostructured 5083 al-mg alloy. *J. Mater. Res.*, 16:938–944, 2001.

[129] V. L. Tellkamp, M. L. Lau, A. Fabel, and E. J. Lavernia. Thermal spraying of nanocrystalline Inconel 718. *Nanostructured Materials*, 9:489–492, 1997.

[130] I. Thomson, V. Pershin, J. Mostaghimi, and S. Chandra. Experimental testing of a curvilinear gas shroud nozzle for improved plasma spraying. *Plasma Chem. Plasma Process.*, 21:65–82, 2001.

[131] T. C. Totemeier, R. N. Wright, and W. D. Swank. Microstructure and stresses in HVOF sprayed iron aluminide coatings. *J. Therm. Spray Techn.*, 11:400–408, 2002.

[132] N. Wagner, K. Gnadig, H. Kreye, and H. Kronewetter. Particle velocity in hypersonic flame spraying of WC-Co. *Surface Technology*, 22:61–71, 1984.

[133] G-X Wang, V. Prasad, and S. Sampath. Rapid solidification in thermal spray deposition: Microstructure and modelling. *Sadhana-Academy Proceedings in Engineering Sciences*, 26:35–57, 2001.

[134] K. Wegner and S. E. Pratsinis. Nozzle-quenching process for controlled flame synthesis of titania nanoparticles. *AIChE J.*, 49:1667–1675, 2003.

[135] T. D. Xiao, M. Benaissa, R. Perez, P. R. Strutt, and M. J. Yacaman. Microstructural characteristics of chemically processed manganese oxide nanofibres. *Acta Materialia*, 45:1685–1693, 1997.

[136] T. D. Xiao, P. R. Strutt, M. Benaissa, H. Chen, and B. H. Kear. Synthesis of high active-site density nanofibrous MnO_2-base materials with enhanced permeabilities. *Nanostructured Materials*, 10:1051–1061, 1998.

[137] Q. Xu, V. V. Gupta, and E. J. Lavernia. On the mechanism of mushy layer formation during droplet-based processing. *Metall. Mater. Trans. B*, 30:527–539, 1999.

[138] Y. W. Xun, E. J. Lavernia, and F. A. Mohamed. Synthesis of nanocrystalline Zn-22 pct Al using cryomilling. *Metall. Mater. Trans. A*, 35:573–581, 2004.

[139] X. Yang and S. Eidelman. Numerical analysis of a high-velocity oxygen-fuel thermal spray system. *J. Therm. Spray Techn.*, 5:175–184, 1996.

[140] A. V. Zagorski and F. Stadelmaier. Full-scale modelling of a thermal spray process. *Surf. Coat. Tech.*, 146-147:162–167, 2001.

[141] D. Zhang, S. J. Harris, and D. G. McCartney. Microstructure formation and corrosion behaviour in HVOF-sprayed Inconel 625 coatings. *Mat. Sci. Eng. A*, 344:45–56, 2003.